

**STUDY OF NICKEL(111) BY PHOTOEMISSION
SPECTROSCOPY**

Mr. Wiwat Wongkokua

**A Thesis Submitted in Partial Fulfillment of the Requirements for
the Degree of Doctor of Philosophy in Physics**

Suranaree University of Technology

Academic Year 2004

ISBN 974-533-411-1

การศึกษานิเกล(111) โดยโฟโตอิมิชันสเปกโทรสโกปี

นายวิวัฒน์ วงศ์ก่อเกื้อ

วิทยานิพนธ์นี้เป็นส่วนหนึ่งของการศึกษาตามหลักสูตรปริญญาวิทยาศาสตรดุษฎีบัณฑิต

สาขาวิชาฟิสิกส์

มหาวิทยาลัยเทคโนโลยีสุรนารี

ปีการศึกษา 2547

ISBN 974-533-411-1

STUDY OF NICKEL(111) BY PHOTOEMISSION SPECTROSCOPY

Suranaree University of Technology has approved this thesis submitted in partial fulfillment of the requirements for the Degree of Doctor of Philosophy.

Thesis Examining Committee

P. Manyum

(Asst. Prof. Dr. Prapun Manyum)

Chairperson

P. Songs

(Asst. Prof. Dr. Prayoon Songsiriritthigul)

Member (Thesis Advisor)

T. Ishii

(Prof. Dr. Takehiko Ishii)

Member

P. Suebka.

(Assoc. Prof. Dr. Prasart Suebka)

Member

Hideki Nakajima

(Dr. Hideki Nakajima)

Member

P. Suebka.

S. Sujitjorn

(Assoc. Prof. Dr. Sarawut Sujitjorn)

Vice Rector for Academic Affairs

(Assoc. Prof. Dr. Prasart Suebka)

Dean of Institute of Science

วิวัฒน์ วงศ์ก่อเกื้อ : การศึกษานิเกิล(111) โดยโฟโตอิมิชชันสเปกโทรสโกปี (STUDY OF NICKEL(111) BY PHOTOEMISSION SPECTROSCOPY) อาจารย์ที่ปรึกษา : ผู้ช่วยศาสตราจารย์ ดร.ประยูร ส่งสิริฤทธิกุล, 242 หน้า. ISBN 974-533-411-1

ในงานวิทยานิพนธ์นี้ ได้มีการตรวจสอบวิเคราะห์สเปกตรัมของ *MVV* super Coster-Kronig (sCK) ของโลหะนิเกิล รูปร่างของสเปกตรัมของแถบ *MVV* sCK แสดงให้เห็นถึงลักษณะเด่น ณ ค่าพลังงานจลน์ของอิเล็กตรอนเท่ากับ 49.8, 56.3, 59.5 และ 60.5 อิเล็กตรอนโวลต์ จากทฤษฎีของ ซินิ-ซาวาทซกี (Cini-Sawatzky) พบว่าค่ามากที่สุดของพลังงานดูลอมบ์ในอะตอมเท่ากับ 8 อิเล็กตรอนโวลต์เมื่อพิจารณาให้ลักษณะเด่นที่ตำแหน่ง 49.8 อิเล็กตรอนโวลต์เป็นแถบของพลังงาน split-off atomic-like band รูปร่างของแถบ *MVV* sCK มีการเปลี่ยนแปลงเมื่อมีการเปลี่ยนค่าพลังงานของแสงที่กระตุ้น ซึ่งค่าพลังงานที่ทำให้มีการเปลี่ยนแปลงรูปร่างดังกล่าวมีค่าตั้งแต่ค่าพลังงานที่มีค่าเท่ากับพลังงานที่จะกระตุ้นให้อิเล็กตรอน $3p$ หลุดออกจากอะตอมของนิเกิลและเหนือกว่าจนถึงประมาณ 10 อิเล็กตรอนโวลต์ เมื่อพลังงานจลน์ของแถบ *MVV* sCK เริ่มทับซ้อนกับพลังงานของแถบ two-hole-bound-state พบว่า รูปร่างของแถบ *MVV* sCK มีการเปลี่ยนแปลงเป็นอย่างมากและแถบทั้งสองทับซ้อนกันชนิดที่ไม่สามารถแยกแยะได้ ตำแหน่งของแถบ two-hole-bound-state เลื่อนในทิศทางเข้าสู่ค่าพลังงานยึดเหนี่ยวที่สูงขึ้นเมื่อพลังงานที่ใช้ในการกระตุ้นมีค่าเข้าสู่ระดับพลังงานกำหนด $3p-3d$ ผลที่ได้ดังกล่าวสามารถตีความได้ว่าการเกิดอันตรกิริยาของสถานะสุดท้าย (final state interaction) ข้อเสนอที่ว่าสถานะระหว่างกลางและสถานะสุดท้ายเป็นขั้นตอนเดียวกัน สอดคล้องกับสเปกตรัมของสถานะเริ่มต้นคงที่และสเปกตรัมของผลรวมอิเล็กตรอนทั้งหมด นอกจากนั้นยังได้นำเอาเทคนิคการวัดโฟโตอิมิชชันแบบแยกแยะเชิงมุมไปใช้ในการวัดผิวของโลหะนิเกิลที่มีระนาบผลึก (111) ขนานกับผิว

สาขาวิชาฟิสิกส์
ปีการศึกษา 2547

ลายมือชื่อนักศึกษา วิวัฒน์ วงศ์ก่อเกื้อ
ลายมือชื่ออาจารย์ที่ปรึกษา อ.ประยูร
ลายมือชื่ออาจารย์ที่ปรึกษาร่วม อ.สุวิทย์
ลายมือชื่ออาจารย์ที่ปรึกษาร่วม อ.วิภากร อภิบาล

WIWAT WONGKOKUA : STUDY OF NICKEL(111) BY
PHOTOEMISSION SPECTROSCOPY. THESIS ADVISOR : ASST. PROF.
PRAYOON SONGSIRIRITTHIGUL, Ph.D. 242 PP. ISBN 974-533-411-1

SUPER COSTER-KRONIG/AUGER/PHOTOEMISSION/NICKEL(111)

In this thesis work, the *MVV* super Coster-Kronig (sCK) spectra of metallic nickel have been investigated. The measured spectral shape of the *MVV* sCK band shows the features at electron kinetic energy of 49.8 eV, 56.3 eV, 59.5 eV and 60.5 eV. Based on the Cini-Sawatzky theory, the effective intra-atomic Coulomb energy at a large value was found to be 8 eV when the feature at 49.8 eV is considered to be the split-off atomic-like band. The shape of *MVV* sCK spectrum changed as the excitation energy changed occurs from the $3p$ threshold to 10 eV above it. As the kinetic energy for the *MVV* sCK band starts to overlap that of the two-hole-bound-state band, the *MVV* sCK band changes its shape considerably and the two bands get inseparable. The location of the apparent two-hole-bound-state band shifts toward higher binding energy on the $3p-3d$ resonance. This can be interpreted as a kind of the final state interaction. The suggested intermediate and final states of the single step transition are consistent with the constant-initial-state spectra and total-photo yield spectrum. In addition, angle-resolved photoemission (ARPES) measurements on a metallic Ni(111) sample have been carried out.

School of Physics

Academic Year 2004

Student's Signature Wiwat Wongkokua

Advisor's Signature P. Song.

Co-advisor's Signature P. Jit

Co-advisor's Signature P. Suebka . .

ACKNOWLEDGEMENTS

This thesis would not have been completed without assistance and guidance by many persons in various ways. It is my pleasure to express my gratitude to the following persons for their contribution:

- Asst. Prof. Dr. Prayoon Songsiriritthigul, my thesis advisor, for the invaluable advice and the unfailing support during the course of my studies at the School of Physics.

- I am grateful to Prof. Dr. Takehiko Ishii for his enlightening guidance and encouragement. His ideas have been of vital importance for this thesis.

- Assoc. Prof. Dr. Prasart Suebka, the dean of Institute of Science of the Suranaree University of Technology, for his advice and kind support.

- Dr. Hideki Nakajima for his helping and training in the experiments.

- I would like to thank Mr. Samred Kantee, Mr. Somchai Tancharakorn, and Mr. Ritthikrai Chai-ngam for their generous help.

- Ministry of Education (MOE) and National Synchrotron Research Center (NSRC) for partially financial support.

Wiwat Wongkokua

CONTENTS

	Page
ABSTRACT IN THAI	I
ABSTRACT IN ENGLISH	II
ACKNOWLEDGEMENTS	III
CONTENTS.....	IV
LIST OF TABLES	VIII
LIST OF FIGURES	X
 CHAPTER	
I INTRODUCTION.....	1
1.1 Introductory Remark.....	1
1.2 Solid State Properties.....	6
1.3 Energy-band.....	14
1.4 Synchrotron Radiation	36
1.4.1 High Flux and High Brilliance.....	37
1.4.2 Tunability	39
1.4.3 Polarization	40
1.4.4 Theoretical Spectrum.....	44
1.4.5 Pulsed Light	44
1.4.6 Cleanliness	44
1.5 Photoemission.....	45

CONTENTS (Continued)

	Page
1.6 Two-hole-bound-state	77
1.7 MVV sCK Spectra	87
1.8 Cini-Sawatzky Theory	95
1.9 Purpose of the Research.....	102
II EXPERIMENTAL TECHNIQUES AND PROCEDURES	103
2.1 Outline of the Experiment.....	103
2.2 Sample Preparation	105
2.3 Light Sources	115
2.3.1 Helium Discharge Lamp	115
2.3.2 X-ray Tube	117
2.3.3 Synchrotron Light Source	120
2.4 Optical Beamline	123
2.5 Experimental Station.....	127
2.5.1 Vacuum Chamber	127
2.5.2 Sample Holder	131
2.5.3 Energy Analyzer	131
2.5.3.1 ARPES Analyzer	132
2.5.3.2 CLAM	132
2.5.4 Electron Gun	136
2.5.5 Ion Gun	136
2.5.6 LEED System.....	139

CONTENTS (Continued)

	Page
2.6 Photoemission Measurements.....	141
2.6.1 AIPES Measurements	141
2.6.2 ARPES Measurements	145
2.6.3 TY and CIS	146
III EXPERIMENTAL RESULTS.....	147
3.1 Introduction to the Measurements of the super Coster-Kronig Spectra of Ni	147
3.2 Angle-integrated Spectra	155
3.2.1 Angle-integrated Spectra	155
3.2.2 Auger (super Coster-Kronig) Spectra	160
3.2.3 Excitation Energy Dependence of the Spectral Band Shapes of Angle-integrated Emission.....	177
3.3 Angle-resolved Spectra	184
3.3.1 Surface Energy-band.....	184
3.3.2 Dependence on Polarization of Excitation Light	185
IV DISCUSSION	190
4.1 Resonant Photoemission	190
4.1.1 Profile of the <i>MVV</i> sCK Spectrum.....	190
4.1.2 Resonant of the <i>MVV</i> sCK and the Two-hole-bound-state.....	194
4.2 Energy-band Structure	209
V CONCLUSION	210

CONTENTS (Continued)

	Page
REFERENCES	213
APPENDICES	
Appendix A	224
Appendix B	226
B.1 Nearly-Free-Electron (NFE) Approximation	226
B.2 Cellular Method.....	227
B.3 Augmented Plane Wave (APW) Method	227
B.4 Linear-Combination-of-Atomic-Orbitals (LCAO) Method	228
B.5 Orthogonalized Plane Wave Approximation	229
B.6 Pseudo-Potential Method	233
B.7 Other Methods.....	234
Appendix C	235
Appendix D	240
CURRICULUM VITAE	242

LIST OF TABLES

Table	Page
1.1 The solid state properties of nickel (Kittel, 1996). The RT and ATP denote the room temperature and atmospheric pressure, respectively.	10
1.2 Comparison of calculated μ_B and DOS. (Connolly, 1967)	24
1.3 The energy levels at symmetry points as determined by Eberhardt and Plummer (1980) (units are electron volts).	35
1.4 Escape depth at different kinetic energy of photoelectron	55
1.5 Fraction of the contribution of photoelectron from the surface layer.....	55
2.1 The machine parameters of the storage ring of the Siam Photon Source.	122
2.2 Parameters of the gratings used in the BL-4 beamline.	124
2.3 Specification of the ARUPS10 analyzer.....	132
2.4 Specification of the CLAM2 analyzer.....	133
4.1 Relations between the <i>MVV</i> sCK spectrum and the excitation photon energy. d_k : Filled $3d$ band; \hat{d}_k : $3d$ band with a hole in the ground state; \hat{d}_k^n : $3d$ band with n holes; \hat{d}_s^2 : Two-hole-bound-state; \hat{d}_k^* : $3d$ band with a hole with higher binding energy; c_k : Conduction band; \hat{c}_k : Conduction band with an extra hole; c_k^* : Conduction band with a high energy electron; u_l : States of high energy electrons; u_A : State of the sCK electron; \hat{p} : $3p$ hole state.	208

LIST OF TABLES (Continued)

Table	Page
D.1 Spectroscopic and X-ray notation.....	240

LIST OF FIGURES

Figure		Page
1.1	Schematic illustration of the LVV CK and MVV sCK transitions in metallic Ni. The spin-orbit splitting of the $3p$ level is ignored. The L_2VV CK transition is not shown here.....	2
1.2	The schematic illustration of the energy of the $4s$ levels (\circ) and $3d$ levels (\times) of $3d$ transition metals. The energy of the $3p$ levels and the $4p$ levels of some elements are also shown. The electronic configurations of some selected elements are shown. n_d : Average number of $3d$ electrons. Z : Atomic number. The upward arrow indicates the location of Ni. The ordinate scale is not quantitatively correct but just qualitative.....	9
1.3	Rigid band model for Ni and Cu. Hatched areas exhibit the bands filled with electrons.	19
1.4	Photoelectron EDC curves expected from DOS curve in Fig. 1.3.....	20
1.5	Hund's rule as applied to the split $3d$ levels with 9 electrons. The splitting is caused by the exchange interaction. J : exchange energy.....	21
1.6	Schematic illustration of the DOS curves of a ferromagnetic transition metal. Down-spin band is shifted from the up-spin band by the amount of the exchange energy, J . E_F : the Fermi level.....	23

LIST OF FIGURES (Continued)

Figure	Page
1.7 Density-of-states curves of fcc Ni. Upper panel: DOS for up-spin electrons. Lower panel: DOS for down-spin electrons. E_F : Location of the Fermi level. (Connolly, 1967).....	27
1.8 DOS curves of paramagnetic Ni. Upper panel: Total DOS. Lower panel: Partial DOS for $d\varepsilon$ electrons (full line) and that for $d\gamma$ electrons (broken line). (Wakoh and Yamashita, 1964).....	28
1.9 Panel (a): Energy-band dispersion of Ni. Full line: Up-Spin band (α). Broken line: Down-Spin band (β). Numbers label the different bands. Panel (b): Splitting of the $3d$ and $4s$ band by mixing. (Wakoh, 1965)	29
1.10 Binding energy dependence of spin polarization of photoelectrons and the pertinent EDC. Upper curve: EDC. Lower figure: Spin polarization. (Kinoshita <i>et al.</i> , 1993)	33
1.11 Empirical-band structure of nickel along some symmetry lines. The solid lines indicate spin-up states, the dashed lines spin-down states. The experimental values are given by squares. The zero of energy is the experimental Fermi energy. The Fermi energy is $E_F = 0.0548$ eV. (Weling and Callaway, 1982)	34
1.12 Schematic illustration of spectral distribution of synchrotron radiation.....	41
1.13 Spectral distribution of synchrotron radiation.	42
1.14 Spatial distribution of the synchrotron radiation intensity.....	43

LIST OF FIGURES (Continued)

Figure		Page
1.15	Energy conservation relation in photoemission. E_i : Initial state energy of the system. E_f : Final state energy of the system. N : Total electron number. E_g : Ground state energy of the sample. $E_f(N-1)$: Final state energy of the sample missing an electron. $h\nu$: Excitation photon energy. ε_u : Kinetic energy of the photoelectron.	48
1.16	Energy level diagram of a photoelectron. E_F : Fermi level. E_V : Vacuum level. $h\nu$: Photon energy. ε_u : Kinetic energy in the material. ε_k : Kinetic energy outside the material. $\hat{\varepsilon}_k$: Kinetic energy measured. ε_B : Binding energy. ε_i : Initial level energy. χ_A : Work function of the material. χ_B : Work function of the energy analyzer slit. V_c : Contact potential. V_R : Retardation potential.	52
1.17	Three step process for photoelectron generation.	53
1.18	Kinetic energy dependence of the escape depth.	56
1.19	Kinetic energy dependence of the escape probability (escape function).	60
1.20	Photon energy dependence of ionization cross sections for the 3d and 4s of Ni. (Lindau, 2001)	61
1.21	Schematic illustration of the relation between EDC and the DOS curve. In EDC the background caused by inelastically scattered electrons overlaps intrinsic EDC. (Ishii, 1989)	65

LIST OF FIGURES (Continued)

Figure	Page
1.22 Concept of angle-resolved photoemission. (Ishii, 1989)	66
1.23 Energy dispersion in the nearly free electron model for photoelectrons in ARPES. The right half represents the energy levels in a crystal. Curves illustrated by dots are energy-bands. Full lines are energy-band for the nearly free electron model. The left half represents the energy levels outside the crystal. K is a reciprocal lattice vector. $h\nu$: Photon energy. χ : work function. ε_u : Kinetic energy in the crystal. ε_k : Kinetic energy is a free space. E_F : The Fermi level. E_V : Vacuum level. V_0 (or E_0): Crystal potential. (Ishii, 1989)	69
1.24 Experimental E vs k energy-band dispersions for nickel. Unoccupied bands just above the Fermi level E_F and their Fermi-level crossings are drawn after Zornberg's calculation, which was fit to de Haas-van Alphen data. The lowest band has been extrapolated by a free-electron parabola matched to the experimental points. The final-energy scale gives the final-band energy used to determine the component of k normal to the crystal surface. Only a portion of the lower Λ_3 band is seen owing to small matrix elements, and Δ_2 and Δ'_2 bands are not shown since normal emission from them is forbidden. (Himpsel <i>et al.</i> , 1979).....	70

LIST OF FIGURES (Continued)

Figure	Page
1.25	Positions of the band structure of ferromagnetic Ni along the $\Gamma - K - X$ direction in the bulk Brillouin zone. The binding energies of the peaks obtained by normal-emission measurements are represented by open circles. The solid and dashed curves denote the majority (\uparrow) and minority (\downarrow) spin bands with Σ_1 and Σ_4 symmetries calculated by Weling and Callaway (1982). For convenience, the position of the 6-7 eV feature obtained by angle-integrated measurements is also plotted (crosses). (Sakisaka <i>et al.</i> , 1987b)71
1.26	Spin-resolved photoemission EDC of Ni and the temperature dependence of the exchange splitting. (Hopster <i>et al.</i> , 1983).....73
1.27	Representative photoelectron energy-distribution curves for the valence-shell electrons in MnCl_2 . (Kakizaki <i>et al.</i> , 1983).....74
1.28	Schematic illustration of the process of the resonant photoemission. State propagations in the transition probability expressed in the Green function representation are shown. Full circles: Electrons open circles: Holes. Arrows: Transitions and propagations. Encircled letters: Operators. c: Core levels. v: Valence levels. (Ishii, 1989)76
1.29	Possibility that two 3d holes exist at one lattice site. White circles: Ni atom at lattice sites. Black circles: 3d holes. Arrow: Repulsive Coulomb force.78

LIST OF FIGURES (Continued)

Figure	Page
1.30 Energy dependence of the self-energy part of the Green function showing the energy state of Ni. $\omega = \varepsilon - \varepsilon_k$ is the linear part in the denominator. Full line: Real part. Broken line: Imaginary part. (Liebsch, 1979)	82
1.31 Expected DOS of the many electron state with holes. (a) \uparrow spin. (b) \downarrow spin. (Liebsch, 1979).....	83
1.32 Upper panel: Production of excited 3d hole by photoemission. Lower panel: Generation of the two-hole-bound-state. $h\nu$: Excitation photon. (see text).....	84
1.33 Spin polarized of the two-hole-bound-state exhibited on resonance.....	86
1.34 Auger effect. The transition from v_1 to c emits virtual photon with energy $h\nu_{vc}$. This photon is absorbed by an electron in v_2 and the electron emission occurs.....	88
1.35 Auger transition. Instead of the emission and absorption of a virtual photon, the potential, V_A , to cause the transition is shown.....	93
1.36 Expression of the Auger transition in the quantum field theory. On the left panel, parameters related to energy are shown. On the right panel, the transition probability is shown.....	94
1.37 Energy relation for MVV sCK transition.....	98

LIST OF FIGURES (Continued)

Figure	Page
1.38 <i>CVV</i> Auger process showing expected spectra. $n(E)$: Valence band DOS curve. $D^\circ(E)$: Convoluted DOS curve. $D(E)$: Expected band spectrum. (Bennett <i>et al.</i> , 1983)	100
1.39 Dependence of expected <i>CVV</i> Auger spectra on the magnitude of U/W . W : Band width. U : Intra-atomic Coulomb energy. (Bennett <i>et al.</i> , 1983).....	101
2.1 Procedure of the sample preparation. (1) Crystal rod sample with (111) surface is cut out of a single crystal rod. (2) The surface is polished. (3) The sample is cleaned in a solvent. (4) The sample is further cleaned in vacuum.....	109
2.2 Cutting machine model ACCUTOM-5 from Struers Co.....	110
2.3 Polishing machine model ROTOPOL-25 with a force control option model ROTOFORCE-1 from Struers Co.....	111
2.4 Auger spectra of Ni(111) surface. (a) Contaminated surface and (b) Clean surface. Lines showing up in the region between 700 and 850 eV are those of the <i>LMM</i> CK lines of bulk Ni.....	113
2.5 LEED patterns of Ni(111) surface. (a) Contaminated surface. (b) Clean well-defined surface.....	114
2.6 Schematic illustration of UV discharge lamp showing the operation principle.	118

LIST OF FIGURES (Continued)

Figure	Page
2.7 Schematic diagram of a dual-anode X-ray source. (a) Overall feature (b) Head portion.....	119
2.8 The magnet arrangement of the storage ring of the Siam Photon Source.	121
2.9 The photo shows the BL-4 optical beamline of the Siam Photon Laboratory.....	125
2.10 The optical layout of the BL-4 beamline at the Siam Photon Laboratory.	126
2.11 Photoemission system shown above is an experimental station of the BL-4 beamline.	129
2.12 Schematic diagram of the photoemission system. CLAM2 and ARUPS10 energy analyzers are the main instruments.	130
2.13 Azimuthal and polar rotation and translational movements of the sample controlled by the manipulator.	134
2.14 Schematic diagram of CLAM2 with an electrostatic lens.	135
2.15 Schematic diagram of the LEG63 electron gun.	137
2.16 Schematic diagram of the EX03 ion gun.	138
2.17 Schematic diagram of rear view LEED set-up.	140
2.18 Fermi edge of a Au poly-crystal sample spectrum and minus of the first derivative to be fitted with a Gaussian function (not shown). The spectrum was measured by using the CLAM2 analyzer. The excitation energy was 21.22 eV of the helium discharged lamp.	142

LIST OF FIGURES (Continued)

Figure	Page
2.19 Fermi edge of a Au poly-crystal sample spectrum and minus of the first derivative to be fitted with a Gaussian function (not shown). The spectrum was measured by using the ARUPS10 analyzer. The excitation energy was 21.22 eV of the helium discharged lamp.	143
2.20 Schematic diagram of AIPES measurements set-up.....	144
3.1 EDC of Ni(111) measured in the angle-integrated mode. Vertical bars indicate major features in the spectrum. EDC exhibits both <i>MVV</i> sCK and valence band spectra.	157
3.2 EDC's in the binding energy region of the valence band photoemission as measured with excitation light with energy below the <i>3p</i> excitation threshold. Vertical bars indicate the locations of features at 11, 8.3, and 6.3 eV. The backgrounds are subtracted.....	158
3.3 EDC's in the binding energy region of the valence band photoemission as measured with excitation light energy around the <i>3p</i> threshold and above. Vertical bars indicate the locations of the two-hole-bound-state feature at 6.3 eV. The arrow heads indicate the features at 11 and 13.5 eV. The backgrounds are subtracted.....	159

LIST OF FIGURES (Continued)

Figure	Page
3.4 EDC of the <i>MVV</i> sCK electron. The spectrum is obtained by averaging seven EDC's measured at excitation energy from 80 to 110 eV at an interval of 5 eV. The solid line indicates the smoothed curve obtained by the 13-point average. Vertical bars at 49.8, 56.3, 59.5 and 60.5 eV indicate major features of the EDC. An arrow at 63.5 eV indicates the high energy limit of the <i>MVV</i> sCK band.....	167
3.5 EDC's showing the change in the spectral shapes of the <i>MVV</i> sCK band and the two-hole-bound-state band as the excitation photon energy is changed. Vertical bars indicate the locations of the features of the <i>MVV</i> sCK band at 49.8, 56.3, 59.5, 60.5 eV and those of a few features occurring in the area between 57 and 59.5 eV. Arrows show the locations of the 11 eV satellite. The backgrounds are subtracted.....	168
3.6 The <i>MVV</i> sCK and two-hole-bound-state spectra in the excitation photon energy range from 71 to 79 eV. Vertical bars indicate the locations of the features at 49.8, 56.3, 59.5, 60.5 eV and those of a few features occurring the area between 57 and 59.5 eV. Arrows show the locations of the high energy limit of the <i>MVV</i> sCK band given in Fig. 3.4.	169

LIST OF FIGURES (Continued)

Figure	Page
3.7 The $3p$ core level lines measured by excitation with the Mg $K\alpha$ radiation. Features in the spectrum are indicated with vertical bars. The feature indicated as $K\alpha_{3,4}$ is the main $3p$ line excited with the Mg $K\alpha_{3,4}$ radiation.	170
3.8 The MVV sCK spectrum exhibited in Fig. 3.4 (top) as compared with the MVV sCK spectrum obtained by excitation with Mg $K\alpha$ radiation (middle). The L_3VV CK spectrum from Mårtensson <i>et al.</i> (1984) (bottom) is also shown for comparison. The L_3VV CK spectrum is placed in the figure so that the major peak is aligned to those of other two spectra. Features in each spectrum are indicated with vertical bars. The backgrounds are subtracted.....	171
3.9 The two-hole-bound-state spectra in the excitation energy range from 66 to 70 eV. Upward arrows indicate the peak positions. Downward arrows indicate the locations of the weak component of the MVV sCK band occurring at kinetic energy of 49.8 eV. The numbers given under the two-hole-bound-state bands are the values of the FWHM of the bands indicated with horizontal bars. The backgrounds are subtracted.....	172

LIST OF FIGURES (Continued)

Figure	Page
3.10 The relation between the excitation photon energy ($h\nu$) and the peak positions of features in the spectra of the second derivative of EDC. The dots indicate the locations of the peaks (negative sign). Black horizontal bands exhibit features and their locations occurring in the second derivative spectra. The intensities of the horizontal bands indicate the depths of the negative peaks. In the excitation energy region from $h\nu = 69$ to 76 eV, the areas where the continuous bands exist is shown by hatches.....	176
3.11 CIS spectrum for photoelectrons with binding energy of 6.5 eV. Weak peaks at 52 , 60.5 and 77 eV are indicated by vertical bars. The main resonance band has its peak at 68 eV and the onset position is recognized as a dip at 64 eV. The $3p$ excitation threshold is assigned to occur at 66.2 eV and exhibited with an arrow.	181
3.12 CIS spectrum of the main $3d$ band at binding energy of 0.6 eV. Vertical bars indicate the locations of the features at 49.5 , 55 , 63 and 70 eV. An arrow indicates the location of the threshold of the $3p$ excitation at 66.2 eV.....	182

LIST OF FIGURES (Continued)

Figure	Page
3.13 The total photoelectron yield spectrum. The abscissa represents the excitation photon energy and the ordinate the flowing photocurrent the specimen. Vertical bars indicate the locations of weak features at 54, 63 and 81 eV. The location of the threshold of the $3p$ excitation is shown by an arrow.	183
3.14 Angular dependence of angle-resolved spectra along $\bar{\Gamma}-\bar{T}-\bar{K}$ symmetry.....	186
3.15 Angular dependence of angle-resolved spectra along $\bar{\Gamma}-\bar{\Sigma}-\bar{M}$ symmetry.....	187
3.16 Experimental surface energy-band map of the Ni(111), second derivative plotted, compared with a theoretical calculated by GGA method based on density function theory, opened triangles (Mittendorfer <i>et al.</i> , 1999), separated for up-spin (a) and down-spin (b).	188
3.17 Polarization dependence of photoemission spectra.	189
B.1 The structure schematically showing OPW.	232
C.1 Definitions for calculation of the Shirley method algorithm.	239

CHAPTER I

INTRODUCTION

1.1 Introductory Remark

This thesis describes the experimental research of the electronic structure of the Ni(111) surface by the photoemission spectroscopy (PES). The studies were separated into two parts. The first part is the investigation of the MVV super Coster-Kronig (sCK) spectra. In the atomic spectroscopy, the relevant transition is written as $M_{2,3}M_{4,5}M_{4,5}$ ($3p3d3d$). This is often abbreviated as MMM . Since the $3d$ electron in metallic Ni forms the valence band, we use letter V instead of M to represent the $3d$ level in the notation of the super Coster-Kronig transition as MVV sCK. In a similar way, we write LVV CK to express the $L_{2,3}M_{4,5}M_{4,5}$ Coster-Kronig transition. The MVV sCK and LVV CK transitions are schematically illustrated in Fig. 1.1. The CK and sCK transitions are kinds of Auger effect. Therefore they are governed by the dynamical process of the state-change in matter. The concomitant processes leading to the CK and sCK spectra include both electronic structure of the excited state and many electron interactions in the state-change. In case of metallic Ni, the LVV CK spectra have been well investigated but the MVV sCK spectra have not. Therefore, we expect that the study will provide us with useful information on both the electronic structure and the dynamic effect of the electronic transition.

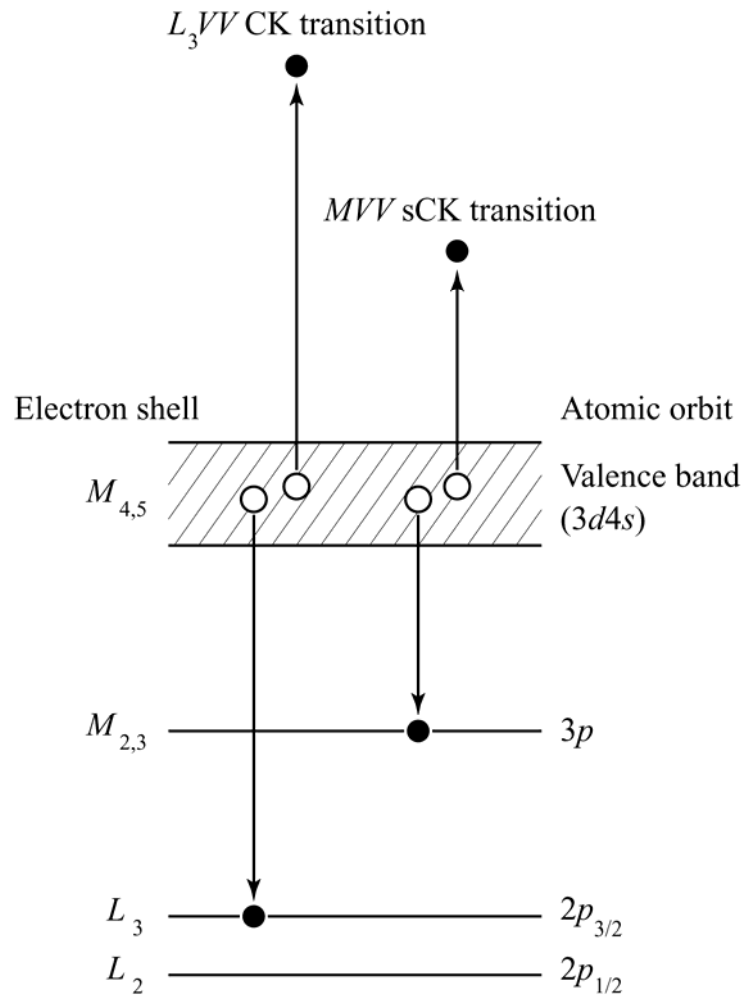


Fig. 1.1 Schematic illustration of the L_3VV CK and MVV sCK transitions in metallic Ni. The spin-orbit splitting of the $3p$ level is ignored. The L_2VV CK transition is not shown here.

The sCK spectra are obtained in the photoemission measurement, since they are associated with the photoemission spectra. In the present case, the analyses of the curves of photoelectron intensities versus photoelectron kinetic energy in the valence band region give us the relevant spectra. We obtain these spectra through measurements of angle-integrated photoemission spectroscopy (AIPES). The analyses have been done in both kinetic energy and binding energy regime; both spectra are essentially the same. The plot of photoelectron intensity versus kinetic or binding energy is called energy distribution curve (EDC).

The other part is the investigations of the energy-band structure. It is well known that EDC obtained in AIPES gives the direct information of the partial density of states (DOS) of condensed matter. Under favorable conditions, EDC's are proportional to DOS curves. If we measure EDC in the angle-resolved mode and analyze the peak shift in EDC by varying some parameters, we can map the dispersion of the energy-bands. In other words we can obtain the curve of $E(\mathbf{k})$ versus \mathbf{k} , where $E(\mathbf{k})$ is the band energy and \mathbf{k} is the electron wave vector. The method used here is referred to as angle-resolved photoemission spectroscopy (ARPES).

As the target material we select a single crystal of Ni. Since the materials having the (100) and (110) has been investigated by many researchers, we select Ni(111) crystal as the sample on which only a few report has appeared so far. Ni is a typical 3d transition metal and quite suitable for the investigation of the nature of the localized electron system in solids. Particularly, the question about the origin of its ferromagnetism is one of the important issues of solid state physics. Through various researches, it is well known that the valence state of metallic Ni has the electronic configuration as $3d^9 4s$ on average. From this configuration, we know the Fermi level

of metallic Ni is formed by the $3d$ electrons. Although the hybridization with the $4s$ state is possible, the majority of electrons responsible for the electrical conductivity is the $3d$ electron. Then a further question follows: how is the magnetic moment is generated by itinerant electrons carrying electric currents? Thus, the central solid state issue of this metal is the clarification of apparent opposed pieces of nature, localized versus itinerant.

Photoemission spectra reflect the electronic structure of the sample directly. Therefore, the background of the solid state properties of Ni is obtained by the photoemission-spectroscopic experiments. Especially, both the dynamic nature of the optical transition showing up as the sCK effect and the pertinent electronic structure as the energy-band dispersion are investigated in the present thesis. The results show quite interesting aspect of the resonant transition between two different channels.

Photoemission phenomena of solids are quite surface sensitive. This is because the escape depth of primary photoelectrons is very short. It is in the range of inter-atomic distance. Therefore, the analysis of photoelectrons provides us mostly with the information of the surface layers of solids. The surface layer of a crystal has its own special nature. At the surface, the translational symmetry toward the direction normal to the surface is broken. Only the translational symmetry is hold among the direction parallel to the surface. Obviously, the magnitude of the potential acting on electrons is different at the surface from that in the bulk area of the crystal. By means of photoemission measurements, we can analyze the surface energy-bands. In the present thesis this sort of investigation is also carried out.

In this chapter, I describe the solid state properties of Ni to explain interesting issues concerning this material. The energy-bands of Ni have been investigated both

theoretically and experimentally by many researchers. Therefore, brief description is given to this issue. It is also related with the studies made in the present thesis. Then, a very distinctive feature in the excited state of is described. This is the two-hole-bound-state. The occurrence of the two-hole-bound-state is the representative aspect of the localized-versus-itinerant properties of metallic Ni. It plays an important role in the data analyses in the studies for the present thesis. The *MVV* sCK spectra are of investigated in detail in the present thesis. Really this part is the first work ever published. Thus, the relevant background information is presented here. Then, the photoemission process is explained. This is necessary to understand what we observe.

The study made here is carried out using synchrotron radiation. Without it, such studies as ones shown here cannot be performed. The work presented here is the first application study of synchrotron radiation from the National Synchrotron Research Center and thus the first work on the synchrotron radiation application research in Thailand. Therefore, fundamental of synchrotron radiation is briefly described here.

Then, the purpose of the study is presented in the summary form. The content is itemized there.

In the second chapter, the essential information regarding the experimental procedure is given. It covers the items of sample preparation to experimental apparatus. Experimental procedure is also presented. In this chapter, the necessary minimum for the explanation of the experimental part is collected.

In chapter III, the experimental results are described. All the issues described above concerning physics of Ni are presented there. In chapter IV, the discussion of the experimental data is made. The data analysis or interpretation of the data will be

performed on the basis of solid state electronic structure. In case the energy-band analysis this is obvious. In the analysis of the *MVV* sCK spectra, we carry out the analysis on the basis of solid state electronic structure. This is contrasted to the case of the *LIV* CK spectra, where the atomic models are used. This will form the central issue of the thesis. Finally in chapter V, the conclusion is given.

1.2 Solid State Properties

Nickel is a $3d$ transition metal of which the atomic number is 28. The electronic configuration of metallic nickel is $[1s^2 2s^2 2p^6 3s^2 3p^6] 4s 3d^9$ or $[\text{Ar}] 4s 3d^9$ while the electronic configuration of atomic nickel is $[\text{Ar}] 4s^2 3d^8$ on average. The difference of the electronic configuration between the atomic and solid nickel is the average number of $4s$ and $3d$ electrons per atom. In metallic Ni, the $4s$ electrons consisting conduction electrons are trapped by the localized $3d$ orbits and stay there for a short time. Then the trapped electrons are ejected into the conduction band. Thus the number of the $3d$ electrons is fluctuating. It takes the configurations, $3d^{10}$, $3d^9$, and $3d^8$, and the average number is considered to be 9.4 (Kittel, 1996). The situation is understood from the energy level point of view. It is shown in Fig. 1.2.

Fig. 1.2 shows the schematic illustration of the change in the energy of the $3d$ and the $4s$ levels of $3d$ transition metals. The energy of the $3p$ and the $4p$ levels of some elements are also indicated. The abscissa represents the atomic numbers, Z , of the elements. Just below them the corresponding elements are indicated. The average numbers of $3d$ electrons per atom in solid transition metals are indicated. The electronic configurations of some selected elements are shown. The upward arrow

exhibits the location of Ni. In case of Sc, both metallic state ($4s3d^2$) and the isolated-atom state ($4s^23d$) are shown. In case of Ni, only the metallic state is indicated. Since the illustration is schematic and qualitative, the ordinate scale is incorrect. On moving from Ar ($Z = 18$, $1s^22s^22p^63s^23p^6$) to K ($Z = 19$), the $4s$ orbit is filled with an electron but no $3d$ electron appears. The $3d$ orbit is getting filled above $Z = 21$ (Sc). For $Z \geq 21$, the energy of the $3d$ is lowered to be below zero. As Z increases, the number of electrons occupying the $3d$ orbit increases. At $Z = 29$ (Cu), the $3d$ orbit is filled up with 10 electrons and the energy of $3d$ level is lower than that of the $4s$ level. Ni comes to the border. Existing one $3d$ hole (or nine $3d$ electrons) plays an important role in generating the distinctive nature of Ni.

Before looking into the distinctive nature, it is of interest to see general aspects of the solid state nature of Ni. They are summarized in Table 1.1. In the table it is remarked that the nearest neighbor distance, b , is related with the inter-atomic distance, a , as

$$a = \sqrt{2}b \quad (1.1)$$

in the face centered cubic structure.

As mentioned above, the transition metal atoms have the d shell which is not completely filled up with electrons. As already mentioned, this characteristic electronic structure of atomic transition metal generates remarkable nature of metallic transition metals. In case of $3d$ transition metals, the features of $4s$ electrons are understandable in that they form the wide conduction band. The real question is the aspect of the states of $3d$ electrons. There are two conflicting concepts regarding this problem. One is that the $3d$ electron is localized at a specific atom. In ionic crystals

containing $3d$ electrons this localized electron model is well applicable. This model can explain the complicated magnetic properties of magnetic ionic crystals.

However, this model cannot explain the properties of transition metals. The electronic specific heats of the transition metals are considerably larger than those of simple metals. This indicates that the $3d$ electrons also carry electric current. The simple atomic model cannot explain that the magnitude of the saturated magnetization of ferromagnetic Ni, Co, and Fe is not integral multiple of the Bohr magneton. The conclusion of such consideration is that the $3d$ electron is itinerant and its energy state should be described by means of the energy-band picture.

The wave function of the $3d$ electron is not like the plane wave type as the s and p conduction electron but considerably localized in the atom. In the energy-band picture, the electron is itinerant. When an electron jumps from one lattice site to another, more charge must exist instantaneously at a lattice site than the average value. Such charge fluctuation assumes the generation of extra negative charge at a lattice site. The large intra-atomic Coulomb energy caused by the extra negative charge may not allow the charge fluctuation. This concept is against the energy-band picture.

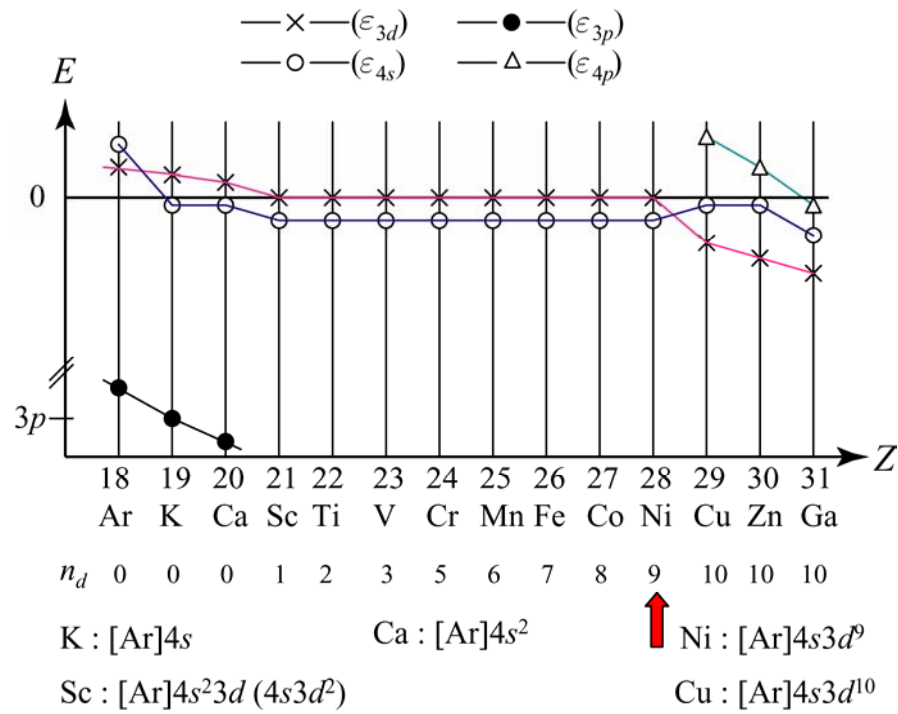


Fig. 1.2 The schematic illustration of the energy of the 4s levels (\circ) and 3d levels (\times) of 3d transition metals. The energy of the 3p levels and the 4p levels of some elements are also shown. The electronic configurations of some selected elements are shown. n_d : Average number of 3d electrons. Z: Atomic number. The upward arrow indicates the location of Ni. The ordinate scale is not quantitatively correct but just qualitative.

Table 1.1 The solid state properties of nickel (Kittel, 1996). The RT and ATP denote the room temperature and atmospheric pressure, respectively.

Properties	Reported Values
Crystal structure (RT)	Face centered cubic
Lattice parameter (RT)	3.52 Å
Atomic number	28
Electron configurations	[Ar] 3d ⁹ 4s
Density (RT, ATP)	8.91 g cm ⁻³
Atomic concentration (RT, ATP)	9.14×10 ²² cm ⁻³
Nearest-neighbor distance (RT, ATP)	2.49 Å
Cohesive energies (0K, 1 ATM)	428 kJ/mol, 4.44 eV/atom
Melting points	1728 K
Isothermal bulk modulus	1.86×10 ¹¹ N/m ²
Ionization energy (one electron)	7.63 eV
Electrical conductivity (295 K)	1.43×10 ⁵ (ohm-cm) ⁻¹
Electrical resistivity (295 K)	7.0×10 ⁻⁶ ohm-cm

The difficulty met in the simple energy-band picture for the $3d$ electron has been removed by the introduction of the correlation interaction to the calculation. Owing to the upgrading of the computer, the accuracy of the calculation has been enhanced appreciably. This determined the energy-band structure accurately and the shape of the Fermi surface can be calculated with a considerable accuracy. On the other hand, the experimental technique has advanced greatly. This is brought about by the advance in the sensitivity of a detector, the amplifier system, and the computer control system. The theoretically calculated shape of the Fermi surface is found to coincide with the results of the experimental observation. The magnetic structure factor obtained by the neutron diffraction measurements also agrees with that calculated by the energy-band model.

In this way, the solid state nature of the $3d$ transition metals has been revealed to be consistent with the energy-band picture. It is quite obvious that photoemission data provide us with more direct information on the electronic structure. The partial density-of-states curves and the band dispersion curves are obtained by means of photoemission. The results of photoemission measurements have shown the indispensable contribution of the correlation interaction. This issue will be treated later.

One important properties of metallic nickel is its ferromagnetism at room temperature. Among single element materials only iron, cobalt, nickel and some lanthanide metals exhibits ferromagnetism. The Curie temperatures are 1043, 1394 and 631 K for iron, cobalt and nickel, respectively.

The ferromagnetism originates in the spontaneous magnetization. The spontaneous magnetization is caused by aligning spins under the zero external fields.

The alignment of spins is caused by the electrostatic interaction, the exchange interaction. The exchange energy reduces the interacting electrons if their spins are aligned parallel. If we assume that the internal fields to generate the magnetization is caused by the exchange interaction and apply the temperature dependence of the susceptibility of a paramagnet, *i.e.*, the Curie law, the temperature dependence is modified to be applicable to a ferromagnet. Simple calculations lead to the formula of the temperature dependence of the magnetic susceptibility, χ , as

$$\chi = \frac{C}{T - T_c} \quad (1.2)$$

Here C is the Curie constant and T_c is the Curie temperature. The formula given in (1.2) is referred to as Curie-Weiss law. If T is much larger than T_c , χ becomes small as in the paramagnet. As T approach T_c , χ becomes infinity suggesting that the magnetic ordering occurs. In the temperature range, $T > T_c$, we have the paramagnetic phase and in the temperature range, $T < T_c$, we are in the ferromagnetic phase. Again, we emphasize that the ferromagnetic ordering is caused by the spontaneous magnetization and the spontaneous magnetization is caused by the exchange interaction leading to the alignment of spins.

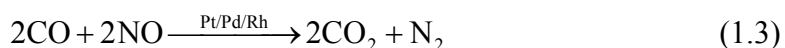
It is realized that an important material for everyday life is stainless steel. Stainless steel is very stable and highly corrosion resistant. A famous stainless steel is that assigned as the number 304 which is also be used for making the vacuum chambers or vacuum components in our laboratory. Nickel is about 10% of the composition of the stainless steel.

Another important type of the alloys is permalloy. The permalloy is an approximately 80:20 alloy of nickel and iron. Because the permalloy has high magnetic permeability, we use permally for making photoelectron energy analysis chamber to shield the outside magnetic field including the earth magnetic field. This is important because trajectory is deformed by the magnetic field. Sometime we call this type of material as μ -metal which is actually a registered trade mark.

The third important alloy composing of Ni and Fe is invar. This was found more than 100 years ago. In 1897, Guillaume discovered an alloy composed of 35% Ni and 65% Fe which has a thermal expansion coefficient 1/10 times ($\sim 10^{-6}/\text{K}$) as small as those of ordinary metals and alloys. This alloy was named invar after “invariable”. The crystal structure of invar is face centered cubic (fcc) and it is ferromagnetic. A ternary alloy consisting of 4%Co, 32%Ni, and 64%Fe is named superinvar. The thermal expansion coefficient of superinvar is practically zero. There are many useful alloys containing Ni but we are not concerned with them here.

An important chemical nature of metallic Ni is the catalytic action. The catalytic action of Ni is not strong enough to be used to promote various chemical reactions for practical use. However, the investigation of the adsorption of molecules on metallic Ni offers important fundamental information on the catalytic behaviors.

The catalytic materials have given a very impact the chemical industry especially fuel and polymer industry. Catalysis is also important for reducing the pollution generated by automobiles. This is realized by converting poisonous exhaust gases into more harmless molecules. This is called catalytic convertor. Unfortunately, the catalytic convertors are made of expensive metals like platinum, palladium and rhodium (Clark, 2002). The pertinent chemical reactions can be written as



Nickel is a good heterogeneous catalyst (Clack, 2002) because it can absorb reactants strongly enough to hold and activate the reactants but not so strongly that the products can not break away. Heterogeneous catalysis is that the catalyst is in a different phase from the reactants. For instant, the nickel is in those of solid phase while the reactants are in the liquid or gas phases. On the other hand, the homogeneous catalysis is that the catalyst is in the same phase as those of the reactants. One important of industrial use nickel catalyst is for the hydrogenation of vegetable oils to make margarine (Clack).

1.3 Energy-band

Many solid state properties of materials such as electrical properties, optical properties, thermal properties, magnetic properties and others should be explained from their electronic structures. As mentioned repeated already, the energy states of conductors are well approximated by the energy-band picture. Even in $3d$ transition metals, the d electron state can be described by the energy-band picture, though some modification is necessary. There very many atoms in a crystal and accordingly there are many electrons there. Electrons feel attractive forces from ionic cores and repulsive forces from other electrons. Such interactions are complicated in principle but they can be simplified to one particle potential. This is because there are very many particles and the complicated interactions are averaged. Suppose one electron in a crystal sees such an averaged potential, $V(\mathbf{r})$, for which \mathbf{r} is the electron coordinate. Then $V(\mathbf{r})$ has the periodicity of the crystal lattice, since the atoms are aligned regularly in crystal. So we have

$$V(\mathbf{r}) = V(\mathbf{r} + \mathbf{a}) \quad (1.4)$$

Here, \mathbf{a} is a lattice translation vector. The solution of the Hamiltonian equation with the potential given in (1.4) is given as

$$E = E_n(\mathbf{k}) \quad (1.5)$$

$$\psi_{n\mathbf{k}}(\mathbf{r}) = e^{i\mathbf{k}\cdot\mathbf{r}} u_{n\mathbf{k}}(\mathbf{r}) \quad (1.6)$$

Here n is a quantum number assigning the state and \mathbf{k} is the electron wave vector defined as

$$\begin{aligned} \mathbf{k}_x &= \frac{\pi}{2a_x} \left(\frac{l}{N} \right) \\ \mathbf{k}_y &= \frac{\pi}{2a_y} \left(\frac{m}{N} \right) \\ \mathbf{k}_z &= \frac{\pi}{2a_z} \left(\frac{n}{N} \right) \end{aligned} \quad (1.7)$$

Here, a_x , a_y , and a_z are lattice constants; l , m , and n are integers in the range

$$-N \leq l, m, n \leq N \quad (1.8)$$

The reciprocal lattice vector, \mathbf{K} , are defined as

$$\mathbf{K} = \left(\frac{\pi}{a_x}, \frac{\pi}{a_y}, \frac{\pi}{a_z} \right) \quad (1.9)$$

E and $\psi_{n\mathbf{k}}(\mathbf{r})$ are periodic in the \mathbf{k} space as

$$E_n(\mathbf{k}) = E_n(\mathbf{k} + \mathbf{K}) \quad (1.10)$$

$$\psi_{n\mathbf{k}}(\mathbf{r}) = \psi_{n\mathbf{k}+\mathbf{K}}(\mathbf{r}) \quad (1.11)$$

The eigen function given as (1.6) is called the Bloch function. Since N is a large number, \mathbf{k} is practically continuous. For a given n , $E_n(\mathbf{k})$ distributes in a range with a

width. Thus, $E_n(\mathbf{k})$ is referred to as the energy-band. The dependence of E on \mathbf{k} is called the energy dispersion. Drawing the energy dispersion curves for various n is called the energy-band mapping. The Bloch function extends over the whole crystal. It represents the state where the electron is itinerant. Therefore it includes implicitly the state where the charge is fluctuating at a lattice site.

It is practically impossible to solve the Hamiltonian equation for given $V(\mathbf{r})$. Therefore we approximate the Bloch function. One extreme case is the tight binding approximation. There, we take electrons to be bound at lattice sites and approximate the Bloch function with linear combination of atomic orbitals. Another extreme is the nearly free electron approximation where the Bloch function is formed by plane waves with different wave vectors. The two extreme cases are not used in the practical calculation. Instead better approximations are used. They are the orthogonalized plane wave (OPW) method, the augmented plane wave (APW), and the Green function method. In order to introduce the effect of the correlation interaction, a method called the α method has been proposed and used. Recently, the method called the density functional calculation is quite popular. Recent advance in computer calculation technique and upgrading of computers have made it possible to calculate the energy-bands and associated Bloch functions with high accuracy.

It is not practical to introduce the calculation methods here, since the description must be lengthy and we do not deal with the theoretical calculation. Instead, we introduce the reported results of the energy-band calculation in what follows.

As mentioned already, physical quantities like the specific heat, the electrical conductivity, magnetic susceptibility, the shapes of the Fermi surfaces are calculated

by the energy-band model and compared with pertinent experimental data. In solid state spectroscopy, particularly in photoemission, two quantities are compared with experimental data. One is the energy-band dispersion. The quantity to be calculated is given in (1.5). This is quite straightforward. The other is the density of states (DOS) $D(E)$. In the calculation, we obtain the number of states in an interval from E to $E + dE$. Then we divide the number by dE .

$$D(E) = \frac{2}{(2\pi)^3} \int \int \int_E^{E+dE} d\mathbf{k} \quad (1.12)$$

The integration is performed in the k space between the two equi-energy surfaces E and $E + dE$.

Before we proceed further, we briefly mention the rigid band model, which is quite useful to understand the DOS curves of Ni qualitatively. If electrons are not widely spread from a lattice site, the width of the energy dispersion is narrow. Therefore, localized electron forms a narrow and high density band. If electron wave functions are widely spread in a crystal, they form a broad weak band. The $3d$ electrons are localized and $4s$ electrons are shown schematically in top panel of Fig. 1.3. We fill the bands with electrons from the bottom. In Ni, the $3d$ band is not completely filled up; one electron is missing from the $3d$ band. Thus the Fermi level occurs in the $3d$ band as illustrated in the middle panel. In Cu, the $3d$ band is filled up as $3d^{10}$. Then the electrons are filling up the empty $4s$ band above $3d$ band as illustrated in the bottom panel. Therefore the Fermi level occurs in the $4s$ level. Suppose the photoelectron EDC's are reflecting the DOS curve. The expected EDC's are as shown in Fig. 1.4. This is what is experimentally observed. In the argument

given above, the DOS curve is fixed and the number of electrons is changed to predict the actually observed spectra. This model is called the rigid band model.

As already mentioned, the magnetic moments of Fe, Co, and Ni are not integral multiples of the Bohr magneton, μ_B . Quantitatively, the deviation cannot be explained by the spin-orbit splitting. According to Hund's rule, electrons occupy energy levels so that the total spin takes the maximum value. If the 3d band is split into two bands by exchange interaction, the lower level is first filled up with up-spin electrons and then the upper level is filled with down-spin electrons. This situation is shown for the case of Ni in Fig. 1.5. In this case, the magnetic moment corresponding to one spin occurs as the net value.

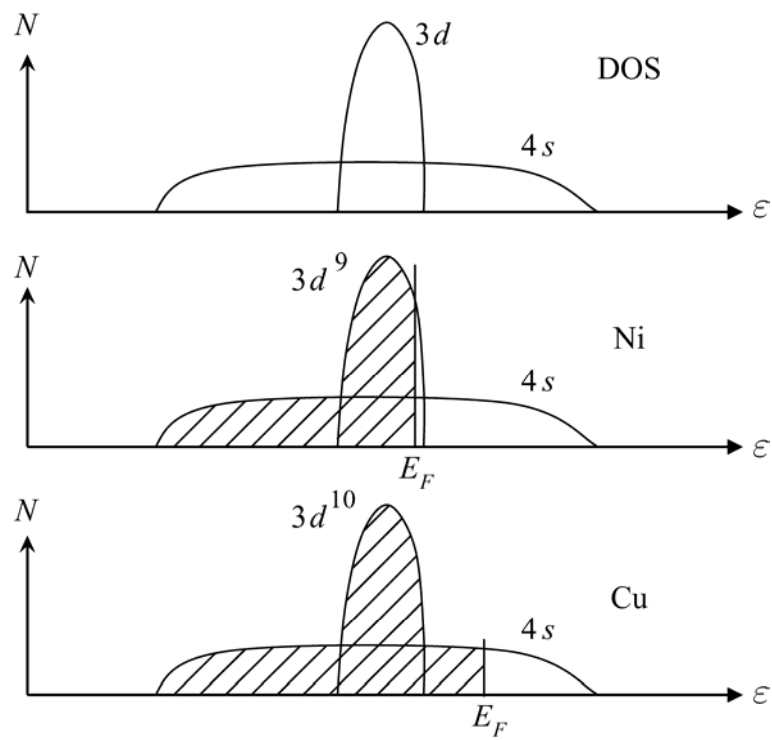


Fig. 1.3 Rigid band model for Ni and Cu. Hatched areas exhibit the bands filled with electrons.

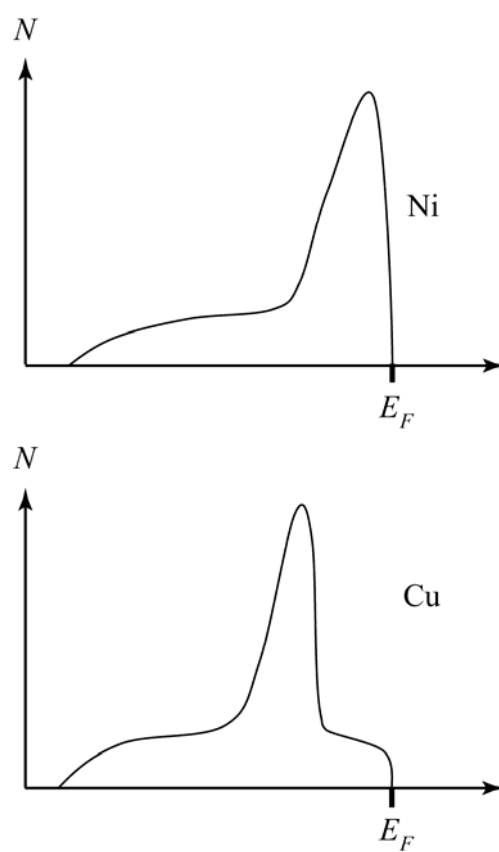


Fig. 1.4 Photoelectron EDC curves expected from DOS curve in Fig. 1.3.

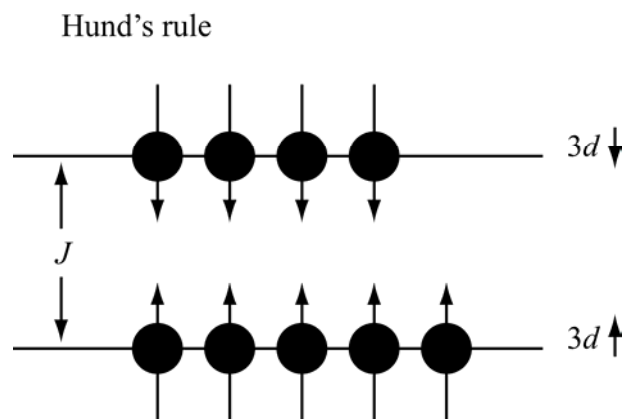


Fig. 1.5 Hund's rule as applied to the split $3d$ levels with 9 electrons. The splitting is caused by the exchange interaction. J : exchange energy.

On the basis of the energy-band picture, the deviation is explicable by the exchange splitting between the up-spin band and the down-spin band. This is shown in Fig. 1.6. The magnetic moment is determined by the difference of the number of down-spin electrons and that of up-spin electrons. The value of J is independent of μ_B . Thus resulting net number of the difference take values different from an integer and then the concomitant magnetic moments can take values different from integral multiples of μ_B . In ferromagnetic Ni, the number of down-spin electrons is 4.4 on average and the number of up-spin electron is 5. When we make alloys by adding Cu to Ni, the vacancies in the down-spin band are filled with electrons and the $3d$ band is completely filled up in the alloy with 40% Ni and 60% Cu. Experimentally, ferromagnetism is found to disappear at this concentration. In this explanation, the rigid band model used in that the addition of Cu to Ni does not change the shape of the DOS curve. The rigid bands split by the exchange interaction are schematically shown in Fig. 1.6.

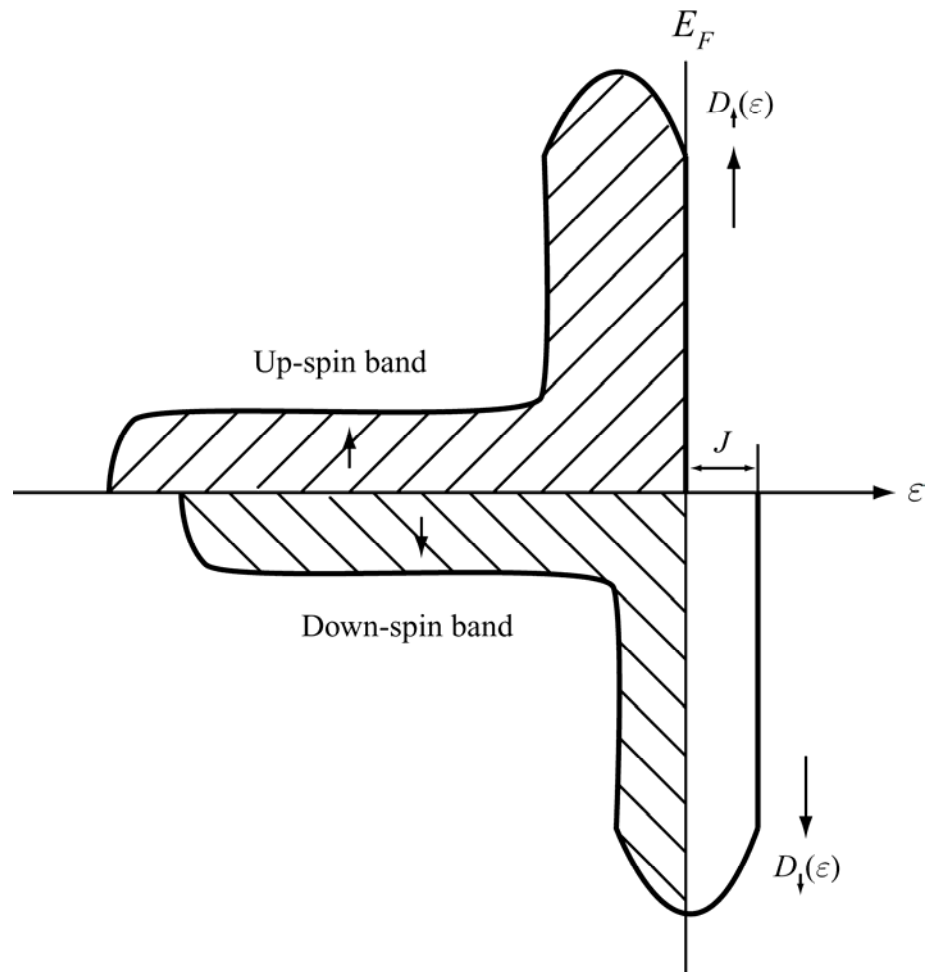


Fig. 1.6 Schematic illustration of the DOS curves of a ferromagnetic transition metal.

Down-spin band is shifted from the up-spin band by the amount of the exchange energy, J . E_F : the Fermi level.

Connolly (1967) calculated DOS of nickel. He calculated the potential within the frame work of the unrestricted Hartree-Fock scheme in which the exchange terms were approximated by a local potential. The augmented-plane-wave was used to find the eigen values of the approximate Hamiltonian. The results are in Fig. 1.7. The data is old but by the middle of 1960's, the accuracy of the energy-band calculation increased tremendously. This is because the advanced calculation methods had been invented on one hand and the progress of computer technology had been quite fast. If we find the $V(\mathbf{r})$, the energy-band is calculated without any serious difficulty. The self-consistency was achieved by iteration. In practice, averaged free-electron exchange potential $V_{\text{ex}} = -6(6\rho/8\pi)^{1/3}$, was used, where ρ is the electron density. Connolly determined $V(\mathbf{r})$ completely self-consistently including the exchange interaction. No parameter obtained experimentally was used concerning magnetization. Calculated μ_B and DOS are shown in Table 1.2. Agreement between the calculated results and the experimental data is good.

Table 1.2 Comparison of calculated μ_B and DOS. (Connolly, 1967)

	Calculated Values	Experimental Values
μ_B /atom	0.62	0.606
DOS at the Fermi Surface	2.7	3.1

The calculation of the energy-bands were also made by (Wakoh and Yamashita, 1964) as well as Weling and Callaway (1982). Basic features are almost the same as those shown in Fig. 1.7. The DOS curves show the aspect that the 3d band

with the high DOS is embedded in the wide sp band. The $3d$ level splits into two sub-levels called $d\varepsilon$ and $d\gamma$ in the cubic electrostatic field. Thus, it is interesting to find the contributions of the two kinds of electrons. The results of such calculations are shown in Fig. 1.8. In the figure, the upper panel shows the total DOS curve. The lower panel shows the partial DOS curves for $d\varepsilon$ and $d\gamma$ electrons. The calculation was carried out for the paramagnetic state. Therefore the DOS curve shown in the upper panel is to be compared with of the DOS curves shown in Fig. 1.7 or the average of the two by letting J to be zero. The agreement between data shown in Fig. 1.7 and Fig. 1.8 is good. From the partial DOS curves shown in the lower panel, we know that the first peak and the third peak arise from the $d\varepsilon$ states. In the same way, we understand that the second peak arises from the $d\gamma$ state.

We have mentioned that the narrow $3d$ band is embedded in the wide weak $4s$ band. The calculated DOS curves support this view. It is interesting to see this situation in the calculated energy-band-dispersion curves. Fig. 1.9 shows the energy-band-dispersion curves, the E - \mathbf{k} curves, calculated by Connolly (1967). The panel (a) on the left-hand side shows the E - \mathbf{k} curves. Full lines correspond to the up-spin band. Broken lines correspond to the down-spin band. They are designated with Greek letters α and β , respectively. The numbers given to the curves distinguish different bands. The bands are calculated in the panel (a), the bands indicated with arrows are similar to the curves of wave-vector dependence of the energy of a free electron as

$$E(\mathbf{k}) = \frac{\hbar^2}{2m} \mathbf{k}^2 \quad (1.13)$$

The parabolic curve has a large gap slightly above the center of the Δ axis. The occurrence of the gap is interpreted as illustrated in the panel (b) on the right-

hand side. The gap is caused by the splitting of the parabolic band. In the panel (b), the parts of the E - \mathbf{k} curves not split are shown with broken lines. The longer parabola arises from nearly-free electrons and the band with less dispersion in the $3d$ band. The $3d$ band crosses the nearly-free-electron band and degenerate state occurs at the cross point. Because of the perturbation due to the electron-electron interaction the degeneracy is lifted and the band splits. The simple mathematical proof of this is presented in Appendix A. The $3d$ bands have dispersion larger than those expected from the atomic energy levels. This is caused by the mixing of the nearly-free-electron states.

From the consideration described above the $3d$ band of Ni must show the spin polarization. Experimentally, spin-resolved photoemission data shows the existence of the exchange split $3d$ band (Kisker, Schröder, Gudat, and Campagna, 1985). Prior to the experiments by Kisker *et al.*, Himpsel, Knapp, and Eastman, (1979), Eberhardt and Plummer (1980) measured the energy-band dispersion of Ni by high resolution angle-resolved photoemission, E - \mathbf{k} curves, and found the fine structure of EDC's in which some peaks exist in pairs.

An important way for investigating the validity of the energy-band calculation is to compare the calculated results with those of photoemission. As will be described in section 1.5, the partial DOS with specific orbital symmetry is proportional to the photoemission intensity as

$$N(\varepsilon_B) = A\rho_l(\varepsilon_B)$$

Also the binding energy of a peak observed in angle-resolved EDC represents the energy difference between two different energy-bands.

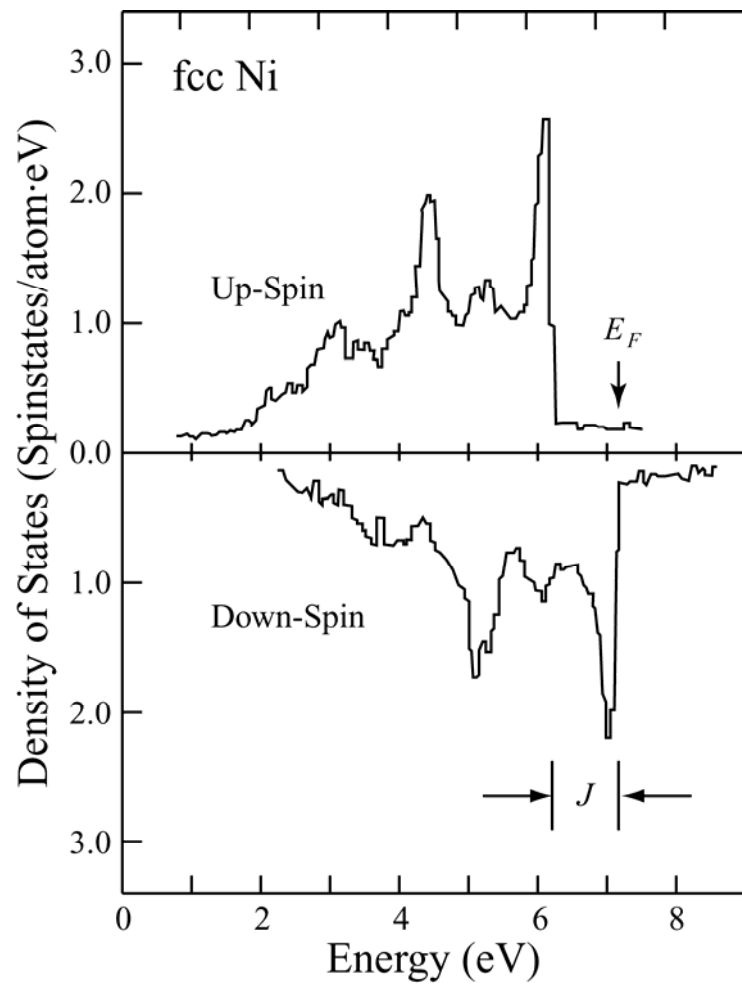


Fig. 1.7 Density-of-states curves of fcc Ni. Upper panel: DOS for up-spin electrons.

Lower panel: DOS for down-spin electrons. E_F : Location of the Fermi level.

(Connolly, 1967)

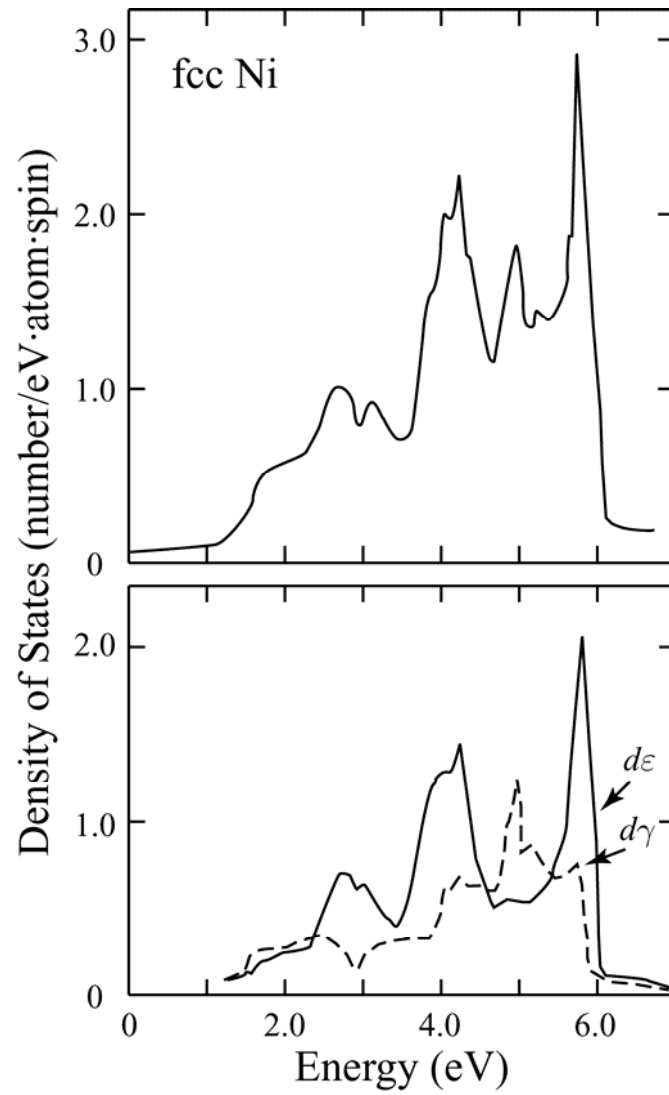


Fig. 1.8 DOS curves of paramagnetic Ni. Upper panel: Total DOS. Lower panel: Partial DOS for $d\varepsilon$ electrons (full line) and that for $d\gamma$ electrons (broken line). (Wakoh and Yamashita, 1964)

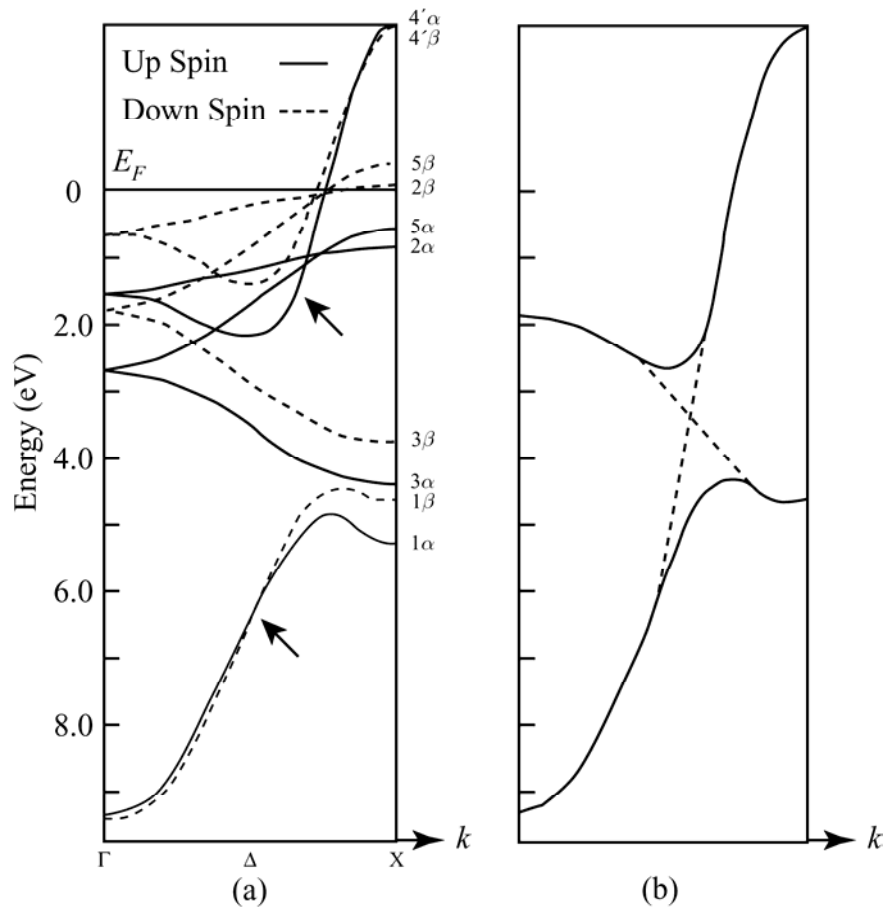


Fig. 1.9 Panel (a): Energy-band dispersion of Ni. Full line: Up-Spin band (α). Broken line: Down-Spin band (β). Numbers label the different bands. Panel (b): Splitting of the 3d and 4s band by mixing. (Wakoh, 1965)

The validity of the results of the energy-band calculation is judged by comparing them with the experimentally decided E - k curves. As will be described in Section 1.5, the dispersion curves are obtained by angle-resolved photoemission. As is obvious, the overall width of the $3d$ band shown in Fig. 1.9 does not coincide with the result of the angle-resolved photoemission. The width of the $3d$ band in Fig. 1.9 is about 4.3 eV which is about 4.1 times as large as that found in Fig. 1.10. Although the energy-band calculation can explain the shape of the Fermi surface obtained by the measurements of de Haas-van Alfen effects, it cannot explain the overall energy-band shape.

We find from comparison of the calculated DOS curves with photoelectron EDC's that the calculated DOS curves do not agree with the photoemission data. The DOS curves in Fig. 1.7 and Fig. 1.8 indicate that the width of the main $3d$ band is about 4.5 eV. The width of the $3d$ band shown in Fig. 1.10 is much narrower than this value (Kinoshita *et al.*, 1993). The data shown in Fig. 1.10 is for the spin polarization of the two-hole-bound-state and will be explained later in Sec. 1.6. It should be remarked that the fine structures as found in Fig. 1.7 and Fig. 1.8 are not found. One of the reasons for this is the low experimental resolution, phonon broadening, and lifetime broadening. However, it is plausible that some intrinsic discrepancy exists. The width of the experimental main $3d$ band is about 2 eV. A broad band occurring at 6.3 eV is caused by the two-hole-bound-state which does not appear in the energy-band. It will be discussed in Sec. 1.6. The disagreement of the band width between the calculated energy-band and the photoemission EDC arises from the many electron interaction and will be explained in Sec. 1.6.

It is difficult to improve the calculation introducing the electron correlation sufficiently well. Instead, it is possible to determine the parameters occurring in the calculation are decided so that the calculated results reproduce the experimental data. The results of such calculations are shown in Fig. 1.11 (Weling and Callaway, 1982). Weling and Callaway calculated the energy-band dispersion using the wave functions formed by the linear combinations of atomic orbitals (LCAO) and the orthogonalized plane wave (OPW). They used five d functions for the atomic orbitals:

$$|xy\rangle, |yz\rangle, |zx\rangle, |x^2 - y^2\rangle, \left| \frac{3z - r^2}{\sqrt{3}} \right\rangle$$

OPW was formed by plane waves,

$$|\mathbf{k} + \mathbf{K}_i\rangle \quad (i = 1, 2, 3, 4)$$

and pseudo-potentials. The pseudo-potential will be explained in Appendix B.

In the calculation of the matrix element in the LCAO-LCAO block, only the matrix elements between nearest neighbors other than the diagonal element were used. The Hamiltonian matrix consists of 9×9 elements from the LCAO-LCAO block, the LCAO-OPW block, and the OPW-OPW block:

$$[H] = \begin{array}{|c|c|} \hline \text{LCAO-LCAO} & \text{LCAO-OPW} \\ \hline \text{OPW-LCAO} & \text{OPW-OPW} \\ \hline \end{array} \quad (1.14)$$

The calculation of energy was made for good symmetry points in the Brillouin zone. The 20 energy values were to be calculated. The numbers of parameters appearing in the expressions were altogether 14. In practice, the parameters were determined, so that the calculated energy fit the various values of energy at the symmetry points in the Brillouin zone obtained by angle-resolved photoemission. The energy values used are tabulated in Table 1.3 (Eberhardt and Plummer, 1980). The energy values for other \mathbf{k} values were determined by the interpolation method. The functions expressing the dispersion of the energy-band are analytically expressed using trigonometric functions and the spherical Bessel functions. The results are those shown in Fig. 1.11.

The energy-bands illustrated in Fig. 1.11 were calculated so that they reflect the results of angle-resolved photoemission. This is quite evident that the calculated bands reproduce the results of the angle-resolved photoemission. In addition to the photoemission data, the calculated energy-bands should agree with the shape of the Fermi surface obtained by de Haas-van Alphen experiments. For realizing this, the parameters used in the calculation were slightly adjusted further. The results of the calculation reproduced the experimental shape of the Fermi surface.

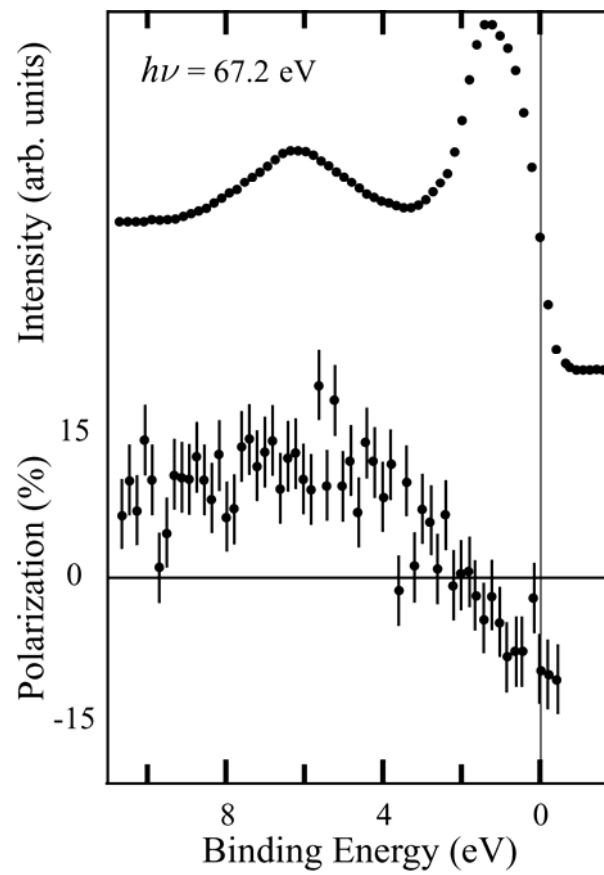


Fig. 1.10 Binding energy dependence of spin polarization of photoelectrons and the pertinent EDC. Upper curve: EDC. Lower figure: Spin polarization. (Kinoshita *et al.*, 1993)

Fig. 1.11 Empirical-band structure of nickel along some symmetry lines. The solid lines indicate spin-up states, the dashed lines spin-down states. The experimental values are given by squares. The zero of energy is the experimental Fermi energy. The Fermi energy is $E_F = 0.0548$ eV. (Weling and Callaway, 1982)

Table 1.3 The energy levels at symmetry points as determined by Eberhardt and Plummer (1980) (units are electron volts).

Symmetry	Experiment ^a		Theory ^c		Fit ^d	
	average ^b	spin-up	average	average	spin-up	spin-down
Γ_1	-8.8 ± 0.2		-8.93		-8.8	-8.8
$\Gamma_{25'}$	-1.1 ± 0.2		-2.04		-1.3	-0.9
Γ_{12}	-0.4 ± 0.1		-0.92		-0.45	-0.35
X_1	-3.3 ± 0.2		-4.31	-3.24	-3.2789	-3.1942
X_3	-2.8 ± 0.2		-3.81		-3.0000	-2.6000
X_2	-0.85 ± 0.1		-0.18	-0.16*	-0.2079	-0.1079
X_5			0.02	0.05	-0.1500	0.2500
L_1	-3.6 ± 0.2		-4.63	-3.50	-3.6638	-3.3413
L_{31}	-1.3 ± 0.1		-2.07		-1.4035	-1.2045
$L_{2'}$	-1.0 ± 0.2		-0.40		-1.0000	-1.0000
L_{32}		-0.2 ± 0.1	-0.17	-0.06*	-0.2016	0.0994
$W_{2'}$	-2.6 ± 0.2		-3.59		-2.6422	-2.5583
W_3	-1.7 ± 0.2		-2.77		-1.8937	-1.5067
W_1	-0.65 ± 0.1		-1.00		-0.6998	-0.6000
$W_{1'}$		-0.15 ± 0.1	0.02		-0.1500	0.2500
K_1	-3.1 ± 0.2		-3.66	-2.70	-2.7549	-2.6549
K_1	-2.55 ± 0.1		-3.45	-2.40	-2.5787	-2.2119
K_3	-0.9 ± 0.2		-1.81		-1.0916	-0.7088
K_4	-0.45 ± 0.1		-0.77	-0.50*	-0.5492	-0.4492
K_2			-0.25	-0.09	-0.2881	0.1119

^aW. Eberhardt and E. W. Plummer, Phys. Rev. B **21**, 3245 (1980). The experimental Fermi energy was chosen as zero of energy.

^bAverage over the spin directions.

^cC. S. Wang and J. Callaway, Phys. Rev. B **9**, 4897 (1974).

^dFor the sake of clarity we only indicate the values found for the energy levels which have not been used for the fit. The values followed by an asterisk are the readjusted input values [Eq. (14)]. The fit accurately reproduced the experimental data which were used as input. The values are given relative to the experimental Fermi energy as for the column based on experiment.

1.4 Synchrotron Radiation

In the present thesis work, photoemission experiments are carried out. As excitation photons, synchrotron radiation is used. Prior to the explanation of photoemission, some distinctive aspects of synchrotron radiation are briefly described here.

The electromagnetic radiation we see is generated by electrons making accelerated motion. A practical, we consider that synchrotron light is electromagnetic radiation emitted by electrons or positrons making circular or wiggling motion with a speed near the light velocity with energy above 100 MeV. Such an electronic motion is seen typically in an electron synchrotron or an electron storage ring. The wiggling motion is realized in insertion devices called wiggler or an undulator which is inserted in a straight section of a storage ring.

Nowadays, a synchrotron radiation source becomes popular and important in physics and other scientific researches. The electrons storage rings a kind of accelerator which store electrons with a fixed energy on a closed orbit. It consists of bending magnets, quadrupole magnets, an RF acceleration chamber, and some magnets for the orbit correction. Electrons are stored in an ultrahigh-vacuum chamber installed between the magnet poles. The bending magnets deflect the electron orbit; quadrupole magnets focus the electron beam; the RF field imposed in the RF acceleration chamber accelerates the electron energy lost by emitting synchrotron radiation.

The research of materials using synchrotron radiation has a scale for much exceeding the size of experiments carried out in an ordinary laboratory. It is a sort of big science. The facility that produces high quality light to be used in the advance

fundamental studies in science is a storage ring with a circumference larger than several hundred meters and a big amount of construction cost is needed to have it. Thus, the research in this field inevitably is a national project. On the other hand, a synchrotron radiation source for the semiconductor industrial applications such as microlithography and LIGA will be smaller in size.

Years have passed since the characteristics of synchrotron radiation were first investigated experimentally (Tombouliau and Hertman, 1956). Synchrotron radiation was first applied to the spectroscopic measurements on rare gases in the vacuum ultraviolet region (Madden and Codling, 1963). Ever since this work had been made, a horribly large number of reports were published on the applications of synchrotron radiation. This is because synchrotron radiation has unique characteristics described below. Concerning the qualities of lights synchrotron radiation cannot exceed lasers. However, in the short wavelength region where lasers are not available, synchrotron radiation is unique. In the description of the properties of synchrotron radiation is made only qualitatively. The details of mathematical expressions are omitted.

Representative properties of synchrotron radiation are described in the following:

1.4.1 High Flux and High Brilliance

Synchrotron light has a wide continuous spectrum. The spectrum energy covers over the range from the infrared to hard X-ray region. Synchrotron radiation has quite high brilliance and the light intensity available at the experimental station is quite high. This is due to the facts that the light source size is small and the light beam divergence is small. Since the source size is small, the loss of the light intensity

inevitable in the optical line where the magnifying mirror system and slits are installed is suppressed. The low divergence of the light beam also helps decreasing the loss of intensity in the optical system. Fig. 1.12 shows the schematic special distribution of synchrotron radiation. In the figure β is the quantity appearing in the special relativity theory as

$$\beta = \frac{v}{c} \quad (1.15)$$

Here, c is the light velocity and v is the velocity of the electron.

If $v \ll c$, the wave front of light is just like that of the ordinary dipole radiation. If v takes the value near to c , the relativity effect comes in and the wave front deforms to a shape like a narrow cone directed to the direction of the electron motion. The vertical divergence angle is $1/\gamma$ where γ is given as

$$\gamma = \frac{E}{m_0 c^2} = \frac{1}{\sqrt{1 - \beta^2}} \quad (1.16)$$

Here, E is the electron energy and m_0 is the electron rest mass. Numerically, γ is given as

$$\gamma = 1957 E \quad (1.17)$$

E is measured in GeV.

The total power emitted as synchrotron radiation is given as

$$P(kW) = 2.65 E^3 B J \quad (1.18)$$

Here B is the magnetic field of a bending magnet and J is the beam current. In fact, B is proportional to E . So P is proportional to E^4 . In case $B = 10$ kG, $E = 1$ GeV, and $J = 200$ mA, P is 5 kW. This is a big amount. Since the brilliance of light is very high, we can increase the light intensity falling on a sample. This increases the

resolution and the accuracy of measurements. The efficiency of the experiments is greatly enhanced. It is intense light. The flux or intensity of a synchrotron light is far much higher than that of the conventional laboratory sources.

1.4.2 Tunability

The mechanism that the continuous spectrum is generated is explained as follows: The electromagnetic radiation seen at a point away from the source point is a very short pulse since the pencil of the light beam is very narrow and the electron travel along the circular trajectory with the light velocity. This pulsed radiation field is formed by light with various frequencies. The intensity-versus-frequency relation is just the Fourier transform of the $E-t$ relation. Since the $E-t$ relation has a very short pulse, resulting $I-\omega$ relation has the shape of a wide continuous spectrum. The analytical form of the spectrum was derived by Schwinger (1949). Instead of describing the analytic form of the synchrotron radiation spectrum, the spectrum of the radiation from the Siam Photon Source is shown in Fig. 1.13.

In the spectra shown in Fig. 1.13, the bottom curve illustrates the spectrum of radiation emitted in the bending magnet part. The abscissa is the photon energy and the ordinate is the brilliance of radiation. These curves in the upper part show the spectra of the peaks of undulator light which move as the magnet gap is altered.

Since synchrotron radiation has a continuous spectrum, we can take out radiation with a frequency we need. This is very convenient in the experimental investigation of matter. The resonant photoemission measurements are possible using

this property. On the other hand, the property of small divergence described already is conveniently used in angle-resolved-photoemission experiments.

1.4.3 Polarization

The synchrotron light from a bending magnet part is linearly polarized in the plane where the electron beam exists. It can be used in the measurements of the dependence of the photoelectron intensity on the polarization of excitation light in the photoemission spectroscopy measurements. Strictly speaking, synchrotron radiation is linearly polarized completely only in the plane of electron orbit. Radiation emitted off this plane is elliptically polarized. Instead of describing the analytical formula, we exhibit the polarization of radiation in Fig. 1.14.

In Fig. 1.14, the abscissa represents the angle, ψ , of the direction of the light beam measured from the plane of the electron beam. $I_{//}$ represents the intensity of light with its electric vector in the plane of the electron beam. I_{\perp} represents the intensity of light with its electric vector perpendicular to the plane of the electron beam. The electron beam energy is assumed to be 5 GeV. Data for three different pieces of photon energy are shown. Note that the abscissa scale is different for the data for the photon energy; $h\nu = 10^4$. The data indicates that the light beam is narrower and degree of polarization is larger for hard X-rays.

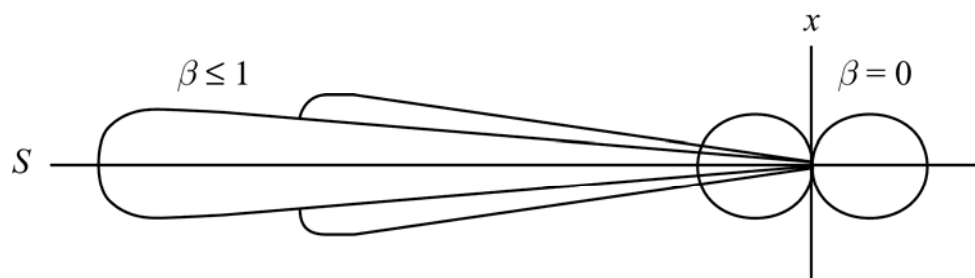


Fig. 1.12 Schematic illustration of spectral distribution of synchrotron radiation.

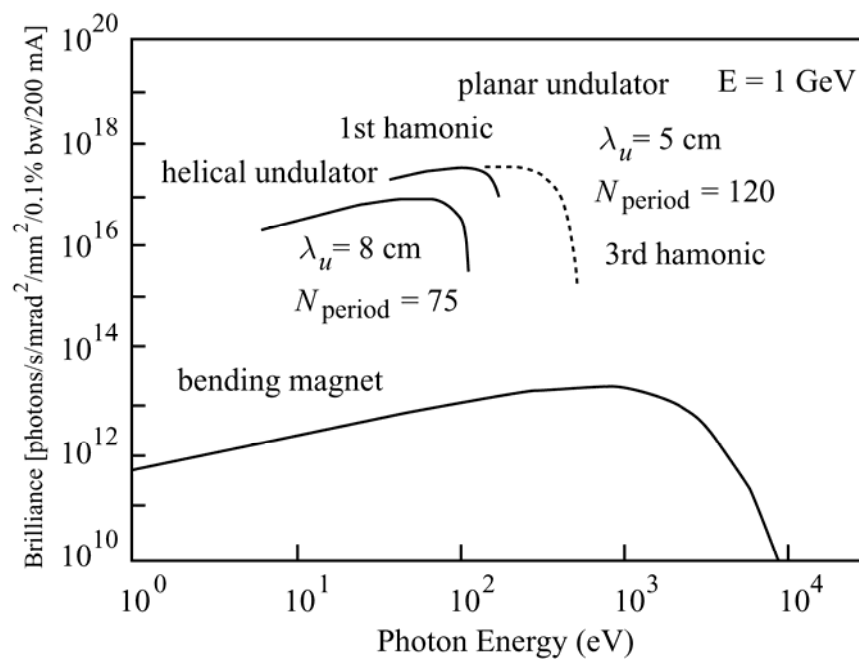


Fig. 1.13 Spectral distribution of synchrotron radiation.

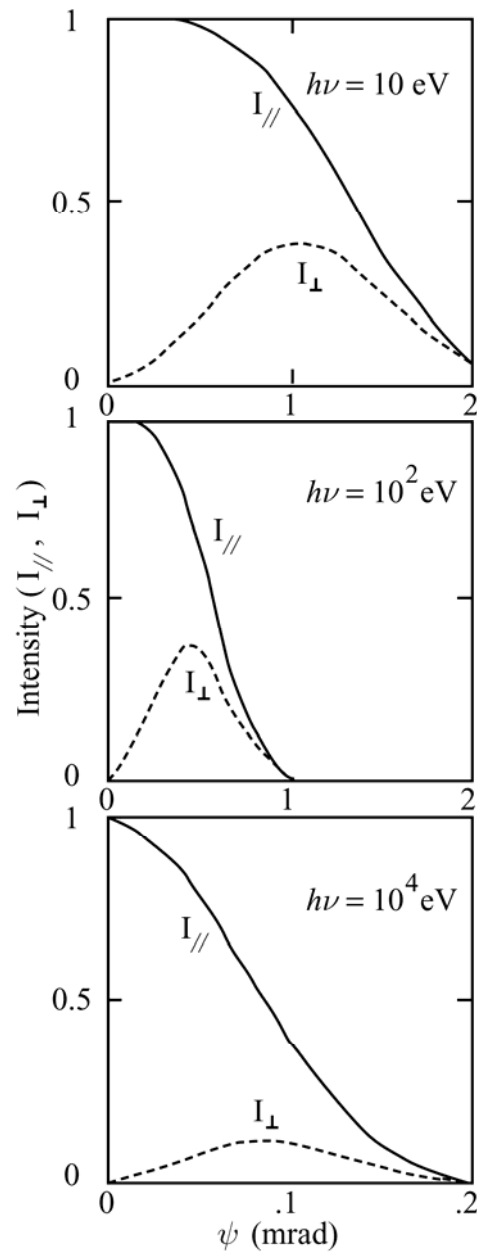


Fig. 1.14 Spatial distribution of the synchrotron radiation intensity.

1.4.4 Theoretical Spectrum

The spectrum is determined perfectly by theoretical calculation (Schwinger, 1949). In this calculation, the absolute intensity in the ordinate is accurate. This means that synchrotron radiation can be used as a light intensity standard in metrology. This situation is very useful particularly for vacuum ultraviolet light and X-rays for which the other intensity standard does not exist.

1.4.5 Pulsed Light

Synchrotron radiation from a storage ring has the time structure of the repetition of short pulses. This pulse is essentially different from that discussed in 1.4.2. The pulse we considered there is the nature inherent in the generation synchrotron radiation and not affected by other conditions due to the light source. This is the nature of radiation produced by an electron. The electrons in a storage ring are bunched. The bunching is caused by the RF frequency. In the optical beam line we can see the source with a finite length. When an electron bunch passes this source area, we can see synchrotron radiation. Since the electron storage ring is filled with such electron bunches, we see synchrotron radiation as the repetition of short pulses.

1.4.6 Cleanliness

A storage ring is a clean light source. For the storage of the electron beam, the chamber must be evacuated to ultrahigh vacuum below 10^{-10} Torr. Therefore no gas contaminating the measurement system comes out of the light source into the light beam line. This is very useful in experiments in which the sample surface must be kept clean.

1.5 Photoemission

In this thesis, we use photoemission spectroscopy for the investigation of the electronic structure of Ni(111) surface. We also investigate photoemission leading to the emission of electrons. The final state interaction pertaining to excited states is an important target of the investigation. In all of these processes, photoemission is the start point of the argument. Thus we briefly summarize the essence of the photoemission phenomena in this section.

When a material is irradiated with ionizing radiation with photo energy, electrons are emitted out of the material. This is photoemission and emitted electrons are referred to as photoelectrons. In the present thesis we limit the sample material to Ni. Thus we mention about metallic samples. In photoemission spectroscopy experiments a sample is irradiated with monochromatic light with photon energy, $h\nu$. The kinetic energy of emitted photoelectrons is analyzed in the experiments. Let the measured number of photoelectrons with kinetic energy, ε_k , be $N(h\nu, \varepsilon_k)$. We plot the curve, $N(h\nu, \varepsilon_k)$ versus ε_k , which is called the energy distribution curve (EDC). In addition to EDC, we measure the spectrum called photoyield spectrum which is defined as the curve of the total number, $N(h\nu)$, of photoelectrons versus excitation photon energy. This spectrum is considered to be proportional to the photoabsorption spectrum. More detailed explanation is given later. In some cases, the spectra called the constant final state (CFS) spectrum and the constant initial state (CIS) spectrum are quite useful. The CFS spectrum is defined as the curve of the number of photoelectrons with fixed kinetic energy, $N(h\nu, \varepsilon_k(\text{fixed}))$ versus $h\nu$. The CIS spectrum is defined as the curve of the number $N(h\nu, \varepsilon_B(\text{fixed}))$ of photoelectrons

with fixed binding energy, ε_B . The binding energy will be defined later. In many case, it is given by

$$\varepsilon_B = h\nu - \varepsilon_k - \chi_s \quad (1.19)$$

Here, χ_s , is the work function of the entrance slit to the energy analyzer. We summarize the distributions described about as follows:

- (1) A sample is irradiated with monochromatic light with energy, $h\nu$.
- (2) Photoelectron with kinetic energy ε_k is emitted from the sample.
- (3) The number of photoelectrons $N(h\nu, \varepsilon_k)$ is measured.

The spectra we measure are those given below.

- (1) Energy distribution curve (EDC)

$$N(h\nu, \varepsilon_k) \text{ versus } \varepsilon_k$$

- (2) Photoyield spectrum (Total yield spectrum)

$$N_{(h\nu)} \equiv \int d\varepsilon_k N(h\nu, \varepsilon_k); \quad N(h\nu) \text{ versus } \varepsilon_k$$

- (3) Constant final state (CFS) spectrum

$$N(h\nu, \varepsilon_k(\text{fixed})) \text{ versus } h\nu$$

- (4) Constant initial state (CIS) spectrum

$$N(h\nu, \varepsilon_B(\text{fixed})) \text{ versus } h\nu$$

We define binding energy, ε_B , of a photoelectron as the energy difference of the system between final states of the sample with one electron missing

$$\varepsilon_B \equiv E_f(N-1) - E_g \quad (1.20)$$

In Fig. 1.15, we illustrate the energy conservation relation pertinent to the photoemission process. In the initial state, the whole system has energy, E_i . In the

final state, the whole system has energy E_f . The initial state consists of a sample with energy, E_g , and a photon with energy, $h\nu$. So we have

$$E_i = E_g + h\nu \quad (1.21)$$

$$E_f = E_f(N-1) + \varepsilon_u \quad (1.22)$$

During the photoemission process, no extra energy flows into the system and no energy flows out of the system. Then, the energy conservation law tells that the energy of the initial state is equal to that of the final state. Thus we have

$$E_i = E_f \quad (1.23)$$

$$E_g + h\nu = E_f(N-1) + \varepsilon_u \quad (1.24)$$

$$\varepsilon_u = h\nu + E_g - E_f(N-1) \quad (1.25)$$

Substituting (1.25) into (1.20), we obtain

$$\varepsilon_B = h\nu - \varepsilon_u \quad (1.26)$$

This is another way to define the binding energy.

In the photoemission measurements, we do not measure ε_u but we measure the kinetic energy outside the sample. When an electron leaves the sample, it sees the barrier potential caused by the electron affinity. Apart from the escape probability, which will be discussed later, the kinetic energy of electron is reduced by the amount of the barrier equal to the electron affinity, $e\phi$. Instead of using electron affinity, we use the work function, χ , which is equal to the electron affinity. The work function is equal to the potential difference between the vacuum level, E_V , and the Fermi level, E_F .

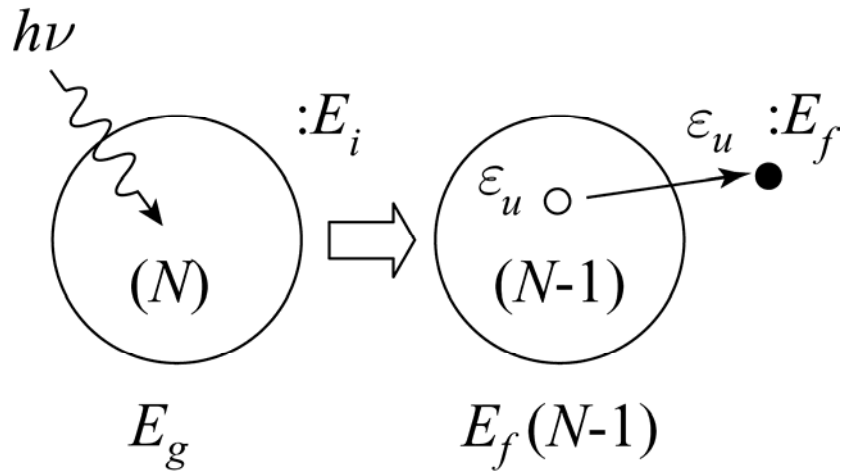


Fig. 1.15 Energy conservation relation in photoemission. E_i : Initial state energy of the system. E_f : Final state energy of the system. N : Total electron number. E_g : Ground state energy of the sample. $E_f(N-1)$: Final state energy of the sample missing an electron. $h\nu$: Excitation photon energy. ε_u : Kinetic energy of the photoelectron.

When two metals contact, electrons flow from one to another until the Fermi levels of both metals reach the same height. As a result of this electron flow, the contact potential, V_c , is formed at the boundary. Since the contact potential is equal to the difference of the work functions of two metals as

$$V_c = \chi_B - \chi_A \quad (1.27)$$

In the practical measurements, photoelectrons see the work function of the entrance slit of the energy analyzer system. We let the value be χ . Usually, we impose the retardation potential, V_R , to the energy analyzer slit. Then the vacuum level is further shifted by this potential. The relation described above is depicted in Fig. 1.16. We read χ_B as χ_s there. Then we have

$$\varepsilon_u = \hat{\varepsilon}_k + \chi_s + V_R \quad (1.28)$$

Here, $\hat{\varepsilon}_k$ is the kinetic energy that the photoelectrons have in the energy analyzer.

From (1.26) and (1.28) we have

$$\varepsilon_B = h\nu - \hat{\varepsilon}_k - \chi_s - V_R \quad (1.29)$$

The equation (1.29) is used for converting the kinetic energy to the binding energy.

In the case of one electron approximation, we assume that an electron with energy ε_i in the sample is independent of other $(N-1)$ electrons. Thus we approximate

$$E_g = E_{gi}(N-1) + \varepsilon_i \quad (1.30)$$

Usually, if we remove an electron from the N electron system the remaining $(N-1)$ electron system has energy different from $E_{gi}(N-1)$, since we have to take the relaxation energy E_{RX} into account. Thus, we have

$$E_f(N-1) = E_{gi}(N-1) + E_{RX} \quad (1.31)$$

In case E_{RX} is negligible and $V_R = 0$, (1.20), (1.30), and (1.31) yield (1.32) are the basis of the concept leading to (1.19).

$$\varepsilon_B = -\varepsilon_i \quad (1.32)$$

Equation (1.32) indicates that the binding energy is always positive because the bound electrons energy is negative.

So far, we have considered what the photoelectron kinetic energy or the binding energy is. In photoemission experiments, we measure the number of photoelectron emitted. Photoelectron EDC is given with the number $N(h\nu, \varepsilon_u)$. Then, the question arises what $N(h\nu, \varepsilon_u)$ is. In the argument described above, we consider the photoemission process as follows: At the beginning, there is a solid material and a photon. At the end, the photon disappears and the material in the different state and a photoelectron exists. Meanwhile, something very complicated occurs although the processes are in a black box. Obviously, these processes in the black box include optical excitation, inelastic scattering, and related many electron interactions. All attempts to challenge this problem have not been successful.

Instead, an empirical method called the three step process has been successfully used by many investigators. In the three step processes, we assume that photoabsorption, the migration to the surface, and the escape from the surface occur step wise. Namely, (1) incident excitation light is first absorbed to produce a photoelectron; (2) then the photoelectron migrates to the surface; (3) finally it leaves the solid surface. The generation of photoelectrons occurs proportionally to the

number of absorbed photons. Suppose the light intensity absorbed in the layer dz at the distance, z , from the surface is

$$dI = I_0 S \mu(\nu) \cdot e^{-\mu(\nu)z} dz \quad (1.33)$$

Here I_0 is the light intensity falling normally on the sample surface, $\mu(\nu)$ is the absorption coefficient, and ν is the frequency of light. Complicate scattering processes are renormalized in a escape length, \hat{l} , which is equal to the mean free path for inelastic scattering. The probability for the survival, p , is equal to

$$p = \exp(-z / \hat{l} \cos \theta) \quad (1.34)$$

Then the number, dN , of photoelectron produced in the layer dz at z and escaping from the surface is given by

$$\begin{aligned} dN &= dI \cdot p \cdot t(\varepsilon_u) \\ &= \frac{1}{4\pi} I_0 S \mu(\nu) \cdot t(\varepsilon_u) \exp \left\{ -(\mu(\nu) + \frac{1}{\hat{l}_\theta})z \right\} \sin \theta d\theta d\phi dz \end{aligned} \quad (1.35)$$

Here, $\hat{l}_\theta = \hat{l}(\varepsilon_u) \cos \theta$ and $t(\varepsilon_u)$ is the probability of the escape from the surface. S is the area of the surface.

Integration (1.35) over $d\theta \cdot d\phi \cdot dz$, we have the number of photoelectrons ΔN emerging from the solid angle $\Delta\Omega$ on the surface as

$$\frac{\partial N}{\partial \Omega} = \frac{I_0 S}{4\pi} \cdot t(\varepsilon_u) \frac{\sigma N_0 \hat{l}_\theta}{\sigma N_0 \hat{l}_\theta + 1} \quad (1.36)$$

Here σ is the absorption cross section of light and N_0 is the density of atoms absorbing light. The arrangement of the layer to produce photoelectrons in the three step process is shown in Fig. 1.17.

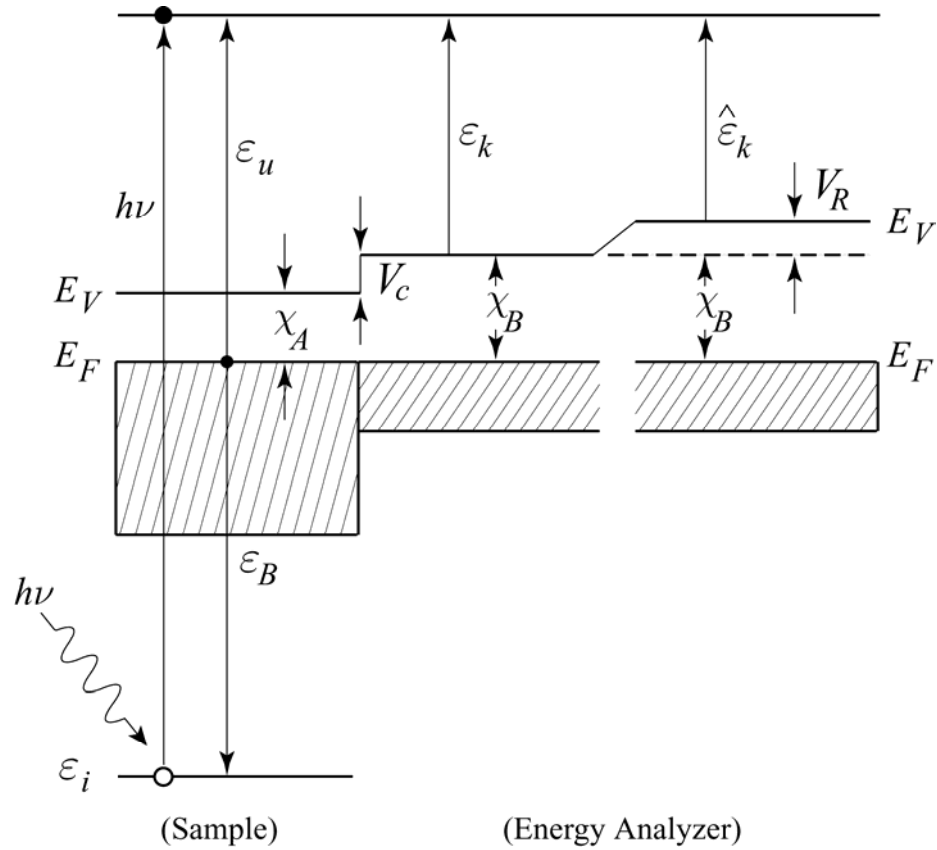


Fig. 1.16 Energy level diagram of a photoelectron. E_F : Fermi level. E_V : Vacuum level. $h\nu$: Photon energy. ε_u : Kinetic energy in the material. ε_k : Kinetic energy outside the material. $\hat{\varepsilon}_k$: Kinetic energy measured. ε_B : Binding energy. ε_i : Initial level energy. χ_A : Work function of the material. χ_B : Work function of the energy analyzer slit. V_c : Contact potential. V_R : Retardation potential.

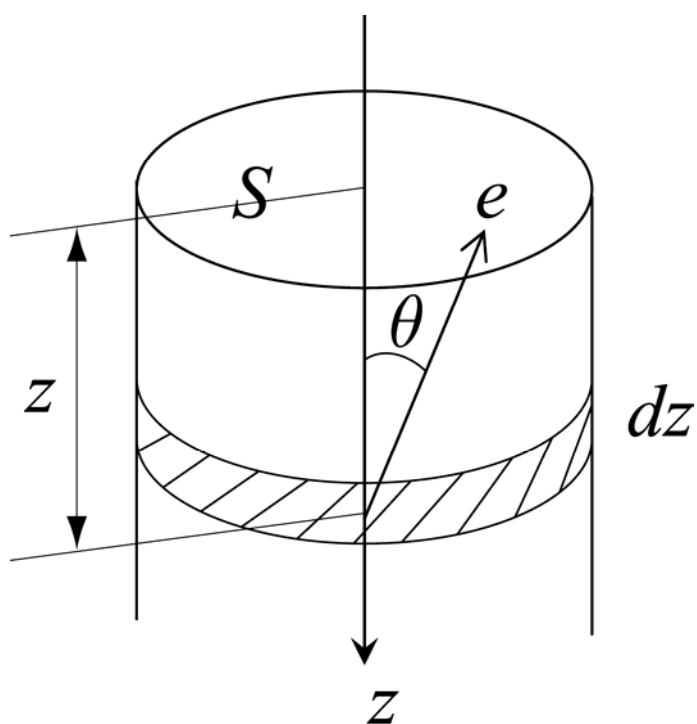


Fig. 1.17 Three step process for photoelectron generation.

The escape depth is the function of the photoelectron kinetic energy. It is found only empirically and shown in Fig. 1.18. From Fig. 1.18, we find $\hat{l}_\theta \leq 10^{-7}$ cm in the photoelectron energy range of interest. Since the absorption coefficient $\mu(=\sigma N_0) \cong 10^{-5}$ cm, $\sigma N_0 \hat{l}_\theta \cong 10^{-2} (< 1)$, we have

$$\frac{\sigma N_0 \hat{l}_\theta}{\sigma N_0 \hat{l}_\theta + 1} \cong \sigma N_0 \hat{l}_\theta$$

Thus we have

$$\frac{\partial N}{\partial \Omega} = \frac{I_0 S N_0}{4\pi} t(\varepsilon_u) \hat{l}_\theta(\varepsilon_u) \sigma(\varepsilon_u, \nu) \quad (1.37)$$

This indicates that the photoemission is governed by three steps independently of each other. One is the photoabsorption expressed by $\sigma(\varepsilon_u, \nu)$, the second is the migration expressed by $\hat{l}_\theta(\varepsilon_u)$ and the third is the escape expressed by $t(\varepsilon_u)$. This exactly what the three step model indicates.

The empirical values escape depth, $\hat{l}_\theta(\varepsilon_u)$, shown in Fig. 1.18 are tabulated in Table 1.4 for a few different values of photoelectron kinetic energy in the crystal. In case of sCK spectra, the kinetic energy, ε_u , is near 70 eV. Therefore \hat{l}_{av} (70 eV) estimated from Table 1.4 is 3.75 Å. In Ni(111), the inter-atomic distance in the [111] direction is $\sqrt{3}a$ and equal to 6.1 Å. The interlayer distance of the (111) plane is $a/\sqrt{3}$ and equal to 2.03 Å. According to the argument leading to (1.37), it is shown that the fraction of the photoelectrons coming out of the layer with the thickness, d , from the surface is given as

$$\frac{N(d)}{N(\infty)} = 1 - \exp(-d/\hat{l}_\theta) \quad (1.38)$$

The values of the fraction are tabulated Table 1.5. If we use the value, 3.75 Å, of the escape depth, we find about 80% of photoelectrons are from the surface layer and adjacent layer containing the nearest neighbor atom. On the other hand, about 42% of photoelectrons are from the surface layer and the adjacent atomic layers.

Table 1.4 Escape depth at different kinetic energy of photoelectron

ϵ_u	l	$l_{av.}$
50-200 eV	2.5-5 Å	3.75 Å
70 eV	2.5-5 Å	3.75 Å
40 eV	3.5-7.5 Å	5.5 Å
20 eV	8-14 Å	11 Å

Table 1.5 Fraction of the contribution of photoelectron from the surface layer.

m	$\exp(-\frac{d}{l})$	$N(d)/N(\infty)$
1	$e^{-1}=0.368$	$1-e^{-1}=0.652$
2	$e^{-1/2}=0.607$	$1-e^{-1/2}=0.393$
3	$e^{-1/3}=0.716$	$1-e^{-1/3}=0.284$
4	$e^{-1/4}=0.719$	$1-e^{-1/4}=0.221$

Suppose $l = md$; d : inter-atomic distance; $\therefore \frac{d}{l} = \frac{1}{m}$

The kinetic energy dependence of the escape depth is not of the fast change type. Therefore we can safely assume that the kinetic energy dependence of the escape depth does not deform EDC seriously.

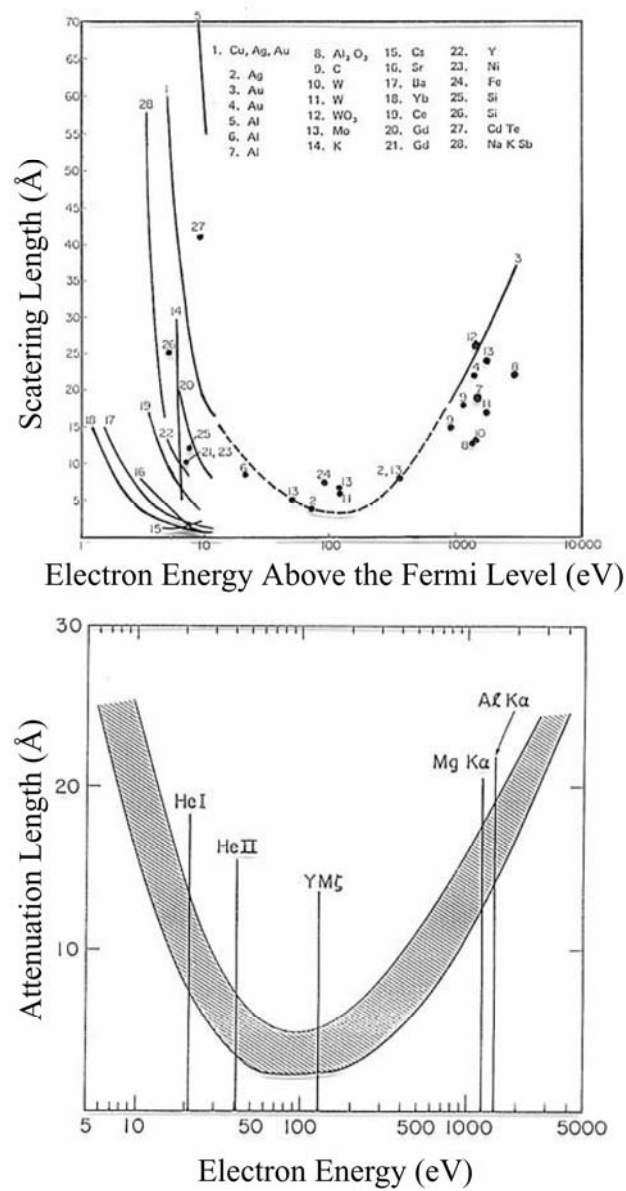


Fig. 1.18 Kinetic energy dependence of the escape depth.

In case of the escape depth, we know its kinetic energy dependence only empirically. On the contrary, the escape probability cannot found experimentally. Instead this is known only by theoretical consideration (Berglund and Spicer, 1964). The results are given as

$$\begin{aligned} t(\varepsilon_u) &= \frac{1}{2} \left[1 - \left(\frac{\chi}{\varepsilon_u} \right)^{3/2} \right] & \text{for } \varepsilon_u > \chi \\ &= 0 & \text{for } \varepsilon_u < \chi \end{aligned} \quad (1.39)$$

Similarly we have

$$\begin{aligned} t(\varepsilon_B) &= \frac{1}{2} \left[1 - \left(\frac{\chi}{h\nu - \varepsilon_B} \right)^{3/2} \right] & \text{for } h\nu > \varepsilon_B + \chi \\ &= 0 & \text{for } h\nu < \varepsilon_B + \chi \end{aligned} \quad (1.40)$$

In Fig. 1.19, the escape function, $t(\varepsilon_u)$, is depicted. The abscissa represents ε_u / χ . In the region where $\varepsilon_u < 3\chi$, $t(\varepsilon_u)$ change steeply. Suppose the work function, χ , is about 3 eV. Then $t(\varepsilon_u)$ changes steeply below $\varepsilon_u = 9$ eV. The corresponding region for ε_k is $\varepsilon_k < 6$ eV. In this region, the escape functions, $t(\varepsilon_u)$, deforms appreciably. In the region where $\varepsilon_u > 5\chi$, the change of $t(\varepsilon_u)$ with ε_u is slow. In this region, the escape function does not deform the shape of EDC appreciably.

In this way, the spectral shape of EDC is decided by the ionization cross section as (1.37) indicates. This is expressed more generally and resulting EDC is given by

$$\begin{aligned} n(\varepsilon_B, \nu) &= C t(\varepsilon_u) \hat{\ell}(\varepsilon_u) \times \sum_f \left| \langle \psi_f | T | \psi_g \rangle \right|^2 \\ &\quad \times \delta(E_f - E_g - h\nu) \times \delta(E_f(N-1) - E_g - \varepsilon_B) \\ &= B \sum_{f,i} \left| \langle \psi_f(N-1) | \psi_{gi}(N-1) \rangle \right|^2 \cdot \left| \langle f | p_e | g_i \rangle \right|^2 \\ &\quad \times \delta(E_f - E_g - h\nu) \cdot \delta(E_f(N-1) - E_g - \varepsilon_B) \end{aligned} \quad (1.41)$$

Here T is the transition matrix operator to be described later and p_e the electron momentum operator. More in the abbreviated form, (1.41) is written as

$$\begin{aligned}
 n(\varepsilon_B, \nu) &= B \sum_{f,i} \left| \langle \psi_f(N-1) | \psi_{gi}(N-1) \rangle \right|^2 \cdot \left| \langle h\nu - \varepsilon_B | p_e | g_i \rangle \right|^2 \\
 &\quad \times \delta(E_f - E_g - h\nu) \cdot \delta(E_f(N-1) - E_{gi}(N-1) - \varepsilon_i - \varepsilon_g) \\
 &\equiv B \sum_{f,i} M_{fi}(\nu) \times \delta(E_f(N-1) - E_{gi}(N-1) - \varepsilon_i - \varepsilon_g)
 \end{aligned} \tag{1.42}$$

Here we assume $\left| \langle \psi_f(N-1) | \psi_{gi}(N-1) \rangle \right| = 1$. We put

$$M_{fi}(\nu) = \left| \langle h\nu - \varepsilon_B | p_e | g_i \rangle \right|^2 \tag{1.43}$$

We can see similarity of (1.42) to the density-of-states curve expressed by

$$\rho_{Dh}(\varepsilon) = \sum_{f,i} \delta(E_f(N-1) - E_{gi}(N-1) - \varepsilon_i - \varepsilon_B) \tag{1.44}$$

This is the basis of the argument that the photoelectron EDC provides us with the DOS curve.

In (1.42), the transition moment defined by (1.43) is strongly dependence on the angular momentum quantum number. In Fig. 1.20, the plot energy dependence of the ionization cross sections of the $3d$ and $4s$ electrons of Ni is presented (Lindau, 2001). In the comparison of the intensity of the $3d$ emission with the $4s$ emission, the situation shown in Fig. 1.20 must be taken into account. Obviously the intensity is given by

$$I = N\sigma \tag{1.45}$$

Then the ratio of the number of the $3d$ electrons to that of $4s$ electron in Ni is

$$N_{3d} / N_{4s} = 9 \tag{1.46}$$

From Fig. 1.20, we see

$$\sigma_{3d}(70 \text{ eV})/\sigma_{4s}(70 \text{ eV}) = 8.5/0.09 \quad (1.47)$$

From (1.45) through (1.47), we have

$$\begin{aligned} I_{3d}(70 \text{ eV})/I_{4s}(70 \text{ eV}) &= 9 \times 8.5/1 \times 0.09 \\ &= 850:1 \end{aligned} \quad (1.48)$$

This indicates that the emission intensity of the 4s electron at $h\nu = 70 \text{ eV}$ is about three order of magnitude as small as that of the 3d electron. This situation will be mentioned again later.

Since the emission from the orbitals with some specific symmetry can exceeds that from other orbitals, it is convenient to define the partial DOS with specific orbital symmetry. Total DOS can be expanded with the partial DOS as

$$\begin{aligned} P_{Dh}(\varepsilon) &= \sum_{f,i} \delta(E_f(N-1) - E_{gi}(N-1) - \varepsilon_i - \varepsilon) \\ &\equiv \sum_{\ell} \sum_{f,i} \delta(E_f^{(\ell)}(N-1) - E_{gi}^{(\ell)}(N-1) - \varepsilon_i^{(\ell)} - \varepsilon) \\ &\equiv \sum_{\ell} P_{Dh}^{(\ell)}(\varepsilon) \\ P_{Dh}^{(\ell)}(\varepsilon) &= \sum_{f,i} \delta(E_f^{(\ell)}(N-1) - E_{gi}^{(\ell)}(N-1) - \varepsilon_i^{(\ell)} - \varepsilon) \end{aligned} \quad (1.49)$$

Correspondingly, EDC can be expanded regarding the orbital symmetry as

$$n(\varepsilon_B, \nu) = B \sum_{\ell} M_{\ell}(\nu) P_{Dh}^{(\ell)}(\varepsilon_B) \quad (1.50)$$

In the case where the l dependence is negligible, we have

$$\begin{aligned} n(\varepsilon_B, \nu) &= BM(\nu) \sum_{\ell} P_{Dh}^{(\ell)}(\varepsilon_B) \\ &= BM(\nu) P_{Dh}(\varepsilon_B) \end{aligned} \quad (1.51)$$

This shows that the photoelectron EDC is proportional to the DOS curve. However, as (1.50) indicates, EDC is proportional to partial DOS curve.

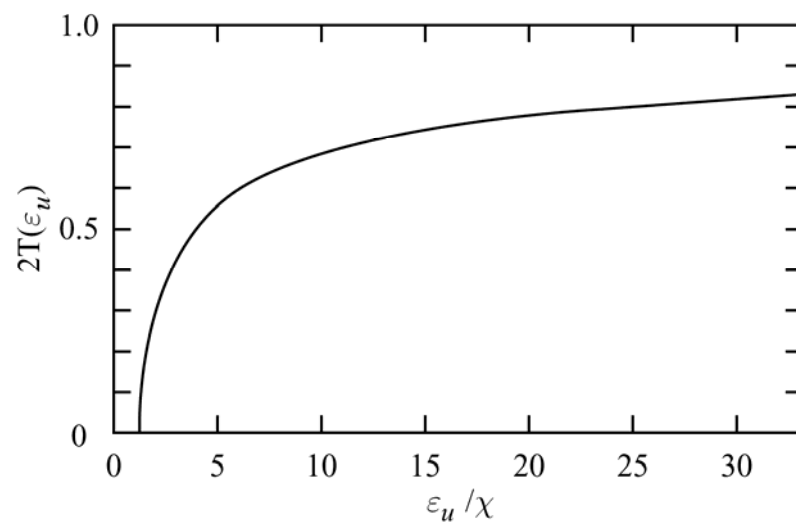


Fig. 1.19 Kinetic energy dependence of the escape probability (escape function).

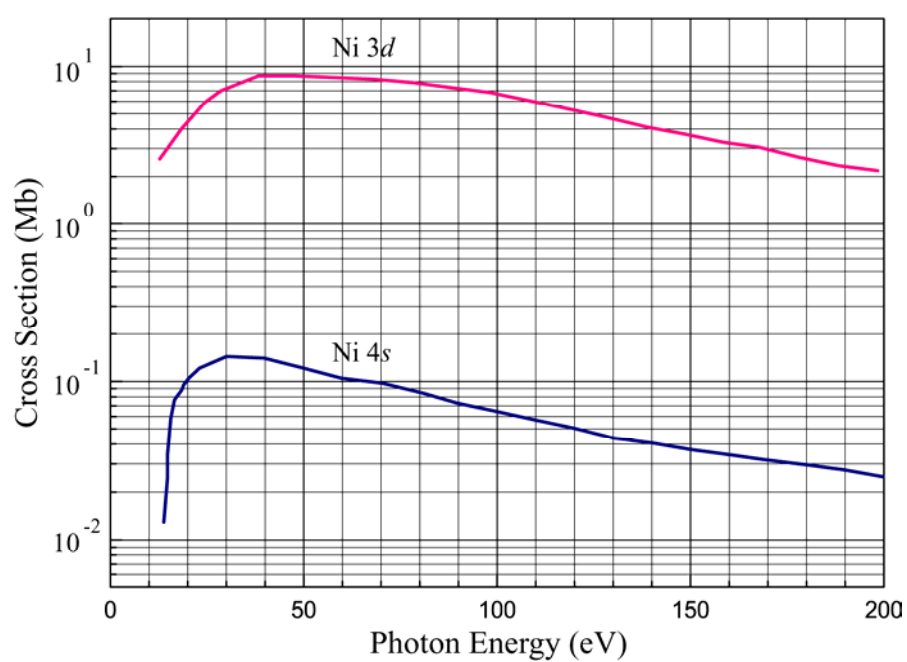


Fig. 1.20 Photon energy dependence of ionization cross sections for the $3d$ and $4s$ of Ni. (Lindau, 2001)

In the case where the electronic states are described by the energy-band picture, the relations described above are written as follows:

$$\begin{aligned} \text{EDC: } n(\varepsilon_B, \nu) &= B \sum_{\mathbf{v}\mathbf{k}\mathbf{K}\mathbf{K}'} \left| \langle h\nu - \varepsilon_B, \mathbf{k}' | p_e | \mathbf{v}, \mathbf{k} \rangle \right|^2 \delta(\mathbf{k}' - \mathbf{k} - \mathbf{K}) \delta(-\varepsilon_{\mathbf{v},\mathbf{k}} - \varepsilon_B) \\ &= B \sum_{\mathbf{v}\mathbf{k}\mathbf{K}} \left| \langle h\nu - \varepsilon_B, \mathbf{k} + \mathbf{K} | p_e | \mathbf{v}, \mathbf{k} \rangle \right|^2 \delta(-\varepsilon_{\mathbf{v},\mathbf{k}} - \varepsilon_B) \end{aligned} \quad (1.52)$$

$$\text{Partial DOS: } \rho_D^{(\ell)}(\varepsilon) = \sum_{\mathbf{v}\mathbf{k}} \delta(-\varepsilon_{\mathbf{v},\mathbf{k}}^{(\ell)} - \varepsilon) \quad (1.53)$$

$$\begin{aligned} \text{DOS: } \rho_D(\varepsilon) &= \sum_l \rho_D^{(\ell)}(\varepsilon) \\ &= \sum_{\mathbf{v}\mathbf{k}} \delta(-\varepsilon_{\mathbf{v},\mathbf{k}} - \varepsilon) \end{aligned} \quad (1.54)$$

In Fig. 1.21, the relations among the energy levels, the DOS curve, and expected EDC are shown. On the left hand side of the figure, the energy levels are illustrated. In this part, the basic energy conservation relation expressed by (1.26) is depicted. In the part adjacent to this, the energy levels are given. On the right hand side of the figure, the DOS curve associated with the energy levels are illustrated. EDC is shown there. Intrinsic EDC is accompanied by the broad background band with no structure. The background is caused by inelastic scattered electrons. A background subtraction method used in this thesis work is described in Appendix C.

As already pointed out, photoemission spectroscopy provides us with the energy-band dispersion curves, E - \mathbf{k} curves. This is achieved by the angle-resolved measurements. In Fig. 1.22, the concept of the measurements of angle-resolved photoemission is shown. A single crystal is used. For simplicity, we define the x , y , and z directions as illustrated in the figure. The sample is rotatable around the x and z axes. The energy analyzer which accepts emitted electrons is also rotatable around the sample. Let θ and ϕ be the polar angle and the azimuthal angle of the direction of

the emitted electrons. In the figure, the direction of the incidence of excitation light makes an angle, α , from the z axis. θ , ϕ , and α can be varied by rotating the sample and the energy analyzer. The angle-resolved photoemission spectroscopy is often abbreviated as ARPES.

From the photoelectron kinetic energy analysis, we know the kinetic energy, ε_u , of the photoelectron in the crystal. This energy is related with the absolute value of the electron momentum as

$$\varepsilon_u = \frac{|\mathbf{p}|^2}{2m} \quad (1.55)$$

If we observe the emission direction (θ, ϕ) we obtain the electron momentum as

$$\mathbf{p} = p(\theta, \phi) \quad (1.56)$$

In the escape of photoelectrons from the surface, the surface barrier potential changes the kinetic energy of a photoelectron. Therefore the barrier changes the momentum of the photoelectron. However, the component parallel to the surface is conserved.

$$\begin{aligned} p_{\parallel} &= p \sin \theta \\ &= \hbar k_{\parallel} \end{aligned} \quad (1.57)$$

Here θ is the angle of the emission direction as measured from the surface normal.

Therefore we obtain the parallel component of the electron wave vector as

$$\begin{aligned} k_{\parallel} &= \frac{1}{\hbar} \sqrt{2m\varepsilon_u} \sin \theta \\ &= (0.51 \text{ \AA}^{-1}) \sqrt{\varepsilon_u (\text{eV})} \sin \theta \end{aligned} \quad (1.58)$$

$$\varepsilon_{\mathbf{vk}} = \varepsilon_u + \chi - h\nu \quad (1.59)$$

We should point out important backgrounds concerning angle-resolved photoemission. First, we see two important δ functions in the formalism of EDC given in (1.52). They give us

$$\varepsilon_{\mathbf{v}\mathbf{k}} = \varepsilon_B \quad (1.60)$$

$$\mathbf{k}' = \mathbf{k} + \mathbf{K} \quad (1.61)$$

\mathbf{K} is the reciprocal lattice vector and \mathbf{k}' is the wave vector of the excited photoelectron. The process where $\mathbf{K} \neq 0$ is called the umklapp process. The argument about the umklapp process is very important, we ignore although it at present. The electron wave vector is originally defined in the Brillouin zone, *i.e.*, the reciprocal lattice space. However, we obtain the wave vector in the coordinate in real space. In (1.57), we obtain \mathbf{k} with \mathbf{p} . This is correct, because the exponential factor $e^{i\mathbf{k}\mathbf{r}}$ in the Bloch function connect \mathbf{r} in the real space with \mathbf{k} in reciprocal space through the same coordinate system.

In a two dimensional crystal such as a layered crystal, electrons move in a two dimensional plane. In a case like this the component of the wave vector normal to this plane, k_{\perp} , not be a good quantum number describing the electronic state of the crystal and not important. Then, practically we have

$$\mathbf{k} = \mathbf{k}_{//} \quad (1.62)$$

From (1.60), we have

$$\varepsilon_B = \varepsilon_v(k_{//}) \quad (1.63)$$

If we measure $k_{//}$ from (1.57) and ε_B from EDC, we can plot (1.63). This gives us the dispersion curve of the two dimensional energy-band. Thus, the method described above gives us the E - \mathbf{k} curve of the surface energy-band.

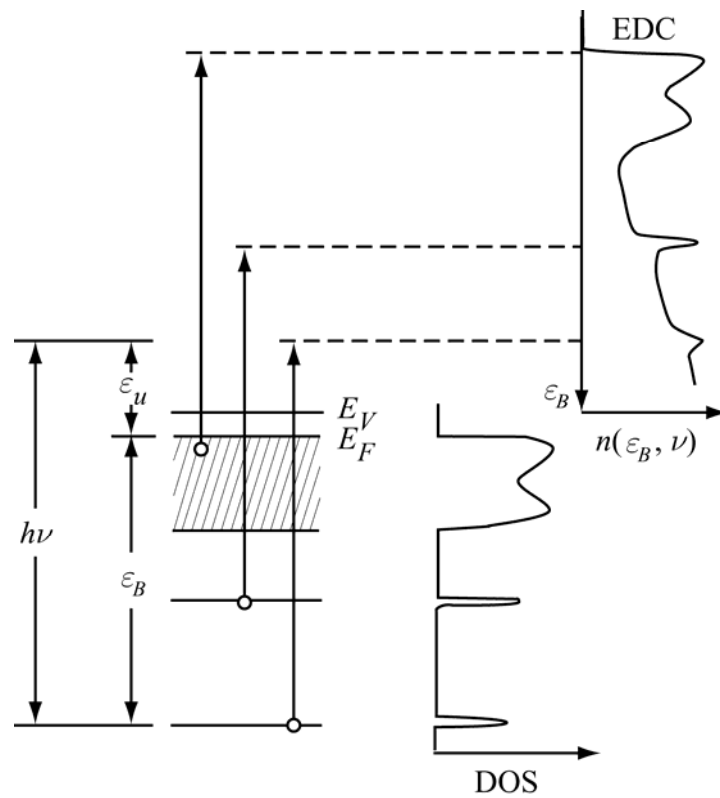


Fig. 1.21 Schematic illustration of the relation between EDC and the DOS curve. In EDC the background caused by inelastically scattered electrons overlaps intrinsic EDC. (Ishii, 1989)

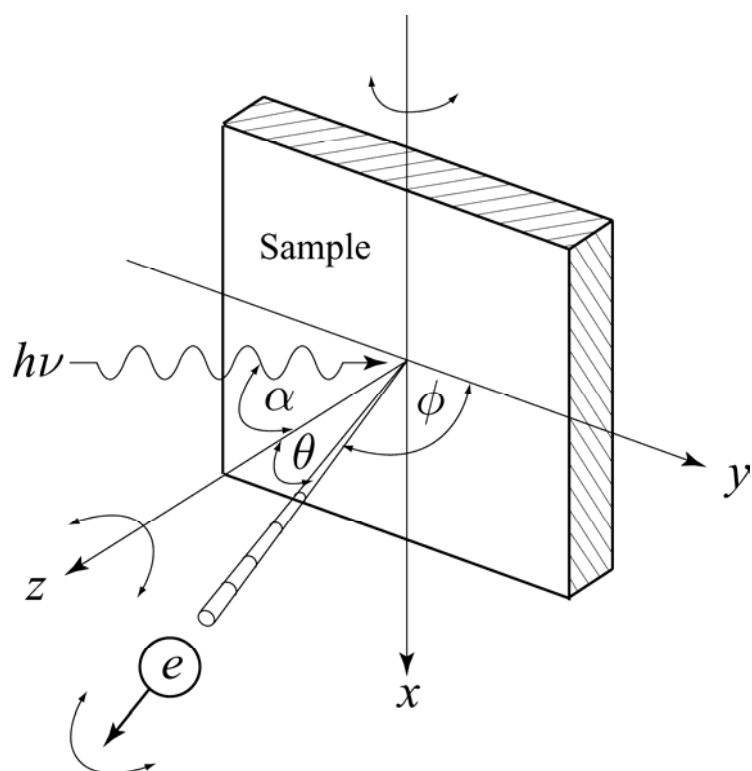


Fig. 1.22 Concept of angle-resolved photoemission. (Ishii, 1989)

In case of bulk energy-band, which is three dimensional usually, the situation is complicated. If we assume that the excited photoelectron is in the nearly-free-electron state, we can simplify the situation. Although there is no theoretical validity of this assumption, we know empirically that the assumption give us reasonable results. Under this assumption, we have

$$\varepsilon_u = \frac{\hbar \mathbf{k}^2}{2m} - E_0 \quad (1.64)$$

Then from (1.28), we have

$$\frac{\hbar \mathbf{k}^2}{2m} = \varepsilon_k + (E_0 + \chi) \quad (1.65)$$

in case $V_R = 0$. We put

$$E_0 + \chi \equiv V_0 \quad (1.66)$$

E_0 and V_0 are referred to as the crystal potential. We usually use V_0 as the crystal potential.

In the three dimensional energy-band cases, the normal emission mode measurements are quite effective. In these measurements, we collect electrons emitted normally to the sample surface. We assume photoelectrons lose a part of kinetic energy equal to the amount of the work function. In general, we have

$$\begin{aligned} (\hbar \mathbf{k}_\perp)^2 &= 2m(\varepsilon_k + V_0) - (\hbar \mathbf{k}_\parallel)^2 \\ &= 2m(\varepsilon_k + V_0) - 2m\varepsilon_k \sin^2 \theta \end{aligned}$$

θ is defined before in (1.57).

Then we have

$$\begin{aligned} k_\perp &= \frac{1}{\hbar} \sqrt{2m(\varepsilon_k \cos^2 \theta + V_0)} \\ &= (0.51 \text{ \AA}) \sqrt{\varepsilon_k \cos^2 \theta + V_0} \end{aligned} \quad (1.67)$$

Since we have $\varepsilon_B(\mathbf{k})$, we can plot the $E\text{-}\mathbf{k}$ curve. In the normal emission mode, $k_{\parallel} = 0$. Then we have

$$\begin{aligned} k_{\perp} &= \frac{1}{\hbar} \sqrt{2m(\varepsilon_k + V_0)} \\ &= (0.51 \text{ \AA}^{-1}) \sqrt{\varepsilon_k + V_0} \end{aligned} \quad (1.68)$$

In the experiment, we have to measure ε_B . This is achieved by changing excitation photon energy. Thus the use of synchrotron radiation is essential. The crystal potential, V_0 , is determined so that the results fit the calculated band well.

In Fig. 1.23, we show the concept of the ARPES measurements in the normal emission mode. In the practical measurements, we select the surface of the crystal so that the direction perpendicular to the surface is a good symmetry line of the crystal. The shift of peaks in EDC is traced as the excitation energy is change.

In Fig. 1.24 and Fig. 1.25, $E\text{-}\mathbf{k}$ curves measured on metallic Ni are shown (Himpsel *et al.*, 1979; Sakisaka *et al.*, 1987b). In Fig. 1.24, the measured band dispersion is fitted to the $E\text{-}\mathbf{k}$ curves calculated by Weling and Callaway (1982). The agreement is excellent, since the energy-bands were calculated using the experimental energy level values as pointed out. The data shown in Fig. 1.25 is to show the shift of the location of the two hole-bound-state band. During the course of the measurements the dispersion curves were also obtained the data agree with the calculation by Weling and Callaway (1982) as expected.

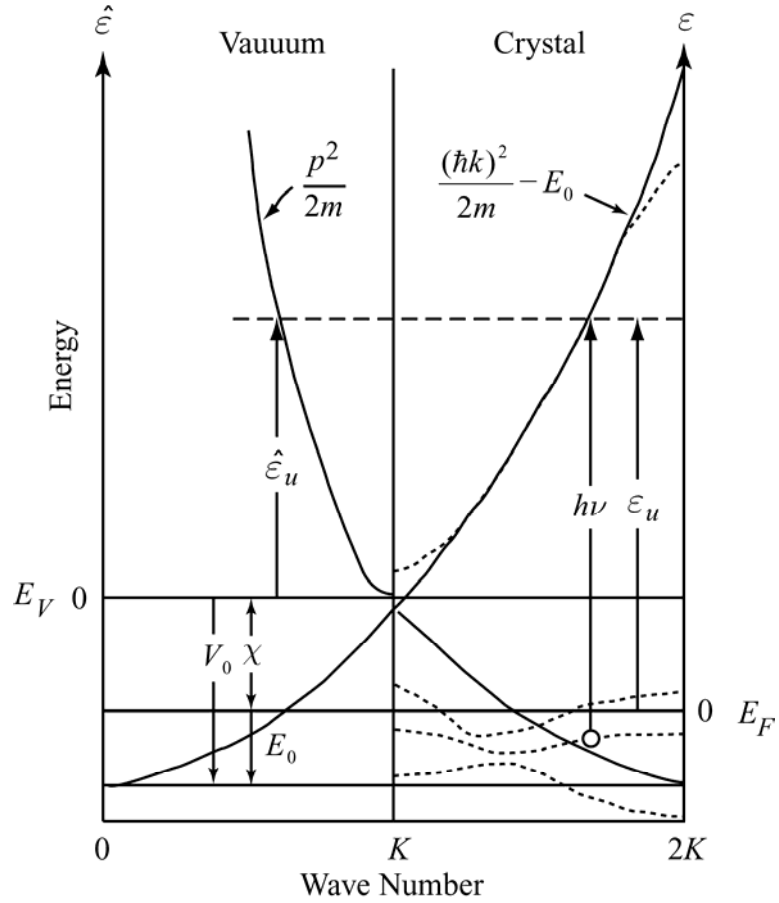


Fig. 1.23 Energy dispersion in the nearly free electron model for photoelectrons in ARPES. The right half represents the energy levels in a crystal. Curves illustrated by dots are energy-bands. Full lines are energy-band for the nearly free electron model. The left half represents the energy levels outside the crystal. K is a reciprocal lattice vector. $h\nu$: Photon energy. χ : work function. ε_u : Kinetic energy in the crystal. ε_k : Kinetic energy in a free space. E_F : The Fermi level. E_V : Vacuum level. V_0 (or E_0): Crystal potential. (Ishii, 1989)

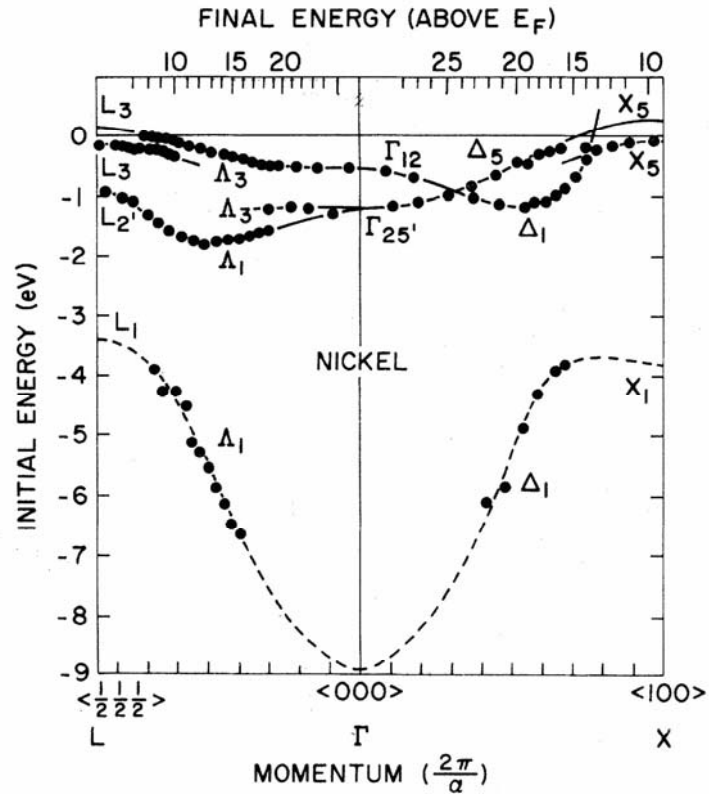


Fig. 1.24 Experimental E vs k energy-band dispersions for nickel. Unoccupied bands just above the Fermi level E_F and their Fermi-level crossings are drawn after Zornberg's calculation, which was fit to de Haas-van Alphen data. The lowest band has been extrapolated by a free-electron parabola matched to the experimental points. The final-energy scale gives the final-band energy used to determine the component of k normal to the crystal surface. Only a portion of the lower Δ_3 band is seen owing to small matrix elements, and Δ_2 and Δ'_2 bands are not shown since normal emission from them is forbidden. (Himpsel *et al.*, 1979)

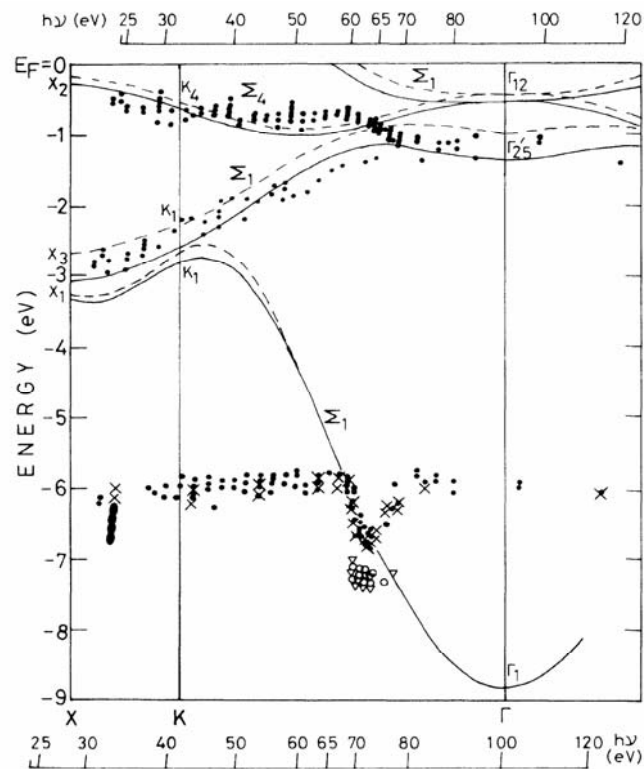


Fig. 1.25 Positions of the band structure of ferromagnetic Ni along the $\Gamma-K-X$ direction in the bulk Brillouin zone. The binding energies of the peaks obtained by normal-emission measurements are represented by open circles. The solid and dashed curves denote the majority (\uparrow) and minority (\downarrow) spin bands with Σ_1 and Σ_4 symmetries calculated by Weling and Callaway (1982). For convenience, the position of the 6-7 eV feature obtained by angle-integrated measurements is also plotted (crosses). (Sakisaka *et al.*, 1987b)

In Fig. 1.26, spin-resolved ARPES bands of Ni(110) are shown (Hopster *et al.*, 1983). In this experiment, the degree of spin polarization was first measured as a function of the binding energy. Then, the ARPES 3*d* band in the normal emission mode was measured. The spectra of the spin polarization were used to decompose the ARPES EDC into the up-spin band and the down-spin band. Similar measurements were repeated at various temperatures. The figure in the left panel of Fig. 1.26 indicates that the separation between up-spin and the down-spin band decreases as the sample temperature is increased. In the right panel the dependence of the amount of the splitting between the up-spin band and the down-spin band on temperature is illustrated. This splitting is considered to be equal to the exchange splitting. The temperature dependent curve is found to be similar to that of the magnetization curve.

In the photoemission phenomena, we see a very distinctive effect referred to as the resonant photoemission. When we measure the outer shell electron emission by changing excitation photon energy, we observe that the emission intensity is greatly enhanced. This is considered to be caused by the resonance between the innershell excitation and the outershell excitation. Fig. 1.27 shows the change in the shape of EDC of MnCl₂ as the excitation photon energy is changed (Kakizaki *et al.*, 1983). The excitation photon energy is indicated on the left hand side of each EDC. The threshold of the 3*p*→3*d* excitation occurs around $h\nu = 49$ eV. It is recognized that the intensity of the 3*d* band emission is enhanced above this energy.

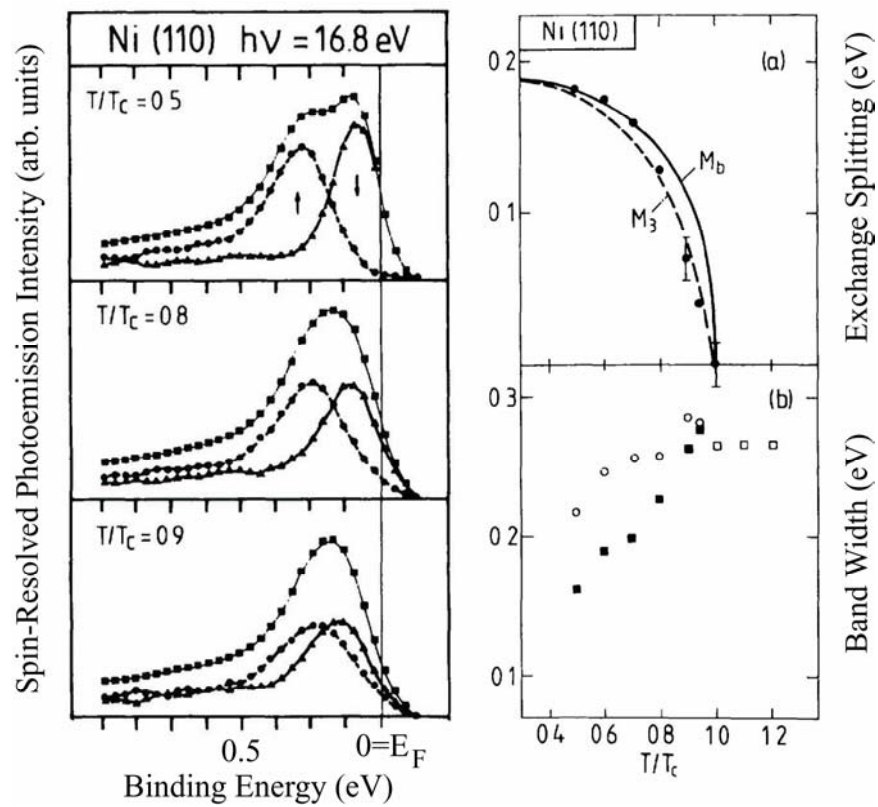


Fig. 1.26 Spin-resolved photoemission EDC of Ni and the temperature dependence of the exchange splitting. (Hopster *et al.*, 1983)

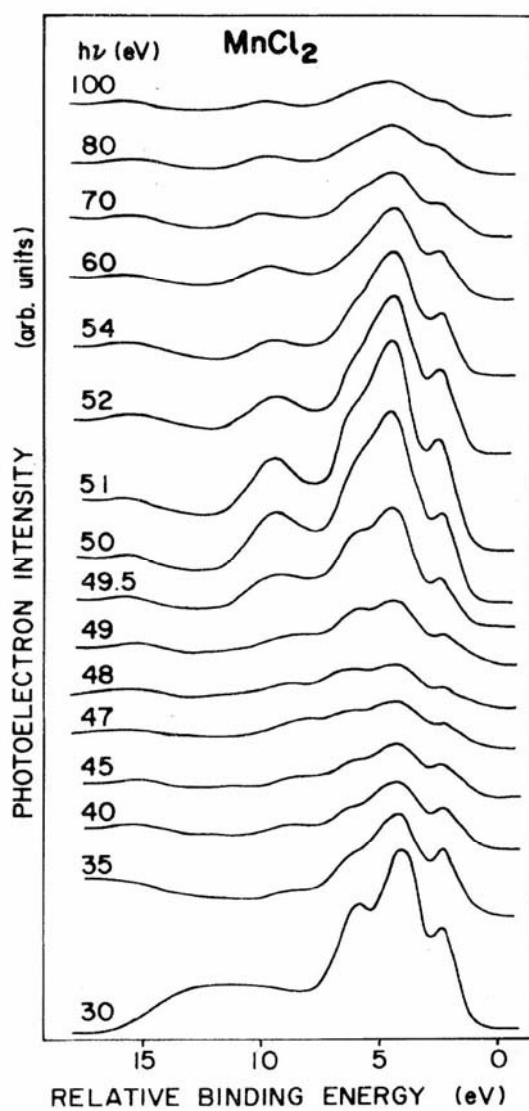
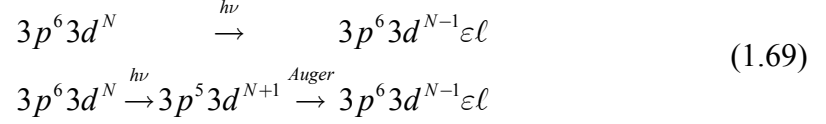


Fig. 1.27 Representative photoelectron energy-distribution curves for the valence-shell electrons in MnCl_2 . (Kakizaki *et al.*, 1983)

The resonance in this case occurs between the two transition channels as follows:



The occurrence of the resonance is inherent in the transition probability. The transition matrix is given by

$$T = V + V \frac{1}{\varepsilon - H_0 - V + iO_+} V \quad (1.70)$$

Here V is the perturbation potential, H_0 is the unperturbed Hamiltonian operator, and ε is the energy parameter. The transition matrix element is given by

$$\begin{aligned} M &= \left| \langle f | T | g \rangle \right|^2 \\ &= \left| \left\langle f \left| V_T + V_T \frac{1}{h\nu + E_g - H - V_T + iO^+} V_T \right| g \right\rangle \right|^2 \\ &= \left| \left\langle f | p_e | g \right\rangle + \sum_{mm'} \langle f | V_A | m \rangle \left\langle m \left| \frac{1}{\zeta - H - V_A} \right| m' \right\rangle \langle m' | p_e | g \rangle \right. \\ &\quad \left. + \sum_{mf'} \langle f | V_A | m \rangle \left\langle m \left| \frac{1}{\zeta - H - V_A} \right| f' \right\rangle \langle f' | p_e | g \rangle \right|^2 \\ \zeta &\equiv h\nu + E_g + iO^+; V_T = p_e + V_A \end{aligned} \quad (1.71)$$

The structure of the matrix element given in (1.71) is depicted in Fig. 1.28.

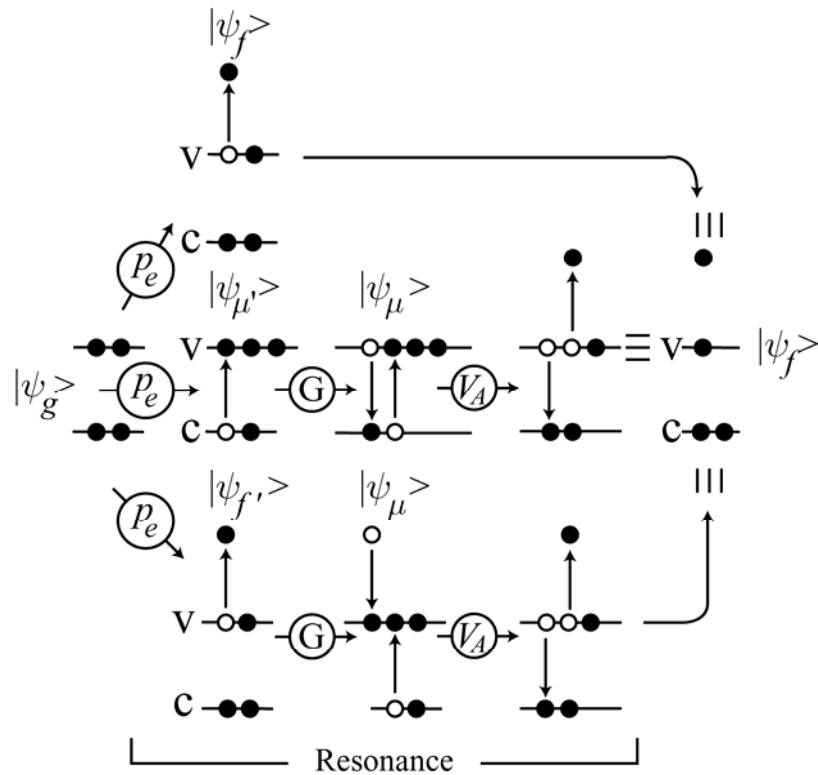


Fig. 1.28 Schematic illustration of the process of the resonant photoemission. State propagations in the transition probability expressed in the Green function representation are shown. Full circles: Electrons open circles: Holes. Arrows: Transitions and propagations. Encircled letters: Operators. c: Core levels. v: Valence levels. (Ishii, 1989)

1.6 Two-hole-bound-state

Let us ignore the screening effect at first. Suppose two holes occur at one lattice site. In this situation, only one hole is assumed exist at each site around that where two holes exist. One hole of the two cannot jump into the adjacent site because of the repulsive force from the neighboring sites. This leads possibly to the localization of the two $3d$ holes at one site. The localized two holes are depicted in Fig. 1.29. Arrows in the figure illustrate the repulsive force. While circles indicate Ni atoms and dark circles the $3d$ holes.

Theoretical treatment of this localization can be done as follows: We first assume that there is one $3d$ hole per lattice site on the ground state. An extra $3d$ hole is brought about by photoemission. The final state of photoemission is obviously an excited state which is considered here. As already described in Fig. 1.5, five up-spin electrons and four down-spin electrons occupy the exchange split $3d$ levels. This is equivalent to the existence of the vacancy of down spin electron, *i.e.*, one hole with up-spin. We consider the total energy of the crystal.

We describe the photoemission phenomena in the many electron approximation. For simplicity, we assume that the correlation interaction occurs between the up-spin electron and the down-spin electron. In other words, the correlation is postulated to be very small in the emission of the down-spin electron and it is considerable in the emission of the up-spin electron; the correlation occurs between the up-spin and the down-spin pair.

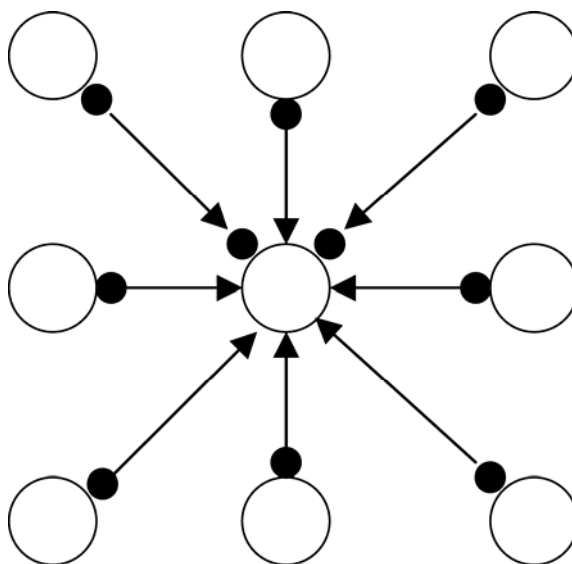


Fig. 1.29 Possibility that two $3d$ holes exist at one lattice site. White circles: Ni atom at lattice sites. Black circles: $3d$ holes. Arrow: Repulsive Coulomb force.

Let the state representing the band filled up with up-spin electrons be $|\phi\rangle$. The ground state is formed by filling the $|\phi\rangle$ further with L down-spin electron as

$$|\psi_g\rangle = \prod_{j=1}^L d_{\mathbf{k}j\downarrow}^\dagger |\phi\rangle \quad (1.72)$$

The final state of photoemission is approximated by the tight-binding band, and thus by the Bloch sum as

$$|\psi_f\rangle = \sum_j \exp(\mathbf{k}\mathbf{R}_j) d_{j\uparrow} \prod_{j'=1}^L d_{\mathbf{k}j'\downarrow}^\dagger (j) |\phi\rangle \quad (1.73)$$

By the operation by Π , we consider the state expressed by Slater determinant.

The photoemission spectra, *i.e.*, EDC can be calculated with the Green function given by

$$A_\uparrow(\varepsilon, \varepsilon_{\mathbf{k}}) = -\frac{1}{\pi} \text{Im} G(\mathbf{k}_\uparrow, \varepsilon) \quad (1.74)$$

$$G(\mathbf{k}_\uparrow, \varepsilon_{\mathbf{k}}) = \frac{1}{\varepsilon - \varepsilon_{\mathbf{k}\uparrow} + S(\mathbf{k}_\uparrow, \varepsilon - i0^+) - i0^+} \quad (1.75)$$

Here, S is the self-energy part. The energy of a quasi-particle is given by the roots of the equation given as

$$\varepsilon - \varepsilon_{\mathbf{k}\uparrow} + \text{Re} S(\mathbf{k}_\uparrow, \varepsilon - i0^+) = 0 \quad (1.76)$$

The solutions of (1.76) give us the peaks caused by the quasi-particle introduced by the correlation interaction. This is a simple description of the many electron interaction in photoemission.

The theory leading to two-hole-bound-state, introduce the statistical distribution function, $f_{\mathbf{k}\sigma}$, in the Green function formalism. The theory start with the Hubbard Hamiltonian as

$$H = \sum_{\mathbf{k}\sigma} \varepsilon_{\mathbf{k}\sigma} d_{\mathbf{k}\sigma}^\dagger d_{\mathbf{k}\sigma} + U \sum_i n_\uparrow(i) n_\downarrow(i) \quad (1.77)$$

Here, $n_\sigma(i) = d_\sigma^\dagger d_\sigma$. The Green function is given by

$$G(\mathbf{k}\sigma, \varepsilon) = \frac{f_{\mathbf{k}\sigma}}{\varepsilon - \varepsilon_{\mathbf{k}\sigma} - S(\mathbf{k}\sigma, \varepsilon) + i0^+} \quad (1.78)$$

The matrix elements appearing in the formalism are calculated by the use of the solutions of the Hamiltonian. The solution can be obtained only as the approximation. Various kinds of expansion are proposed there. $S(\mathbf{k}\sigma, \varepsilon)$ is the self-energy part. U is the intra-atomic Coulomb energy. G^0 is the zeroth order Green function. The self-energy part and the Green function of the zeroth order are given by

$$S(\mathbf{k}\sigma, \varepsilon) = - \sum_{\mathbf{k}'} (1 - f_{\mathbf{k}'\sigma}) \frac{U}{1 + U G_{\mathbf{k}\sigma, \mathbf{k}'\sigma}^0(\varepsilon + \varepsilon_{\mathbf{k}'\sigma})} \quad (1.79)$$

$$G_{\mathbf{k}\sigma, \mathbf{k}'\sigma}^0 = \sum_{\mathbf{q}} \frac{f_{\mathbf{k}+\mathbf{q}, \sigma} f_{\mathbf{k}'-\mathbf{q}, \sigma}^\dagger}{\varepsilon - \varepsilon_{\mathbf{k}+\mathbf{q}, \sigma} - \varepsilon_{\mathbf{k}'-\mathbf{q}, \sigma} - i0^+} \quad (1.80)$$

The energy of the quasi-particle is given as the solution of the Dyson equation as

$$\varepsilon - \varepsilon_{\mathbf{k}\sigma} - S(\mathbf{k}\sigma, \varepsilon) = 0 \quad (1.81)$$

In Fig. 1.30, the calculated self-energy parts are shown. The full lines show the real part of the self-energy part and the broken lines the imaginary part. There are three poles of the Dyson equation as shown by white circles in the figure. The values of parameters used in the expansion are indicated in the figure, although they are not explained here. The pole occurring around -8 eV may be caused by the two-hole-bound-state. The DOS curves calculated on the basis of the Green function are shown in Fig. 1.31. Two different data with different parameters are illustrated. The DOS curves for the t_{2g} ($d\varepsilon$) electrons are shown with full lines and those for the e_g ($d\gamma$) are shown with broken lines. In the approximation made here, two holes exist in the

optical excited states leading to photoemission. The bands around -8 eV are those for the two-hole-bound-state. Peak occurring in the lower energy region may be a satellite state. They are different from those of the multi-hole state.

In the calculation described above, the single-hole state appears in the final state at around -4 eV. The single-hole state is brought about by the removal of one hole through the scattering of conduction electrons. Let designate the ground state as $\hat{d}_k c_k$. This express the state \hat{d}_k with a hole in the $3d$ band and the conduction band state, c_k . When an electron is emitted out of the $3d$ band, the state changes into $\hat{d}_k^2 c_k$ where two $3d$ holes are generated.

If a $3d$ hole is destroyed by the scattering of conduction electrons, one hole is left behind in the $3d$ band. The important difference from the ground state is that the $3d$ hole is stuck to the Fermi level in the ground state but the $3d$ hole is in the excited state in the final state of photoemission; the hole can be distributed through out the whole $3d$ band. This situation is depicted in the upper panel of Fig. 1.32.

If two holes generated by the emission of a $3d$ electron are screened by conduction electrons incompletely, two holes remain undestroyed. The holes combine together to form the two-hole-bound-state, $\hat{d}_s^2 c_k$. It is possible that a conduction electron is bound loosely to the bound holes. However, the bound state is not much tight as an exciton in as ionic crystal.

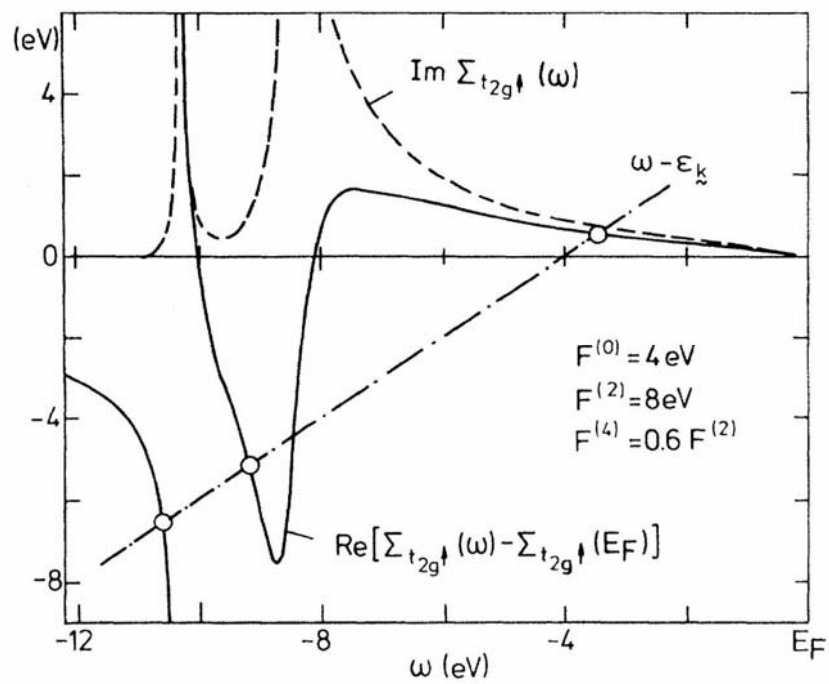


Fig. 1.30 Energy dependence of the self-energy part of the Green function showing the energy state of Ni. $\omega = \varepsilon - \varepsilon_k$ is the linear part in the denominator. Full line: Real part. Broken line: Imaginary part. (Liebsch, 1979)

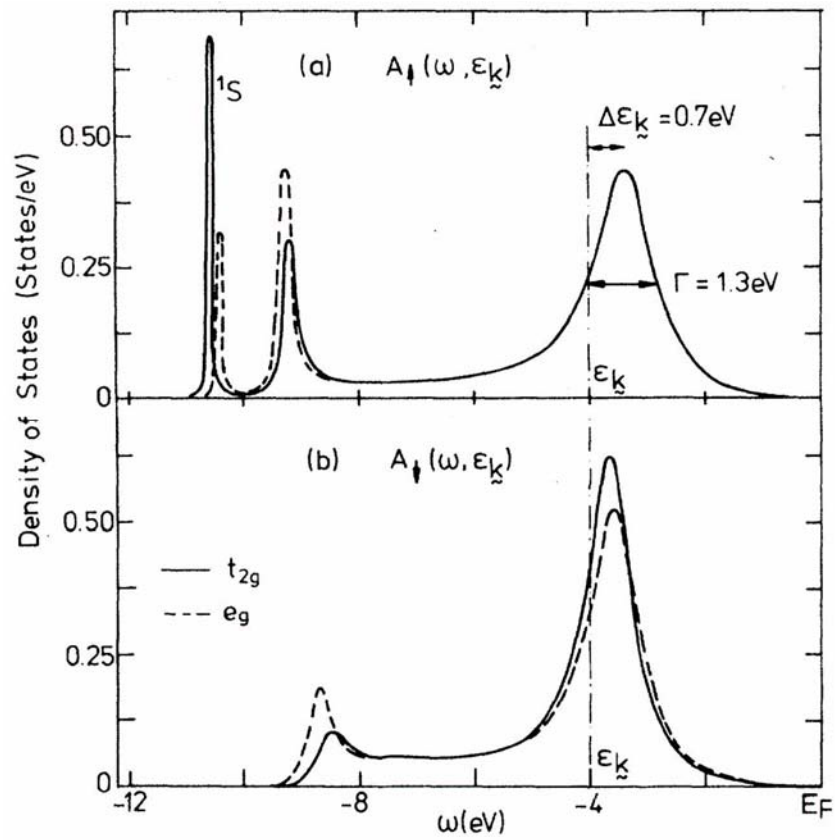


Fig. 1.31 Expected DOS of the many electron state with holes. (a) \uparrow spin. (b) \downarrow spin. (Liebsch, 1979)

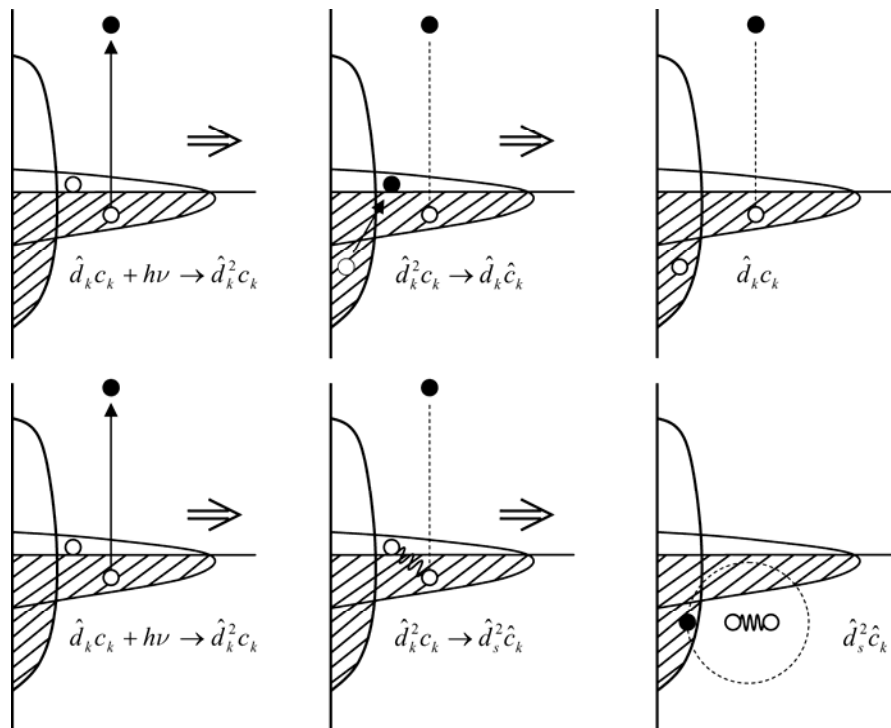


Fig. 1.32 Upper panel: Production of excited 3d hole by photoemission. Lower panel: Generation of the two-hole-bound-state. $h\nu$: Excitation photon. (see text)

The peak caused by the two-hole-bound-state has been found experimentally. This band appears at 6.3 eV, as indicated in Fig. 1.10. The cause of the spin polarization is illustrated in Fig. 1.33. Only the down spin electron is excited from the $3p$ level as the $3p-3d$ transition. After this excitation, the $3d$ band is completely filled up. If the MVV sCK transition occurs after this, only the down spin electron jumps into the $3p$ level, since only the $3p$ hole with down spin exists in the $3p$ level. By the sCK transition, either up-spin electron or down-spin electron jumps up. If the up-spin electron is excited, both the triplet and singlet state is possible to occur. If the down-spin electron is ejected, only the triplet state occurs in the final state. From the results of the atomic transition probability calculation, the ratio of the probability leading to the triplet state to that of the singlet state is given as 1:4. The spin polarization of the two-hole-bound-state band as observed on the $3p-3d$ resonance gives the positive polarizability as expected. This provides us with the direct experimental evidence of the existence of the two-hole-bound-state.

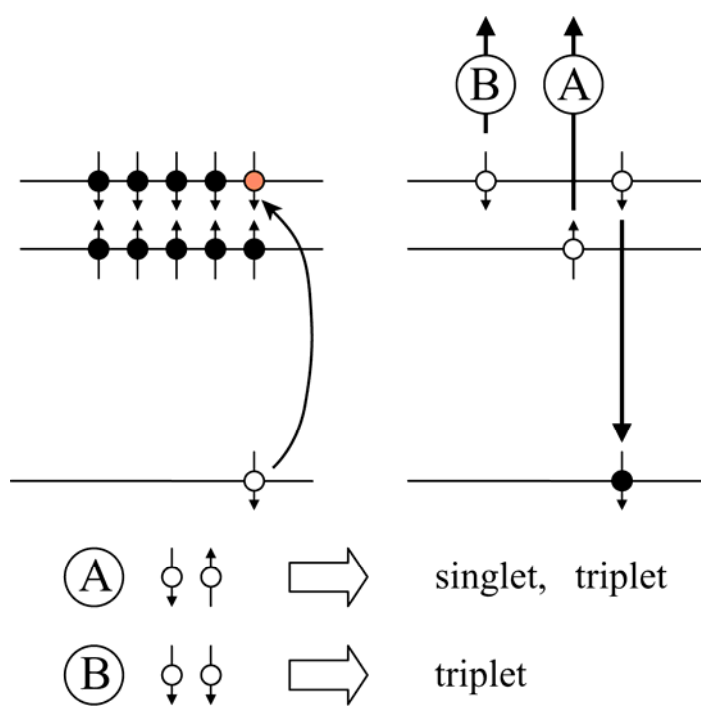


Fig. 1.33 Spin polarized of the two-hole-bound-state exhibited on resonance.

1.7 *MVV* sCK Spectra

In this thesis, the *MVV* sCK spectra of Ni are investigated. The *MVV* sCK transition is a kind of the Auger transition. The Auger nomenclature is described in Appendix D. The transitions are illustrated in Fig. 1.1 and the fundamental concepts associated with definition are mentioned there. In this section, we see the mechanism of the Auger transition is described. We describe how is the famous transition matrix element, $\left\langle \frac{1}{r_{12}} \right\rangle$, is derived.

In addition to Fig. 1.1, The Auger transition is illustrated in Fig. 1.34. The principal quantum numbers of the electronic energy levels pertaining to the Auger transition as N_1 , N_2 , N_3 and ε_u . The levels are indicated as c , v_1 , v_2 , and ε . When $N_1 = N_2 \neq N_3$, the Auger transition is called the Coster-Kronig (CK) transition and when $N_1 = N_2 = N_3$, the Auger transition is called super Coster-Kronig transition. In the present case, we deal with the transition, $3d \rightarrow 3p$ & $3d \rightarrow \varepsilon$, we refer to this transition as *MMM* sCK transition. Since the $3d$ level from the valence band we use the name, *MVV*, instead of *MMM*. In a similar way we treat the *LVV* CK transition.

The quantum theory tells us that the excited state is not stable and it fall down to ground state by loosing its energy. In the quantum electrodynamic theory, it is shown that the spontaneous optical transition occurs. Albert Einstein showed the occurrence of the spontaneous transition in a more intuitive way. The Auger transition is spontaneous. It can be understood that the excited state relaxes simply to the ground state by emitting an electron. However, how to we describe the cross section? Here we analyze the process more in principle.

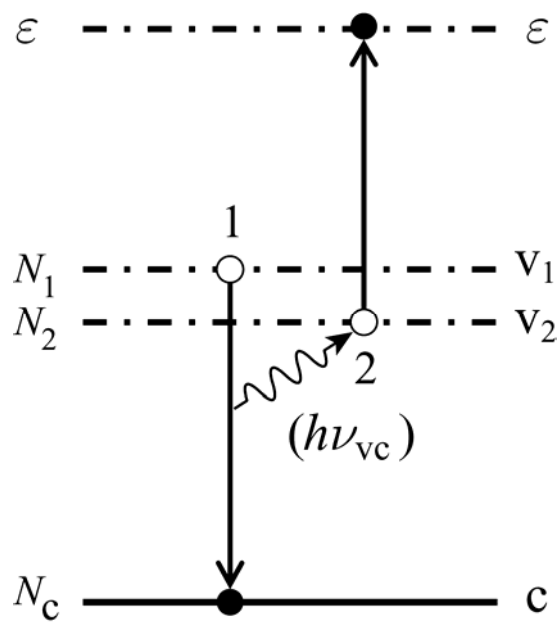


Fig. 1.34 Auger effect. The transition from v_1 to c emits virtual photon with energy $h\nu_{vc}$. This photon is absorbed by an electron in v_2 and the electron emission occurs.

We start with the classical theory of the generation of electromagnetic waves. In other words, we employ the process using the semiclassical treatment of radiation. First we write Maxwell's electromagnetic equations as

$$\nabla^2 \phi' - \frac{1}{c^2} \frac{\partial^2 \phi'}{\partial t^2} = -4\pi\rho \quad (1.82)$$

$$\nabla^2 \mathbf{A}' - \frac{1}{c} \frac{\partial^2 \mathbf{A}'}{\partial t^2} = -\frac{4\pi}{c} \mathbf{j} \quad (1.83)$$

$$\phi' = \phi - \frac{1}{c} \frac{\partial \chi}{\partial t} \quad (1.84)$$

$$\mathbf{A}' = \mathbf{A} + \nabla \chi \quad (1.85)$$

The solutions of equations of (1.82) through (1.85) are oscillatory functions with time in the classical form. The parameters appearing in the solutions are quantized and formally written in the form of matrix element. They are written as shown in (1.86) through (1.88). Among them, (1.88) gives the energy conservation condition.

$$\rho \equiv \rho_{vc} e^{-2\pi i \nu_{vc} t} \quad (1.86)$$

$$\mathbf{j} \equiv \mathbf{j}_{vc} e^{-2\pi i \nu_{vc} t} \quad (1.87)$$

$$\nu_{vc} \equiv (\varepsilon_v - \varepsilon_c) / \hbar \quad (1.88)$$

The practical form is given by

$$\rho_{vc} \equiv -e \psi_v^* \psi_c \quad (1.89)$$

$$\mathbf{j}_{vc} \equiv ce \psi_v^* \boldsymbol{\alpha} \psi_c \quad (1.90)$$

Here, ψ_v and ψ_c are eigen functions expressing the valence and the core level states. $\boldsymbol{\alpha}$ is the operator occurring in the magnetic part of the Dirac's equation. In the

quantum state, ρ , and \mathbf{j} are taken to be fluctuating between the core and the valence orbitals.

$$i\hbar \frac{\partial \psi}{\partial t} + i\hbar c \boldsymbol{\alpha} \nabla \psi - \beta m c^2 \psi = 0 \quad (1.91)$$

This equation is simplified by putting

$$E = i \frac{\partial \psi}{\partial t}$$

$$(E - c \boldsymbol{\alpha} \mathbf{p} - \beta m c^2) \psi = 0 \quad (1.92)$$

Here the operator $\boldsymbol{\alpha}$ is given by

$$\boldsymbol{\alpha} = \begin{bmatrix} 0 & \boldsymbol{\sigma} \\ \boldsymbol{\sigma} & 0 \end{bmatrix} \quad (1.93)$$

$\boldsymbol{\sigma}$ is Pauli's spin matrix. Using the solutions, the scalar potential and the vector potential are given as

$$\phi = -e \int d^3 \mathbf{r}_1 \frac{\psi_v^* \psi_c}{|\mathbf{r}_1 - \mathbf{r}_2|} \exp[2\pi i \nu_{vc} (\frac{|\mathbf{r}_1 - \mathbf{r}_2|}{c} - t)] \quad (1.94)$$

$$\mathbf{A} = -e \int d^3 \mathbf{r}_1 \frac{\psi_v^* \boldsymbol{\alpha} \psi_c}{|\mathbf{r}_1 - \mathbf{r}_2|} \exp[2\pi i \nu_{vc} (\frac{|\mathbf{r}_1 - \mathbf{r}_2|}{c} - t)] \quad (1.95)$$

Here, we have used the conversation, (1.89) and (1.90), in the classical solutions for the electromagnetic field. Since we consider the process of the Auger transition as the emission and absorption of a virtual photon, we write the potential which acts as the perturbation as

$$V_A = \frac{e}{c} \{ \phi + (\boldsymbol{\alpha} \cdot \mathbf{A}) \} \quad (1.96)$$

In this way, the transition matrix element can simply be written as

$$\langle f | V_A | g \rangle = \langle \varepsilon_u | V_A | \mathbf{v} \rangle \quad (1.97)$$

The illustration presented in Fig. 1.34 is now rewritten as depicted in Fig. 1.35. We changed the virtual photon, $h\nu_{vc}$, to the Auger potential, V_A .

We calculate the transition matrix element as follow:

$$\begin{aligned} \langle f|V_A|g\rangle &\propto e^2 \iint d^3\mathbf{r}_1 d^3\mathbf{r}_2 [\psi_c^*(\mathbf{r}_1)\psi_{\varepsilon_u}^* - \psi_c^*\psi^*(\mathbf{r})] \\ &\times \frac{(1-\mathbf{a}_1 \cdot \mathbf{a}_2)}{|\mathbf{r}_1 - \mathbf{r}_2|} \exp[i(\mathbf{\kappa}_{vc}|\mathbf{r}_1 - \mathbf{r}_2| - 2\pi\nu_{vc}t)] \\ &\times [\psi_{v_1}(\mathbf{r}_1)\psi_{v_2}(\mathbf{r}_2) - \psi_{v_1}(\mathbf{r}_2)\psi_{v_2}(\mathbf{r}_1)] \end{aligned} \quad (1.98)$$

We have to change the time dependent part by integrating from minus infinity to plus infinity. For implementing this, the time dependent part of the wave equation is given by

$$\begin{aligned} \varphi(t) &= \prod_{\lambda} \varphi_{\lambda}(t) \\ &= \prod_{\lambda} e^{-2\pi i \nu_{\lambda} t} \varphi_{n_{\lambda}} \\ &= e^{-2\pi i \nu t} \prod_{\lambda} \varphi_{n_{\lambda}} \end{aligned} \quad (1.99)$$

The integration over t merely gives the energy conservation. By second quantizing (1.98) is written as

$$\begin{aligned} \langle f|V_A|g\rangle &= e^2 \left\langle \varepsilon_u \mathbf{c} \left| \frac{(1-\mathbf{a}_1 \cdot \mathbf{a}_2)}{r_{12}} \right| v_1 v_2 \right\rangle a_{\varepsilon_u}^{\dagger} a_{v_1} a_c^{\dagger} a_{v_2} + \text{c.c.}] \exp[i(\mathbf{\kappa}_{vc} \cdot \mathbf{r}_{12})] \\ r_{12} &= |\mathbf{r}_1 - \mathbf{r}_2| \end{aligned} \quad (1.100)$$

In (1.100), \mathbf{a}_1 and \mathbf{a}_2 give the magnetic interaction and it is small unless the electron energy is quite high. Therefore we ignore this term. On the other hand, r_{12} is considered to be of the size of Bohr's atomic radius of hydrogen. Thus,

$$\begin{aligned} r_{12} &\approx 0.5\text{\AA} \\ &= 5 \times 10^{-12} \text{ m} \\ &= 5 \text{ pm} \\ &= 5 \times 10^{-3} \text{ nm} \end{aligned}$$

Also the wavelength of the virtual photon in the MVV sCK transition is about 100\AA .

Then we have

$$\begin{aligned}\kappa_{\text{vc}} &= 2\pi\lambda_{\text{vc}}^{-1} = 2\pi/100\text{\AA} \\ &= 2\pi \times 10^{-2} / \text{\AA} \\ &= 2\pi \times 10^{-1} \text{nm}^{-1}\end{aligned}$$

Then we have

$$\kappa_{\text{vc}} r_{12} \approx 3 \times 10^{-3} \ll 1$$

Thus we can put

$$\exp(i\kappa_{\text{vc}} r_{12}) = 1$$

Then (1.100) is further simply to give

$$\langle f|V_A|g\rangle = \left[\left\langle \varepsilon_u \mathbf{c} \left| \frac{e^2}{r_{12}} \right| \mathbf{v}_1 \mathbf{v}_2 \right\rangle a_{\varepsilon_u}^\dagger a_{v_2} a_c^\dagger a_{v_1} + \text{c.c.} \right] \quad (1.101)$$

In this way, we know the mechanism of Auger transition. However, we see this from a general law of the quantum mechanics. The quantum theory tells us that the state cannot be stationary and the transition is induced if the Hamiltonian contains time explicitly. Two types of the time dependent potential are found in the quantum theory. One is that of the electromagnetic wave and has the form as

$$\left(\mathbf{p} + \frac{e}{c} \mathbf{A} \right)^2$$

This term oscillates with time. The other is the scattering potential. The Coulomb interaction between two particles changes in time, since the distance between them change with time. The potential has the form of $1/r_{12}$ obviously. Since the Auger transition is spontaneous, the state propagation is as shown in Fig. 1.36.

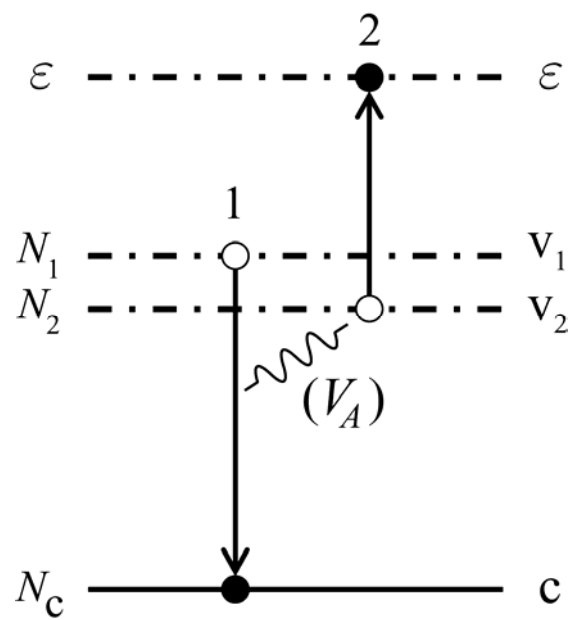


Fig. 1.35 Auger transition. Instead of the emission and absorption of a virtual photon, the potential, V_A , to cause the transition is shown.

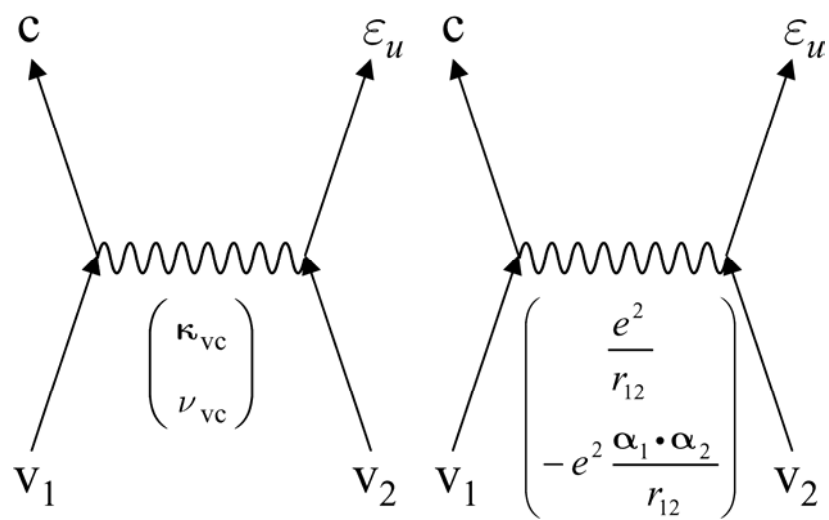


Fig. 1.36 Expression of the Auger transition in the quantum field theory. On the left panel, parameters related to energy are shown. On the right panel, the transition probability is shown

1.8 Cini-Sawatzky Theory

In this thesis work, the MVV sCK transition is treated. The Auger transitions include the innershell state and the transition is confined in a very narrow area. On the other hand, the outershell electron is in the band state, at least, in the ground state and spreads out over the whole crystal. Then, how is the transition matrix element is described? How does the spectrum look like? It is quite interesting that two pieces of theoretical work preceded the emergence of experimental work. Two investigators (Cini, 1977; Cini, 1978; Sawatzky, 1977; Sawatzky and Lenselink, 1980) carried out the concomitant theoretical calculations independently. Their results coincide with each other. Later their work has been refined by their collaborators (Bennett, Fuggle, Hillebrecht, Lenselink, and Sawatzky, 1983; Cini and D'Andrea, 1984). We refer to the theory as Cini-Sawatzky theory. In what follows, we describe the derivation of the results briefly, and then eventually, what the results of the model calculations suggest.

In the following, we use the formalism in the second-quantized manner. The Hamiltonian, the Green function, and the commutation relation are given by

$$H = \sum_{k\sigma} \varepsilon_k d_{k0}^+ d_{k0} + U \sum_i d_{i\sigma}^+ d_{i\sigma} d_{i\hat{\sigma}}^+ d_{i\hat{\sigma}} \quad (1.102)$$

$$G_{ml}^{00} = \left\langle \left\langle \psi_\theta \left| d_{m\hat{\sigma}}^+ d_{l\sigma}^+ d_{0\sigma} d_{0\hat{\sigma}} \right| \psi_g \right\rangle \right\rangle_\omega \quad (1.103)$$

$$d_{m\hat{\sigma}} = \frac{1}{\sqrt{N}} \sum_i \exp(-ik_m R_i) d_{i\hat{\sigma}} \quad (1.104)$$

$$G(\varepsilon) = G_{00}^{00}(\varepsilon) = \frac{1}{N} \sum_{ml} G_{ml}^{00}(\varepsilon) \quad (1.105)$$

$$\begin{aligned} [d_{m\hat{\sigma}}^+ d_{l\sigma}, H] = & -(\varepsilon_{k_l} + \varepsilon_{k_m}) d_{m\hat{\sigma}} d_{l\sigma}^+ \\ & - \frac{U}{N} \sum_{k, \hat{k}} \left(d_{m\hat{\sigma}}^+ d_{k_l + \hat{k}\sigma}^+ d_{k\hat{\sigma}}^+ d_{k + \hat{k}, \hat{\sigma}} - d_{k, \sigma}^+ d_{k - \hat{k}, \sigma} d_{k_m - \hat{k}, \hat{\sigma}}^+ d_{k_l, \sigma}^+ \right) \end{aligned} \quad (1.106)$$

$$\left[d_{m\sigma}^+ d_{l\sigma}^+, H \right] = -(\varepsilon_{k_m} + \varepsilon_{k_l} + 2U) d_{k_m\sigma}^+ d_{k_l\sigma}^+ + \frac{U}{N} \sum_{\hat{k}} d_{k_m-\hat{k}}^+ d_{k_l+\hat{k},\sigma}^+ \quad (1.107)$$

Then the Green function can be written as

$$\varepsilon G_{ml}^{00}(\varepsilon) = -\frac{1}{2\pi N} \cdot (\varepsilon_{k_l} - \varepsilon_{k_m} + 2U) G_{ml}^{00}(\varepsilon) + \frac{U}{N} \sum_{\hat{k}} G_{k_m-\hat{k}, k_l+\hat{k}}^{00}(\varepsilon) \quad (1.108)$$

So far we have used the Bloch sum for the valence band. This appears also in the Green function as

$$\begin{aligned} G_{KR}^{00}(\varepsilon) &= \frac{1}{\sqrt{N}} \sum_j \exp(-iKR_j) G_{R_j, R_j+R}^{00}(\varepsilon) \\ &= \frac{1}{\sqrt{N}} \sum_l \exp(iK_l R) \cdot G_{k_l, k-k_l}^{00}(\varepsilon) \\ G &\equiv G_{00}^{00}(\varepsilon) = \frac{1}{\sqrt{N}} \sum_K G_{KO} \end{aligned} \quad (1.109)$$

We carry out the analytical calculations further and obtain the result as

$$\begin{aligned} G(\varepsilon) &= \frac{1}{2\pi N} \sum_k \left(\frac{I(\varepsilon, K)}{1 - UI(\varepsilon K)} \right) \\ I(\varepsilon, K) &= \sum_{kl} \left(\varepsilon + \varepsilon_{k_l+K/2} + \varepsilon_{k-K/2} + 2U \right)^{-1} \end{aligned} \quad (1.110)$$

Such a situation is illustrated in Fig. 1.37.

We use the Bloch sum for the band state and calculate the transition cross section as

$$|\mathbf{k}\rangle = \frac{1}{\sqrt{N}} \sum_{\mathbf{R}} e^{i\mathbf{k}\cdot\mathbf{R}} |\mathbf{R}\rangle \quad (1.111)$$

$$\begin{aligned} \frac{d\sigma}{d\varepsilon_\mu} &\propto \sum_F \left(\left| \langle \psi_F | \psi_{v_1}(0) \psi_{v_2}(0) \rangle \right|^2 \delta(E_F + \varepsilon(k) - E_l) \right) \\ |\psi_F\rangle &= \frac{1}{\sqrt{2}} |\mathbf{v}_1(k_1) \mathbf{v}_2(k_2)| \end{aligned} \quad (1.112)$$

In case the band width is large and the energy-band prevails,

$$\begin{aligned}\frac{d\sigma}{d\varepsilon_u} &\propto \sum_{k_1 k_2} \delta(\varepsilon(k_1) + \varepsilon(k_2) + \varepsilon_u - E_l) \\ &\propto \int E(\varepsilon) E(E_l + \varepsilon(k) - \varepsilon) d\varepsilon\end{aligned}\quad (1.113)$$

In case U is large and the energy-band picture does not hold we have

$$\psi_F(\mathbf{k}) = \sum_{\mathbf{R}} U_{\mathbf{K}}(\mathbf{R}) e^{i\mathbf{K}\mathbf{R}} \psi_{\mathbf{R}}(\mathbf{r}) \psi_{\mathbf{R}+\hat{\mathbf{R}}}(\mathbf{r}) \quad (1.114)$$

For generating the localized state from the band state, we adopt the “exciton” approximation as shown in (1.115) through (1.118).

$$\frac{d\sigma}{d\varepsilon_u} = -\frac{1}{2\pi N} \text{Im} \left[\sum_{\mathbf{K}} \frac{I(\varepsilon\mathbf{K})}{1 - UI(\varepsilon\mathbf{K})} \right] \quad (1.115)$$

$$I(\varepsilon\mathbf{K}) = \frac{1}{N} \sum_{\mathbf{k}} \frac{1}{\varepsilon + W(\hat{k} + \frac{\mathbf{K}}{2}) + W(\hat{k} - \frac{\mathbf{K}}{2}) + 2U} \quad (1.116)$$

$$\varepsilon(\mathbf{K}) \equiv W \cdot (\cos K_x a + \cos K_y a + \cos K_z a) \quad (1.117)$$

$$\begin{aligned}I(\beta\mathbf{K}) &= i \int_0^\infty dt e^{i\beta t} J_0\left(\frac{K_x a}{2}\right) J_0\left(\frac{K_y a}{2}\right) J_0\left(\frac{K_z a}{2}\right) \\ &\equiv A(\beta\mathbf{K}) - iB(\beta\mathbf{K}) \\ \beta &\equiv \frac{3(\varepsilon + 2U)}{W} \quad J_0 : \text{Bessel function (0th order)}\end{aligned}\quad (1.118)$$

If we proceed the analytical calculation, we obtained

$$\frac{d\sigma}{d\varepsilon_u} \propto \frac{B(\beta\mathbf{K})[1 + A(\beta\mathbf{K}) - UA(\beta\mathbf{K})]}{[1 - UA(\beta\mathbf{K})]^2 + U^2 B^2(\beta\mathbf{K})} \quad (1.119)$$

The finalized simplified forms are given as follow:

$$\begin{aligned}\frac{d\sigma}{d\varepsilon_u} &\propto \frac{D(\varepsilon)}{[1 - UF(\varepsilon)]^2 + \pi^2 U^2 D^2(\varepsilon)} \\ F(\varepsilon) &= P \int_{-\infty}^{\infty} \frac{D(\hat{\varepsilon})}{\varepsilon - \hat{\varepsilon}} d\hat{\varepsilon}\end{aligned}\quad (1.120)$$

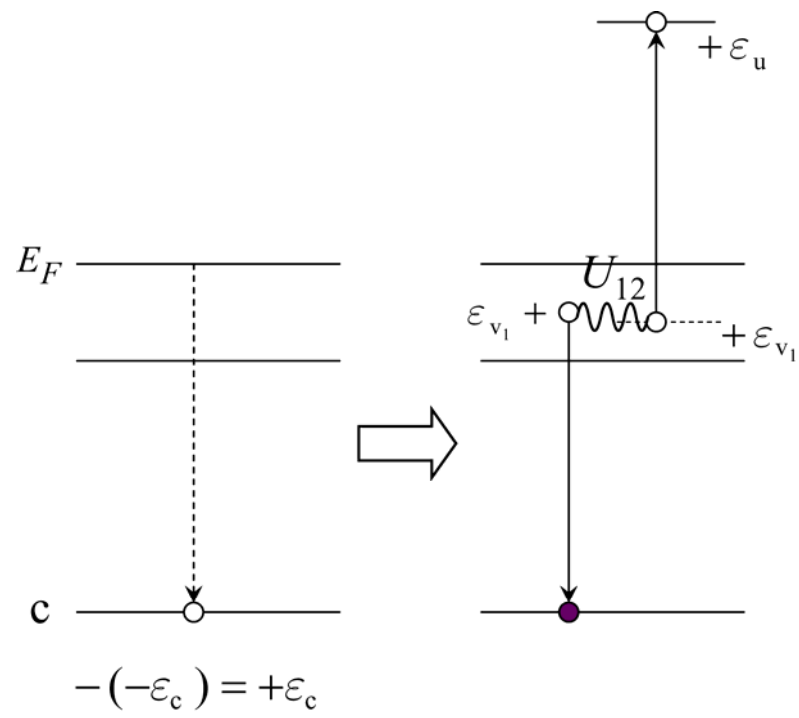


Fig. 1.37 Energy relation for MVV sCK transition.

Simplified schematic illustration of the results shown in (1.120) in the band-picture case is shown in Fig. 1.38. Suppose the core level is located at c . The valence band DOS is given as $n(E)$. If we self-convolute the valence band we expect the band as $D^\circ(E)$. Since the intra-atomic Coulomb interaction modifies the convoluted band, we expect the real spectrum is as $D(E)$. The difference of the peak of self-convoluted band $D^\circ(E)$ and that of the deformed band $D(E)$ gives the value of the intra-atomic Coulomb energy, U .

In Fig. 1.39, we show the result of the model calculation of the dependence of the spectral shape on the value of U/W , where U is the intra-atomic Coulomb energy and W is the width of the band spectra expected from (1.120) are indicated. We assumed a band with the DOS curve of the rectangular shape with a width of W . The self-convolution of the band gives us a triangular band with the half-height width of W . If the sCK band is described by the energy-band picture completely, we expect the sCK band of the rectangular shape. On the other hand, only a spectral line is expected in the complete atomic case, where U is very large. In the intermediate case, the band spectrum is deformed and atomic line is observed.

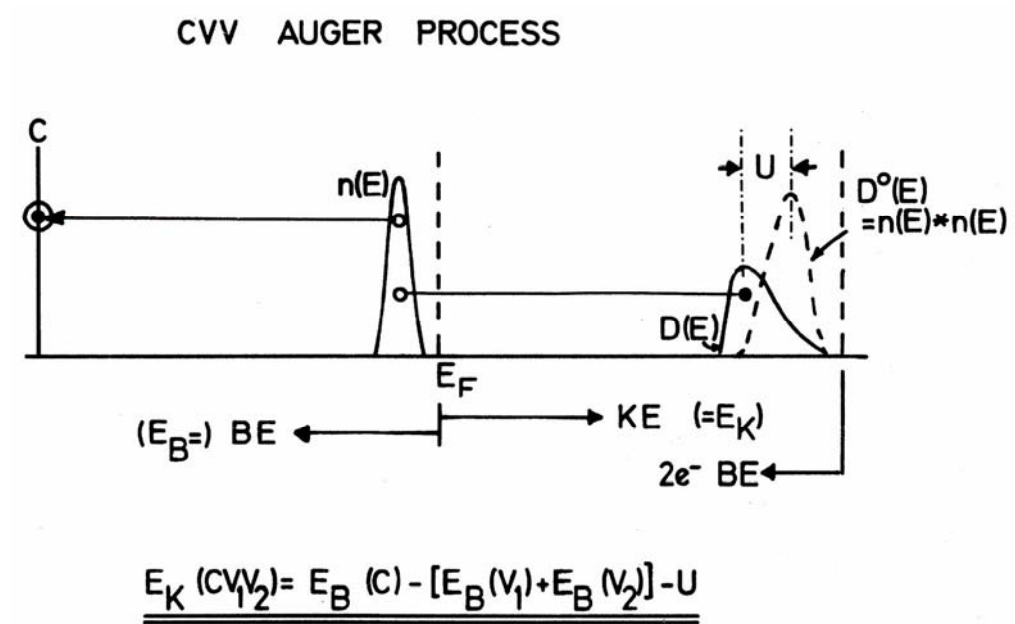


Fig. 1.38 *CVV* Auger process showing expected spectra. $n(E)$: Valence band DOS curve. $D^o(E)$: Convoluted DOS curve. $D(E)$: Expected band spectrum.
(Bennett *et al.*, 1983)

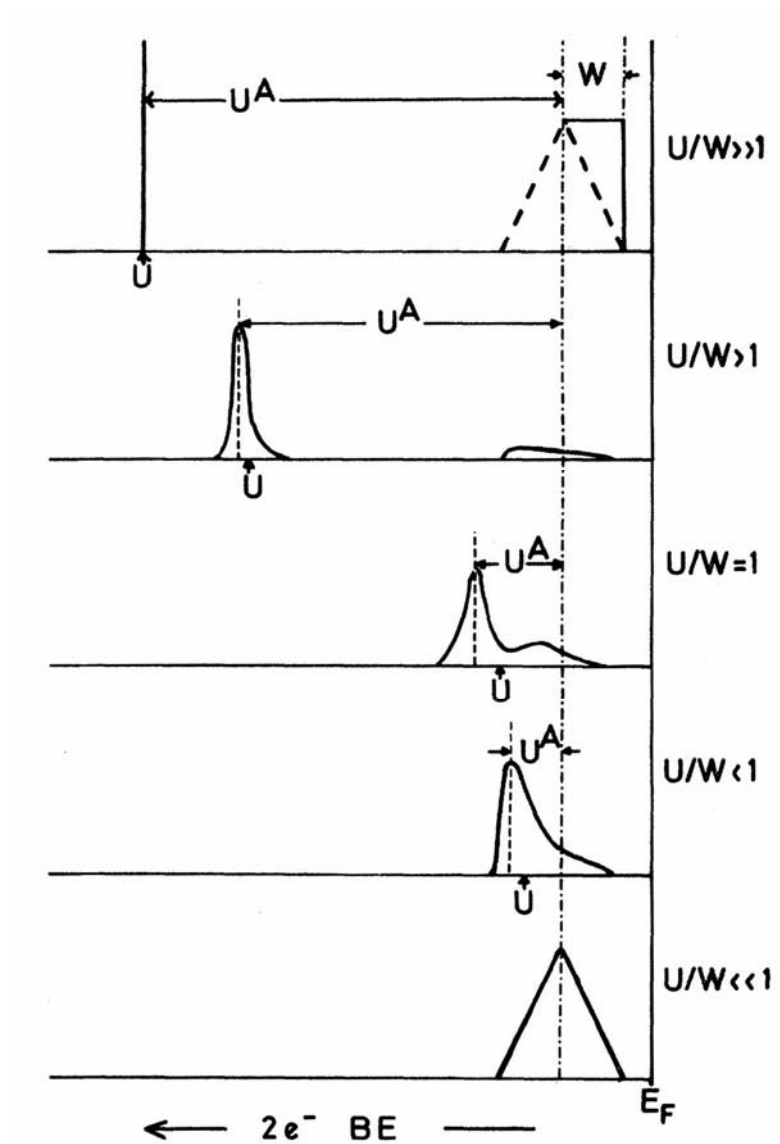


Fig. 1.39 Dependence of expected CVV Auger spectra on the magnitude of U/W . W :

Band width. U : Intra-atomic Coulomb energy. (Bennett *et al.*, 1983)

1.9 Purpose of the Research

The purposes of this thesis research are summarized as follows:

(1) The spectral shape of the two-hole-bound-state and the MVV sCK band will be studied by AIPES.

(2) The MVV sCK band spectra are analyzed using Cini-Sawatzky theory.

(3) The change in the spectral band shape of the MVV sCK band is traced.

(4) Inter-relation between the two-hole-bound-state band and the MVV sCK band is analyzed in the photon energy region where the resonance occurs.

(5) Excitation spectrum is also measured and analyzed.

(6) The total yield spectrum and the constant initial state spectrum will be measured.

(7) The surface energy-band structure of Ni(111) along two symmetry lines; $\bar{\Gamma}-\bar{T}-\bar{K}$ and $\bar{\Gamma}-\bar{\Sigma}-\bar{M}$, will be mapped. The measurements will be carried out by ARPES.

(8) The polarization dependence of the photoemission spectrum, s- and p-polarized, will be carried out by normal emission of ARPES.

CHAPTER II

EXPERIMENTAL TECHNIQUES AND PROCEDURES

This chapter describes the experimental techniques and procedures used in this thesis work. First, the outline of the experimental issues is described. Then, the preparation of the sample is mentioned. Following sections are all for description of the experimental instruments. Explanations are made on the element located along the beamline from the upstream portion to the downstream portion.

2.1 Outline of the Experiment

A sample used is a slice cut out of a single crystal of Ni(111) bought from Goodfellow Cambridge Co.,. The purity of the crystal is 99.999%. The slice was polished by an ordinary procedure. By measuring X-ray Laue patterns, we confirmed the sample surface has the orientation of (111).

We cleaned the sample surface with alcohol and pure water in an ultrasonic cleaning machine. The sample surface was further cleaned *in situ* in vacuum of 10^{-10} Torr. The final cleaning of the sample was made by the repetition of Ar^+ ion bombardment followed by baking by electron bombardment for 48 hrs. The temperature of the sample was monitored with a thermocouple fixed to the sample holder and a pyrometer to measure the surface temperature. The temperature indication of both monitors was different: When the sample holder temperature was 1030 K, the sample surface temperature was 900 K. By the Auger analyses, the

existence of foreign atoms or molecules on the sample surface such as O, S, and CO was examined. Cycles of Ar⁺ ion bombardment and baking were repeated for a month before a clean surface was obtained. The well-defined (111) surface was confirmed by measuring the low-energy electron diffraction pattern.

Photoemission measurements were performed at BL-4 of the Siam Photon Source of the National Synchrotron Research Center of Thailand. The details of the beam line were reported elsewhere (Prayoon Songsiriritthigul, Weerapong Pairsuwan, T. Ishii, and A. Kakizaki, 2003; Prayoon Songsiriritthigul *et al.*, 2004). Light from a bending magnet part of a 1 GeV storage ring was used. The light beam is focused onto the entrance slit of a monochromator with a toroidal mirror. The monochromator is of a vertical dispersion type and equipped with plane gratings of non-linear groove spacing. By using three gratings with average groove spacings of 300 lines/mm, 600 lines/mm, and 1200 lines/mm, optical measurements can be carried out over the range from $h\nu = 20$ eV to 240 eV. An intermediate slit and a focusing mirror are installed between the incident slit and the grating. A rear mirror focuses monochromatized light to a small spot on the sample surface.

Angle-integrated energy distribution curves (EDC's) of photoelectrons and Auger electrons were measured with a Thermo VG Scientific CLAM2 energy analyzer. For angle-resolved EDC measurements, a hemispherical analyzer of a different type is also installed in the analyzer chamber. The angle-resolved EDC's will be reported in this thesis.

A He discharge tube and an X-ray tube are installed in the analyzer chamber as additional light sources. The performance of the energy analyzer was measured with the He I line (21.2 eV). The spectra in the X-ray photoemission spectroscopy

(XPS) were also measured to obtain complementary data. The resolution of the energy analyzer was estimated at 234 meV from the measurement of the Fermi edge of Au by excitation with the He I line. This is the energy resolution of our system for the *MVV* sCK measurements. Since the intensity of excitation light was not high, we were not able to make the slit width narrow. The overall resolution in the photoemission measurements was 620 meV at $h\nu = 60$ eV.

Measurements of photoemission were carried out at room temperature with light incident on the sample surface at normal incidence. The electric vector of light was parallel to the sample surface. The surface condition was frequently examined and cleaned by Ar^+ ion bombardment and following baking, if the surface was degraded. The pressure in the measurement chamber was in the 10^{-11} Torr range and a clean surface lasted for about 8 hrs.

2.2 Sample Preparation

Since photoemission is a surface sensitive phenomenon, we have to prepare a clean well-defined surface in the photoemission experiments particularly in case of metallic sample. The clean surface is necessary, since the adsorption of foreign atoms or molecule alters the intrinsic nature of the surface regarding both atomic arrangement and the electronic structure.

The preparation of the good sample is really essential to carry out the correct experiments. Therefore, in this section we describe some details of the sample preparation. First we describe the procedure for the sample preparation in Fig. 2.1 in a cartoon way. We first obtain a single crystal rod with the $[111]$ crystal axis along the rod. We cut rod so that a thin sample with the (111) surface is obtained. The following

procedure is to polish the sample surface. The sample was cleaned. The cleaned sample was mounted in the sample holder and the surface was further cleaned in vacuum.

(1) Cutting out the sample

A sample used in this thesis work is a 12 mm disk of Ni(111) with 1 mm thick, which has been cut from a cylindrical rod of single crystal nickel with purity of 99.999%. The original rod was purchased from Goodfellow Cambridge Co. Ltd. The crystal had been grown in the way that the [111] direction was along the rod axis. The sample was cut out so that its surface the (111) plane. The crystal orientation was confirmed by X-ray diffraction measurements using a diffractometer at the Center for Scientific and Technological Equipment at the Suranaree University of Technology. The cutting was done using a Struers ACCUTOM-5 cutting machine with a diamond cutting wheel. The picture of the machine is shown Fig. 2.2. A good surface was obtained by properly choosing the speed of the cutting wheel and reducing the cutting rate.

(2) Surface polishing

The Ni(111) disk was then manually ground on a silicon carbide grinding paper. This procedure was necessary to remove rough step-wise structure. The surface was carefully polished so that the surface orientation was not changed from that of (111). After this polishing work the sample was further polished using a Struers ROTOPOL-25 polishing machine with a Struers ROTOFORCE-1 force control. The picture of the polishing machine is shown in Fig. 2.3. A diamond suspension plate was used for polishing in the initial grinding step. The grain size of diamond was changed according to the flatness of the surface which changed the coarse state to the

fine state. Practically, we started with grain size of 6 μm and then reduced the size to 3 μm and finally to 1 μm . A finer grinding step followed the polishing with diamond grains was carried out using alumina abrasive with distilled water as lubricant. Two kind of alumina abrasive were used. One had a grain size 0.3 μm and the other of 0.1 μm . In the last grinding step, we used silica of 0.04 μm grain size as abrasive. The polishing was completed when a surface like a spectrum no scratch was obtained. After the procedure of polishing the sample surface had been completed, the sample was cleaned by ultrasonic cleaning. In addition to the physical removing of the layer of adsorbed molecules by ultrasonic vibration, some liquid solvents were used to remove organic compounds sticking to the surface. The solvents used were acetone and ethyl-alcohol. Finally distilled water was used. These three kinds of liquid were used in the tub of ultrasonic cleaning machine as media to transform the ultrasonic vibration.

After polishing and ultrasonic cleaning, the sample was fixed to a molybdenum sample holder. The sample surface was further cleaned vacuum in the sample preparation chamber of the photoemission measurement system in the experimental station of the BL-4 beamline.

When the surface of a crystalline metal is clean, two different methods are used in sequence. One is described in the preceding subsection. The other is the Ar^+ ion sputtering and heating in vacuum. The Ar^+ ion sputtering is performed by discharge around the sample in Ar gas in the way that the sample surface is bombarded by Ar^+ ions formed by the discharge. Molecules adsorbed on the surface are sputtered off by the bombardment of Ar^+ ions. Ar^+ ions injected into the sample are removed by the subsequent heating of the sample. The Ar^+ ion sputtering is quite

effective to remove foreign atoms or molecules adsorbed on the surface. However, impurities contained in the bulk of the sample cannot be removed by this method.

In the interior of the sample impurity atoms such as O, C, and S are contained. They are incorporated into the metal during the course of crystallization process. In case of O atoms, for example, they emerge from the bulk onto the surface slowly. On the surface they form metal oxides or combine with hydrogen in the residual gas in the sample chamber to generate H_2O . At high temperature H_2O molecules are desorbed. Or we can remove the molecules by Ar^+ ion sputtering at appreciably high temperature, the metal oxides are decomposed. In case of C, compound such as CO and CO_2 are formed. In case of S, the processes occur in the heating and sputtering is similar to the case of O. Since impurity atom in metals move very slowly, it takes a horribly long time to remove impurity atoms and obtain a clean surface.

The cleaning procedures in vacuum were made by a repetition of Ar^+ ion sputtering followed by electron bombardment heating. During the course of the cleaning in vacuum, the sample surface was examined by measuring the Auger spectrum. Since the energy of the Auger lines are characteristic of the elements. By measuring the Auger lines, atoms existing on the sample surface are identified. The repeated cleaning of the surface by the Ar^+ ion sputtering and the subsequent heating in vacuum was continued until no detectable surface impurity was observed. The temperature of the sample was monitored with a thermocouple fixed to the sample holder and a pyrometer. The temperature at the surface of the Ni(111) sample measured by the pyrometer during heating was 900 K. Indication of the thermocouple was 1030 K.

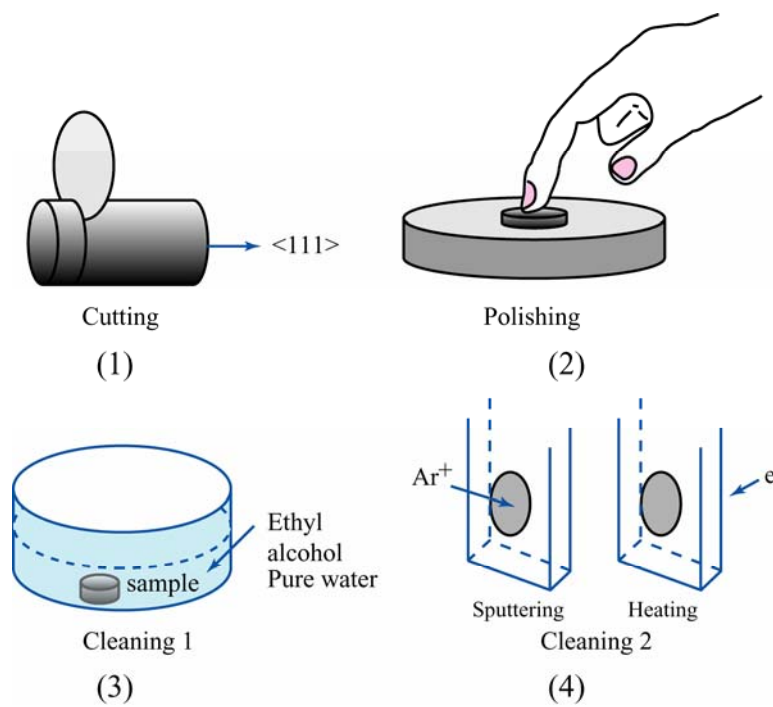


Fig. 2.1 Procedure of the sample preparation. (1) Crystal rod sample with (111) surface is cut out of a single crystal rod. (2) The surface is polished. (3) The sample is cleaned in a solvent. (4) The sample is further cleaned in vacuum.



Fig. 2.2 Cutting machine model ACCUTOM-5 from Struers Co.



Fig. 2.3 Polishing machine model ROTOPOL-25 with a force control option model ROTOFORCE-1 from Struers Co.

Fig. 2.4 shows Auger electron spectra taken from the Ni(111) sample before and after cleaning by cycles of Ar^+ sputtering and heating. The main impurities on the surface were carbon, nitrogen and oxygen atoms as shown in Fig. 2.4a. Sulfur was also observed (not shown in the figure) to be the impurity. It took a long time to suppress the S line below the detection limit of the instrument used here. Sulfur was from the bulk and segregate to the surface of the sample as mentioned already. The *LMM* CK spectrum measured on the clean surface is shown in Fig. 2.4b.

The clean and well-defined (111) surface was also confirmed by the low-energy-electron-diffraction (LEED) measurement. The LEED pattern reflects the atomic arrangement of the surface. If the surface is contaminated, we cannot obtain a clear diffraction pattern. Therefore, the LEED pattern also makes the good indication of the perfectness of the surface. Fig. 2.5 shows the LEED patterns of the contaminated and clean Ni(111) surface. It has been found that the clean and well-defined surface is maintained at a pressure of 10^{-10} mbar for approximately 8 hours before the degradation of the surface occurs. The deterioration of the surface was caused by the adsorption of residual gas molecules. Thus, the sample has been cleaned from time to time during photoemission experiments in the present thesis work.

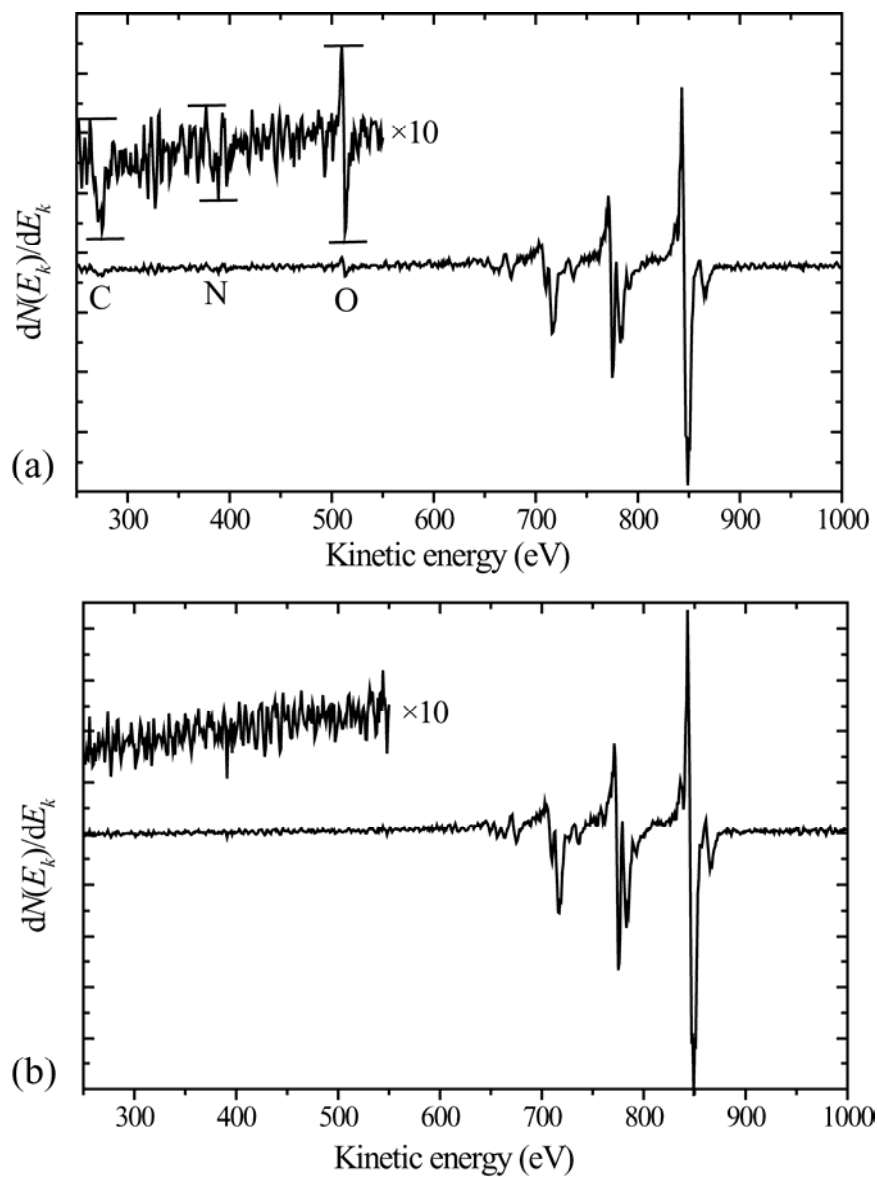
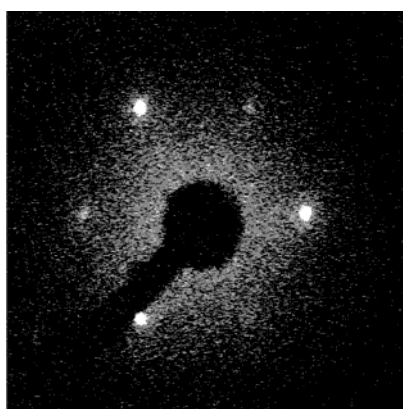
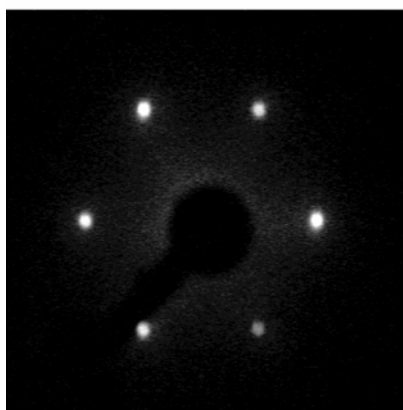


Fig. 2.4 Auger spectra of Ni(111) surface. (a) Contaminated surface and (b) Clean surface. Lines showing up in the region between 700 and 850 eV are those of the *LMM* CK lines of bulk Ni.



(a)



(b)

Fig. 2.5 LEED patterns of Ni(111) surface. (a) Contaminated surface. (b) Clean well-defined surface.

2.3 Light Sources

In the present thesis work, three different types of photoemission experiments were carried out. The main experiment is one made using synchrotron radiation. With synchrotron radiation the excitation energy dependence of the spectral shape of EDC investigated in relation to the $3p-3d$ resonance and the MVV sCK transition. The dispersion curves of surface energy-band have also been measured by APRES using synchrotron radiation. The second type measurements are ultraviolet photoemission spectroscopy (UPS) using excitation light from a He discharge lamp. These measurements were auxiliary ones for adjusting the energy analyzer. The third type was X-ray photoemission spectroscopy (XPS) using the Mg $K\alpha$ light. The data used to obtain information on the core level lines.

In this way, we used three different types of light source. In what follows, we briefly explain the light sources used here.

2.3.1 Helium Discharge Lamp

A gas discharged lamps used in spectroscopic measurements is usually a hollow cathode type. The cathode has a shape of a cylinder in which glow-discharge occurs. In the gas discharge lamp used in photoemission measurements of solid materials the essential condition to be fulfilled is differential pumping. The sample side of the vacuum chamber must be evacuated to ultrahigh vacuum. The pressure there must be below 10^{-8} mbar. On the contrary, the pressure must be as high as 0.1 mbar. Therefore the lamp should be equipped with a device called the differential pumping system to maintain the pressure difference. It is evident that we cannot use a

diaphragm to isolate the discharge lamp in vacuum, because it reduces or completely cut off light generated by the discharge.

The second condition imposed is that the discharge is preferably compressed in a narrow area. This increases the light intensity (radiation density) considerably. In the He lamp used in the present studies, the discharge occurs in a capillary tube.

The third condition is that positive ions, He^+ , do not strike the optical element, *i.e.*, the first mirror if any. In the present case no mirror is used. Therefore the target is the sample surface. If the sample surface is bombarded with He^+ ions, the surface is degraded easily. This is avoided if the polarity of the dc discharge is arranged so that the anode is installed at the position nearer to the light outlet. In this case, ions are accelerated to the direction opposite to the light exit. The He discharge lamp used in the present studies is designed in this manner.

The He discharge generates two spectral lines with photon energy at 21.2 eV and 40.8 eV. The 21.2 eV line has a width of 2 meV. Because of this narrow width the He discharge lamp is conveniently used as an excitation source for photoelectrons.

Fig. 2.6 shows the schematic illustration of the He discharge lamp used in the present studies. Discharge occurs in a narrow hollow tube. Discharge starts at a high voltage of 5 kV. As soon as the discharge is maintained, the cathode voltage is reduced to 600 V. The diaphragm with a small hole as the light passage separates two evacuation chambers. Through the resistance of the small hole, the pressure difference is introduced. Light is taken out of the second pumping stage through a capillary. The amount of gas, Q , flowing out the capillary tube is given by

$$Q = a\Delta pS / l \quad (2.1)$$

Here Δp is the pressure difference across the tube, S the cross section, l the length and a is proportionality constant. Since S is small and l is large, Q is small. Thus ultrahigh vacuum (UHV) is maintained in the analyzer chamber. The alignment of two capillary tubes must be made accurately. Otherwise light does not come out. The head of the capillary tube comes near the sample surface.

2.3.2 X-ray Tube

The X-ray source used here is a head-on anode type. The original tube of this type is called the Henke tube after the name of the inventor. Since a high voltage is applied between electrodes in X-ray tube, the tube occupies a wide space in a vacuum chamber if the tube is of the type in which X-rays are taken out of the tube. The head-on type X-ray tube is convenient in that it does not occupy a wide space and the anode of the X-ray tube can be located near to the sample surface

The anode is water-cooled. This cooling water is highly electrical insulating. Since we use a positive anode voltage, we must use pure water with high electrical resistance. This water line forms a closed line. In the X-ray tube of the head on type, many elements are installed in a narrow space and good electrical insulation among different coaxial types in the X-ray tube is quite important.

The schematic illustration of the X-ray tube is shown in Fig. 2.7. The filament works as the cathode which is grounded. The space around the cathode (filament) is surrounded with a shield case for focusing. The electric field formed by the anode and the shield case is such that accelerated electrons make a focusing beam. Then the electron beam bombards a narrow area on the anode face. As a result, the beam density at the bombarded area is high and the source is near the point source.

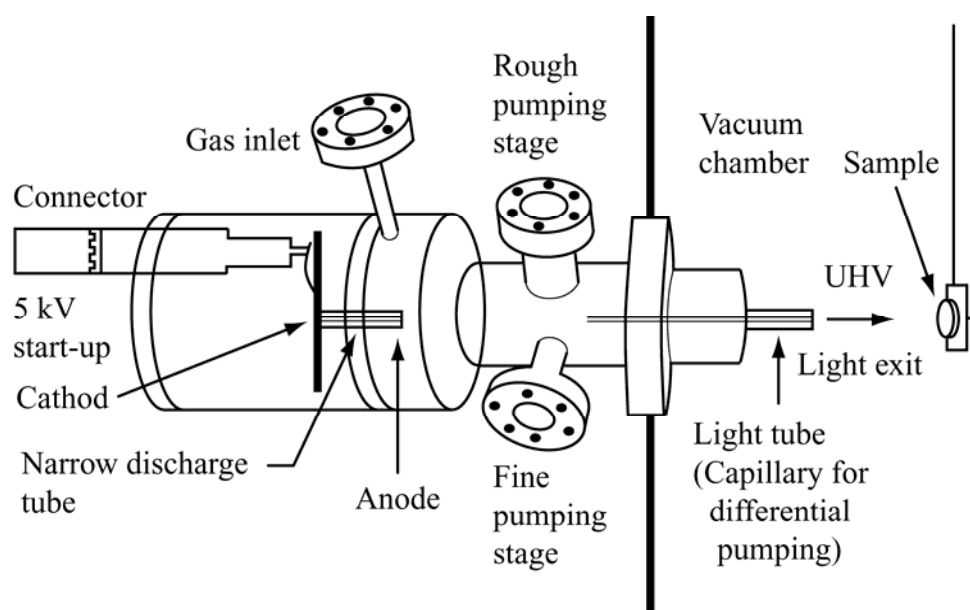


Fig. 2.6 Schematic illustration of UV discharge lamp showing the operation principle.

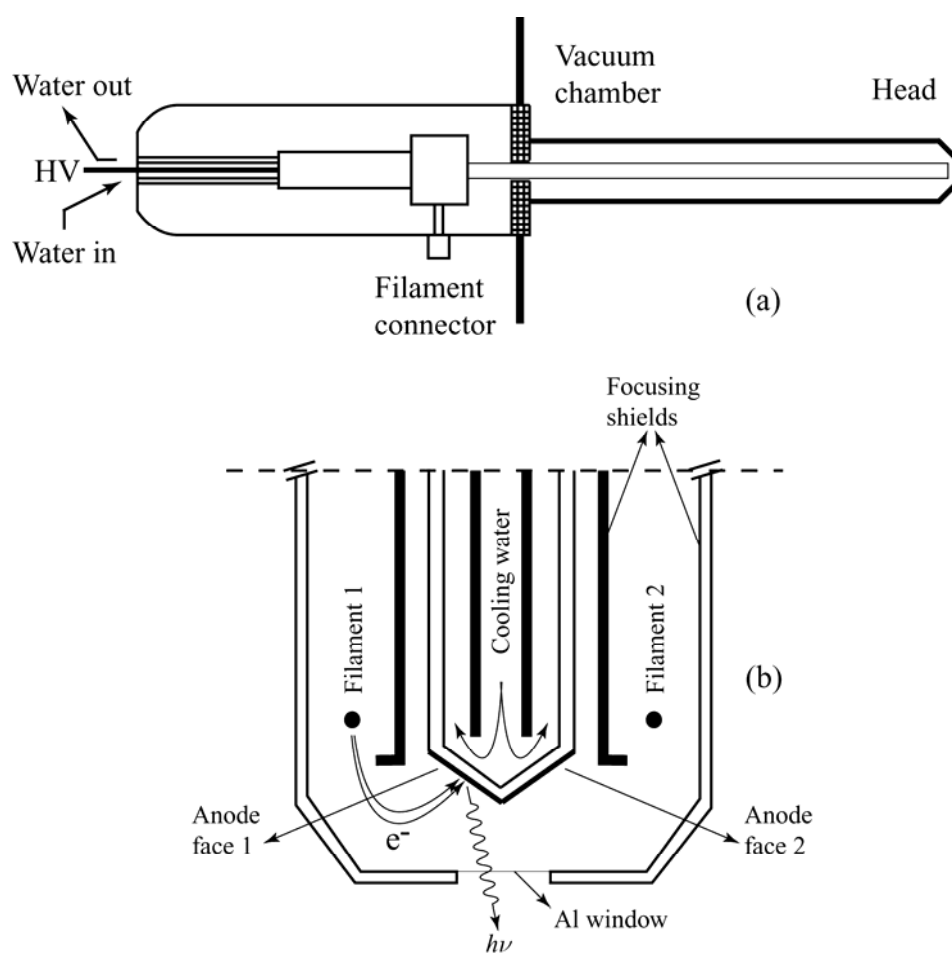


Fig. 2.7 Schematic diagram of a dual-anode X-ray source. (a) Overall feature (b) Head portion.

The filament has a rod form. It is made of a material with high emissivity, such as LaB₆. The acceleration voltage is 15 kV. The anodes are made of Mg and Al metals. X-rays we used is the Mg $K\alpha_{1,2}$ line. The energy is 1253.6 eV and the natural line width is 0.8 eV.

2.3.3 Synchrotron Light Source

Synchrotron light is an electromagnetic wave emitted from relativistic charged particles moving with a curve motion. A synchrotron light consists of two main parts, *i.e.*, the injection system and storage ring. The synchrotron light source used in this thesis work is the Siam Photon Light (SPL) source at the National Synchrotron Research Center (NSRC) of Thailand as shown in Fig. 2.8. The injection system consists of a linear accelerator and a booster synchrotron. The injection system produces a beam of electrons with energy up to 1 GeV and then injects into the storage ring. The machine parameters of the storage ring are shown in Table 2.1. The storage ring comprises of a series of magnet lattices, which are designed to keep electrons circulating in the vacuum chambers of the storage ring. In the bending magnet, synchrotron light is emitted when electrons are experienced with the Lorentz force due to the presence of a dipole magnetic field perpendicular to the electron orbit.

Utilization of synchrotron in photoemission measurements expands the scope of many research fields. This is because of the special properties of synchrotron light together with the development of beamline instruments. The properties of synchrotron light which enhance the capability of photoemission technique are given in Chapter I.

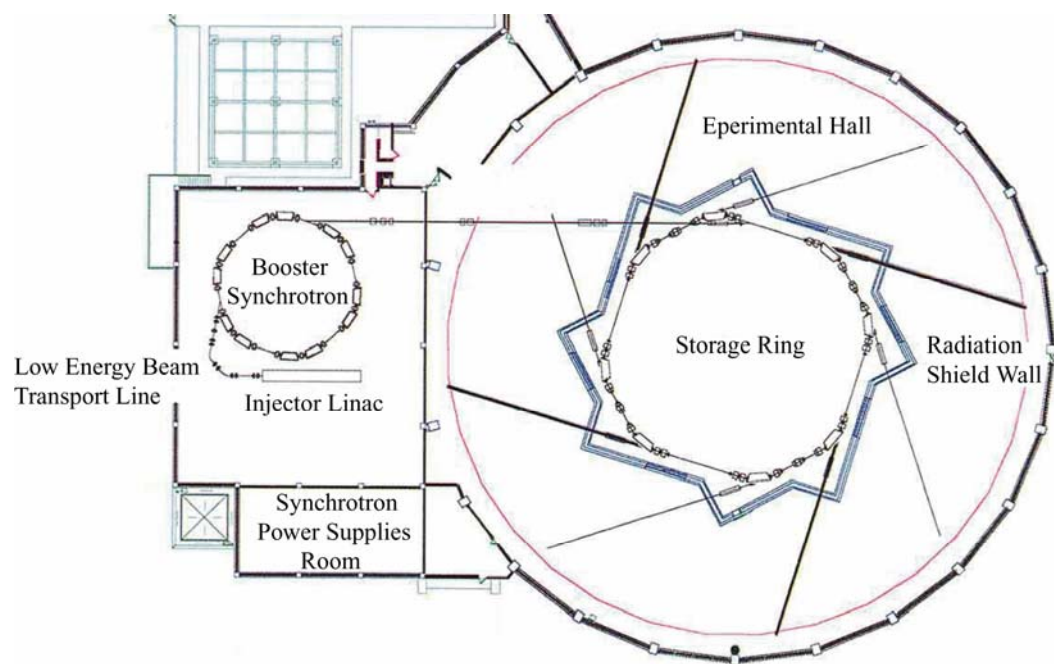


Fig. 2.8 The magnet arrangement of the storage ring of the Siam Photon Source.

Table 2.1 The machine parameters of the storage ring of the Siam Photon Source.

Parameters of the storage ring	
Electron energy	1.0 GeV
Circumference	83.1 m
Magnet lattice	Double bend achromat
Super periodicity	4
Long straight section	7 m \times 4
Betatron wave numbers, ν_x / ν_y	4.71 / 2.78
Momentum compaction factor, α	0.0241
Natural emittance	72 π nm.rad
Natural chromaticities, ξ_x / ξ_y	-7.96 / -6.45
RF voltage, V_{RF}	120 kV
RF frequency, f_{RF}	118 MHz
Harmonic number, h	32
Energy spread	5.02 $\times 10^{-4}$
Energy loss per turn	31.8 keV
Synchrotron oscillation frequency, f_s	13.5 kHz
Critical energy of SR, ε_c	798 eV
Bunch length	135 ps
Beam sizes, σ_x / σ_y	0.94 / 0.15 mm
Damping times, $\tau_x / \tau_y / \tau_z$	18.9 / 17.0 / 8.1 ms

2.4 Optical Beamline

Photoemission measurements reported in this thesis were carried out at the BL-4 beamline at the Siam Photon Laboratory of the National Synchrotron Research Center (NSRC) of Thailand, shown in Fig. 2.9. The beamline was developed for the investigation of electronic structures of solids using photoemission technique. The beamline employs a varied line-spacing plane grating (VLSPG) monochromator, which provides photons with energy between 20-240 eV (Prayoon Songsiriritthigul *et al.*, 2003; Prayoon Songsiriritthigul *et al.*, 2004). The experimental station of the BL-4 beamline is a photoemission system which allows angle-resolved and angle-integral photoemission measurements to be carried out. The measurements can be performed using either synchrotron light or laboratory excitation sources.

The optical layout of the BL-4 beamline is illustrated in Fig. 2.10. The optical beamline consists of a pre-focusing toroidal mirror (M0), a VLSPG monochromator and a post focusing toroidal mirror (M2) (Prayoon Songsiriritthigul *et al.*, 2001). The beamline utilizes light from a BM4 bending magnet of the storage ring. Synchrotron light with acceptance angle of 5 mrad and 3 mrad for the horizontal and vertical directions respectively is used for the BL-4 beamline. The monochromator comprises of an entrance slit (S1), focusing mirror (M1), an aperture, three exchangeable VLSPG and an exit slit (S2). The three exchangeable gratings with the line density at the center of the grating of 300, 600 and 1200 lines/mm are used to provide photon energy ranges of 20-80, 40-120 eV and 80-240 eV respectively. The detailed specifications of the gratings are given in Table 2.2.

The advantage of this type of monochromator is that scanning of photon energy can simply be done by rotating the grating. For the whole photon energy range,

the monochromatic light is focused virtually at the position of the exit slit, S2. Thus, no movement of the exit slit along the optical axis is necessary when photon energy is changed. The post-focusing toroidal mirror M2 is used to re-focus the monochromatic light on the sample.

Table 2.2 Parameters of the gratings used in the BL-4 beamline.

Grating No.	N_0 (lines/mm)	Groove depth (nm)
VPG-1	300	43
VPG-2	600	22
VPG-3	1200	12

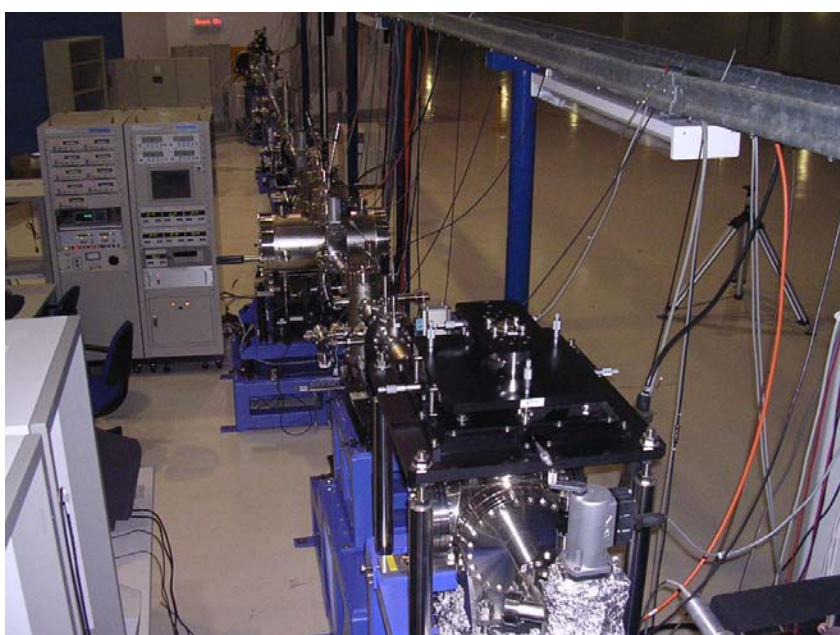


Fig. 2.9 The photo shows the BL-4 optical beamline of the Siam Photon Laboratory.

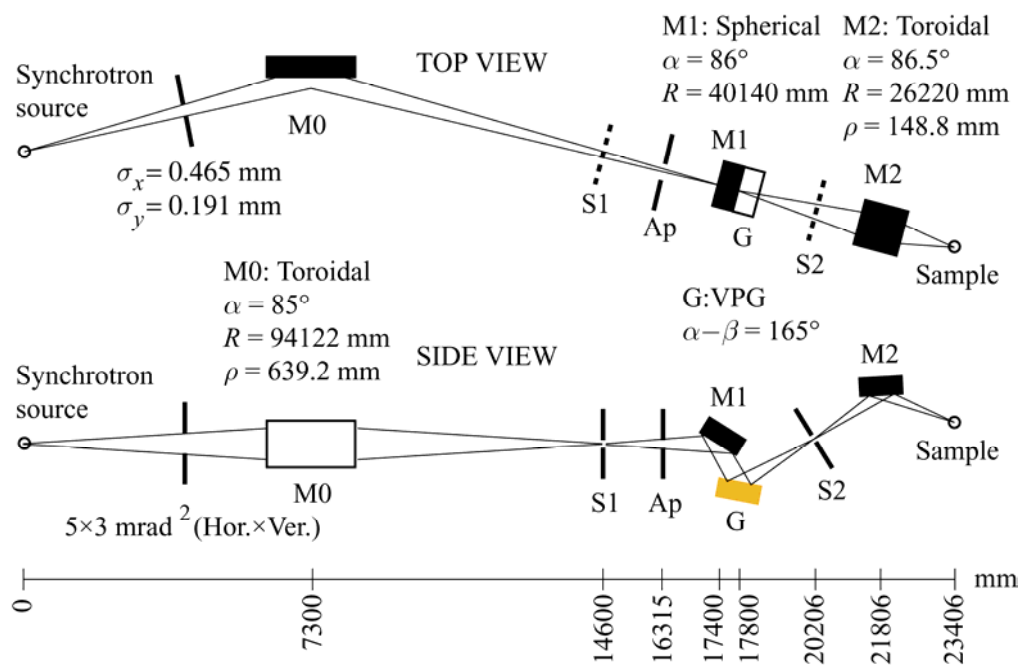


Fig. 2.10 The optical layout of the BL-4 beamline at the Siam Photon Laboratory.

2.5 Experimental Station

The experimental station of the BL-4 is a photoemission system shown in Fig. 2.11. Both angle-resolved and angle-integral photoemission experiments can be performed. The experimental station consists of three main ultra-high vacuum (UHV) chambers, *i.e.*, an analysis chamber, a sample preparation chamber and a load-lock chamber.

2.5.1 Vacuum Chamber

Photoemission measurements have to be performed in a UHV environment. A μ -metal chamber is normally used to enclose the UHV environment because it can also reduce the disturbance of the trajectory of photoelectrons by external magnetic fields, *e.g.*, earth magnetic field. With modern vacuum technology, a proper-designed vacuum system can reach vacuum pressure in a range of 10^{-10} mbar or better. Most of modern photoemission systems employ a sputter ion pump combined a titanium sublimation, to produce a UHV environment. Baking of photoemission systems is essential to remove desorbed gas molecules on the interior surface vacuum chamber and the surface of tools in the vacuum system. The baking is normally done at 150°C for at least one day

The three chambers are vacuum-isolated by gate valves as illustrated in Fig. 2.12. The availability of the preparation system allows *in situ* analysis of samples treated in the preparation system. UHV environment is essential as photoemission is a surface sensitive technique. Breaking of UHV condition of the analysis chamber is avoided as the load-lock system is employed. Two ion pumps and two titanium sublimation pumps are used to obtain UHV in the preparation and analysis chambers

with typical based vacuum pressure of $\sim 2 \times 10^{-10}$ mbar. A turbo-molecular pump is used for extra pumping during cleaning surface of samples and for loading samples into the analysis chamber. The analysis chamber is connected to the end of the optical beamline via a line-of-sight valve. This provides possibility to disconnect the experimental station from the beamline without breaking the vacuum condition.

Investigations of gas species generated in the photoemission system of the BL-4 beamline prior to photoemission studies of Ni(111) (Wiwat Wongkokua and Prayoon Songsiriritthigul, 2005). That was essential since photoemission is a very surface-sensitive technique and that a good vacuum condition is required. The base pressure in the analysis chamber is $\sim 2 \times 10^{-10}$ mbar. The residual gases are H_2 , CO/N_2 , CO , H_2O and CH_4 . However, it was found that the vacuum pressure increases one order of magnitude when there is a linear movement of the sample manipulator. Laboratory excitation sources also cause the increase of the vacuum pressure, as shown in Figs. 4-7 in the paper, which deteriorates the quality of the results due to the accumulation of contamination of the surface of the sample. Synchrotron light allows photoemission measurements to be performed at the base pressure.

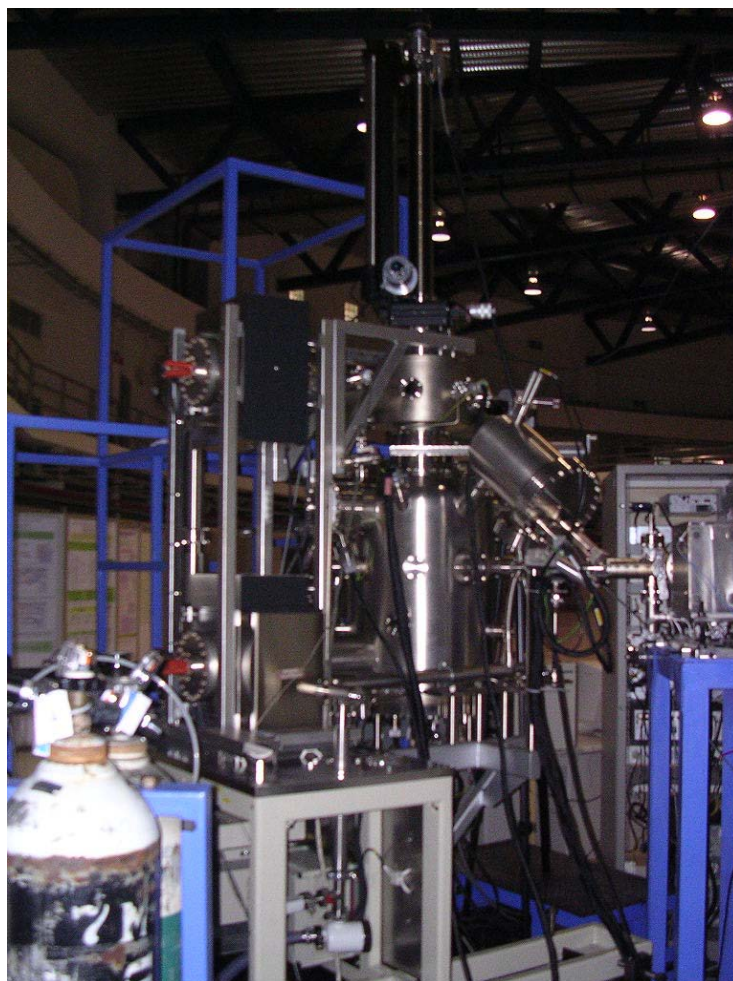


Fig. 2.11 Photoemission system shown above is an experimental station of the BL-4 beamline.

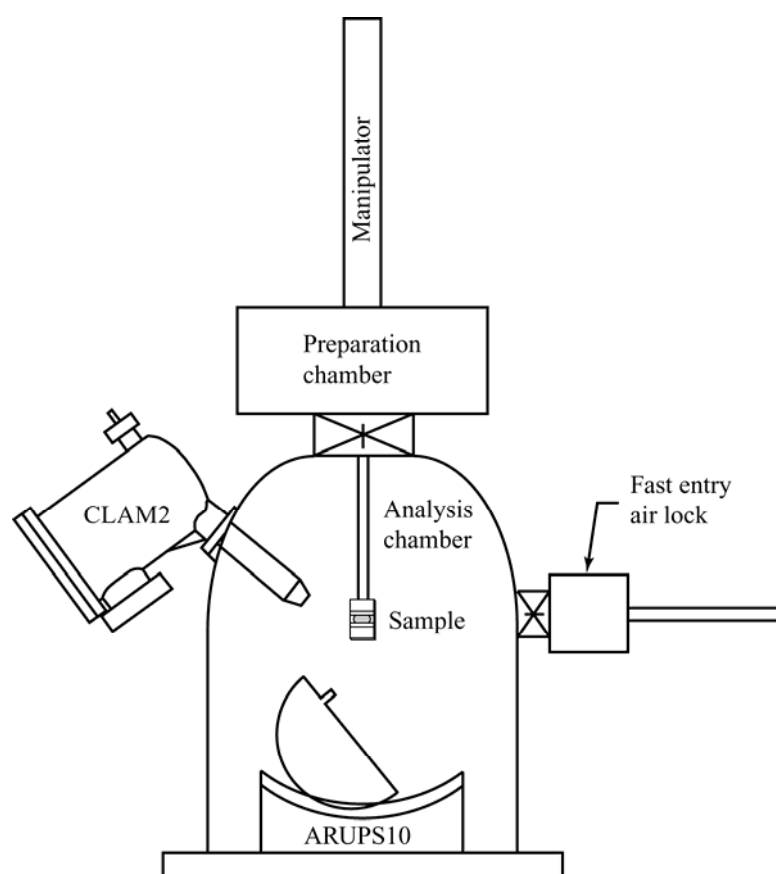


Fig. 2.12 Schematic diagram of the photoemission system. CLAM2 and ARUPS10 energy analyzers are the main instruments.

2.5.2 Sample Holder

Manipulator is normally used to position and align the sample with respect to the angle of incidence of excitation light and the angle of emission of photoelectron. The manipulator may be equipped with heating and cooling facilities to control the temperature of the sample. Heating of sample can be done by either direct heating or electron bombardment. With proper designed and constructed, sample temperature up to 1200°C can be obtained. With advanced cryogenic technology, sophisticated manipulators allow samples to be cooled down to nearly the absolute zero temperature (~ 100 K). The sample holder is shown in Fig. 2.13.

2.5.3 Energy Analyzer

Different types of energy analyzer have been developed in the past. It is agreed among scientists in the field of electron spectroscopy that a concentric hemispherical analyzer (CHA) is the most suitable type for photoemission studies. This type of analyzer provides important features such as high-energy resolution, high transmission and compatibility to UHV. In addition, an electron static lens can be integrated into the analyzer allowing longer working distances and controllable size of the analyzed area.

The analysis chamber is equipped with two CHA electron energy analyzers manufactured by Thermo VG Scientific (U.K.). The two analyzers are an ARUPS10 analyzer and a CLAM2 analyzer.

2.5.3.1 ARPES Analyzer

ARUPS10 is a hemispherical analyzer with a mean radius of 75 mm. The analyzer is installed on a goniometer allowing the rotation of the analyzer around the sample position. Thus, the ARUPS10 analyzer is used for angle-resolved photoemission measurements. The specifications of the ARUPS10 analyzer are summarized in Table 2.3.

Table 2.3 Specification of the ARUPS10 analyzer.

Analyzer	75 mm mean radius, hemispherical, 180° with 30 mm hemisphere gap
Lens	Multi-element, electronically switchable acceptance angle from $\pm 0.4^\circ$ to $\pm 2.00^\circ$ ($\pm 0.2^\circ$ with point source and lens switched off)
Detector	Multi-channel plate electron multiplier (MCP)
Goniometer	2-axis: 360° polar rotation, >90° azimuthal rotation, 0.1° vernier readouts
Chamber	5 mm thick μ -metal vacuum envelope

2.5.3.2 CLAM

CLAM2 analyzer is a 150° spherical sector energy analyzer with a mean radius of 100 mm. It is used for angle-integral photoemission measurements. The controller of the analyzer provides different mode of measurements. Thus the CLAM2 analyzer is not only used for photoemission measurement but also AES measurements. The specifications of the CLAM2 analyzer are summarized in Table 2.4.

Table 2.4 Specification of the CLAM2 analyzer.

Analyzer	100 mm mean radius, 150° spherical sector
Lens	Two element transfer lens can be used in two distinct modes
Detector	Pulse counting, single-channel electron multiplier
Working distant	Flange to sample distance, 240 mm
Housing	μ -metal

Fig. 2.14 shows a schematic of CLAM2. An electrostatic lens, which consist with two elements, is used to define the optics of electron emitted from the sample and be transported to the entrance slit of the analyzer. Before electrons entering the entrance slit, they experience a retarding or accelerating voltage to allow electrons with desired kinetic energy to pass through the analyzer and detected by the detector, which is located behind the exit slit. The resolution is defined by the pass energy. The electron-energy distributions are obtained by measuring the electron detected by the detector as a function of the retarding or accelerating voltage.

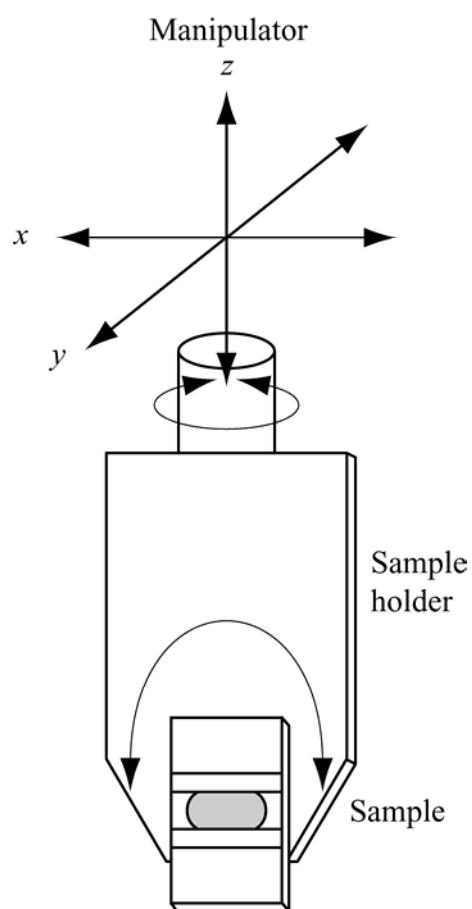


Fig. 2.13 Azimuthal and polar rotation and translational movements of the sample controlled by the manipulator.

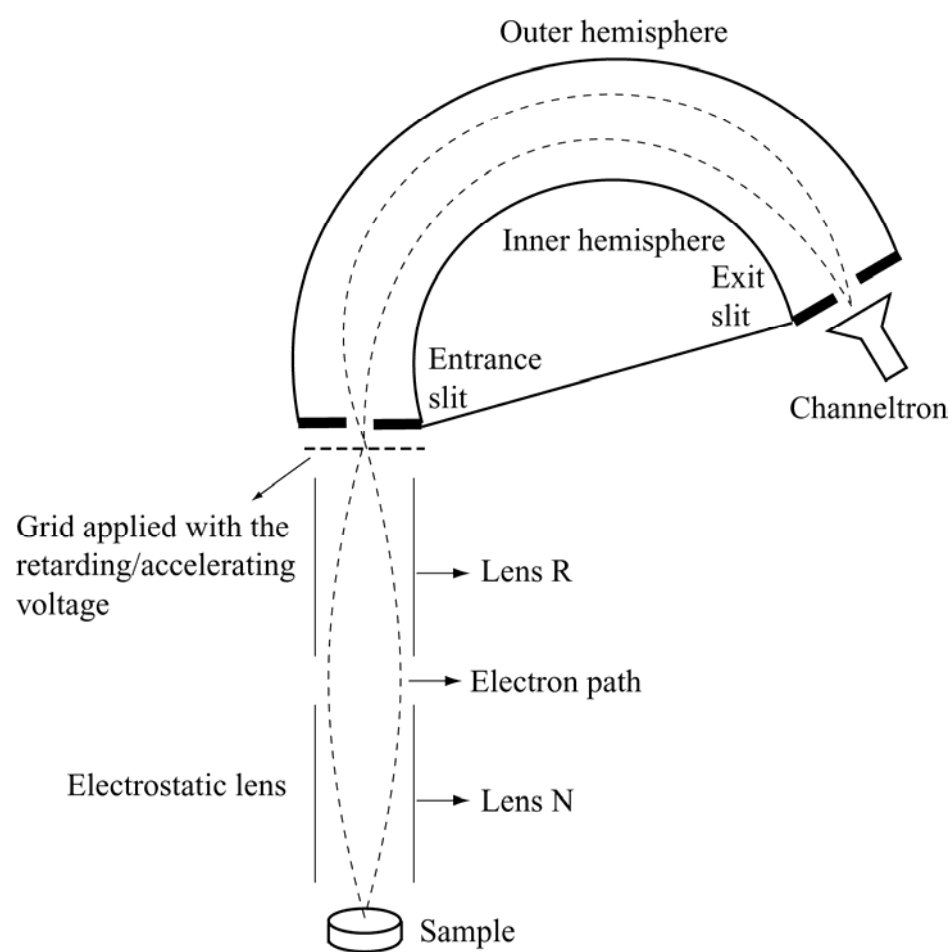


Fig. 2.14 Schematic diagram of CLAM2 with an electrostatic lens.

2.5.4 Electron Gun

Fig. 2.15 shows a schematic diagram of the electron gun used for the AES measurements. The electron gun is LEG63 form Thermo VG Scientific (U.K.). The LEG63 is a medium resolution 5 keV electron source designed for pulse-counting Auger electron spectroscopy. The gun consists of a filament, grid, lenses, apertures, and scanning quadrupoles. The spot size is less than 50 μm at 10 nA. The recommended working distance is 60 mm.

For AES measurements, the sample is located just in front of the CLAM2 analyzer. A cone of Auger electrons emitted from the sample with appropriate kinetic energy pass through the entrance and exit slits of the analyzer when the potential difference is applied to the hemispheres. A channeltron located after the exit slit is used to detect the electrons. Electron-energy distributions can be obtained by slowly sweeping the analyzer deflection voltage of the hemispheres.

2.5.5 Ion Gun

The ion gun is an instrument for the sample cleaning by ion sputtering technique. The EX03 from Thermo VG Scientific (U.K.) was used in this thesis work. The gases species can be used for this model of ion gun are Ar, He, Ne, Kr, and Xe. We selected the Ar gas for the sample cleaning processes. The energy of the gun can be varied between 300 eV to 3 keV. The Ar gas can be fed into the ion gun via a needle valve. The working distant is 100 mm but it can be in the range of 50-200 mm. The operating pressure should be less than 1×10^{-5} mbar. A schematic diagram of the EX03 ion gun is shown in Fig. 2.16.

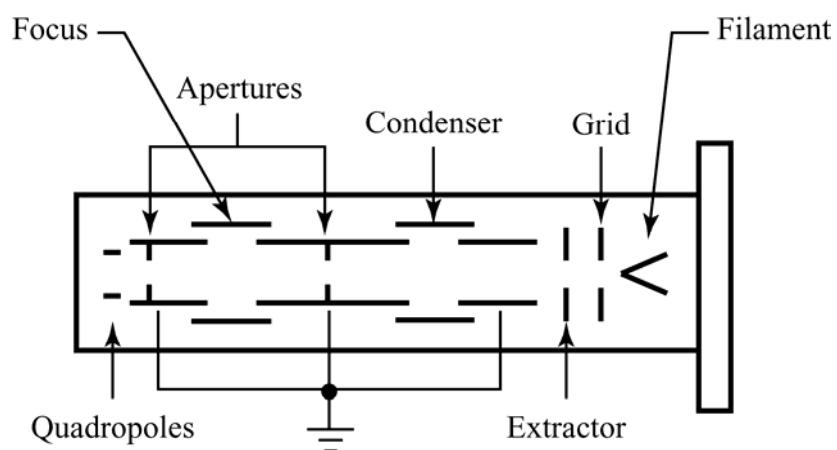


Fig. 2.15 Schematic diagram of the LEG63 electron gun.

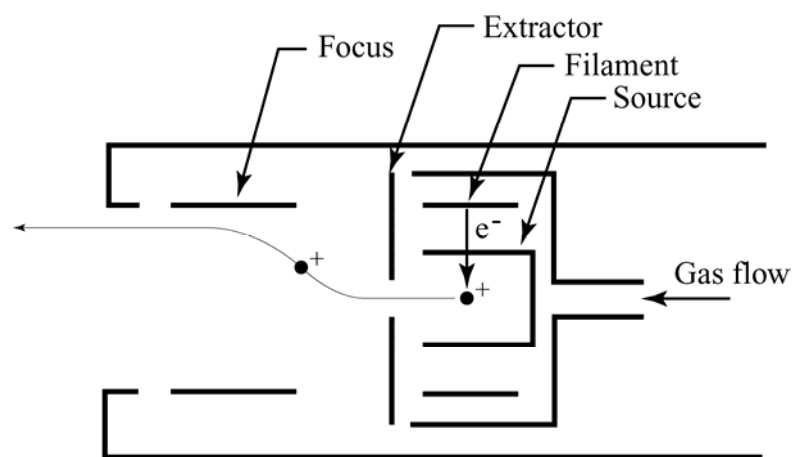


Fig. 2.16 Schematic diagram of the EX03 ion gun.

2.5.6 LEED System

Low-energy electron diffraction (LEED) has long been used as an analysis to determine crystal surfaces ordering. In this technique, a beam of electrons with energy in the range 20-500 eV are used as a probe because of their de Broglie wavelength is less than typical inter-atomic spacings $\sim 1 \text{ \AA}$ (corresponding to the kinetic energy of an electron: $E = (h/\lambda)^2 / 2m \cong 150 \text{ eV}$). More importantly, this energy is the region around the minimum of the universal curve of electron mean free path. When electrons with energy in the range 20-500 eV are elastically backscattered from a crystal surface, they will form a Fraunhofer diffraction that is the Fourier transform of the surface atom arrangement.

Fig. 2.17 shows a schematic diagram of the experimental set-up for LEED measurements. The instrument is RVL-900 rear view LEED incorporating the LEG24 high current miniature electron gun from Thermo VG Scientific (U.K.). The electron gun can be operated over the energy range from 5 to 1000 Volts for LEED measurements. In addition, the RVL-900 can be set up for AES measurements for the energy range 0 to 3 kV.

The measurements are normally carried out in an ultra-high vacuum environment (10^{-9} mbar or better) to attain well-defined surface condition. To observe LEED pattern, a crystal with clean and well-defined surface is placed normal to the LEED screen, which is a fluorescent screen. The grids with proper bias voltage located in front of the fluorescent screen prevent electrons that are inelastically backscattered from the crystal to reach the screen. The voltage difference between the screen and the grid located just in front of the screen accelerates the elastically backscattered electrons to hit the screen.

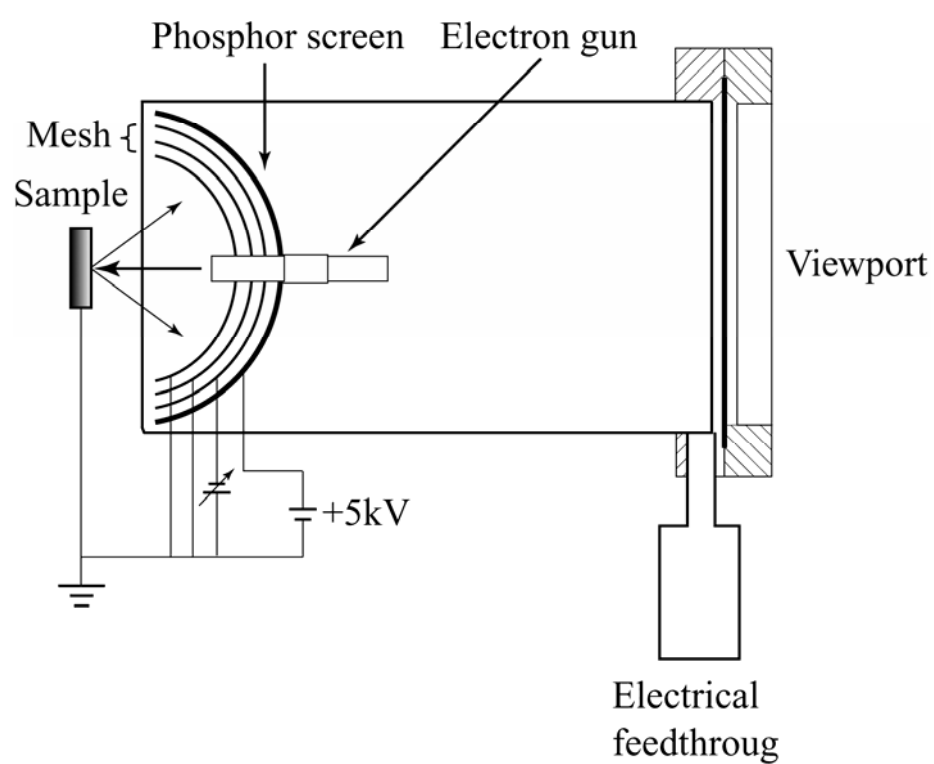


Fig. 2.17 Schematic diagram of rear view LEED set-up.

2.6 Photoemission Measurements

The work function of the electron energy analyzers has been determined from gold spectra using He I radiation. The work functions were 4.27 and 4.30 eV for the CLAM2 and the ARUPS10 respectively. The overall resolution of photoemission measurement at room temperature was also determined to be 234 and 278 meV for the CLAM2 and ARUPS10 analyzers, as shown in Fig. 2.18 and Fig. 2.19, respectively.

The CLAM2 work function was needed for the BL-4 calibration. The BL-4 beamline was calibrated by measuring a Au poly-crystalline sample using the CLAM2 analyzer. The Fermi-edge, the zero binding energy, of the Au sample was used as the reference for the two gratings covering 20-60 eV and 40-120 eV ranges while the $4f_{7/2}$ binding energy peak of Au, which is 84.00 eV (Briggs and Seah, 1996), was used as the reference position for the grating covering 60-240 eV range.

2.6.1 AIPES Measurements

AIPES EDC measurements were carried out with the set-up as shown in Fig. 2.20. The Ni(111) sample was aligned in such a way that the electric vector of the incident light was parallel to the surface of the sample, *i.e.*, the light direction is perpendicular to the surface of the sample. The CLAM2 analyzer is fixed to the photoemission chamber at the angles of 50° and 40° with respect to the direction of the incident light in the horizontal and vertical directions, respectively.

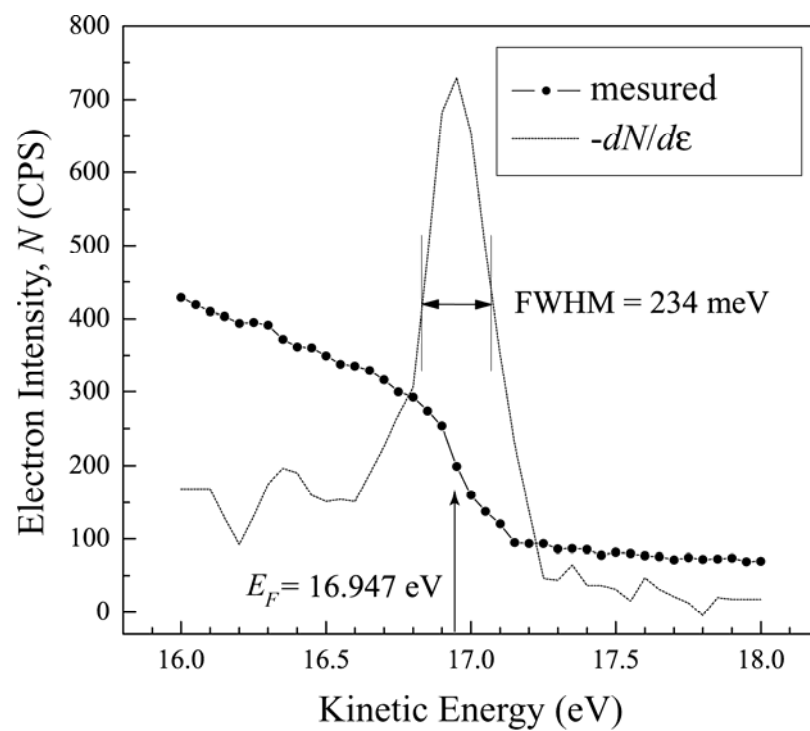


Fig. 2.18 Fermi edge of a Au poly-crystal sample spectrum and minus of the first derivative to be fitted with a Gaussian function (not shown). The spectrum was measured by using the CLAM2 analyzer. The excitation energy was 21.22 eV of the helium discharged lamp.

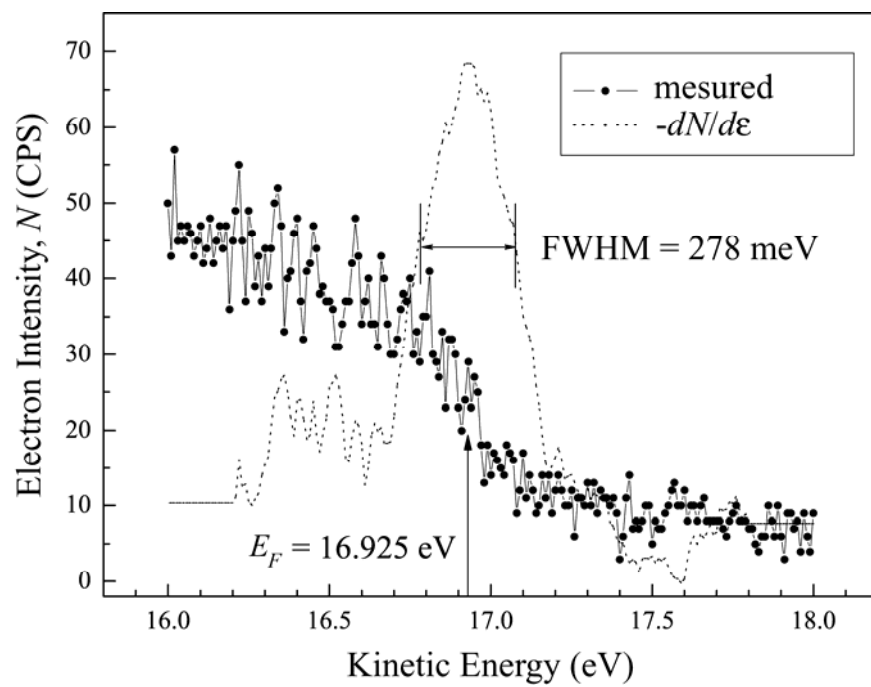


Fig. 2.19 Fermi edge of a Au poly-crystal sample spectrum and minus of the first derivative to be fitted with a Gaussian function (not shown). The spectrum was measured by using the ARUPS10 analyzer. The excitation energy was 21.22 eV of the helium discharged lamp.

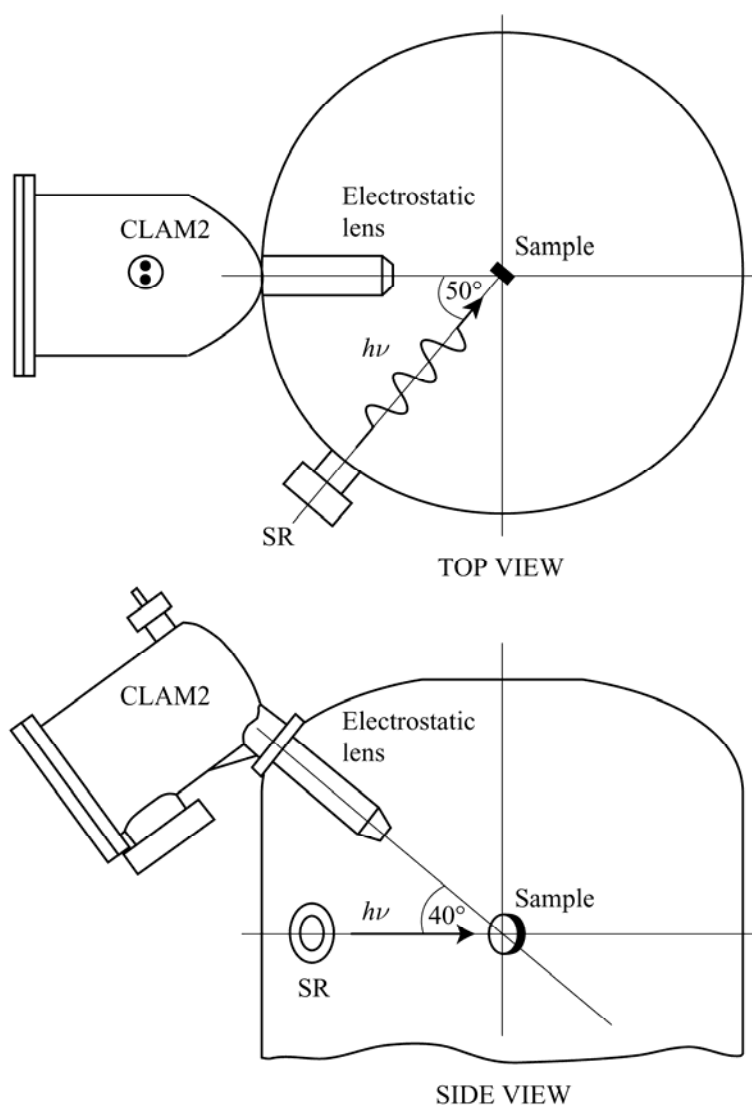


Fig. 2.20 Schematic diagram of AIPES measurements set-up.

EDC's were measured with the excitation photons with energy between 48-115 eV. The spectra were normalized to the incidence photon flux measured by the drain current of a gold mesh located between the sample and the rear focusing mirror of the beamline. The data acquisition system for AIPES measurement is a home-developed system (Samred Kantee, Supat Klinkhieo, Prayoon Songsiriritthigul, submitted for publication in Suranaree J. Sci. Technol.).

2.6.2 ARPES Measurements

The ARUPS10 analyzer was used for the ARPES measurements. The VGX900 data acquisition software provided by the maker of the analyzer, (VG Microtech, Computer Program, 1998) was used. The drain current of the Au mesh could not be measured, thus the current of the electron beam in the storage ring was used for the normalization EDC's instead.

For ARPES measurement, the accurate alignment of the sample and the analyzer with respect to the direction of the excitation photon beam is crucial. The manipulator provides azimuthal and polar rotation of the sample, shown in Fig. 2.13. The sample is 20° tilted in the horizontal direction with respect to the direction of the photon beam. Thus s-polarized light is used for the excitation. The polar rotation of the sample was necessary to provide the major symmetry lines, $\bar{\Gamma}-\bar{\Sigma}-\bar{M}$ and $\bar{\Gamma}-\bar{T}-\bar{K}$, aligned on the horizontal and vertical planes, respectively. Accurate adjustment of the sample orientation can be obtained using the LEED pattern as guidance. This alignment allows simple measurement procedure to obtain EDC's along each symmetry line by one movement of the ARUPS10 analyzer. Photons with energy of 35 eV were used for the excitation in the EDC measurements.

The normal emissions ARPES were also performed. The sample was aligned with the angle of incidence of the photon beam of 20° and 60° with respect to the normal of the sample surface. The direction of the incident photon beam was on the $\bar{\Gamma}-\bar{\Sigma}-\bar{M}$ plan. The difference angle of incidence allowed polarization dependence of the sample to the excitation light to be studied. The excited photon energy were scanned from 50 to 65 eV with a 5 eV step.

2.6.3 TY and CIS

With a newly home-developed data acquisition system, different modes of measurements could be performed using. The system allows the constant initial state (CIS) and total yield (TY) to be acquired simultaneously. CIS and TY measurements were carried out by varying the excitation photon energy from 40 to 100 eV. The CIS spectra provided the final state information while the TY provided the information similar to optical absorption of the crystal.

CHAPTER III

EXPERIMENTAL RESULTS

3.1 Introduction to the Measurements of the super Coster-Kronig Spectra of Ni

The electronic structure of transition metals is quite interesting, since localized and itinerant aspects coexist there. Particularly, the valence shell photoemission of metallic Ni shows distinctive aspects originating from the correlation involving a $3d$ hole existing in the ground state. The relevant phenomena (Guillot *et al.*, 1977) are the generation of the two-hole-bound-state and the associated p - d resonance excitation. A lot of work has been carried out on the two-hole-bound-state. Up to the present, pertinent scientists have agreed upon the electronic structure and the generation mechanism of the two-hole-bound-state (Penn, 1979; Kotani and Toyozawa, 1974; Liebsch, 1979; Davis and Feldkamp, 1981; Jo, Kotani, Parlebas, and Kanamori, 1983; Girvin and Penn, 1990; Ohmura and Sato, 1990).

The two-hole-bound-state occurs through the direct optical excitation of the many electron system of conduction electrons and considerably localized $3d$ electrons interacting with each other through the intra-atomic Coulomb interaction (Penn, 1979; Kotani and Toyozawa, 1974; Liebsch, 1981; Davis and Feldkamp, 1981; Jo *et al.*, 1983; Girvin and Penn, 1990; Ohmura and Sato, 1990).

The p - d resonance involving the two-hole-bound-state takes place because the two-hole-bound-state as the final state of the direct transition can also be reached by the indirect Auger transition such as the Coster-Kronig (CK) and super Coster-Kronig (sCK) effects initiated by the optical excitation of the pertinent core electron. Thus, the investigations of the Auger effects are attractive. In this thesis, we deal with the MMM sCK transition in relation to the $3p-3d$ resonance; hereafter MMM is designated MVV , where V stands for the valence band. The MVV sCK spectra have not been well investigated. We have found only one reported by Björneholm *et al.* (1990) so far. Optical excitation of a $4s$ electron, a conduction electron, is not taken into account in the present study, since it is weak and gives only a broad background feature.

The aspects of the MVV sCK spectra of metallic Ni are contrasted to the case of atomic Ni on which some reports (Schmidt, Schröder, Sonntag, Voss, and Wetzel, 1984; Tiedtke *et al.*, 1999) have appeared. The reported data on atomic Ni are different from those of metallic Ni. Schmidt *et al.* (1984) measured the MVV sCK spectra of some transition metal atoms by excitation with electron beams. Their MVV sCK spectra of atomic Ni is different from corresponding spectra of metallic Ni by Björneholm *et al.* (1990) nor from those presented in this report (Prayoon Songsiriritthigul *et al.*, 2005). The MVV sCK spectra of atomic Ni excited with synchrotron radiation soft X-rays were reported by Tiedtke *et al.* (1999). Those spectra are quite different neither from the spectrum obtained by excitation with electron beams (Schmidt *et al.*, 1999) nor from those of metallic Ni. In this thesis, we refer to metallic Ni as Ni unless otherwise stated.

Before we discuss about the MVV sCK spectra, we take a brief look at the two-hole-bound-state through. It is closely related with the argument made here. First, the number of $3d$ electrons per Ni atom in the ground state is taken to be 9, so that the electronic configuration of the valence shell is $3d^9 4s$. We express this state as $\hat{d}_k c_k$. Subscript k stands for the energy-band and \hat{d}_k represents the state in which a hole exists in the $3d$ band in the ground state. Thus, $\hat{d}_k c_k$ represents the ground state of metallic Ni. In a similar way, $3\hat{d}_k^n$ represents the state in which n holes exist in the $3d$ band; c_k represents the conduction band in the ground state and d_k the filled $3d$ band. Here we define the hole as the state where an electron is missing in the band which is to be completely occupied otherwise. We ignore thermally produced electrons and holes around the Fermi level. The hole in the excited state to be dealt with here is extra one generated optically or by inelastic scattering. Its existence is out of the thermal equilibrium. The hole thus defined moves in a crystal with wave vector \mathbf{k} . This is shown by angle-resolved photoemission, since the dispersion of the $3d$ band is observed (Himpsel *et al.*, 1979; Eberhardt and Plummer, 1980; Sakisaka *et al.*, 1987a). Even the exchange splitting of the $3d$ band was found (Himpsel *et al.*, 1979; Eberhardt and Plummer, 1980; Kisker, *et al.*, 1985). However, the observed band width is narrower than that predicted by the energy-band calculation (Himpsel *et al.*, 1979; Eberhardt and Plummer, 1980).

In the final state of emission of electrons from the $3d$ band, two configurations are possible to occur. In one configuration, only one $3d$ -hole exists and in the other configuration two $3d$ holes appear. When a $3d$ electron is ejected from the $3d$ band, conduction electrons screen the generated two holes instantaneously as

$$e(c_k) + h(\hat{d}_k^2) \rightarrow \hat{d}_k^* \hat{c}_k \quad (3.1)$$

Here, \hat{d}_k^* represents the $3d$ state with a hole of higher binding energy and \hat{c}_k is the conduction band with a hole; e and h stand for an electron and a hole, respectively. The valence shell photoemission occurs as

$$\hat{d}_k c_k + h\nu \rightarrow \hat{d}_k^* \hat{c}_k u_l \quad (3.2)$$

Thus, the $\hat{d}_k^* \hat{c}_k u_l$ can be the final state of the photoemission; u_l is the state of a photoelectron with high energy. Practically, the sd hybridization (Davis and Feldkamp, 1981; Jo *et al.*, 1983) obscures the pure $3d$ and $4s$ (conduction) states.

In the final state of photoemission, where the screening by conduction electrons is insufficient, the two-hole-bound-state occurs as

$$\hat{d}_k c_k + h\nu \rightarrow \hat{d}_k^2 c_k u_l \rightarrow \hat{d}_s^2 \hat{c}_k u_l \quad (3.3)$$

Here, \hat{d}_s^2 represents the two-hole-bound-state. The question whether two holes can occupy one lattice site or not was a quite important issue in the theoretical work in early days (Penn, 1979; Kotani and Toyozawa, 1974; Liebsch, 1981; Davis and Feldkamp, 1981; Jo *et al.*, 1983). Mott (1966) suggested the possible occurrence of the two-hole-bound-state. The intra-atomic Coulomb energy of bare $3d$ holes is large (Kanamori, 1963). Thus, the Coulomb repulsion between two $3d$ holes is too large to allow two $3d$ holes to stay at one lattice site. However, the screening by conduction electrons reduces the repulsive force and two $3d$ holes can stay at the same lattice site. The state in which two $3d$ holes occur at one lattice site in the bound form is referred to as the two-hole-bound-state. In spite of the situation mentioned above, the theories (Penn, 1979; Kotani and Toyozawa, 1974; Liebsch, 1981; Davis and Feldkamp, 1981; Jo *et al.*, 1983) indicate that two-hole-bound-state occurs through the strong hole-hole

correlation even without the screening. This is understandable. Suppose the two holes could not stay at a lattice site. In the same way, the optically generated extra hole cannot leave the site where it is generated because of the strong repulsion from holes at adjacent lattice sites. Thus, the two holes bind each other and are located at the lattice site where an extra hole is produced optically. In the present work, however, we consider that the role of screening electrons is indispensable. The two-hole-bound-state, \hat{d}_s^2 , consists of two $3d$ holes and a conduction electron trapped by them. The two-hole-bound-state is a product of the many electron interaction and does not exist in the ground state; the two-hole-bound-state does not appear in the energy-band calculation.

The \hat{d}_s^2 state does not show dispersion. This is proved experimentally (Björneholm *et al.*, 1990; Himpsel *et al.*, 1979; Eberhardt and Plummer, 1980; Sakisaka *et al.*, 1987a; Okane *et al.*, 1993; Kashiwakura *et al.*, 1993). It is intuitively understandable. Thus, the two-hole-bound-state has often been treated as an atomic state with the electronic configuration of $3d^8 4s$. The two-hole-bound-state has two characteristics: One is that it gives rise to the spin polarization of emitted photoelectrons (Clauberg, Gudat, Kisker, Kuhlmann, and Rothberg, 1981; Kinoshita *et al.*, 1993). This offers the direct evidence of the generation of the two-hole-bound-state. In the spite of its importance, we do not deal with the spin polarization in the present work. The second is resonance (Davis and Feldkamp, 1981; Jo *et al.*, 1983; Girvin and Penn, 1990; Ohmura and Sato, 1990; Björneholm *et al.*, 1990; Kanamori, 1963; Okane *et al.*, 1993). In a certain excitation energy region, the two-hole-bound-state is formed by the excitation of a $3p$ or $2p$ electron. By the excitation of a p core

electron near the excitation threshold, the $\hat{p}d_k c_k$ state is generated, where \hat{p} represents the $3p$ or $2p$ hole state. The state becomes the intermediate one for the MVV sCK or $LMM(LVV)$ CK transition as

$$\hat{p}d_k c_k \rightarrow \hat{d}_k^2 c_k u_A \rightarrow \hat{d}_s^2 \hat{c}_k u_A \quad (3.4)$$

Here, u_A represents the state of the Auger electron. The final state involving the two-hole-bound-state produced directly through transition (3.3) cannot be distinguished from that produced through the sCK or CK transition as (3.4) if u_i is almost the same as u_A . Therefore, the transitions through the two channels resonate and interfere with each other (Davis and Feldkamp, 1981; Jo *et al.*, 1983; Girvin and Penn, 1990; Ohmura and Sato, 1990). The resulting excitation spectrum has the profile characteristic of the resonance and interference.

In addition to the research on the two-hole-bound-state, the Auger effect has been investigated on Ni extensively and many reports have appeared in the past 20 years. The theoretical work known as the Cini-Sawatzky theory (Cini, 1977; Cini, 1978; Sawatzky, 1977; Sawatzky and Lenselink, 1980) treats the Auger transition involving the energy-band. The theory starts with a filled valence band and considers the final state with two holes. The Auger spectrum is obtained by calculating pertinent Green's function. The Cini-Sawatzky theory states the following nature of the spectrum: The Auger spectrum is given by the energy-band scheme and has the shape of the self-convolution of the DOS curve of the filled energy-band, if the width of the valence band, W , is much larger than the intra-atomic Coulomb energy, U ($W \gg U$). In case of $W \ll U$, the spectrum is atomic and the line spectrum appears. In the intermediate region, either the atomic and band spectra coexist or the self-convoluted

band is considerably deformed depending on the magnitude of W/U . Sawatzky and Lenselink (1980) and Bennett *et al.* (1983) carried out a model calculation using the Cini-Sawatzky theory with the DOS curve of a rectangular shape and showed how the Auger spectrum changes its shape according to the magnitude of W/U . Bennett *et al.* (1983) measured the LVV CK spectra of Ni and its alloys and compared the results with those of their calculation. No sharp line spectrum was found in their observed results, but they analyzed the composite profile of their spectra in terms of multiplet lines of the final state electronic configuration of d^8 . The Cini-Sawatzky theory indicates that the strong electron correlation destroys or considerably deforms the energy-band in the final state of the Auger transition. In case of Ni, in which the $3d$ band is not filled up, the final state with two holes is reached if the screening by conduction electrons takes place.

Plenty of reports have been published so far on the LVV CK spectra of Ni (Jach and Powell, 1981; Mårtensson, Nyholm, and Johansson, 1984; Cini and D'Andrea, 1984; Wegner, Potthoff, and Nolting, 2000; Tjeng *et al.*, 1993; Anilturk and Koymen, 2001; Weinelt *et al.*, 1997; Suga *et al.*, 1999; Magnuson *et al.*, 1998; Lund, Thurgate, and Wedding, 1997; Ohno, 1998; Iacobucci, Sacchi, Marassi, Marocchi, and Stefani, 1999). This tendency has been continuing up to now. The reported work covers experimental (Bennett *et al.*, 1983; Jach and Powell, 1981; Mårtensson *et al.*, 1984), theoretical (Cini and D'Andrea, 1984; Wegner *et al.*, 2000), resonance (Tjeng *et al.*, 1993; Anilturk and Koymen, 2001; Weinelt *et al.*, 1997; Suga *et al.*, 1999; Magnuson *et al.*, 1998), spin-resolved (Tjeng *et al.*, 1993), and coincidence (Lund *et al.*, 1997; Ohno, 1998; Iacobucci *et al.*, 1999) studies.

Experiments at low temperature will come out in the near future (Petrov and Kamochkin, 2004).

The recent tendency (Knorren, Benneman, Burgermeister, and Aeschlimann, 2000; Coulthard *et al.*, 2001; Föhlisch *et al.*, 2002; Pagliara *et al.*, 2002) is that investigations of the *LVV* CK spectra are being carried out more on Cu than on Ni. In Cu, the *3d* band is filled up and located further below the Fermi level as compared with that of Ni. Even if satellites accompany the main *3d* band, the ambiguity in the analysis is reduced. Because of this, detailed experiments are carried out.

It is found here that most reports on the Auger spectra of Ni are on the analyses of *LVV* CK spectra. Only a piece of work (Björneholm *et al.*, 1990) has been reported on the *MVV* sCK spectra as mentioned already. This may be because the *LVV* CK spectrum is more intense and definite than the *MVV* sCK spectrum. More investigations on the *MVV* sCK spectrum are necessary. This work dealing with the *MVV* sCK spectra will provide new data other than those on the two-hole-bound-state on which the investigations have been concentrated.

In this thesis, we deal with the sCK transition expressed as (3.4) and

$$\hat{p}\hat{d}_k c_k u_l \rightarrow \hat{d}_k^3 c_k u_l u_A \rightarrow \hat{d}_k^2 \hat{c}_k u_l u_A \quad (3.5)$$

$$\hat{p}\hat{d}_k c_k^* \rightarrow \hat{d}_k^3 c_k^* u_A \rightarrow \hat{d}_k^2 c_k u_A \quad (3.6)$$

These processes will be explained later. c_k^* is the conduction band with an excited high energy electron. We consider that there are three kinds of two-hole states. One is state of bare two holes. The two holes remain at a lattice site in a very short time; one of the *3d* holes may be extinguished by combining with a conduction electron. The second is the state of two holes screened by conduction electrons weakly. In this

thesis, this state is referred to as the quasi-two-hole-bound-state. The third is the two-hole-bound-state. We will conclude that the MVV sCK spectrum changes its profile as excitation photon energy approaches the $3p$ excitation threshold; the shape of the MVV sCK band varies in a way that it cannot be distinguished from the two-hole-bound-state band. Thus we have to observe and find the profile of the sCK band definitely with excitation light with energy sufficiently away from the threshold energy.

3.2 Angle-integrated Spectra

Fig. 3.1 shows the photoemission spectrum of the valence band region of Ni(111) and the concomitant MVV sCK spectrum. The abscissa represents the kinetic energy of emitted electrons and the ordinate the electron intensity. EDC was measured with light at $h\nu = 79$ eV. At this excitation energy, the Fermi edge occurs at 74.7 eV in photoelectron kinetic energy, ε_k . The peak of the two-hole-bound-state band is at $\varepsilon_k = 68.4$ eV. This energy of the peak position is equivalence to the binding energy, ε_B , of 6.3 eV. The spectrum shown in Fig. 3.1 coincides with those in reported data on the valence shell photoemission of Ni. The MVV sCK band extends from $\varepsilon_k = 48.5$ to 63.5 eV. The band width is 15 eV. As is obvious in Fig. 3.1, the distinctive aspect of the MVV sCK is that it is very broad and the intensity is low.

3.2.1 Angle-integrated Spectra

In Fig. 3.2, the EDC's on the high binding energy side of the two-hole-bound-state bands were measured with the excitation energy region below the $3p$ core

level threshold which is in the range of $h\nu = 48-60$ eV. Since the intensities are very low, the measured spectra are shown with the expanded ordinate scale. The abscissa represents the binding energy. The features in the spectra are indicated by vertical bars. Among three recognized features, one at $\varepsilon_B = 6.3$ eV corresponds to the generation of the two-hole-bound-state. In addition to this, two features are found at $\varepsilon_B = 8.3$ and 11 eV.

Another set of the EDC's in the binding energy representation are shown in Fig. 3.3. The ordinate represent the photoemission intensity. The spectra were measured with the excitation energy region around the $3p$ threshold and above which is in the range of $h\nu = 60-115$ eV. The 6.3 eV two-hole-bound-state features indicate by vertical bars. The bars deviate from the 6.3 eV position at the excited photon energy between 67-74 eV. The others two features indicated by arrow heads are found at $\varepsilon_B = 11$ and 13.5 eV.

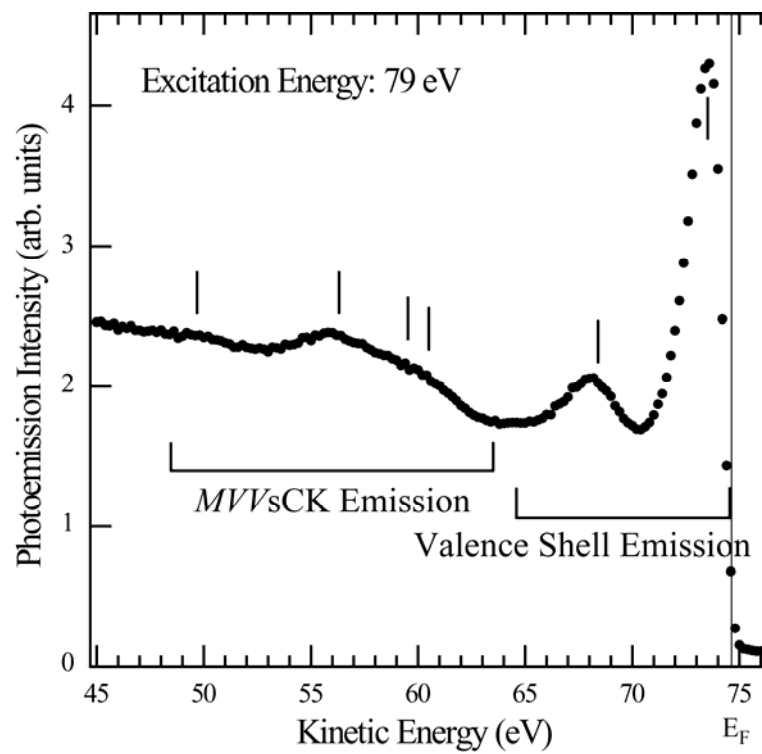


Fig. 3.1 EDC of Ni(111) measured in the angle-integrated mode. Vertical bars indicate major features in the spectrum. EDC exhibits both *MV* sCK and valence band spectra.

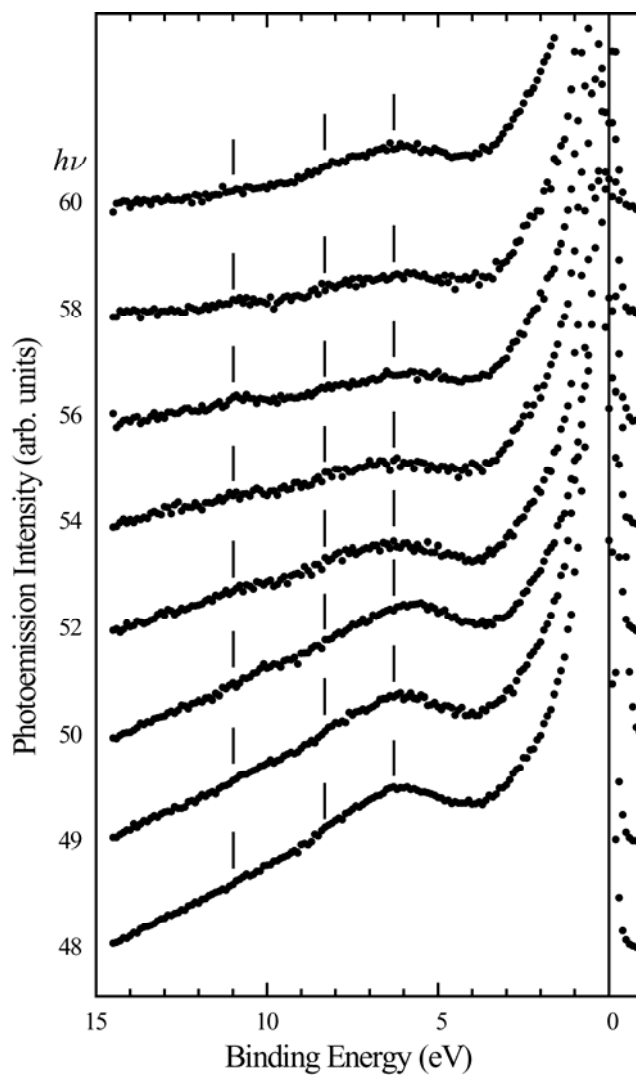


Fig. 3.2 EDC's in the binding energy region of the valence band photoemission as measured with excitation light with energy below the $3p$ excitation threshold. Vertical bars indicate the locations of features at 11, 8.3, and 6.3 eV. The backgrounds are subtracted.

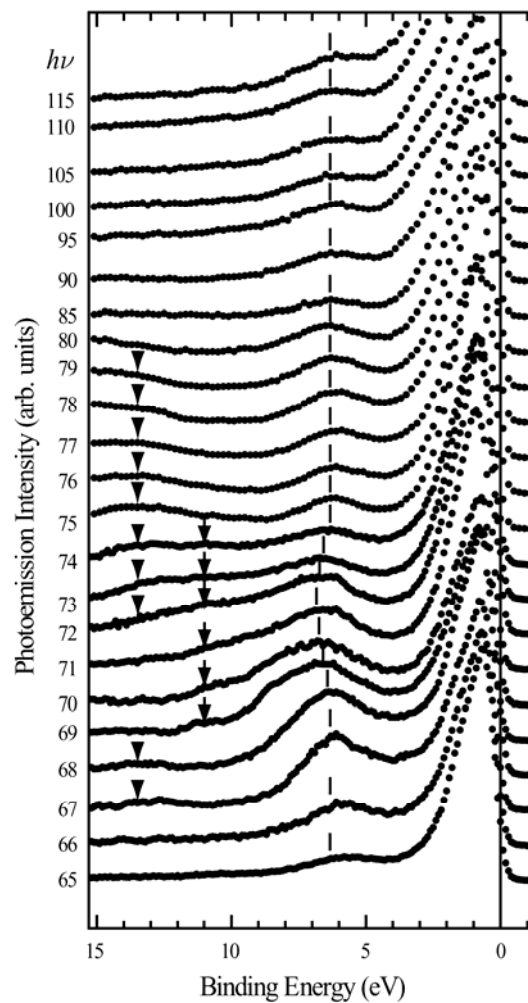


Fig. 3.3 EDC's in the binding energy region of the valence band photoemission as measured with excitation light energy around the $3p$ threshold and above. Vertical bars indicate the locations of the two-hole-bound-state feature at 6.3 eV. The arrow heads indicate the features at 11 and 13.5 eV. The backgrounds are subtracted.

3.2.2 Auger (super Coster-Kronig) Spectra

Fig. 3.4 shows the results of the measurements of the profile of the *MVV* sCK band. The spectrum is the average of seven EDC's measured at excitation energy from $h\nu = 80$ to 110 eV at intervals of 5 eV after backgrounds subtracted. The full line is a smoothed curve of 13 measured points. The abscissa represents the kinetic energy and the ordinate the photoelectron intensity. Vertical bars in the figure indicate the locations of apparent features in EDC. They occur at $\varepsilon_k = 49.8, 56.3, 59.5$ and 60.5 eV. The locations were determined with some ambiguity and thus the values below the decimal point are not accurate. The locations of the features at $\varepsilon_k = 59.5$ and 60.5 eV are confirmed by means of second derivative spectra. An arrow indicates the location of the high energy limit of the *MVV* sCK band at $\varepsilon_k = 63.5$ eV.

The spectrum shown in Fig. 3.4 is broad and no well-defined feature is resolved except one at $\varepsilon_k = 49.8$ eV. This weak feature forms a single resolved band with a half width of 1.7 eV. If the instrumental resolution is taken into account, it has a width of 1.6 eV. It has been reported that the $3p$ core-hole state has a value of spin-orbit splitting of 1.8 eV (Fuggle and Mårtensson, 1980). However, the spectrum in Fig. 3.4 does not show it. In the photoemission spectrum of the $3p$ core level of metallic Ni, several split lines are found (Björneholm *et al.*, 1990). They are attributed to the multiplet lines due to the exchange interaction between the photoproduced $3p$ hole and $3d$ electrons. In the $3p$ spectra of isolated Ni atoms, the number of observed multiplet components is much larger because of the mixing of many different configurations (Tiedtke *et al.*, 1999). This appears to indicate that the *jj* coupling

scheme to form the spin-orbit split levels in the final state of the transition is not dominant.

Fig. 3.5 shows the change in the shapes of the *MVV* sCK band and the two-hole-bound-state band as excitation photon energy is varied. Excitation energy is indicated on the left side of each spectrum. The abscissa represents the kinetic energies and the ordinate the photoelectron intensity. The backgrounds of each EDC were subtracted. Vertical bars in the figure indicate the locations of features in the *MVV* sCK band exhibited in Fig. 3.4. Their locations are $\varepsilon_k = 49.8, 56.3, 59.5$ and 60.5 eV. In addition, the feature at 59.5 eV moves its location so that the binding energy is constant in the excitation energy region from $h\nu = 75$ to 78 eV. In EDC's measured with light at $h\nu = 69$ and 70 eV, the 11 eV satellite is found which are indicated by arrows. As the excitation energy is lowered, the profile of the *MVV* sCK band is changed and the feature at $\varepsilon_k = 59.5$ eV disappears in EDC's for $h\nu \leq 76$ eV. For $h\nu \leq 68$ eV, the feature at $\varepsilon_k = 56.3$ eV is not found.

In order to see the change in the profile of the *MVV* sCK band more clearly, we show EDC's for $79 \text{ eV} \geq h\nu \geq 71 \text{ eV}$ in Fig. 3.6. The abscissa represents the kinetic energies and the ordinate the photoelectron intensity. Excitation energy is indicated on the left side of each EDC. Vertical bars indicate the locations of pertinent features in the spectra. They are the same as those in Fig. 3.5. Arrows at $\varepsilon_k = 56.3$ eV indicate the location of the high energy limit of the *MVV* sCK band as shown in Fig. 3.4. As is distinct in EDC's for $h\nu = 77$ and 78 eV, the profile of the *MVV* sCK band is deformed considerably and the feature at $\varepsilon_k = 59.5$ eV disappears. EDC's in the excitation energy region, $h\nu \leq 76$ eV, do not seem to consist of overlapping

independent bands that are the two-hole-bound-state band and the MVV sCK band. Although the peak around $\varepsilon_B = 6.3$ eV remains distinctly, the original profile of the MVV sCK band is completely dissolved there. In other words, the MVV sCK band and the two-hole-bound-state band mix with each other to form a new band with a complicated profile.

Our XPS spectrum on the emission of $3p$ electrons is shown in Fig. 3.7. The spectrum in Fig. 3.7 agrees qualitatively with that reported by Björneholm *et al.* (1990). The values of the binding energy of features in EDC observed in the present work are slightly different from those of Björneholm *et al.* (1990). Two lines including one at $\varepsilon_B = 59$ eV found in the present work are missing in their spectrum. In Fig. 3.7, vertical bars indicate the locations of features. If the contribution of conduction electrons and the energy-band effect are negligible, the final state of the transition consists of the multiplets formed by the electronic configuration of $3p^5 3d^9$. Possible multiplets are 3F , 3D , 3P , 1F , 1D , and 1P . Out of six possible lines only five lines are found in Fig. 3.7. A weak peak observed around $\varepsilon_B = 59$ eV and not occurring in EDC measured by Björneholm *et al.* (1990) with monochromatized light is possibly caused by the Mg $K\alpha_{3,4}$ satellite line of excitation light, since X-rays for excitation are not monochromatized in the present measurements.

Now we resume the discussion on Fig. 3.4. The emission intensity increases not steeply above $\varepsilon_k = 52$ eV. This might suggest the occurrence of unresolved components around $\varepsilon_k = 54$ eV. Similarly, the possibility that a high energy component exists around $\varepsilon_k = 61$ eV may be considered. However, no definite

conclusion can be drawn out here. Such components cannot be separated without any guiding principle and the decomposition cannot be performed without ambiguity.

In Fig. 3.8, the MVV sCK band presented in Fig. 3.4 is compared with that measured with Mg $K\alpha$ radiation. At the top of the figure, the spectrum illustrated in Fig. 3.4 is indicated. At the middle, EDC measured with Mg $K\alpha$ radiation is shown. For reference, the L_3VV CK spectrum measured by Mårtensson *et al.* (1984) is also shown at the bottom in the figure. The L_3VV CK spectrum is placed so that the main peak at $\varepsilon_k = 846.2$ eV aligns to the main peak of the MVV sCK spectrum. Later, Weinelt *et al.* (1997) measured the L_3VV CK spectrum using synchrotron radiation. The L_3VV CK spectrum shown in Fig. 3.8 coincides almost with that measured with light at $h\nu = 1082.3$ eV. Also it coincides with that measured by Bennett *et al.* (1983).

Three EDC's shown in Fig. 3.8 do not coincide rigorously with each other. In case of L_3VV CK spectrum, the number of features is different from that of MVV sCK band measured with light at $h\nu = 80-110$ eV. The number of features of the MVV sCK spectrum measured with light at $h\nu = 80-110$ eV seems to be different from that of the MVV sCK spectrum measured by excitation with Mg $K\alpha$ radiation. In the XPS spectrum, a weak shoulder feature is found at $\varepsilon_k = 57.5$ eV which is not found in EDC averaged over the region of excitation energy $h\nu = 80-110$ eV. The relative intensities of components of the MVV sCK spectrum measured with excitation light at $h\nu = 80-110$ eV are different from those measured by excitation with Mg $K\alpha$ radiation. The spectrum measured with Mg $K\alpha$ radiation is not well resolved.

Particularly, the component at $\varepsilon_k = 49.8$ eV is not well separated in the spectrum measured with Mg $K\alpha$ radiation.

The profile of the MVV sCK spectrum is clearly different from that of the L_3VV CK spectrum; not only the number and relative locations of the component features but their relative heights are different. Especially the intensity ratio of the highest intensity peak assigned to the 1G level to the highest kinetic energy peak, 3F , of the L_3VV CK spectrum does not coincide with the similar ratio in the MVV sCK spectrum. In the L_3VV CK spectrum, the lowest kinetic energy peak, 1S , has the shoulder profile. In the MVV sCK spectrum, the similar feature has a relatively low intensity. These pieces of disagreement are not ascribable to the final states of the transitions, since the apparent final states are the same in both spectra. The results described so far seem to indicate that the spectral profiles of the MVV sCK and L_3VV CK spectra are not only determined by the valence states in the final states but the intermediate state with optically generated core holes and excited spectator electrons.

Björneholm *et al.* (1990) interpreted the apparent deformation of the MVV sCK spectrum on resonance as being caused by an overlapping satellite band at $\varepsilon_B = 13.5$ eV. In order to obtain more information on this issue, EDC's on the high binding-energy side of the two-hole-bound-state band were measured in the excitation energy region below the threshold of the $3p$ core excitation. Since the intensities are very low, the measured spectra are shown in Fig. 3.2 with the expanded ordinate scale. The ordinate scale is ten times as large as those for EDC's in other figures. In Fig. 3.2, the abscissa represents the binding energy. The features in the spectra are indicated by vertical bars. Among three recognized features, one at $\varepsilon_B = 6.3$ eV corresponds to the

generation of the two-hole-bound-state. In addition to this, two features are found at $\varepsilon_B = 8.3$ eV and 11 eV. No feature is found at $\varepsilon_B = 13.5$ eV. Weak satellites occurring here were also observed by Okane *et al.* (1993). In EDC's measured at $h\nu = 67$ eV and 68 eV, a weak feature is found around $\varepsilon_B = 13.5$ eV. However, they can also be assigned to one of the component feature at $\varepsilon_B = 49.8$ eV of the *MVV* sCK band. In other words, such weak satellites are conspicuous only on resonance. This point will be discussed later regarding the features in the second derivative curves.

The complete merger of the two spectra occurs at excitation photon energy of $h\nu = 68$ eV. It is interesting to investigate the situation from the two-hole-bound-state band side. In Fig. 3.9, EDC's for the generation of the two-hole-bound-state in the excitation energy region, $71 \text{ eV} \geq h\nu \geq 66 \text{ eV}$, are illustrated. In this case, the abscissa represents the electron binding energy. The excitation photon energy is indicated on the left side of each EDC. The full width at half maximum (FWHM) of the pertinent emission band is indicated under each EDC with a horizontal bar. Downward arrows indicate the location of the 11 eV satellite. It may also be a part of the *MVV* sCK band. Regarding the locations of the 11 eV satellite in EDC's for $h\nu = 69$ and 70 eV, we cannot exclude the possibility that a feature ascribable to an origin other than the satellite occurs at this binding energy by accidental coincidence. Suppose it is the satellite, then it should be found at any excitation energy. However, it emerges only on resonance. Regarding the satellite at 13.5 eV, it cannot be separated clearly. A feature is found around 13.5 eV in EDC's for $h\nu = 67$ and 68 eV, although the *MVV* sCK peak at $\varepsilon_k = 49.8$ eV occurs there as indicated with vertical bars.

The distinctive aspect of Fig. 3.9 is that the width of the two-hole-bound-state band is enhanced as the excitation energy is increased and the band shape is changed to be asymmetric and deformed. The peak position which is indicated with an upward arrow is also shifted slightly toward high binding energy. In EDC's for $h\nu = 70$ and 71 eV, the existence of the 11 eV feature makes the asymmetry of the band profile more enhanced. However, the 11 eV feature cannot be separated from the two-hole-bound-state band clearly. Even in EDC's for $h\nu = 66$ and 67 eV, the band width increases in spite of the fact that the band asymmetry is not quite conspicuous. EDC for $h\nu = 69$ eV has a width larger than that of EDC for $h\nu = 66$ eV by about 76%. In EDC for $h\nu = 71$ eV, the width reaches 2.8 times as large as that for $h\nu = 66$ eV. The conclusion drawn out of the observation is that the two-hole-bound-state is also changed. The simple two-hole-bound-state is lost here.

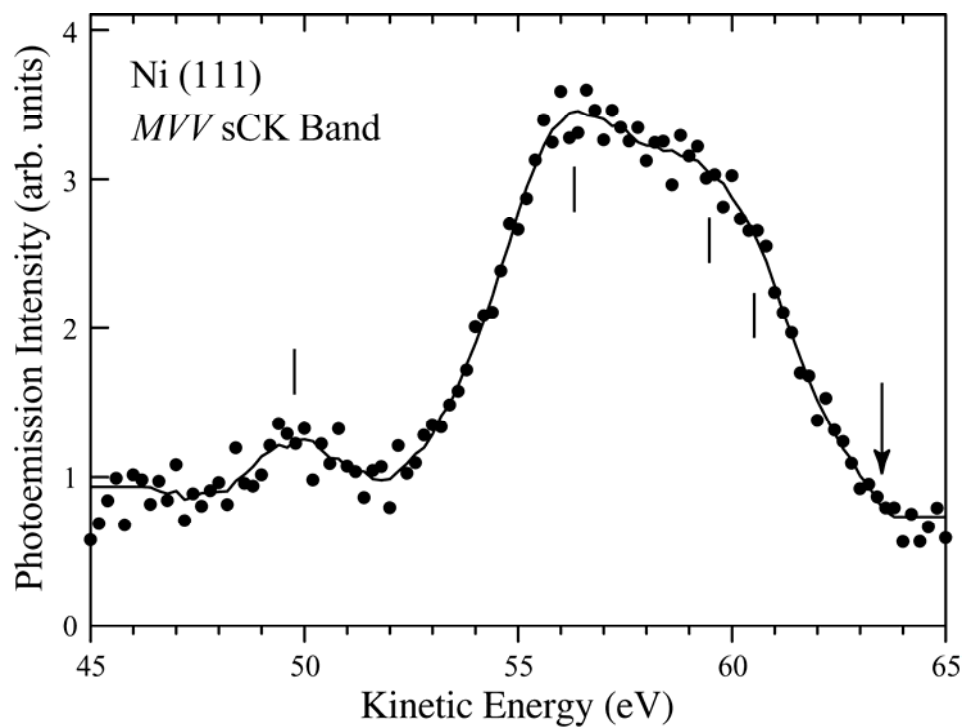


Fig. 3.4 EDC of the *MVV* sCK electron. The spectrum is obtained by averaging seven EDC's measured at excitation energy from 80 to 110 eV at an interval of 5 eV. The solid line indicates the smoothed curve obtained by the 13-point average. Vertical bars at 49.8, 56.3, 59.5 and 60.5 eV indicate major features of the EDC. An arrow at 63.5 eV indicates the high energy limit of the *MVV* sCK band.

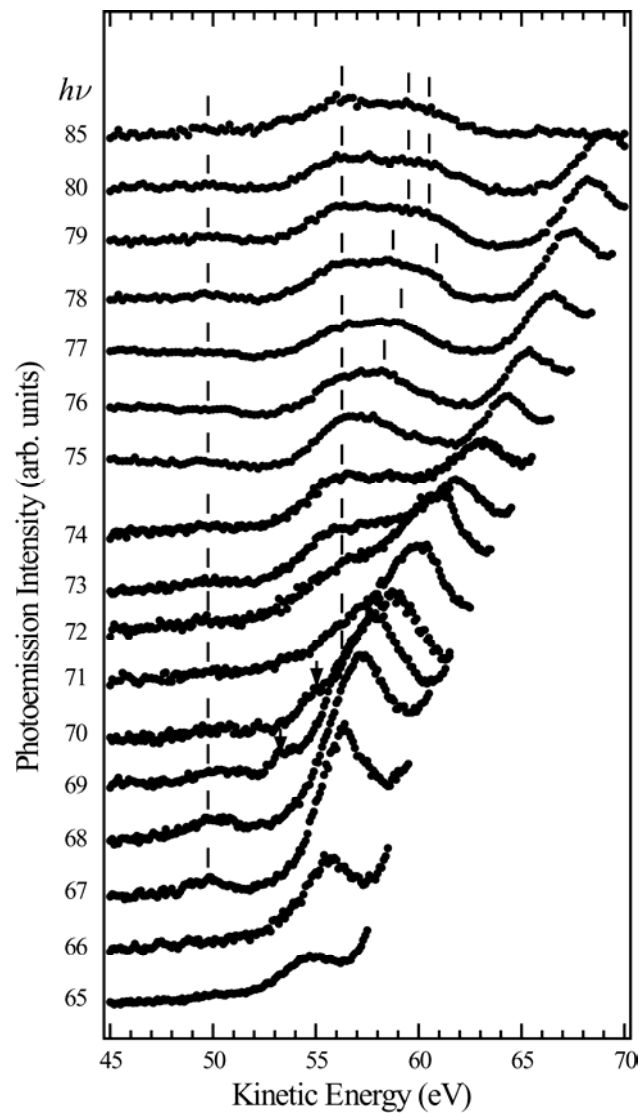


Fig. 3.5 EDC's showing the change in the spectral shapes of the *MVV* sCK band and the two-hole-bound-state band as the excitation photon energy is changed. Vertical bars indicate the locations of the features of the *MVV* sCK band at 49.8, 56.3, 59.5, 60.5 eV and those of a few features occurring in the area between 57 and 59.5 eV. Arrows show the locations of the 11 eV satellite. The backgrounds are subtracted.

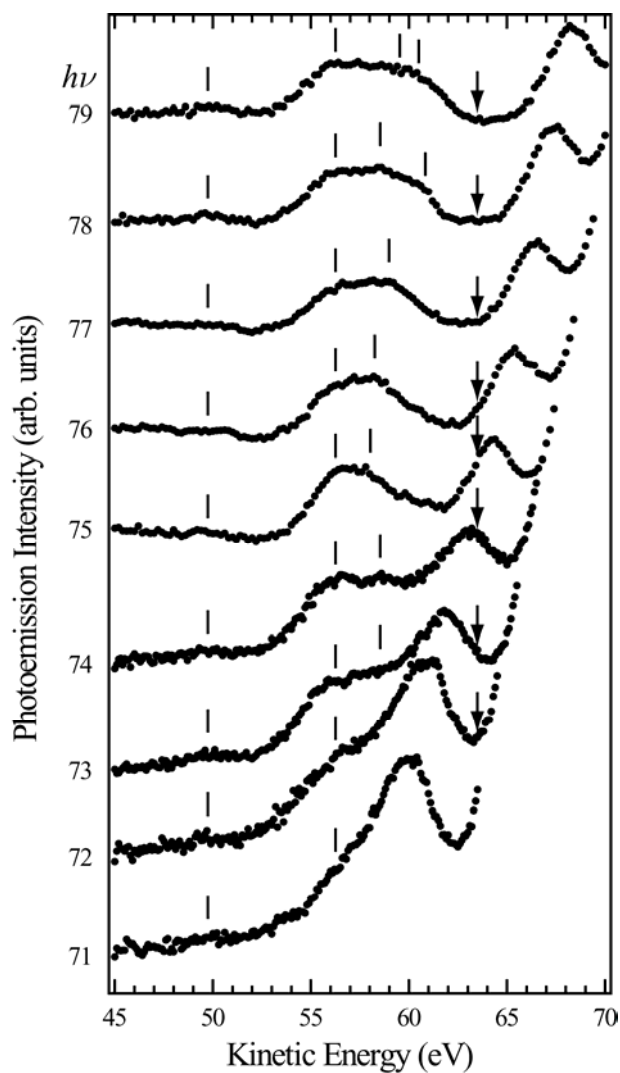


Fig. 3.6 The MVV sCK and two-hole-bound-state spectra in the excitation photon energy range from 71 to 79 eV. Vertical bars indicate the locations of the features at 49.8, 56.3, 59.5, 60.5 eV and those of a few features occurring the area between 57 and 59.5 eV. Arrows show the locations of the high energy limit of the MVV sCK band given in Fig. 3.4.

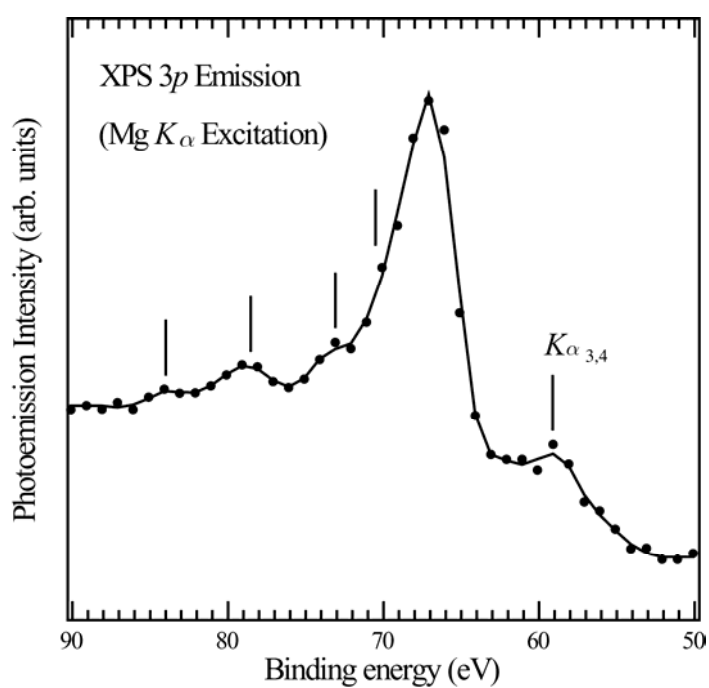


Fig. 3.7 The 3p core level lines measured by excitation with the Mg $K\alpha$ radiation.

Features in the spectrum are indicated with vertical bars. The feature indicated as $K\alpha_{3,4}$ is the main 3p line excited with the Mg $K\alpha_{3,4}$ radiation.

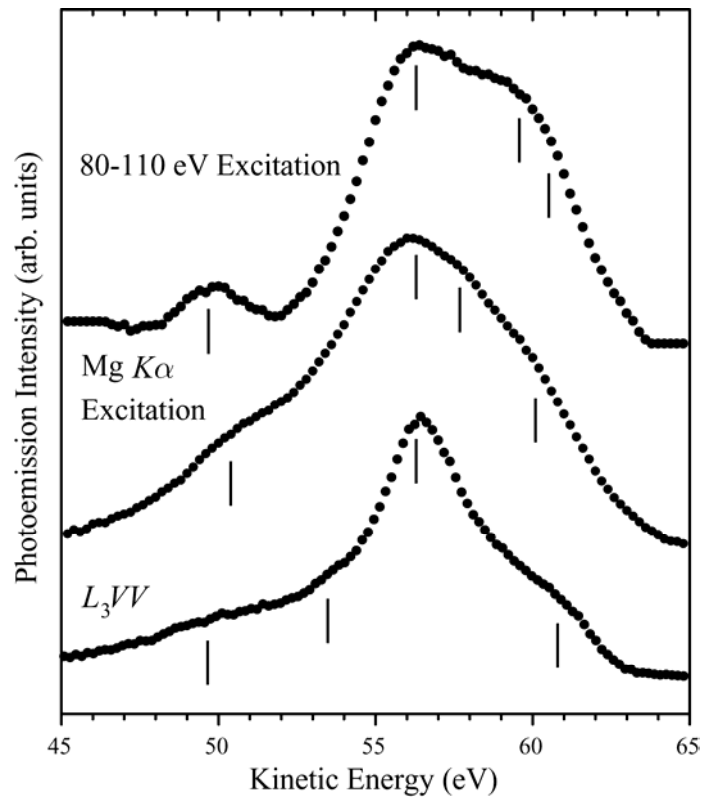


Fig. 3.8 The MVV sCK spectrum exhibited in Fig. 3.4 (top) as compared with the MVV sCK spectrum obtained by excitation with Mg $K\alpha$ radiation (middle). The L_3VV CK spectrum from Mårtensson *et al.* (1984) (bottom) is also shown for comparison. The L_3VV CK spectrum is placed in the figure so that the major peak is aligned to those of other two spectra. Features in each spectrum are indicated with vertical bars. The backgrounds are subtracted.

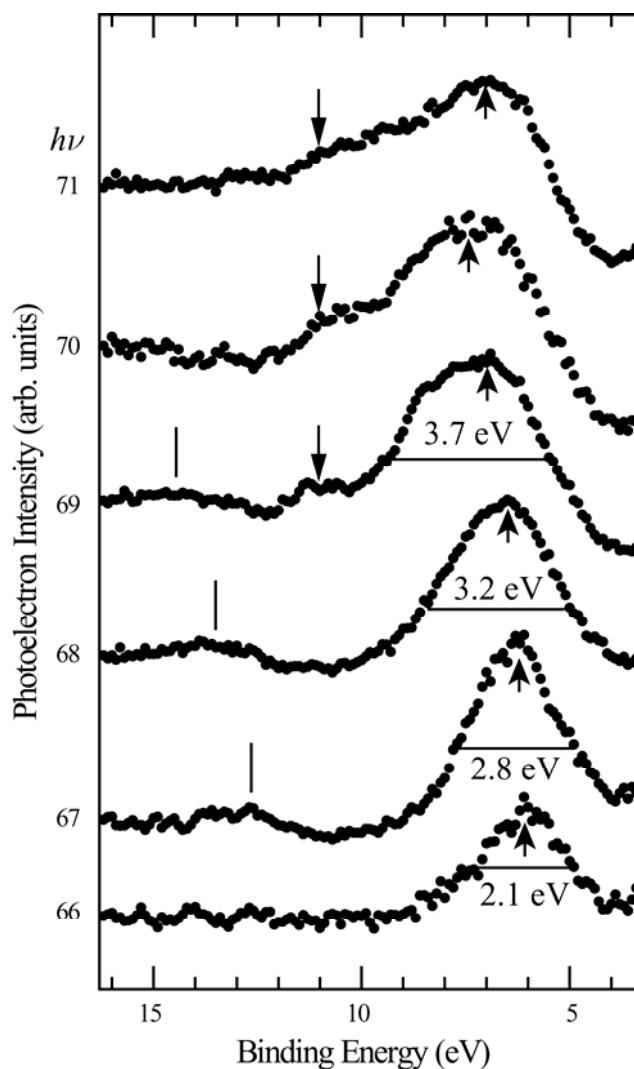


Fig. 3.9 The two-hole-bound-state spectra in the excitation energy range from 66 to 70 eV. Upward arrows indicate the peak positions. Downward arrows indicate the locations of the weak component of the *MVV* sCK band occurring at kinetic energy of 49.8 eV. The numbers given under the two-hole-bound-state bands are the values of the FWHM of the bands indicated with horizontal bars. The backgrounds are subtracted.

In order to recognize the shift of the locations of features clearly, we take the second derivative of EDC. The second derivative deletes the part of the spectrum where the intensity changes slowly and makes the features emerge as definite peaks. Since the second derivative of a band has the negative sign in the band maximum area, we use the negative value of the second derivative. In Fig. 3.10 we plot the locations of the peaks in the second derivative curves versus excitation photon energy. The abscissa represents the kinetic energy of emitted electrons and the ordinate excitation energy. The black bands represent the widths and heights of features. The horizontal width of the band represents the width of a feature in the second derivative curve and the black color intensity represents the peak height. The locations of the peaks of the features are indicated with white dots. The locations of the peaks of the main $3d$ band and the two-hole-bound-state band are shown by connecting with straight lines. The lines represent the relation, $\Delta\varepsilon_k = \Delta h\nu$ (constant-binding-energy-lines). In the photon energy region, $74 \text{ eV} \geq h\nu \geq 67 \text{ eV}$, the locations of the peaks of the two-hole-bound-state bands deviate from the constant-binding-energy line, $\Delta\varepsilon_k = \Delta h\nu$. The deviation occurs toward low kinetic energy. In the LVV CK case, the locations of the two-hole-bound-state peaks deviate from the constant-kinetic-energy line toward the high kinetic energy on resonance (Weinelt *et al.*, 1997; Suga *et al.*, 1999). The deviation of the peak position was also reported by Sakisaka *et al.* (1987a). We will interpret the deviation of the peak position from the constant-binding-energy line as being caused by the final state interaction.

Vertical lines in Fig. 3.10 exhibit the locations of features at $\varepsilon_k = 49.8$, 56.3, 59.5 and 60.5 eV of the MVV sCK band as shown in Fig. 3.4. The broken line

indicates the high kinetic energy limit of the *MVV* sCK band at $\varepsilon_k = 63.5$ eV. In the areas where the *MVV* sCK band cannot be separated from the two-hole-bound-state band, the areas are shown with hatches connecting both bands. It is noticed that the peak position of the second derivative of the apparent two-hole-bound-state band deviates from the constant-binding-energy line in the excitation energy region where the *MVV* sCK band cannot be clearly separated from the two-hole-bound-state band (resonance region) as pointed out already.

The peak around $\varepsilon_k = 56.3$ eV of the *MVV* sCK band aligns along the line of the constant kinetic energy of 56.3 eV. On the other hand, the feature around $\varepsilon_k = 59.5$ eV does not align well on the pertinent constant-kinetic-energy line except for EDC's excited with high energy photons. This is partly because the location of the shoulder feature cannot be assigned uniquely. The appearance of a definite peak in the second derivative curve at the shoulder feature of original EDC cannot necessarily be expected.

In Fig. 3.10, four constant-binding-energy lines are depicted. They are for $\varepsilon_B = 0.6$ eV, the main *3d* band, $\varepsilon_B = 6.3$ eV, the two-hole-bound-state band, $\varepsilon_B = 11$ eV, a satellite, and $\varepsilon_B = 13.5$ eV, a satellite. Some measured peak positions align on these straight lines. It was pointed out that the satellite transition occurring at $\varepsilon_B = 13.5$ eV may resonate with *MVV* sCK transition and change the apparent profile of the *MVV* sCK spectrum on resonance (Björneholm, 1990). However, the satellite at $\varepsilon_B = 13.5$ eV cannot be recognized unless the *MVV* sCK band occurs around $\varepsilon_B = 13.5$ eV as is distinct from Fig. 3.10. Thus, we do not treat the satellite at $\varepsilon_B = 13.5$ eV seriously as the cause of the spectral profile change.

In Fig. 3.10, a peak is evident at $\varepsilon_k = 49.8$ eV. Fig. 3.5 and Fig. 3.9 show that the peak is resonantly enhanced over the excitation energy range from $h\nu = 67$ to 69 eV. In this excitation energy range, other components of the *MVV* sCK band merge into the two-hole-bound-state band completely. The component line at $\varepsilon_k = 49.8$ eV disappears for excitation energy below $h\nu \leq 66$ eV. This is because the threshold of the $3p$ excitation is at $h\nu = 66.2$ eV and the $3p$ hole is not generated for photon energy below $h\nu = 66$ eV. This means that the *MVV* sCK transition does not occur below $h\nu = 66$ eV.

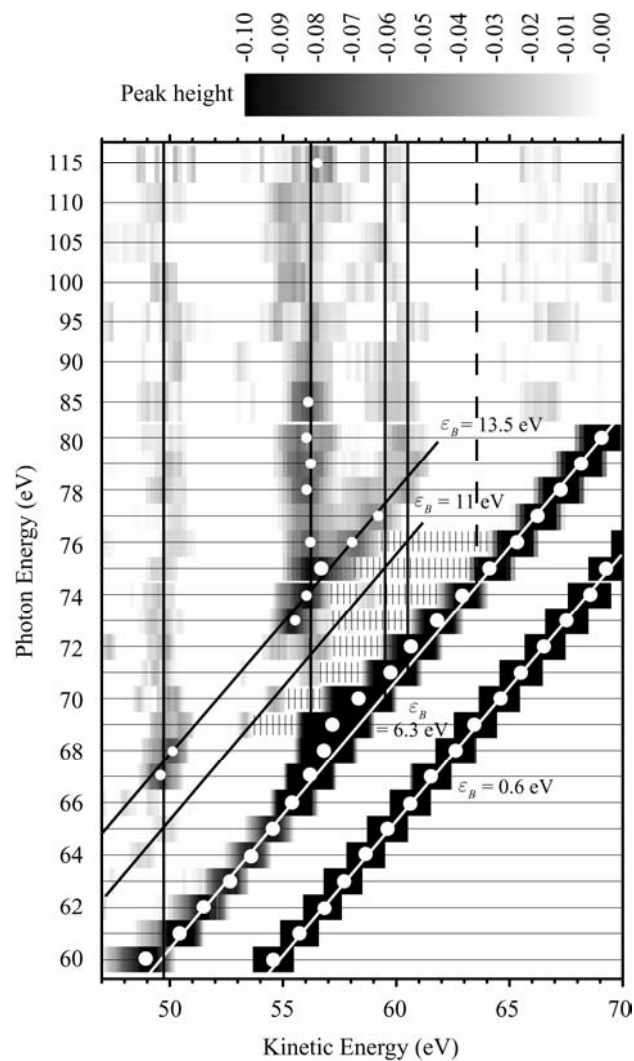


Fig. 3.10 The relation between the excitation photon energy ($h\nu$) and the peak positions of features in the spectra of the second derivative of EDC. The dots indicate the locations of the peaks (negative sign). Black horizontal bands exhibit features and their locations occurring in the second derivative spectra. The intensities of the horizontal bands indicate the depths of the negative peaks. In the excitation energy region from $h\nu = 69$ to 76 eV, the areas where the continuous bands exist is shown by hatches.

3.2.3 Excitation Energy Dependence of the Spectral Band Shapes of Angle-integrated Emission

The excitation spectrum of the two-hole-bound-state band presents quite important information on the consideration of the cause of the deformation of the MVV sCK band. Here we give it in the form of the constant-initial-state (CIS) spectrum. Fig. 3.11 shows the CIS spectrum in which the photoemission intensity at $\varepsilon_B = 6.5$ eV normalized to the incident photon intensity is plotted versus excitation photon energy. In the figure, weak features are indicated with vertical bars. They occur at $h\nu = 52, 60.5,$ and 77 eV. We assign the location of the $3p$ threshold to be at $h\nu = 66.2$ eV and indicate it with an arrow in Fig. 3.11. This value coincides with the reported value of the binding energy of the M_3 ($3p_{3/2}$) level (Fuggle and Mårtensson, 1980). Just below the threshold of the $3p$ excitation, a dip occurs. It is located at $h\nu = 65$ eV. Increase in the photoemission intensity is noticed below $h\nu = 49$ eV. Its origin is unknown at present. The CIS spectrum illustrated in Fig. 3.11 coincides with reported excitation spectrum of the $3p-3d$ resonance (Okane *et al.*, 1993). The origins of a broad band around $h\nu = 52$ eV and a peak at $h\nu = 60$ eV are not known at present. The origin of a shoulder feature around $h\nu = 77$ eV is not known, too. It should be remarked in Fig. 3.11 that the resonance band is broad. The resonance band has a peak at $h\nu = 68$ eV and a FWHM of 5.2 eV. If we consider that the resonance band extends from $h\nu = 64$ eV to $h\nu = 85$ eV, the resonance energy region covers the area of a width of 21 eV. The result described above is contrasted to the resonant inverse photoemission data (Tezuka *et al.*, 2004; Schedin, Warburton, Thornton, and Hoyland, 1998) which indicates the width of the empty $3d$ band enhanced resonantly

to be about 1 eV. The width of the $2p-3d$ resonance band is also narrow to be about 1 eV.

In Fig. 3.12 and Fig. 3.13, two kinds of spectra are presented that offer important information for the interpretation of the change in the spectral profile of the MVV sCK band caused by the change in the excitation energy. Fig. 3.12 shows the CIS spectrum for the emission at $\varepsilon_B = 0.6$ eV. This spectrum presents the partial yield spectrum of the main $3d$ band. The abscissa of the figure represents the excitation photon energy and the ordinate the photoemission intensity at the binding energy of 0.6 eV. Features in the spectrum are indicated with vertical bars. They are located at 49.8, 54, 63 and 70 eV. The threshold of the excitation of $3p$ electrons is indicated with an arrow.

A distinctive aspect of the spectrum shown in Fig. 3.12 is that a broad band extends from $h\nu = 47$ to 66 eV with a peak at $h\nu = 55$ eV. Since the spectral range is located below the $3p$ excitation threshold, the band cannot be attributed to the $3p-3d$ resonance. The straightforward conclusion is that DOS with the f symmetry is large in the region from 50 to 65 eV above the Fermi level or the $3d-\varepsilon f$ partial cross section is large there. An intense peak occurs around $h\nu = 40$ eV although it is not shown in Fig. 3.12. We do not deal with it here.

A weaker band with a peak at $h\nu = 70$ eV is found in the region extending from $h\nu = 67$ to 77 eV. We interpret this band as caused by the $3p-3d$ resonance. In other words, the resonance occurs in the main $3d$ band. This is possible through the sd hybridization or the $s-d$ screening. The resonance is not too strong as in the case of two-hole-bound-state.

Fig. 3.13 shows the total yield spectrum. The abscissa represents the excitation photon energy and the ordinate the photocurrent flowing out of the specimen. The ordinate intensity contains the contribution of secondary electrons brought about by inelastic scattering of photoelectrons. Thus it is not necessarily proportional to the absorption coefficient. However, in the spectrum measured up to $h\nu = 160$ eV, a very broad and intense band is found about $h\nu = 110$ eV. We ascribe this band to electrons suffering inelastic scattering and concomitant electrons excited by scattering. We take the total yield spectrum observed here below 100 eV for being proportional to the absorption spectrum.

In Fig. 3.13, weak peaks are found at $h\nu = 54$, 63, and 81 eV. They are denoted with vertical bars. The intensity rises steeply at the threshold of the $3p$ excitation at $h\nu = 66.2$ eV. The location is indicated with an arrow. Except a weak feature located at $h\nu = 81$ eV, the total yield spectrum above the $3p$ threshold has roughly flat structure. This is quite contrasted to the CIS spectrum for the generation of the two-hole-bound-state shown in Fig. 3.11. The total yield spectrum shown in Fig. 3.13 is also contrasted to the CIS spectrum for the main $3d$ band shown in Fig. 3.12. The CIS spectra in Fig. 3.11 and Fig. 3.12 reflect the partial yield spectra for the ionization of $3d$ electrons but the total yield spectrum reflects the ionization efficiency of all valence electrons including $4s$ (conduction) electrons. Above the $3p$ threshold, the ionization efficiency of $3p$ electrons is also involved.

If we compare the locations of the features occurring in Fig. 3.12 with those in Fig. 3.13, we find some correspondence between them. They are the features occurring at $h\nu = 54$ and 64 eV. No correspondent partner of the 81 eV feature of Fig. 3.13 is found in Fig. 3.12 and no correspondent partner of the 49.8 eV feature of Fig.

3.12 is found in Fig. 3.13. The origins of these features are not known at present. It is evident that the MVV sCK transition is accompanied by inelastic scattering of electrons.

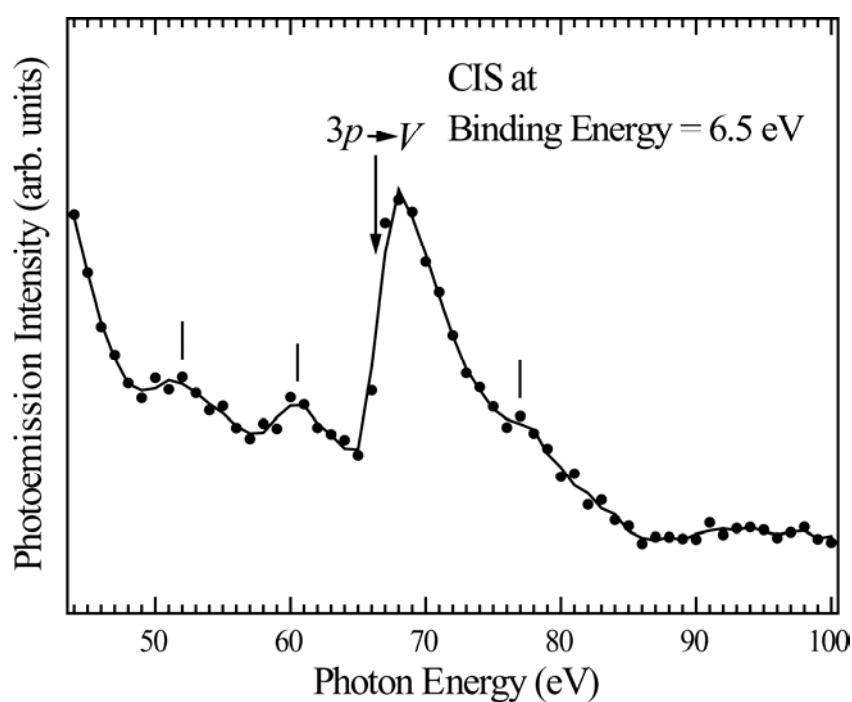


Fig. 3.11 CIS spectrum for photoelectrons with binding energy of 6.5 eV. Weak peaks at 52, 60.5 and 77 eV are indicated by vertical bars. The main resonance band has its peak at 68 eV and the onset position is recognized as a dip at 64 eV. The $3p$ excitation threshold is assigned to occur at 66.2 eV and exhibited with an arrow.

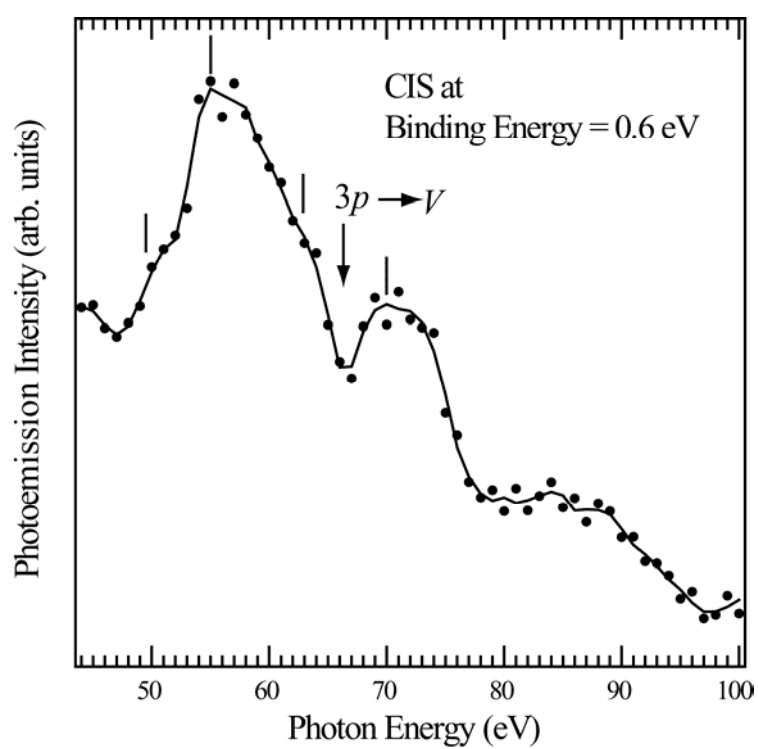


Fig. 3.12 CIS spectrum of the main $3d$ band at binding energy of 0.6 eV. Vertical bars indicate the locations of the features at 49.5, 55, 63 and 70 eV. An arrow indicates the location of the threshold of the $3p$ excitation at 66.2 eV.

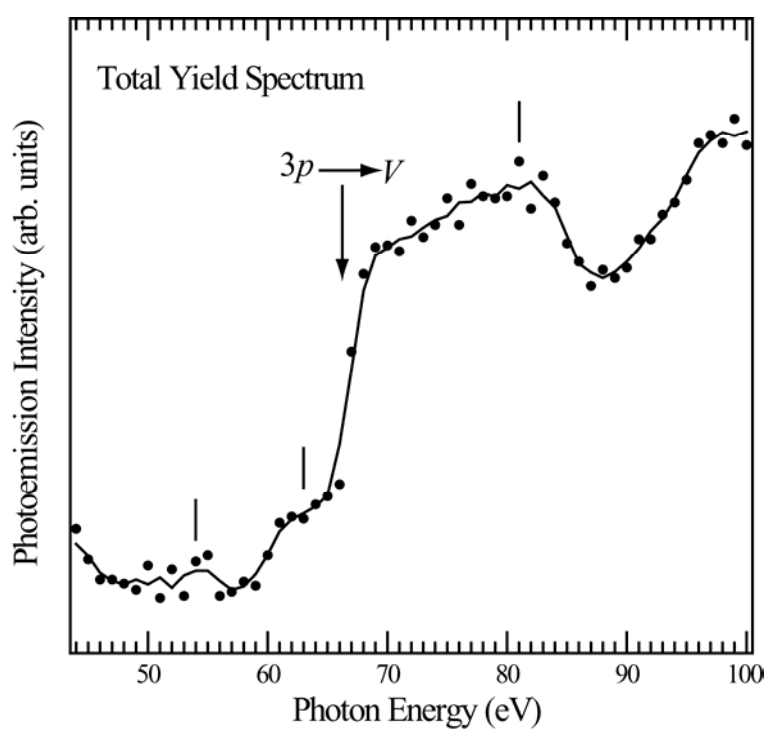


Fig. 3.13 The total photoelectron yield spectrum. The abscissa represents the excitation photon energy and the ordinate the flowing photocurrent the specimen. Vertical bars indicate the locations of weak features at 54, 63 and 81 eV. The location of the threshold of the $3p$ excitation is shown by an arrow.

3.3 Angle-resolved Spectra

We have carried out an angular dependent ARPES of the Ni(111) to be used for a surface energy-band mapped. In addition, the excitation light dependence of normal emission was also investigated.

3.3.1 Surface Energy-band

Fig. 3.14 shows the EDC of the Ni(111) along $\bar{\Gamma}-\bar{T}-\bar{K}$ line of the surface Brillouin zone. The excitation energy was 35 eV with incidence angle of 20° with respect to the surface normal. The abscissa represents binding energy while the ordinate represents photoemission intensity in arbitrary units. The spectra were plotted in the waterfall style. The intensity of the spectra can be directly compared because the spectra were normalized to the electron beam currents of the storage ring. The emission angles were varied between -2° and 45° covering the first Brillouin zone.

Fig. 3.15 show PES spectra of Ni(111) taken along $\bar{\Gamma}-\bar{\Sigma}-\bar{M}$ line of the surface Brillouin zone with the emission angle varied between -2° to 38° . The emission angle needed to cover the first Brillouin zone is smaller than the $\bar{\Gamma}-\bar{T}-\bar{K}$ line because the $\bar{\Gamma}-\bar{\Sigma}-\bar{M}$ line is shorter. The $k_{||}$ of the $\bar{\Gamma}-\bar{\Sigma}-\bar{M}$ line is 1.46 \AA^{-1} while the $\bar{\Gamma}-\bar{T}-\bar{K}$ line is 1.68 \AA^{-1} .

The surface energy-band of Ni(111) can be mapped by from the second derivative of the photoemission spectra. The spectra were combined from the both lines of symmetry. The intensities were normalized again by using the $\bar{\Gamma}$ point intensity. The results were compared to a surface band calculation (Mittendorfer, Eichler, and Hafner, 1999) separated between spin-up and spin-down as shown in Fig.

3.16(a) and Fig. 3.16(b). The abscissa represents the $k_{||}$ while the ordinate represents the binding energy. The upward triangles represent the calculated spin-up while the downward triangles represent the calculated spin-down of the electrons.

3.3.2 Dependence on Polarization of Excitation Light

The polarization dependence of the photoemission spectra experiment was carried out using the photon energy varying from 50 to 65 eV with a step of 5 eV. The incidence angles were 20° and 60° with respect to the surface normal. The 20° incidence angle makes the electric field component of the light almost parallel to the sample surface which is s-polarized light. Another 60° incidence angle makes the electric field component of the light partially perpendicular to the surface normal. This angle provides mixed between s-polarized and p-polarized light.

The s-polarized and p-polarized spectra are compared at the same excitation energy as shown in Fig. 3.17. The spectra were normalized to the same background electrons intensity each excited energy. The Λ_1 band is enhanced by p-polarized light while the Λ_3 band is enhanced by s-polarized light. The vertical bars indicate the bands peak position. Both Λ_1 and Λ_3 bands show small dispersions. However, the Λ_1 band peak positions are more deviated than the Λ_3 band peak position. The Λ_3 band is shift to higher binding energy when using higher excited energy. This may be caused by the reduction of the beamline resolution at higher incident photon energy while the slits width of the monochromator was fixed.

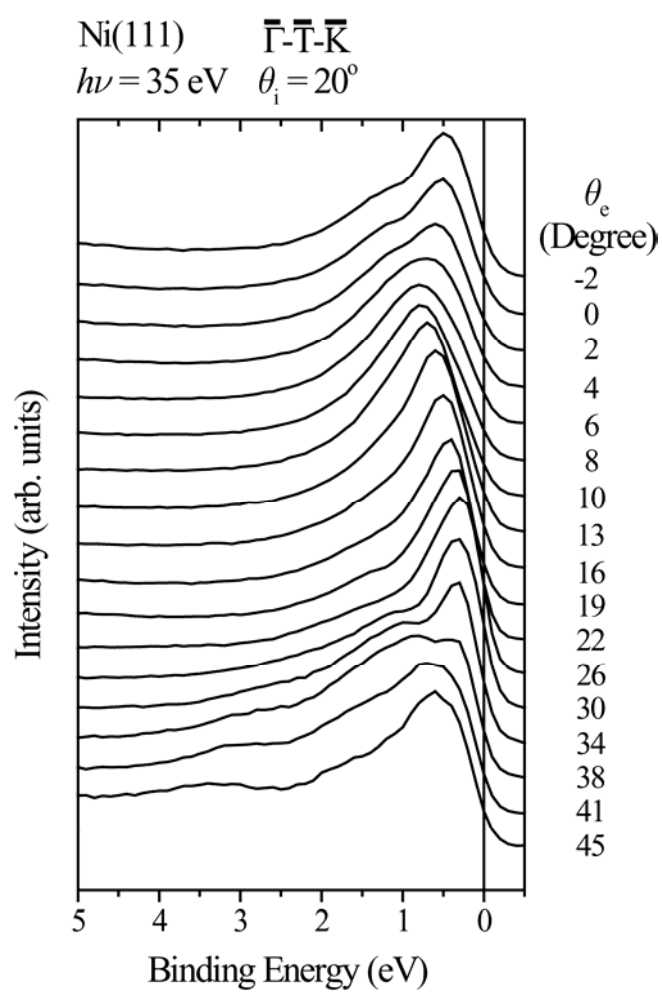


Fig. 3.14 Angular dependence of angle-resolved spectra along $\bar{\Gamma}-\bar{T}-\bar{K}$ symmetry.

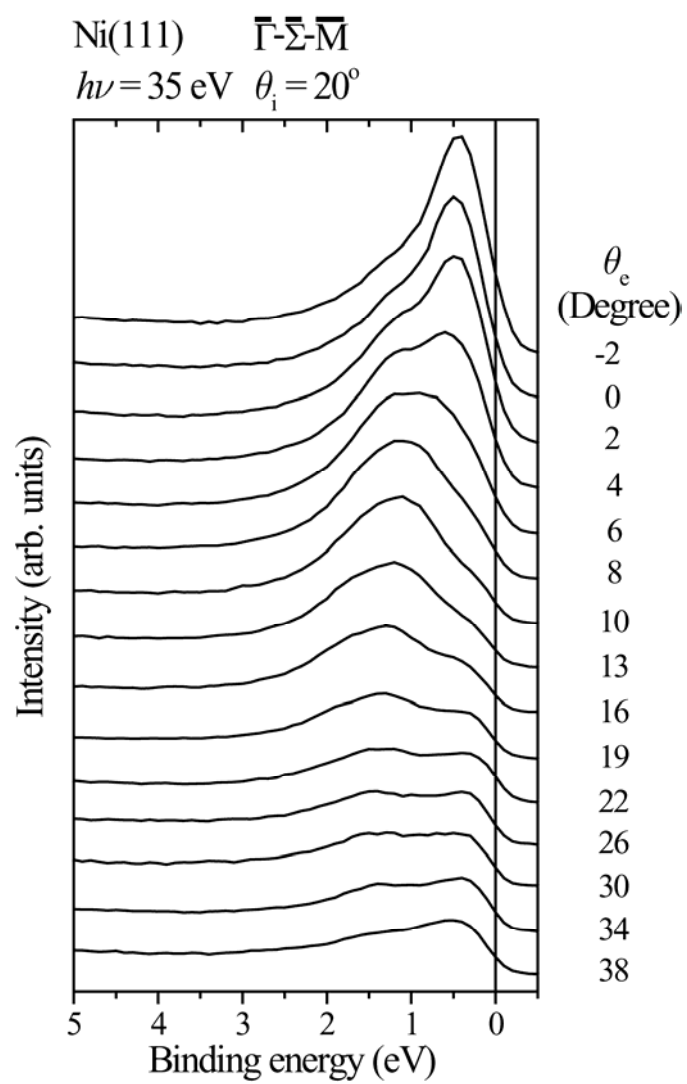


Fig. 3.15 Angular dependence of angle-resolved spectra along $\bar{\Gamma}-\bar{\Sigma}-\bar{M}$ symmetry.

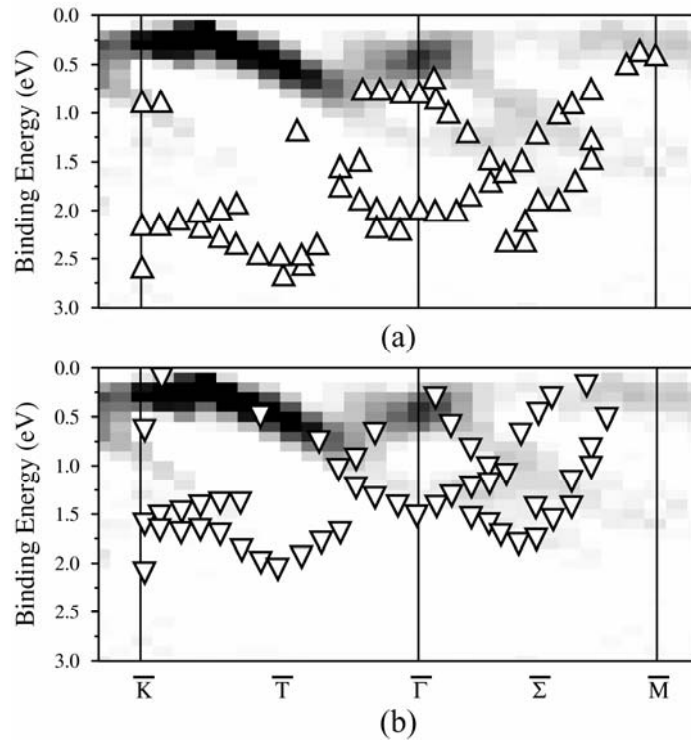


Fig. 3.16 Experimental surface energy-band map of the Ni(111), second derivative plotted, compared with a theoretical calculated by GGA method based on density function theory, opened triangles (Mittendorfer *et al.*, 1999), separated for up-spin (a) and down-spin (b).

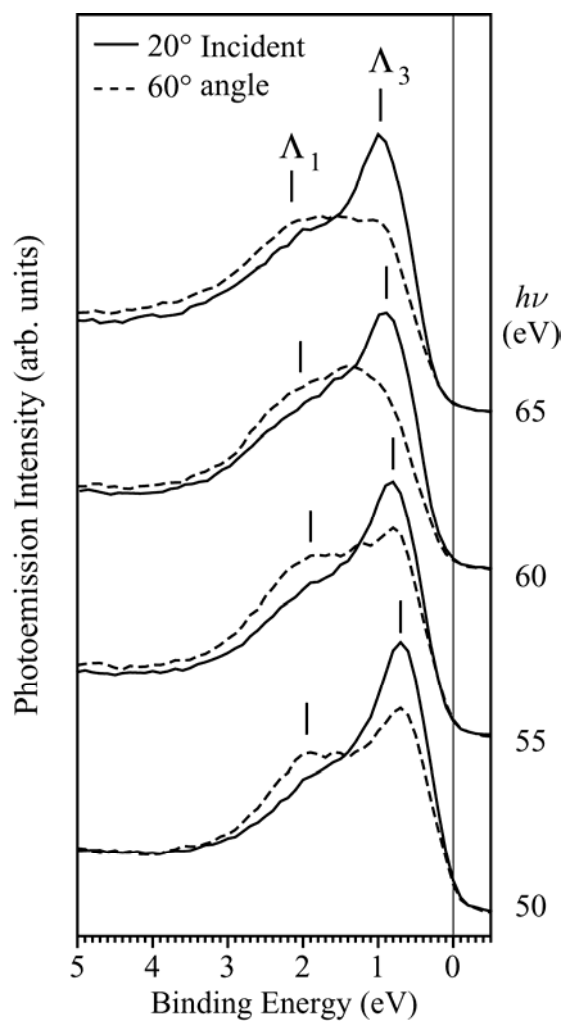


Fig. 3.17 Polarization dependence of photoemission spectra.

CHAPTER IV

DISCUSSION

4.1 Resonant Photoemission

The experimental data presented in the preceding chapter raise two important issues. One is the issue about the profile of the *MVV* sCK spectrum. The other is the issue how it is changed by the change in excitation energy. We summarize the results on the first issue as follows:

4.1.1 Profile of the *MVV* sCK Spectrum

(1) The *MVV* sCK band of Ni has very low intensity. Thus the relaxation processes of the $3p$ hole include the prominent competing processes such as fluorescence.

(2) Four features are found in the *MVV* sCK band. In the excitation energy range investigated in the present work, the lowest kinetic energy feature located at $\varepsilon_k = 49.8$ eV is separated from other features and has a FWHM of 1.7 eV. The width is caused by the lifetime of the state and phonons.

(3) The profile of the *MVV* sCK band excited with Mg radiation does not coincide well with that excited with photons with energy below $h\nu = 110$ eV. Disagreement is distinct as to the relative ratio of the intensity of component features; the feature at $\varepsilon_k = 49.8$ eV is not well separated from other features in EDC measured with the Mg $K\alpha$ excitation.

(4) The profile of the MVV sCK band does not coincide with that of the LVV CK band. Particularly, the MVV sCK band does not have the shape similar to that of LVV CK band ascribable to the multiplet structure arising from atomic d^8 configuration. If the MVV sCK band is ascribable to the spectrum of the atomic d^8 configuration, both LVV CK and MVV sCK bands should give the same profile. Another possibility is that the transition moments of the component lines of the multiplet arising from the d^8 configuration are considerably different between the CK and sCK transitions. However, this assumption does not explain the difference in the locations of the component lines. The MVV sCK spectrum of metallic Ni has the profile completely different from that of the MVV sCK spectrum of an isolated Ni atom that can be interpreted in terms of the multiplet coupling and the configuration interaction (Tiedtke *et al.*, 1999).

The results summarized above appear to indicate that the final state generating MVV sCK spectrum of metallic Ni excited with light cannot be interpreted in terms of the atomic energy levels. Rather, we consider that indispensable magnitude of the energy-band effect should be involved in the transition process. According to the Cini-Sawatzky theory (Cini, 1977; Cini, 1978; Sawatzky, 1977; Sawatzky and Lenselink, 1980; Bennett *et al.*, 1983) the profile of the Auger band becomes the self-convoluted band of the valence band in the limit of the low intra-atomic Coulomb energy. Let us consider a simple picture. Suppose the valence band is composed of two rectangular-shaped bands with the same width, W , separated by energy distance d ; the ratio of the heights is assumed to be $1:h$. The self-convoluted band comprises three component bands of the triangular shape with the same half width of W separated by the same distance, d ; the ratio of the heights of the

component bands is $1:(1/h+h):1$. Suppose that $h = 0.2$ and $d = 6.0$ eV as is the case of the main $3d$ band and the two-hole-bound-state band. Then the intensity ratio must be $1:5.2:1$. If we assume that the features at $\varepsilon_k = 59.5$ eV and 60.5 eV are inseparable, the observed ratio is $1:1.25:0.038$. The component separations are 6.5 eV and 3.2 eV. Any other shapes of the $3d$ band cannot explain the observed MVV sCK band reasonably through the self-convolution. Thus, we conclude that the simple self-convoluted-band picture cannot be applied. This point will be discussed later regarding the cause of the weak and narrow band at $\varepsilon_k = 49.8$ eV.

In this way, the two extreme pictures given in the Cini-Sawatzky theory (Cini, 1977; Cini, 1978; Sawatzky, 1977; Sawatzky and Lenselink, 1980; Bennett *et al.*, 1983) are not applicable to the MVV sCK spectrum of Ni. The spectrum should be taken for expressing the intermediate case where the intra-atomic Coulomb energy between two $3d$ holes, U , is not very much different from the width of the $3d$ band, W . We consider that the final state of the MVV sCK transition is composed of the self-convoluted valence band deformed considerably by the intra-atomic Coulomb interaction between two $3d$ holes. If the valence band consists of a single component, the final state band has two features. If the valence band consists of two component bands, the self-convoluted band has three component bands. Each of them has two component features. Then the MVV sCK band can have 6 component features at maximum. In practice, the component features overlap each other and the lifetime broadening obscures the structures. However, the assumption that the valence band has two component bands as we have made above leads to the situation that one of the components is the two-hole-bound-state. However there is no positive reason that the assumption like this is correct.

In the Cini-Sawatzky theory (Cini, 1977; Cini, 1978; Sawatzky, 1977; Sawatzky and Lenselink, 1980), there is a case where both split-off atomic-like line and the deformed self-convoluted band coexist. Thus, we can interpret the weak and narrow line at $\varepsilon_k = 49.8$ eV as being the split-off atomic-like line. If we consider that the separation between the center of the intense components and the band at $\varepsilon_k = 49.8$ eV gives the rough value of effective U , we can evaluate it as 8 eV. On the other hand, W is about 3 eV. The value of U of 8 eV appears to be too large if we compare the present spectrum with the numerically calculated model spectra given by Sawatzky and Lenselink. We do not find any multiplet components of the 49.8 eV line. The weak intensity of this band makes it difficult to find such a fine structure.

The Cini-Sawatzky theory (Cini, 1977; Cini, 1978; Sawatzky, 1977; Sawatzky and Lenselink, 1980) does not seem to explain the observed MVV sCK spectra quantitatively. This theory is applicable to the filled band like $3d$ band of Cu. We expect the filled $3d$ band in the intermediate state in Ni either in the low energy excitation case or in the case of considerable screening by conduction electrons.

Next we consider the fact that the profile of the MVV sCK band obtained by the Mg $K\alpha$ excitation does not coincide with that excited with light in the region around $h\nu = 100$ eV. With Mg $K\alpha$ radiation ($h\nu = 1253.6$ eV), electrons in the L_1 ($2s$, $\varepsilon_B = 1008.6$ eV), L_2 ($2p_{1/2}$, $\varepsilon_B = 870$ eV), L_3 ($2p_{3/2}$, $\varepsilon_B = 852.7$ eV), M_1 ($3s$, $\varepsilon_B = 110.8$ eV), M_2 ($3p_{1/2}$, $\varepsilon_B = 68.0$ eV), and M_3 ($3p_{3/2}$, $\varepsilon_B = 66.2$ eV) are excited. Then, transitions to extinguish a $2s$ hole, $2p$ holes, a $3s$ hole, and $3p$ holes occur following the pertinent core excitation. All these processes can generate $3p$ holes. As the direct or indirect cascade transitions of the processes, the MVV sCK transition

occurs. Thus, the MVV sCK spectrum in the case of the Mg $K\alpha$ excitation is complex and the widths of the component features are possibly increased. In LVV CK spectrum measurements, the widths of the bands can be decreased by coincidence spectroscopy (Lund *et al.*, 1997).

4.1.2 Resonant of the MVV sCK and the Two-hole-bound-state

The second issue is the change in the profile of the MVV sCK band caused by the change in excitation energy. The observed results are summarized as follows:

(1) The profile is changed at $h\nu = 78$ eV. The changed profile is recognized in the region below this energy, *i.e.*, $h\nu \leq 78$ eV.

(2) For excitation energy above $h\nu = 66$ eV, the width of the two-hole-bound-state band is enhanced as excitation energy is increased.

(3) For the excitation energy region, $76 \geq h\nu \geq 71$ eV, the MVV sCK spectrum overlaps the two-hole-bound-state band and is deformed appreciably. Both bands are inseparable.

(4) In the range $76 \geq h\nu \geq 67$ eV, the location of the highest peak, the apparent peak of the two-hole-bound-state band, deviates from the constant-binding-energy line for $\varepsilon_B = 6.3$ eV.

(5) The complete merger of the MVV sCK band and two-hole-bound-state band occurs in the region $70 \geq h\nu \geq 66$ eV.

(6) The change in the profile of the MVV sCK band cannot be interpreted in terms of the intensity changes of the satellites at $\varepsilon_B = 11$ eV and 13.5 eV caused by resonance.

(7) The CIS spectrum for the two-hole-bound-state band exhibits the $3p-3d$ resonance in the region $80 \geq h\nu \geq 65$ eV. This covers an energy interval of 15 eV.

(8) For the main $3d$ band, the CIS spectrum exhibits features in the spectral region $78 \geq h\nu \geq 48$ eV.

(9) The main $3d$ band shows the weak $3p-3d$ resonance.

In order to understand the observed results summarized above, we consider the outer-shell electronic states of Ni on the basis of the energy-band picture. The energy-bands are formed by the localized and correlated states with the d symmetry and widely spread conduction states with the sp symmetry. The band with d symmetry, referred to as the $3d$ band, is considerably affected by the electron correlation. The bands are also affected by the sd hybridization. The eigen functions are qualitatively expressed in the linear combination of atomic orbitals (LCAO) approximation as (Jo *et al.*, 1983)

$$\begin{aligned} |\varphi_d, n\mathbf{k}\rangle &= a_{n\mathbf{k}} |3d\rangle + b_{n\mathbf{k}} |4s\rangle \\ |\varphi_c, m\mathbf{k}\rangle &= a_{m\mathbf{k}} |3d\rangle + b_{m\mathbf{k}} |4s\rangle \end{aligned} \quad (4.1)$$

Here $a_{j\mathbf{k}}$ ($j = n, m$) and $b_{j\mathbf{k}}$ ($j = n, m$) are constant, \mathbf{k} the electron wave vector, and j the quantum number distinguishing the energy-bands. The electron spin is ignored here. We also ignore the p orbital in this qualitative argument. Although $|3d\rangle$ comprises states with different components of orbital angular momentum quantum

number, we do not indicate it. Thus, in the practical calculation, rigorous formalism must be adopted (David and Feldkamp, 1981; Jo *et al.*, 1983; Tanaka and Jo, 1992). The $3d$ band is not completely filled with electrons but an electron is missing. In other words, a hole exists on average. This state is described as \hat{d}_k . In this band, the unfilled d level exists above the Fermi level. In other words, the Fermi level cuts the $3d$ band in the upper part of the band. The empty conduction band occurs above the Fermi level. The empty band part corresponds to one electron per atom on average. The sd hybridization occurs as expressed in (4.1). Thus \hat{d}_k and c_k are hybridized states.

According to the solid state data, the number of $3d$ electrons in a Ni atom is 9.46 on average (Kittel, 1996). Oh *et al.* (1982) pointed out that the distribution of the $3d^n$ configuration to give the average number of $3d$ electron per atom is given by the bipolynomial distribution if the correlation interaction between $3d$ electrons is ignored. The bipolynomial distribution gives fractions of $3d^n$ to be 0.583, 0.344, and 0.088 for $3d^{10}$, $3d^9$, and $3d^8$, respectively. If this is correct, the major component of the ground state of Ni arises from the $3d^{10}$ configuration. However, this is not the case. Jo and Sawatzky (1991) claimed that the distribution of the $3d$ configurations in the ground state is 15-20% $3d^{10}$, 60-70% $3d^9$, and 15-20% $3d^8$ to explain the experimental data well. Tanaka and Jo (1992) claimed that the distribution is 21%, 61%, and 18% for $n = 10, 9$, and 8 , respectively. This gives the average number of $3d$ electrons per atom is 8.97. Tjeng *et al.* (1993) gave the distribution as $n = 16\%$, 49% , and 35% . The average number of $3d$ electrons per atom in their case is 9.19.

In the present work, we consider the state of metallic Ni in terms of the energy-band. The state expressed as (4.1) is considered to be renormalized in the Bloch functions with the correlation. According to the reported results of the energy-band calculation (Weling and Callaway, 1982), the conduction band with large dispersion occurs in the region of binding energy larger than 4 eV. In this band, the mixing of the state with the d symmetry is weak. The majority of $3d$ band exists in the binding energy region below $\varepsilon_B = 3$ eV. At $\varepsilon_B = 1$ eV the $3d$ band exists with very small dispersion. In the region between $\varepsilon_B = 1$ eV and 3 eV, the bands with definite dispersion occur. They are $3d$ bands with the sd hybridization.

The Auger effect like the MVV sCK transition is caused by the localized transition involving a core hole. If the outershell state is the band state, two holes brought about by the transition may have different wave vectors \mathbf{k} and \mathbf{k}' and not necessarily be on the same lattice site. The Cini-Sawatzky theory (Cini, 1977; Cini, 1978; Sawatzky, 1977; Sawatzky and Lenselink, 1980) employs an interesting approximation like the exciton state. It is similar to the method to make a Wannier exciton in a wide-gap semiconductor. There, the translational symmetry of electron energy and concomitant wave functions regarding the electron wave vector is utilized to introduce the configuration interaction. The translational symmetry regarding the space coordinate is also used. The configuration here stands for the arrangement of the wave functions in terms of the lattice site and the wave vector. By this approximation, the localized eigen functions are formed from the delocalized Bloch states. In this approximation, \mathbf{K} ($= \mathbf{k} - \mathbf{k}'$) has meaning.

The MVV sCK transition generates the \hat{d}_k^2 and \hat{d}_k^3 states. These states are unstable and decay through the screening by conduction electrons. A few final states are expected to occur according to the emergent intermediate states. This is the source of the excitation energy dependence of the profile of the MVV sCK band. This issue will be treated later. The decay occurs quite fast. Thus the appreciable lifetime broadening is inevitable.

In general, the optically induced Auger transition including the sCK and CK transitions occurs to extinguish the core hole generated by the optical excitation. The electron jumping into the core level is in the relaxed outershell level. The MVV sCK transition in the present case, however, is not like this. The $3p$ photoelectron lines exhibited in Fig. 3.7 are found to be wide with FWHM reaching 5 eV. This suggests that the decay of the $3p$ hole occurs very fast. Naturally the sCK decay occurs while the $3p$ hole is being generated. Therefore, the optical excitation and the MVV sCK transition take place almost as a single process not as the two step process where the optical transition occurs first and the sCK transition follows after the excited state is relaxed. The screening by conduction electrons participates also in the transition process.

In the case where the innershell-outershell resonance excitation is not taken into account, the transition cross-section is given as (Jo *et al.*, 1983)

$$\sigma_f = \sum_{mm'} \left| \langle f | V_A | m \rangle \langle m | G | m' \rangle \langle m' | V_R | g \rangle \right|^2 \quad (4.2)$$

Here, $|g\rangle$ represents the ket vector associated with the ground state eigen function; $\langle f |$ is the bra vector of the final state; $|m\rangle$ and $|m'\rangle$ are the kets of the intermediate

state; V_A is the perturbation potential to give rise to the Auger transition and V_R is that for the optical transition; G is the Green function to determine the line shape. In a simple case, the matrix element of G is accompanied by Kronecker's delta, $\delta_{m,m'}$. It should be remarked that the final state with two $3d$ holes is also generated by the optical excitation as already mentioned. This is attributed to the ground state, \hat{d}_k , with one $3d$ hole.

The matrix elements of G and V_A are the functions to give the spectral profile and its excitation energy dependence. In the simplest case, the matrix element of G gives an asymmetric Lorentzian shape as a renormalized form. We write DOS of the final state, \hat{d}_k^2 , as $D(\varepsilon_B, \hat{d}_k^2)$. $D(\varepsilon_B, \hat{d}_k^2)$ arises from the summation as to m and m' in (4.2) on the assumption that the dependence of the matrix elements on m and m' is ignored and they are replaced with an average value. The two factors decide the profile of the MVV sCK band. One is $D(\varepsilon_B, \hat{d}_k^2)$. The other is $\left| \langle f | V_A | m \rangle \right|^2$. Suppose $\left| \langle f | V_A | m \rangle \right|^2$ varies slowly with energy and does not affect the spectral profile appreciably, then the profile is decided by $D(\varepsilon_B, \hat{d}_k^2)$. Thus, we should know what final and intermediate states are generated by the transition.

The final state is reached from $|m\rangle$ through $\left| \langle f | V_A | m \rangle \right|^2$. Therefore, it is our problem to find what $|m\rangle$ is generated by the excitation of a $3p$ electron. It is evident that the optical excitation occurs as follows:

$$\hat{d}_k c_k + h\nu \rightarrow \hat{p} \hat{d}_k c_k u_l. \quad (4.3)$$

A few different intermediate states, $\hat{p}\hat{d}_k c_k u_l$, are brought about through u_l according to the magnitude of excitation energy. We consider three cases qualitatively: (i) $h\nu$ is sufficiently high (ii) $h\nu$ takes an intermediate magnitude (iii) $h\nu$ is low. The results of the consideration are summarized in Table 4.1. In the final state configuration shown in Table 4.1, the first terms in the parenthesis give the major contribution. Other two terms give spectral deformation. The content of Table 4.1 is explained below.

(i) The case of sufficiently high excitation energy

When excitation energy is sufficiently high, the excited electron is raised to a very high energy state. The electron in the state, u_l , does not interact with electrons in the $\hat{d}_k c_k$ state. Thus, the *MVV* sCK transition occurs in the following manner:

$$\hat{p}\hat{d}_k c_k u_l \rightarrow \hat{d}_k^3 c_k u_l u_A \rightarrow \hat{d}_k^2 \hat{c}_k u_l u_A \quad (3.5)$$

We assume that the screening occurs in the process as

$$\hat{d}_k^3 c_k \rightarrow \hat{d}_k^2 \hat{c}_k \quad (4.4)$$

From a different point of view, this can be taken for the result of the *sd* hybridization. The processes described above give the *MVV* sCK spectrum which is not deformed. We add subscript k to emphasize the self-convoluted valence band aspect contributing to this state.

(ii) Intermediate excitation energy case

In this case, we consider that the u_l electron occupies the state of c_k .

The optical transition occurs practically as

$$\hat{d}_k c_k + h\nu \rightarrow \hat{p} \hat{d}_k c_k^* \quad (4.5)$$

Then, the *MVV* sCK transition occurs simultaneously as

$$\begin{aligned} \hat{p} \hat{d}_k c_k^* &\rightarrow \hat{d}_k^3 c_k^* u_A \rightarrow \hat{d}_k^* \hat{c}_k u_A \\ &\rightarrow \hat{d}_s^2 \hat{c}_k u_A \end{aligned} \quad (4.6)$$

$$\hat{p} \hat{d}_k c_k^* \rightarrow \hat{d}_k^3 c_k^* u_A \rightarrow \hat{d}_k^2 c_k u_A \quad (3.6)$$

Thus the final state of the transition is written as

$$\psi = (\hat{d}_k^2 c_k + \hat{d}_s^2 \hat{c}_k + \hat{d}_k^* \hat{c}_k) u_A \quad (4.7)$$

The *MVV* sCK spectra reflect the energy distribution of the state (4.7). The first term in the parenthesis gives the major contribution. The other two give the deformation of the spectrum. The $\hat{d}_k^* \hat{c}_k u_A$ state is realized seemingly through $\hat{p} c_k^* \rightarrow \hat{c}_k u_A$. The probability of generating $\hat{d}_k^* \hat{c}_k u_A$ is considered to be small and the main part of the realized final state is $\psi = (\hat{d}_s^2 \hat{c}_k + \hat{d}_k^2 c_k) u_A$ instead of (4.7). However, the CIS spectrum for $\varepsilon_B = 0.6$ eV illustrated in Fig. 3.12 shows the weak resonance enhancement of the emission intensity above the threshold of the $3p$ excitation. This indicates the existence of the weak $\hat{d}_k^* \hat{c}_k u_A$ final state.

In the intermediate excitation energy range, the *MVV* sCK spectrum has the profile that is mixed with the two-hole-bound-state spectrum and changed considerably with excitation energy. The details of this behavior cannot be explained by the change in the intensity of the components of the multiplets of the $3d^8$ configuration. In the high excitation energy region, the final state of the *MVV* sCK transition is $\hat{d}_k^2 \hat{c}_k u_A$. In the intermediate excitation energy range, a different type of final state occurs: $\hat{d}_k^2 c_k u_A$. The final state with this term gives the deformed *MVV* sCK

spectra through the contribution of other two terms. The ordinary final state of the transition is weakly screened by conduction electrons. It has the form as if a conduction electron is trapped by the two $3d$ holes making a virtual bound state. If the screening is more complete, the two-hole-bound-state, $\hat{d}_s^2\hat{c}_k$, results in. If the screening is far more complete, a single hole state results in and it gives the state similar to the main $3d$ band.

(iii) Low excitation energy case

We consider that the u_l electron occupies the empty $3d$ level leading to the filled up $3d$ band, d_k . In this case, the optical transition occurs practically as

$$\hat{d}_k c_k + h\nu \rightarrow \hat{p} d_k c_k \quad (4.8)$$

Thus, the MVV sCK transition occurs as

$$\begin{aligned} \hat{p} d_k c_k &\rightarrow \hat{d}_k^2 c_k u_A \rightarrow \hat{d}_k^* \hat{c}_k u_A \\ &\rightarrow \hat{d}_s^2 \hat{c}_k u_A \end{aligned} \quad (4.9)$$

The final state of the transition is written as

$$\psi = (\hat{d}_s^2 \hat{c}_k + \hat{d}_k^2 c_k + \hat{d}_k^* \hat{c}_k) u_A \quad (4.10)$$

The intermediate state and, thus, the final state is also reached by the direct excitation as

$$\hat{d}_k c_k + h\nu \rightarrow \hat{d}_k^2 c_k u_l \rightarrow (\hat{d}_s^2 \hat{c}_k + \hat{d}_k^* \hat{c}_k) u_l \quad (4.11)$$

In this way, the final states (4.10) and that of (4.11) cannot be distinguished if u_l is almost equal to u_A . Then, the resonance and the concomitant interference occur.

An important issue here is that the state $\hat{d}_k^2 c_k u_A$ remains also in the final state with a low intensity. The c_k state, *i.e.*, the state of a $4s$ electron, exists from the

beginning as the band electron state. The c_k^* state of (4.5) and (4.6) in the intermediate state is brought about by the optical excitation. In other words, the different intermediate states with different energy reach the different final states. That the main $3d$ state appears in the final state of MVV sCK transition explains the resonance enhancement of the main $3d$ band above the $3p$ excitation threshold as recognized in Fig. 3.12.

When the resonance occurs, the width of the two-hole-bound-state band is broadened. The peak shift is also recognized. As excitation energy increases, the features arising from $\hat{d}_k^2 c_k$ are split off as shown in Fig. 3.6.

In the generation of the MVV sCK transition, the role of the screening electron, the hybridized conduction electron, is important. The excited electron can occupy the state to form a well defined state, or it stays in the spectator electron state according to its kinetic energy. This is similar to the case of the final state interaction referred to as the post-collision interaction describing the relation of atomic photoemission to the Auger effect (Prideaux and Madison, 2003; Hanashiro *et al.*, 1979; Schmidt, Sandner, Mehlhorn, Adam, and Wuilleumier, 1977). Before the excited photoelectron leaves the atom, the Auger transition takes place and the excited photoelectron is affected by the potential of the two holes generated by the Auger transition. On the other hand, the Auger electron is affected the potential screened by the optically excited electron, the spectator electron. Such interactions affect the kinetic energies of pertinent electrons. This phenomenon is distinct when the energy of the optically excited electron is low, since the spectator electron stays around the atomic core for a longer time. The post-collision-interaction phenomenon manifests itself as the shift of the Auger electron peak from the constant-kinetic-energy line

toward high kinetic energy as excitation energy approaches the excitation threshold. A classical theory as well as a semiclassical theory was reported and investigators compared their data with both theories to find the qualitative agreement (Prideaux and Madison, 2003; Hanashiro *et al.*, 1979; Schmidt *et al.*, 1977). The relation between the kinetic energy shift and the excitation energy is dependent on the lifetime broadening of the line (Prideaux and Madison; Hanashiro *et al.*, 2003; Schmidt *et al.*, 1977).

As is obvious in Fig. 3.9 and Fig. 3.10, the deviation of the energy of the sCK electron from the constant-binding-energy line occurs toward high binding energy side or the low kinetic energy side. This tendency is not necessarily against the cause of the energy shift found in the post-collision interaction in atomic spectra. The direct formation of the two-hole-bound-state does not totally participate in the $3p-3d$ resonance. Particularly, the existence of the two-hole-bound-state that does not make resonance must be considered in detail. The phenomenon apparently means that the existence of two different final states having almost same energy is seemingly against the results of simple quantum theory. In the case of the direct generation of the two-hole-bound-state, the photoelectron is affected by the potential of a $3d$ hole. In the case of the MVV sCK transition, the sCK electron is attracted by the potential of a $3p$ hole that is stronger. This makes the binding energy of the $3d$ electron higher and the kinetic energy of the emitted sCK electron lower.

Regarding the exciton-like state proposed in the Cini-Sawatzky theory (Cini, 1977; Cini, 1978; Sawatzky, 1977; Sawatzky and Lenselink, 1980), the excited spectator electron can be trapped by the two holes generated by the sCK transition in the form of the virtual bound state, if the energy of the spectator electron is low. This

is also a kind of final state interaction. If the energy of the excited electron is low, it is raised to the $3d$ state and participates directly in the sCK transition. Thus the form of the final state interaction is complicated. Theoretical investigations should be made on this issue.

At this stage, we should remark an important issue: The peak around $\varepsilon_B = 6.3$ eV is found in the whole excitation energy region. The peak is clearly found in the region where the two-hole-bound-state band considerably overlaps the MVV sCK band and considerably destroys it. This indicates that the peak is attributed to the generation of the two-hole-bound-state by the direct excitation. In other words, the final state of the MVV sCK transition, (4.7), coexists with the final state of the direct excitation of the $3d$ band, (4.10). The direct formation of the two-hole-bound-state does not totally participate in the $3p-3d$ resonance. Although the two final states could have the different energy dependence, the two-hole-bound-state part resonates and the two final states cannot be distinguished. As mentioned already, the resonance takes place incompletely in some excitation energy region. The kinetic energy of the emitted electron is affected by holes in the mixed states. This is a sort of final state interaction and shows up in the shift of the energy of the emitted electron.

In the case of solid Ni, the phenomenon described above raises the problem of the investigation of the intermediate state and the final state in detail. This is especially interesting since the whole transition process must be treated as a single process. The issue has not been investigated theoretically. Igarashi, Unger, Hirai, and Fulde (1994) developed the theoretical treatment of the three-body interaction as applied to the resonance problem. The further development of the theory is invoked.

In the present study, the aspect how two superficially different final states, the two-hole-bound-state and the MVV sCK final state mix and become indistinguishable has been traced. This behavior is seemingly similar to the Lu-Fano effect in atomic spectra (Lu and Fano, 1970).

The CIS spectrum gives the energy distribution of the state with constant binding energy from which photoelectrons are excited. The resonance-interference region of the two-hole-bound-state and the MVV sCK final state extends up to 20 eV above the Fermi level as found in Fig. 3.11. This range is much wider than the width of the empty $3d$ band found in the inverse photoemission data (Tezuka *et al.*, 2004). This wide range is brought about by the $3p-3d$ resonance. It is not the width of the localized state but the energy region of the continuous band that is responsible for the resonance-interference. The relevant conduction state hybridized with the $3d$ state exists in the intermediate excitation energy region. The final state, (4.7), is consistent with this idea.

The CIS spectrum for $\varepsilon_B = 0.6$ eV which is the CIS spectrum for the main $3d$ band has a band with a peak at $h\nu = 55$ eV. In this band, features are found at $h\nu = 50$ eV and 63 eV. This band extending from $h\nu = 47$ eV to 65 eV is located below the threshold of the $3p$ excitation. Thus, this band is not caused by resonance. Possible cause for this is the $3d \rightarrow \varepsilon f$ transition. However, we cannot conclude this definitely. At present, the causes of the features occurring in the total yield spectrum are not clarified.

The difference between the LVV CK and MVV sCK spectra must be remarked. If we consider only the atomic final state with the configuration, $3d^8 4s$,

there is no difference between the final states of the LVV CK and MVV sCK transitions as pointed out already. In fact, Fig. 3.8 shows considerable difference. As described so far, we consider that the simple atomic model is not applicable to the MVV sCK transitions. In the LVV CK transition, the large attractive potential of the $2p$ hole makes the outershell electron orbits shrink and the states of the outershell electrons become more like the atomic states. This is very different from Doniach-Šunjić effect (Doniach and Šunjić, 1970) in which conduction electrons are inelastically scattered by the $2p$ hole. The $2p$ hole does not only give rise to the Fermi-edge singularity but also alter the whole outershell electron state. This is evident in the occurrence of the white lines (Tjeng *et al.*, 1993; Magnuson *et al.*, 1998; Iacobucci *et al.*, 1999; Knorren *et al.*, 2000; Coulthard *et al.*, 2001; Föhlisch *et al.*, 2002; Pagliara *et al.*, 2002). On the other hand, the absorption spectrum of the $3p$ electron known from the total yield spectrum shown in Fig. 3.13 exhibits the steep onset of absorption and roughly flat band above it. This is more like the absorption to the unoccupied energy-band. In the case of the CK transition, it is influenced by the potential of the core hole on the valence state. Even if a $2p$ hole is generated suddenly and the potential for the outershell electron changes abruptly, the overall optical transition follows successively in a finite time (Schiff, 1968). Even though the transition occurs as a single process, the change in the outershell state in the intermediate state definitely affects the observed spectrum.

Table 4.1 Relations between the *MVV* sCK spectrum and the excitation photon energy. d_k : Filled $3d$ band; \hat{d}_k : $3d$ band with a hole in the ground state; \hat{d}_k^n : $3d$ band with n holes; \hat{d}_s^2 : Two-hole-bound-state; \hat{d}_k^* : $3d$ band with a hole with higher binding energy; c_k : Conduction band; \hat{c}_k : Conduction band with an extra hole; c_k^* : Conduction band with a high energy electron; u_l : States of high energy electrons; u_A : State of the sCK electron; \hat{p} : $3p$ hole state.

Excitation region	high energy	intermediate energy	low energy
$h\nu$	$h\nu \geq 79\text{eV}$	$79\text{eV} \geq h\nu \geq 71\text{eV}$	$71\text{eV} \geq h\nu \geq 66\text{eV}$
Final state	$\hat{d}_k^2 \hat{c}_k u_l u_A$	$[\hat{d}_k^2 c_k + \hat{d}_s^2 \hat{c}_k + \hat{d}_k^* \hat{c}_k] u_A$	$[\hat{d}_s^2 \hat{c}_k + \hat{d}_k^2 c_k + \hat{d}_k^* \hat{c}_k] u_A$
Intermediate state	$\hat{p} \hat{d}_k c_k u_l$	$\hat{p} \hat{d}_k c_k^*$	$\hat{p} d_k c_k$
Apparent transition	$\hat{d}_k^3 c_k u_l u_A$	$\hat{d}_k^3 c_k^* u_A$	$\hat{d}_k^2 c_k u_A$
Resonance aspect	non-resonant	weakly resonant	resonant
Name	sCK final state	quasi-two-hole-bound-state and single $3d$ hole state	two-hole-bound-state and single $3d$ hole state
Remarks	unstable final state; large lifetime broadening	mixture of the two-hole-bound-state and the sCK final state; complex spectral shape	peak shift; broadened band

4.2 Energy-band Structure

ARPES is used for the energy-band of an excited or quasiparticle state (Smith and Kevan, 1991) while the energy-band calculation base on DFT is a ground state energy-band calculation. To resolve this problem, the GGA method is developed form the DFT by including the exchange-correlation hole because many-electron ground state system is conveniently calculated by the DFT (Perdew *et al.*, 1992).

Nickel has been used as a prototype of highly electron correlated system. In the case of Ni(111), some difference between the measurement results and the calculated energy-band can be seen in Fig. 3.16 such as the width of *d*-band and the exchange splitting. The experimental *d*-band width is smaller than the calculated. This can be seen when combining the calculated up-spin and down-spin. The up-spin bands in Fig. 3.16 (a) seem less agreement with the experimental bands than the down-spin bands in Fig. 3.16 (b). This is due to the larger of calculated exchange splitting than the measured exchange splitting. The reported experimental exchange splitting is 0.31 ± 0.03 eV for the upper Λ_3 band at the temperature of 300 K (Himpsel *et al.*, 1979). We could not resolve the exchange splitting in our experimental results because the resolution was not high enough.

We used s-polarized light in the surface energy-band measurements. In the case of normal emission at the $\bar{\Gamma}$ point, dipole selection rule can be applied (Hermanson, 1977). The Λ_3 and Λ_1 were obtained as expected. We have checked the intensity dependence of light polarization as in Fig. 3.17. Even the Λ_1 band is suppressed by the s-polarized light it is still obvious because the s-polarized light at the 20° is not 100% s-polarized light.

CHAPTER V

CONCLUSION

The findings of this thesis work can be summarized as follow:

- The relaxation processes of the $3p$ hole in Ni include the prominent competing processes such as fluorescence. This results in very low intensity of the MVV sCK band.
- The measured spectral shape of the MVV sCK band shows the features at electron kinetic energy of 49.8 eV, 56.3 eV, 59.5 eV and 60.5 eV. Based on the Cini-Sawatzky theory, the effective intra-atomic Coulomb energy at a large value was found to be 8 eV when the feature at 49.8 eV is considered to be the split-off atomic-like band.
- The spectral shape of the MVV sCK band measured by excitation with vacuum ultraviolet (VUV) light does not coincide with that obtained by the Mg $K\alpha$ excitation nor with that of the L_3VV CK band.
- The shape of MVV sCK spectrum changes as the excitation energy changes even the excitation is in the VUV regime. The excitation energy in which such spectral change occurs extends from the $3p$ threshold to 10 eV above it. As the kinetic energy for the MVV sCK band starts to overlap that of the two-hole-bound-state band, the MVV sCK band change its shape considerably and the two bands get inseparable. In this excitation energy region, the spectator electron excited optically forms a virtual

bound state with the two $3d$ holes. The location of the apparent two-hole-bound-state band shifts toward higher binding energy on the $3p-3d$ resonance. This can be interpreted as the kind of the final state interaction. The suggested intermediate and final states of the single step transition are consistent with the constant-initial-state spectra and total-photo yield spectrum.

- In addition, the surface energy-band along two lines of symmetry, *i.e.*, $\bar{\Gamma}-\bar{\text{T}}-\bar{\text{K}}$ and $\bar{\Gamma}-\bar{\Sigma}-\bar{\text{M}}$, have been mapped as the first two band mapping at the Siam Photon Laboratory.

REFERENCES

REFERENCES

- Anilturk, O. S., and Koymen, A. R. (2001). Spin polarized Auger electron spectroscopy of Fe and Ni. **Journal of Applied Physics** 89 (11): 7233-7235.
- Bennett, P. A., Fuggle, J. C., Hillebrecht, F. U., Lenselink, A., and Sawatzky, G. A. (1983). Electronic structure of Ni and Pd alloys. III. Correlation effects in the Auger spectra of Ni alloys. **Physical Review B** 27 (4): 2194-2209.
- Berglund, C. N. and Spicer, W. E. (1964). Photoemission studies of copper and silver: theory. **Physical Review** 136 (4A): 1030-1044.
- Björneholm, O., *et al.* (1990). Resonant photoemission at core-level shake-up thresholds: valence-band satellites in nickel. **Physics Review B** 41 (15): 10408-10412.
- Briggs, D. and Seah, M. P. (1996). **Practical surface analysis (vol. 1): Auger and X-ray photoelectron spectroscopy** (2nd ed.). England: John Wiley & Sons Ltd.
- Cini, M. (1977). Two hole resonances in the *XVV* Auger spectra of solids. **Solid State Communications** 24: 681-684.
- Cini, M. (1978). Comment on quasiautomic Auger spectra in narrow-band metals. **Physical Review B** 17 (6): 2788-2789.
- Cini, M., and D'Andrea, A. (1984). Dynamic screening effects on Auger *CVV* line shapes of solids. **Physical Review B** 29 (12): 6540-6547.
- Clark, J. (2002). **Types of Catalysis** [online]. Available:
<http://www.chemguide.co.uk/physical/catalysis/introduction.html>

- Clauberg, R., Gudat, W., Kisker, E., Kuhlmann, E., and Rothberg, G. M. (1981). Nature of the resonant 6-eV satellite in Ni: photoelectron spin-polarization analysis. **Physical Review Letters** 47 (18): 1314-1317.
- Connelly, J. W. D. (1967). Energy-band in ferromagnetic nickel. **Physical Review** 159: 415-426.
- Coulthard, I., *et al.* (2001). Threshold behavior of the Cu $L_3M_{4,5}M_{4,5}$ Auger effect of Cu metal at the L_3 edge. **Physical Review B** 64: 115101.
- Davis, L. C., and Feldkamp, L. A. (1981). Resonant photoemission involving super-Coster-Kronig transitions. **Physical Review B** 23 (12): 6239-6253.
- Doniach, S., and Šunjić, M. (1970). Many-electron singularity in X-ray photoemission and X-ray line spectra from metals. **Journal of Physics C: Solid State Physics** 3: 285-291.
- Eberhardt, W., and Plummer, E. W. (1980). Angle-resolved photoemission determination of the band structure and multielectron excitations in Ni. **Physical Review B** 21 (8): 3245-3255.
- Föhlisch, A., *et al.* (2002). Auger resonant Raman scattering in itinerant electron systems: continuum excitation in Cu. **Physical Review Letters** 88 (2): 027601
- Fuggle, J. C., and Mårtensson, N. (1980). Core-level binding energies in metals. **Journal of Electron Spectroscopy and Related Phenomena** 21: 275-281.
- Girvin, S. M., and Penn, D. (1990). Resonant satellites in photoemission and Auger spectra of d-band metals. **Journal of Applied Physics** 52 (3): 1650-1653.
- Guillot, C., *et al.* (1977). Resonant photoemission in nickel metal. **Physical Review Letters** 39 (25): 1632-1635.

- Hanashiro, H., *et al.* (1979). Post-collision interaction in photoexcited argon *LMM* Auger processes. **Journal of Physics B: Atomic, Molecular and Optical Physics** 12 (24): L775-L778.
- Hermanson, J. (1977). Final-state symmetry and polarization effects in angle-resolved photoemission spectroscopy. **Solid State Communications** 22: 9-11.
- Himpsel, F. J., Knapp, J. A., and Eastman, D. E. (1979). Experimental energy-band dispersions and exchange splitting for Ni. **Physical Review B** 19 (6): 2919-2927.
- Hopster, H., *et al.* (1983). Temperature dependence of the exchange splitting in Ni studied by spin-polarized photoemission. **Physical Review Letters** 51 (9): 829-832.
- Iacobucci, S., Sacchi, M., Marassi, L., Marocchi, V., and Stefani, G. (1999). L_2L_3V Coster-Kronig decay in nickel: the near-edge region. **Physical Review B** 59 (15): 9898-9902.
- Igarashi, J. I., Unger, P., Hirai, K., and Fulde, P. (1994). Local approach to electron correlations in ferromagnetic nickel. **Physical Review B** 49 (23): 16181-16190.
- Ishii, T. (1989). Solid state spectroscopy in the vacuum ultraviolet and soft X-ray region. In H. Winick, D. Xian, Ming-han Ye and T. Huang (eds.). **Applications of synchrotron radiation** (pp. 371-514). New York: Gordon and Breach Science Publishers.
- Jach, T., and Powell, C. J. (1981). L_3VV Auger-electron line shapes and peak positions for near-threshold electron excitation in nickel and copper. **Physical Review Letters** 46 (14): 953-956.

- Jo, T., and Sawatzky, G. A. (1991). Ground state of ferromagnetic nickel and magnetic circular dichroism in Ni $2p$ core X-ray-absorption spectroscopy. **Physical Review B** 43 (10): R8771-R8774.
- Jo, T., Kotani, A., Parlebas, J. -C., and Kanamori, J. (1983). A theory of resonant photoemission in Ni. **Journal of the Physical Society of Japan** 52 (7): 2581-2591.
- Kakizaki, A., *et al.* (1983). Resonant photoemission in transition-metal chlorides. **Physical Review B** 28 (2): 1026-1035.
- Kanamori, J. (1963). Electron correlation and ferromagnetism of transition metals. **Progress of Theoretical Physics** 30 (3): 275-289.
- Kashiwakura, T., *et al.* (1993). Resonant photoemission in CeNi single crystals. **Physical Review B** 47 (12), 6885-6897.
- Kinoshita, T., *et al.* (1993). Evidence for Fano interference in spin polarization of the 6-eV satellite in Ni valence-band photoemission. **Physical Review B** 47 (11): R6787-6790.
- Kisker, E., Schröder, K., Gudat, W., and Campagna, M. (1985). Spin-polarized angle-resolved photoemission study of the electronic structure of Fe(100) as a function of temperature. **Physical Review B** 31 (1): 329-339.
- Kittel, C. (1996). **Introduction to Solid State Physics** (7th ed.). USA: John Wiley & Sons, Inc.
- Knorren, R., Bennemann, K. H., Burgermeister, R., and Aeschlimann, M. (2000). Dynamics of excited electrons in copper and ferromagnetic transition metals: theory and experiment. **Physical Review B** 61 (14): 9427-9440.

- Kotani, A., and Toyozawa, Y. (1974). Photoelectron spectra of core electrons in metals with an incomplete shell. **Journal of the Physical Society of Japan** 37 (4): 912-919.
- Liebsch, A. (1979). Effect of self-energy corrections on the valence-band photoemission spectra of Ni. **Physical Review Letters** 43 (19): 1431-1434.
- Liebsch, A. (1981). Ni *d*-band self-energy beyond the low-density limit. **Physical Review B** 23 (10): 5203-2512.
- Lindau, I. (2001). Subshell Photoionization cross sections. In A. Thompson, *et al.* (ed.). **X-ray data booklet**. USA.
- Lu, K. T., and Fano, U. (1970). Graphic analysis of perturbed Rydberg series. **Physical Review A** 2 (1): 81-86.
- Lund, C. P., Thurgate, S. M., and Wedding, A. B. (1997). Auger photoelectron coincidence spectroscopy studies: trends in the $L_{2,3} - M_{4,5}M_{4,5}$ line shapes across the 3d transition-metal series. **Physical Review B** 55 (8): 5455-5465.
- Madden, R. P. and Codling, K. (1963). New autoionizing atomic energy levels in He, Ne, and Ar. **Physical Review Letters** 10 (12): 516-518.
- Magnuson, M., *et al.* (1998). Resonant Auger spectroscopy at the $L_{2,3}$ shake-up thresholds as a probe of electron correlation effects in nickel. **Physical Review B** 58 (7): 3677-3681.
- Mårtensson, N., Nyholm, R., and Johansson, B. (1984). Four-hole satellites in the L_3VV Auger and the valence-band spectra from nickel. **Physical Review B** 30 (4): R2245-2248.
- Microcal Software, Inc. (1997). Origin (version 5.0) [Computer software]. USA.

- Mittendorfer, F., Eichler, A., and Hafner, J. (1999). Structural, electronic and magnetic properties of nickel surfaces. **Surface Science** 423: 1-11.
- Mott, N. F. (1966). In F. Abeles (ed.). **Optical Properties and Electronic Structures of Metals** (p. 315). Amsterdam: North-Holland.
- Oh, S. -J., Allen, J. W., Lindau, I., and Mikkelsen, J. C., Jr. (1982). Resonant valence-band satellites and polar fluctuations in nickel and its compounds. **Physical Review B** 26 (9): 4845-4856.
- Ohmura, Y., and Sato, T. (1990). On the autoionization emission for X-ray excited Auger spectra. **Journal of the Physical Society of Japan** 59 (2): 725-737.
- Ohno, M. (1998). Theoretical study of Auger-photoelectron coincidence, Auger-electron, and X-ray emission spectra of Ni metal and related systems. **Physical Review B** 58 (19): 12795-12807.
- Okane, T., *et al.* (1993). Angle-resolved resonant photoemission of Ni(100) and Ni(110) single crystals. **Zeitschrift Für Physik B** 91: 437-443.
- Pagliara, S., *et al.* (2002). Coexistence of interfering and noninterfering channels in resonant photoemission spectra across the Cu $2p \rightarrow 3d$ threshold. **Physical Review B** 65: 205107.
- Penn, D. R. (1979). Effect of bound hole pairs on the d -band photoemission spectrum of Ni. **Physical Review Letters** 42 (14): 921-925.
- Perdew, J. P., *et al.* (1992). Atoms, molecules, solids, and surfaces: applications of the generalized gradient approximation for exchange and correlation. **Physical Review B** 46 (11): 6671-6687.

- Petrov, V. N., and Kamochkin, A. S. (2004). Energy analyzer for spin polarized Auger electron spectroscopy. **Review of Scientific Instruments** 75 (5): 1274-1279.
- Prayoon Songsiriritthigul, *et al.* (2001). Comparison of varied-line-spacing plane grating and varied-line-spacing spherical grating monochromators for the Siam Photon Source. **Nuclear Instruments and Methods in Physics Research A** 467-468: 593-596.
- Prayoon Songsiriritthigul, *et al.* (2004). The commissioning results of the first beamline at the Siam Photon Laboratory. In T. Warwick, J. Arthur, H. A. Padmore, and J. Stöhr (eds.). **Synchrotron radiation instrumentation: eight international conference** (pp. 372-375). USA: Springer-Verlag.
- Prayoon Songsiriritthigul, *et al.* (2005). The final state interaction in $3p$ - $3d$ resonance excitation of Ni(111). **Journal of Electron Spectroscopy and Related Phenomena** 144-147: 569-571.
- Prayoon Songsiriritthigul, Weerapong Pairsuwan, Ishii, T., and Kakizaki, A. (2003). Beamline at Siam Photon Laboratory. **Nuclear Instruments and Methods in Physics Research B** 199: 565-568.
- Prideaux, A., and Madison, D. H. (2003). Role of the postcollision interaction in electron-impact ionization of argon and krypton. **Physical Review A** 67: 052710.
- Sakisaka, Y., *et al.* (1987a). New observation of the valence-band satellite in Ni(110). **Physical Review Letters** 58 (7): 733-736.
- Sakisaka, Y., *et al.* (1987b). Photoemission study of the valence-band satellite of Ni(110). **Physical Review B** 36 (12): 6383-6389.

- Samred Kantee, Supat Klinkhieo, and Prayoon Songsiriritthigul. Data acquisition system for the angle-integral photoemission system at the Siam Photon Laboratory. submitted for publication in **Suranaree Journal of Science and Technology**.
- Sawatzky, G. A. (1977). Quasiatomic Auger spectra in narrow-band metals. **Physical Review Letters** 39 (8): 504-507.
- Sawatzky, G. A., and Lenselink, A. (1980). Auger line shape in narrow-band metals. **Physical Review B** 21 (5): 1790-1796.
- Schedin, F., Warburton, D. R., Thornton, G., and Hoyland, M. A. (1998). k -dependent exchange splitting of empty bands in nickel. **Physical Review B** 57 (6): 3491-3494.
- Schiff, L. I. (1968). **Quantum Mechanics** (3rd ed.). New York: McGraw-Hill.
- Schmidt, E., Schröder, H., Sonntag, B., Voss, H., and Wetzels, H. E. (1984). $M_{2,3}$ -shell Auger and autoionisation spectra of free Cr, Mn, Fe, Co, Ni and Cu atoms. **Journal of Physics B: Atomic, Molecular and Optical Physics** 17: 707-718.
- Schmidt, V., Sandner, N., Mehlhorn, W., Adam, M. Y., and Wuilleumier, F. (1977). Post-collision interaction in the xenon $N_{4,5}$ - OO Auger spectrum excited by photon impact. **Physical Review Letters** 38 (2): 63-66.
- Schwinger, J. (1949). On the classical radiation of accelerated electrons. **Physical Review** 75 (12): 1912-1925.
- Shirley, D. A. (1972). High-resolution X-ray photoemission spectrum of the valence bands of gold. **Physical Review B** 5 (12): 4709-4714.

- Smith, K. E., and Kevan, S. D. (1991). The electronic structure of solids studied using angle-resolved photoemission spectroscopy. **Progress in Solid State Chemistry** 21: 49-131.
- Suga, S., *et al.* (1999). $2p$ resonance photoemission and Auger features in NiS_2 and FeS_2 . **Physical Review B** 60 (7): 5049-5054.
- Tanaka, A., and Jo, T. (1992). Resonances and magnetic circular dichroism in valence-band photoemission predicted at Ni $2p$ threshold for ferromagnetic nickel. **Journal of the Physical Society of Japan** 61 (8): 2669-2672.
- Tezuka, Y., *et al.* (2004). Conduction band satellite of Ni metal observed using $3p-3d$ resonant inverse photoemission study. **Physical Review B** 70: 193107.
- Tiedtke, K., *et al.* (1999). Multiplet effects on the shape of the $3p$ photoelectron spectrum of atomic Ni. **Physical Review A** 60 (4): 3008-3012.
- Tjeng, L. H., *et al.* (1993). Magnetic circularly polarized $2p$ resonant photoemission of nickel. **Physical Review B** 48 (18): 13378-13382.
- Tombouliau, D. H., Hartman, P. L. (1956). Spectral and angular distribution of ultraviolet radiation from the 300-Mev Cornell Synchrotron. **Physical Review** 102 (6): 1423-1447.
- Tonner, B. P. (1998). **Numerical analysis of X-ray photoelectron spectroscopy.**
[online]. Available:
http://photon.physics.ucf.edu/XRAY/Courses/Phy904/Protocol_3.pdf
- Tougaard, S. and Sigmund, P. (1982). Influence of elastic and inelastic scattering on energy spectra of electrons emitted from solids. **Physical Review B** 25 (7): 4452-4466.

- VG Microtech. (1998). VGX900 (version 7) [Computer software]. England.
- Wakoh, S. (1965). Band structure of metallic copper and nickel by a self-consistent procedure. **Journal of the Physical Society of Japan** 20 (10): 1894-1901.
- Wakoh, S. and Yamashita, J. (1964). Fermi surface of Ni. **Journal of the Physical Society of Japan** 19 (8): 1342-1350.
- Wegner, T., Potthoff, M., and Nolting, W. (2000). Theory of spin-resolved Auger-electron spectroscopy of ferromagnetic 3*d*-transition metals. **Physical Review B** 61 (2): 1386-1395.
- Weinelt, M., *et al.* (1997). Resonant photoemission at the 2*p* edges of Ni: resonant Raman and interference effects. **Physical Review Letters** 78 (5): 967-970.
- Weling, F. and Callaway, J. (1982). Semiempirical description of energy-bands in nickel. **Physical Review B** 26 (2): 710-719.
- Wiwat Wongkokua and Prayoon Songsiriritthigul (2005). Investigation of gas species generated in the photoemission spectroscopy system at the Siam Photon Laboratory. **Suranaree Journal of Science and Technology** 12 (1): 47-53.

APPENDICES

APPENDIX A

DEGENERACY

Suppose there is a level whose state is degenerate with eigen functions $|u_s\rangle$ and $|u_d\rangle$. Let the energy be E_0 with the Hamiltonian H_0 . Then

$$\left. \begin{aligned} H_0|u_s\rangle &= E_0|u_s\rangle \\ H_0|u_d\rangle &= E_0|u_d\rangle \end{aligned} \right\} \quad (\text{A.1})$$

If the perturbation, V , comes in the system, the eigen functions change. Suppose the eigen functions are given by the linear combination of $|u_s\rangle$ and $|u_d\rangle$, as

$$\psi = a_s|u_s\rangle + a_d|u_d\rangle \quad (\text{A.2})$$

$$(H_0 + V)\psi = E\psi \quad (\text{A.3})$$

If we apply $|u_s\rangle$ and $|u_d\rangle$ to (A.3), we have

$$\left. \begin{aligned} a_s(E_0 + V_{11} - E) + a_d V_{12} &= 0 \\ a_s V_{21} + a_d(E_0 + V_{22} - E) &= 0 \end{aligned} \right\} \quad (\text{A.4})$$

Here the orthogonality, $\langle u_s | u_d \rangle = \langle u_d | u_s \rangle = 0$, is used and we put

$$\begin{aligned} V_{12} &= \langle u_s | V | u_d \rangle \\ V_{21} &= \langle u_d | V | u_s \rangle \\ V_{11} &= \langle u_s | V | u_s \rangle \\ V_{22} &= \langle u_d | V | u_d \rangle \end{aligned} \quad (\text{A.5})$$

The secular equation for (A.4) is given as

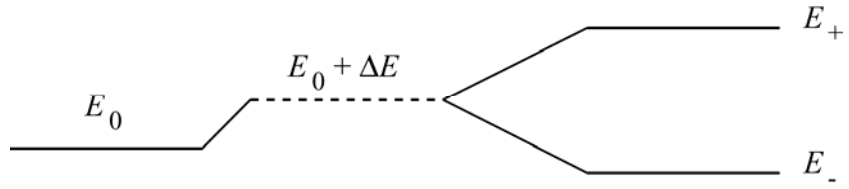
$$\begin{vmatrix} (E_0 + V_{11} - E) & V_{12} \\ V_{21} & (E_0 + V_{22} - E) \end{vmatrix} = 0 \quad (\text{A.6})$$

The solutions of (A.4) are given as

$$E_{\pm} = E_0 + \Delta E \pm \sqrt{(E_0 + \Delta E)^2 + \Delta V^2} \quad (\text{A.7})$$

Here we define

$$\left. \begin{aligned} \Delta E &= \frac{V_{11} + V_{12}}{2} \\ \Delta V^2 &= V_{12} \cdot V_{21} - (E_0 + V_{11})(E_0 + V_{22}) \end{aligned} \right\} \quad (\text{A.8})$$



APPENDIX B

OPW, PSEUDO-POTENTIAL AND OTHER METHODS

Here we briefly review the methods of the energy-band calculations. We try to find appropriate approximation methods to the Bloch function given in (1.6)

$$\psi_{\alpha\mathbf{k}}(\mathbf{r}) = e^{i\mathbf{k}\cdot\mathbf{r}} u_{\alpha\mathbf{k}}(\mathbf{r}) \quad (1.6')$$

Here n in (1.6) is replaced with α in (1.6')

B.1 Nearly-Free-Electron (NFE) Approximation

When the crystal potential is weak, the wave function of an electron in the crystal is like that of a free-electron. We approximate $u_{n\mathbf{k}}(\mathbf{r})$ as

$$u_{\alpha\mathbf{k}}(\mathbf{r}) = \sum_n^N c_{\mathbf{k}}(\mathbf{k}_m) e^{i\mathbf{k}\cdot\mathbf{r}} \quad (B.1)$$

Here \mathbf{k}_m is a reciprocal lattice vector. (B.1) indicates that $u_{\alpha\mathbf{k}}(\mathbf{r})$ is expressed as the expansion like the Fourier series in the Brillouin zone. Since the potential function is periodic in the crystal, it can also be expanded as the Fourier series in the Brillouin zone as

$$V(\mathbf{r}) = \sum_{n=0}^N v(\mathbf{k}_m) e^{i\mathbf{k}\cdot\mathbf{r}} \quad (B.2)$$

Inserting (B.1) and (B.2) into the Schrödinger equation, we have simultaneous algebraic equations, which give $c_{\mathbf{k}}(\mathbf{k}_m)$ as solutions. The energy eigen values depending on \mathbf{k} have the form similar to one given in (1.13)

$$\varepsilon(\mathbf{k}) = \varepsilon_0 + \frac{\hbar^2 \mathbf{k}^2}{2m^*} \quad (\text{B.3})$$

where, m^* is an effective mass.

B.2 Cellular Method

We define the space surrounded by planes perpendicularly cutting the lines connecting neighboring atoms at their centers. The space is a polyhedron not much different from a sphere. The space is called the Wigner-Seitz (WS) cell as the unit cell of the crystal lattice. We assume an appropriate potential in the WS cell and solve the Schrödinger equation in this unit cell. The solutions are connected smoothly on the WS cell with those of the adjacent cells. This method is called the cellular method.

B.3 Augmented Plane Wave (APW) Method

We make a sphere in the WS cell. It is smaller than the WS cell. We assume an appropriate potential, often called the muffin-tin potential, in the sphere and solve the Schrödinger equation in it. The solutions are connected smoothly to plane waves existing in the area between adjacent spheres. The resulting wave equations have the forms of plane waves in the space between the neighboring spheres. Thus the electron is free-electron-like there. In the sphere, the solutions have the nature of atomic functions. Mathematically, the procedure to reach the solutions is complicated but

they are better approximate the real Bloch functions. This method is called the augmented plane wave (APW) method.

B.4 Linear-Combination-of-Atomic-Orbitals (LCAO) Method

We approximate the Bloch function with the Bloch sum defined as

$$\psi_{\alpha\mathbf{k}}(\mathbf{r}) = \frac{1}{\sqrt{N}} \sum_n e^{i\mathbf{k}\mathbf{R}_n} \mu_{\alpha}(\mathbf{r} - \mathbf{R}_n) \quad (\text{B.4})$$

We obtain $\mu_{\alpha}(\mathbf{r} - \mathbf{R}_n)$ by solving Schrödinger equation in the unit cell (WS cell), as

$$\left\{ -\frac{\hbar^2}{2m} \nabla^2 + V_0(\mathbf{r}) \right\} \mu_{\alpha}(\mathbf{r} - \mathbf{R}_n) = \varepsilon_{\alpha} \mu_{\alpha}(\mathbf{r} - \mathbf{R}_n) \quad (\text{B.5})$$

Here α is a quantum number distinguishing different eigen states. The LCAO approximation is suitable for treating the localized electron states like $3d$ states of transition metals. Although V_0 is not the potential of an atom, it is not much different from it. Therefore, we approximate the eigen function $\mu_{\alpha}(\mathbf{r})$ by taking the linear combination of atomic orbitals as

$$|\mu_d\rangle = \sum_j a_j |d_j\rangle \quad (\text{B.6})$$

Here $|d_j\rangle$ is an atomic orbital.

The energy is expressed as

$$\begin{aligned} \varepsilon(\mathbf{k}) &\cong \sum_n e^{i\mathbf{k}\mathbf{R}_n} \varepsilon_{\mathbf{R}_n} \\ \varepsilon_{\mathbf{R}_n} &= \frac{1}{V_c} \langle \psi_{\alpha\mathbf{k}}(\mathbf{r} + \mathbf{R}_n) | H | \psi_{\alpha\mathbf{k}}(\mathbf{r}) \rangle \end{aligned} \quad (\text{B.7})$$

$\varepsilon_{\mathbf{R}_n}$ is not zero only between the nearest neighbor atoms. In the simple-cubic-lattice case, $\varepsilon(\mathbf{k})$ is given as

$$\varepsilon(k) \cong \varepsilon_\alpha + 2\varepsilon_{100}(\cos ak_x + \cos ak_y + \cos ak_z) \quad (\text{B.8})$$

ε_{100} is a constant and a is the lattice constant.

The calculation appears to be simple. However, the calculation is complicated since the overlap integral is practically not small. This leads to the incomplete orthogonalization. In this approximation, NFE waves do not come in even in the region where the potential is effectively zero outside the atom. It is difficult to introduce the Bloch condition to the atomic orbitals which satisfy the boundary condition as

$$\psi_\alpha(\mathbf{r}) \rightarrow 0 \text{ as } \mathbf{r} \rightarrow \infty$$

B.5 Orthogonalized Plane Wave Approximation

As mentioned already, the electronic states are like those of NFE in the region between adjacent atoms where the potential is weak. In the region around the atomic nucleus, a localized eigen function is used. However, the function is not necessarily $|\mu_\alpha\rangle$ as given in (B.6). The alternative approximation is to use the core electron function. Let the function be $b_i(\mathbf{r})$. The corresponding Bloch sum is

$$b_{\mathbf{k}}(\mathbf{r}) = \sum_n e^{i\mathbf{k}\mathbf{R}_n} b_i(\mathbf{r} - \mathbf{R}_n) \quad (\text{B.9})$$

$b_{ik}(\mathbf{r})$ is a linear combination of one-electron functions strongly localized at the atomic core and having the energy, ε_i . It can be solution of the Schrödinger equation of the whole crystal.

Let the solution, $\phi_k(\mathbf{r})$, of the Schrödinger equation with high energy must be orthogonal to $b_{ik}(\mathbf{r})$ as

$$\langle b_{ik} | \phi_k \rangle = 0 \quad (\text{B.10})$$

The function, $\phi_k(\mathbf{r})$, must be like that of NFE. For orthogonal function, the high energy function, we define a new function as

$$\chi_k(\mathbf{r}) = e^{i\mathbf{k}\mathbf{r}} - \sum_i \beta_i b_{ik}(\mathbf{r}) \quad (\text{B.11})$$

Here β_i is defined as

$$\beta_i = \langle b_{ik} | e^{i\mathbf{k}\mathbf{r}} \rangle \quad (\text{B.12})$$

Obviously, we have

$$\langle e^{i\mathbf{k}'\mathbf{r}} | \chi_k \rangle = \delta_{\mathbf{k}'\mathbf{k}} \quad (\text{B.13})$$

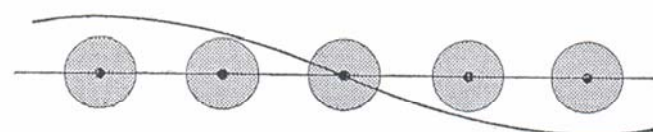
The waves defined by $\chi_k(\mathbf{r})$ are called the orthogonalized plane wave (OPW). OPW satisfies the condition that it is strongly localized at the atomic core, plane-wave like in the region of adjacent cores, and orthogonal to the free wave. The Bloch function is approximated with OPW as

$$\psi_k(\mathbf{r}) = \sum_n \alpha_{\mathbf{k}-\mathbf{R}_n} \chi_{\mathbf{k}-\mathbf{R}_n} \quad (\text{B.14})$$

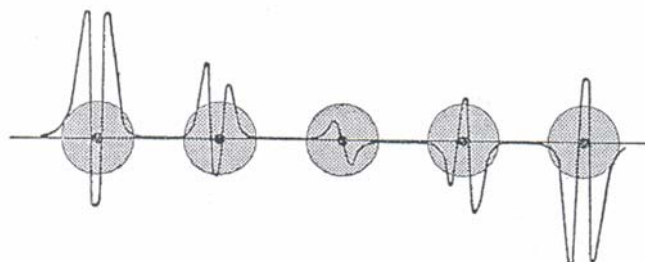
The coefficient, $\alpha_{\mathbf{k}-\mathbf{R}_n}$, must be determined so that the eigen values are minimized.

The Bloch function formed with OPW's converges very fast. In many cases only one piece of OPW is sufficient to express the wave function over a wide range of \mathbf{k} . Even

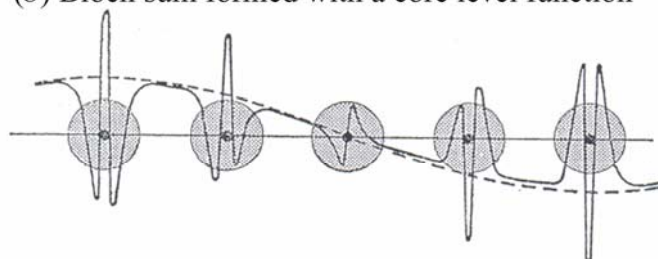
at the zero boundaries, only a few pieces of OPW are necessary. It is recognized that the OPW method is the modification of the NFE method. OPW is depicted schematically in Fig. B.1.



(a) Plane wave



(b) Bloch sum formed with a core level function



(c) OPW = Plan wave - core level Bloch sum

Fig. B.1 The structure schematically showing OPW.

B.6 Pseudo-Potential Method

If we insert the Bloch function formed by a high energy function and similar to OPW into the Schrödinger equation, we have

$$\psi = \phi - \sum_t \langle b_t | \phi \rangle b_t \quad (\text{B.15})$$

$$H\phi - \sum_t \langle b_t | \phi \rangle H b_t = \varepsilon \phi - \varepsilon \sum_t \langle b_t | \phi \rangle b_t$$

Then we have

$$H\phi + \sum_t (\varepsilon - \varepsilon_t) \langle b_t | \phi \rangle b_t = \varepsilon \phi \quad (\text{B.16})$$

This can be written as

$$\begin{aligned} (H + V_R)\phi &= \varepsilon \phi \\ V_R \phi &= \sum_t (\varepsilon - \varepsilon_t) b_t \langle b_t | \phi \rangle \end{aligned} \quad (\text{B.17})$$

Let the potential in H be V , then (B.17) is written as

$$\begin{aligned} \left(-\frac{\hbar^2}{2m} \nabla^2 + V_{\text{eff}} \right) \phi &= \varepsilon \phi \\ V_{\text{eff}} &= V + V_R \end{aligned} \quad (\text{B.18})$$

(B.18) seems to require that we must solve (B.18). However, the Fourier transform of V_{eff} shows that the only the first term in it is important and the other terms are small.

In practice V_R is defined as an operator:

$$\begin{aligned} V_R(\mathbf{r}, \mathbf{r}') &= \sum_t (\varepsilon - \varepsilon_t) b_t(\mathbf{r}) b_t^*(\mathbf{r}') \\ V_R | \phi \rangle &= \int V_R(\mathbf{r}, \mathbf{r}') \phi(\mathbf{r}') d\tau \end{aligned} \quad (\text{B.19})$$

$V(\mathbf{r}, \mathbf{r}')$ is called the pseudo-potential and ϕ the pseudo-function. Instead of making OPW, we solve (B.18) and obtain similar functions, ϕ , and then ψ_0 . This method is called the pseudo-potential method.

B.7 Other Methods

In recent energy-band calculations, more advanced methods as the Green function method (Koringa-Kohn-Rostoker method, KKR method) and the density functional method (GGA approximation is based on this method) is used. Here, we do not deal with them.

APPENDIX C

BACKGROUND SUBTRACTION

Photoemission spectrum consists with an intrinsic spectra and backgrounds. To obtain the intrinsic photoemission spectrum, the backgrounds need to be removed. There are a few types of background employed in the analysis of photoemission spectra, *e.g.*, linear backgrounds, integral backgrounds and backgrounds base on elastic and inelastic loss processes.

The backgrounds of photoemission spectra originate from either elastic or inelastic scattering of the electrons in solid (Tougaard and Sigmund, 1982). Consider a piece of solid sample with a plane surface is shone by an excitation light. The electrons in the solid will be excited and then escape through the surface entering an electron energy analyzer. Some of the electrons will loss their kinetic energy during moving in the solid by the inelastic scattering. This is directly responsible for the backgrounds in the photoemission spectra. Elastic scattering is also important. This will cause the electrons deviated from straight path motion and thus increase the total path length of the electrons traveling to the solid surface. The number of inelastic scattering events is proportional to the total path length.

In this thesis, the Shirley (1972) method which is based on the integral background type was chosen. The method requires an iterative approach and can be performed by a computer programming. An iterative algorithm (Tonner, 1998) was

used for a script writing of the Origin (Microcal Software, Inc., Computer Program, 1997). The algorithm and script can be expressed as follow:

The Shirley background intensity $B(\varepsilon)$, ε is kinetic energy, within the photoemission spectra is define as an integrated intensity of the inelastic scattering electrons at lower kinetic energy with the condition that the background matches the measured spectrum outside the region of the peak;

$$B(\varepsilon) \equiv A \int_{\varepsilon}^{\infty} P(\varepsilon') d\varepsilon' = A \int_{\varepsilon}^{\infty} [(M(\varepsilon') - B(\varepsilon'))] d\varepsilon', \quad (C.1)$$

Where P is the intrinsic spectrum intensity, M is the measured intensity, and A is a constant of the inelastic scattering yield.

The parameters needed for the calculation are defined in Fig. C.1. Given a measured photoemission spectrum M_i , with $i = 1$ at the lowest kinetic energy and $i = N$ at the highest kinetic energy, the background value at the starting points are

$$B_N = B_{N-1} = M_N \quad (C.2)$$

The first guess of A is

$$A^{(0)} = 0.002 \quad (C.3)$$

The first trial of backgrounds, $B_i^{(0)}$, are calculated one by one from high kinetic energy to lower ones using the first guess $A^{(0)}$,

$$B_i^{(0)} = B_N + A^{(0)} \sum_{j=i+1}^N (M_j - B_j^{(0)}) \quad (C.4)$$

The next iteration starts with a corrected $A^{(1)}$,

$$A^{(1)} = A^{(0)} \left(1 + \frac{M_1 - B_1^{(0)}}{M_1} \right) \quad (C.5)$$

The calculation ends when the background at $i = 1$, the lowest kinetic energy, matches the measured spectrum.

```
/*Shirley background subtraction script for the Origin 5.0*/
```

```
/*Prepare a new work sheet with a column name SIG for the photoemission spectrum*/
```

```
worksheet -c BG;           // Create a new column named BG
```

```
worksheet -c TEMP;        // Create a new column name TEMP
```

```
A0=0.002;                 // Initial value for the first guess
```

```
N=41;                     // Number of signal lows
```

```
Loop=10;                  // Loops for iteration
```

```
for(i=1;i<=N;i=i+1){      // Clear values for the column BG and TEMP
```

```
    col(BG)[i]=0;
```

```
    col(TEMP)[i]=0;
```

```
};
```

```
col(BG)[N]=col(SIG)[N];    // Set initial values of backgrounds
```

```
col(BG)[N-1]=col(SIG)[N];
```

```
for(i=N-2;i>=1;i=i-1){    // The first trials of background calculation
```

```
    col(BG)[i]=col(BG)[N]+A0*(col(SIG)[i+1]-col(BG)[i+1]);
```

```
};
```

```
for(j=1;j<=Loop;j=j+1){   // Starting of the iterative calculations
```

```
    col(TEMP)=col(SIG)-col(BG);
```

```
    for(i=N;i>=2;i=i-1){   // Integrating the background
```

```

    col(TEMP)[i-1]=col(TEMP)[i]+col(TEMP)[i-1];

};

for(i=N-1;i>=1;i=i-1){

    col(BG)[i]=col(BG)[N]+A0*col(TEMP)[i+1];    // Update the BG column

};

A1=A0*(1+(col(SIG)[1]-col(BG)[1])/col(SIG)[1]);    // Correcting the A0

A0=A1;    // Update the A0

};

```

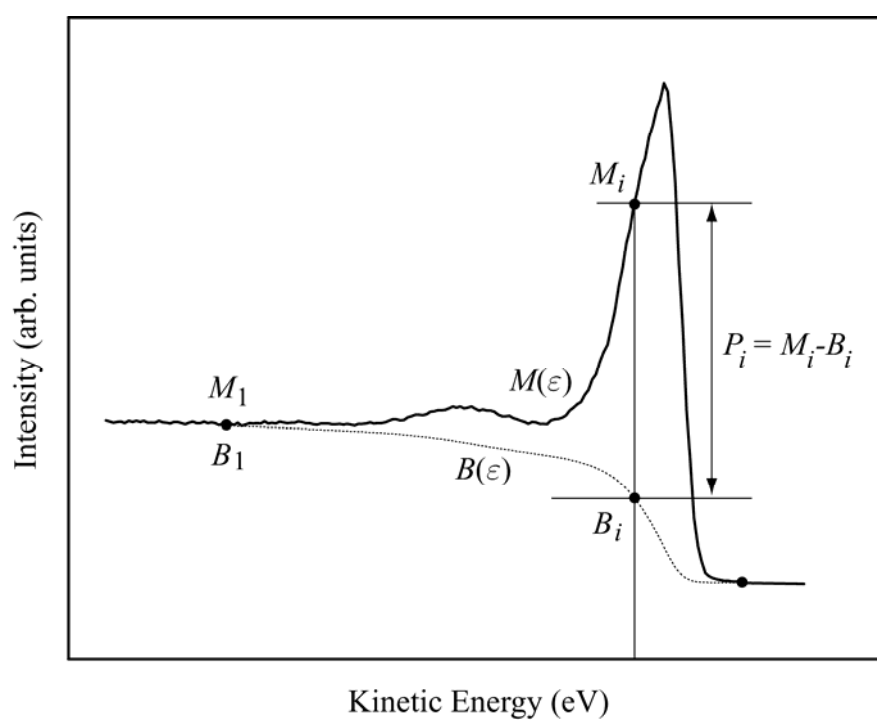


Fig. C.1 Definitions for calculation of the Shirley method algorithm.

APPENDIX D

AUGER NOMENCLATURE

There are two types of electron spectroscopy nomenclature used by scientists which are atomic orbits and electron shells. The first type is also called spectroscopic level while the second type called X-ray level. It is conventional to use spectroscopic notation for a photoelectron feature in photoemission. In case of Auger electron feature, the X-ray notation is almost always used. Table D.1 shows the X-ray level and their spectroscopic equivalents.

Table D.1 Spectroscopic and X-ray notation

Quantum numbers			Spectroscopic level	X-ray level
n	l	j		
1	0	1/2	$1s_{1/2}$	K
2	0	1/2	$2s_{1/2}$	L_1
2	1	1/2	$2p_{1/2}$	L_2
2	1	3/2	$2p_{3/2}$	L_3
3	0	1/2	$3s_{1/2}$	M_1
3	1	1/2	$3p_{1/2}$	M_2
3	1	3/2	$3p_{3/2}$	M_3
3	2	3/2	$3d_{3/2}$	M_4
3	2	5/2	$3d_{5/2}$	M_5
	<i>etc.</i>		<i>etc.</i>	<i>etc.</i>

When describing the Auger transition, the initial hole level is given first, followed by the levels of the final two holes in order of decreasing binding energy such as $L_3M_{4,5}M_{4,5}$ and $M_{2,3}M_{4,5}M_{4,5}$. Levels with a non-zero value of the orbital angular momentum show spin-orbit splitting. In some cases, the magnitude of this splitting is too small to be distinguished. Hence, the double subscript of these levels, *e.g.*, $M_{2,3}$, represent both M_2 and M_3 levels.

CURRICULUM VITAE

Mr. Wiwat Wongkokua

Date of birth: 1 November 1973

Place of birth: Chumporn, Thailand

Nationality: Thai

Address: Department of Physics, Faculty of Science, Kasetsart
University, Bangkok 10900, Thailand.

Education

Academic year

1991-1995 Kasetsart University, Bangkok, Thailand.

Bachelor of Science (Physics)

1996-2000 Kasetsart University, Bangkok, Thailand.

Master of Science (Physics)

2000-2005 Suranaree University of Technology, Nakhon Ratchasima,
Thailand.

Ph.D. in Physics

Academic Experience

1996-at present Lecturer, Department of Physics, Faculty of Science,
Kasetsart University, Bangkok, Thailand.